Ultra-WideBand (UWB) Microwave Tomography using Full-Wave Analysis Techniques for Heterogeneous and Dispersive Media

by

Abas Sabouni

A Thesis submitted to the Faculty of Graduate Studies of

The University of Manitoba

in partial fulfilment of the requirements of the degree of

Doctor of Philosophy

Department of Electrical and Computer Engineering

University of Manitoba

Winnipeg, Manitoba, Canada

Copyright©2011 by Abas Sabouni

ABSTRACT

This thesis presents the research results on the development of a microwave tomography imaging algorithm capable of reconstructing the dielectric properties of the unknown object. Our focus was on the theoretical aspects of the non-linear tomographic image reconstruction problem with particular emphasis on developing efficient numerical and non-linear optimization for solving the inverse scattering problem. A detailed description of a novel microwave tomography method based on frequency dependent finite difference time domain, a numerical method for solving Maxwell's equations and Genetic Algorithm (GA) as a global optimization technique is given. The proposed technique has the ability to deal with the heterogeneous and dispersive object with complex distribution of dielectric properties and to provide a quantitative image of permittivity and conductivity profile of the object. It is shown that the proposed technique is capable of using the multi-frequency, multi-view, and multi-incident planer techniques which provide useful information for the reconstruction of the dielectric properties profile and improve image quality. In addition, we show that when *a-priori* information about the object under test is known, it can be easily integrated with the inversion process. This provides realistic regularization of the solution and removes or reduces the possibility of non-true solutions.

We further introduced application of the GA such as binary-coded GA, real-coded GA, hybrid binary and real coded GA, and neural-network/GA for solving the inverse scattering problem which improved the quality of the images as well as the conversion rate. The implications and possible advantages of each type of optimization are discussed, and synthetic inversion results are presented. The results showed that the proposed algorithm was capable of providing the quantitative images, although more research is still required to improve the image quality. In the proposed technique the computation time for solution convergence varies from a few hours to several days. Therefore, the parallel implementation of the algorithm was carried out to reduce the runtime.

The proposed technique was evaluated for application in microwave breast cancer imaging as well as measurement data from the University of Manitoba and Institut Frsenel's microwave tomography systems.

CONTRIBUTIONS

This dissertation outlines several noteworthy contributions to the art of microwave tomography imaging. Some of these contributions were accomplished with help from colleagues noted herein. The specific contributions of the author include:

- Achieving an understanding of, and clarifying, the non-linear inverse scattering problem.
- Implementing a novel differential-based time-domain inverse solver which uses the multi-view/multi-illumination technique and includes the dispersive and heterogeneous characteristic of the object.
- Implementation of parallel program of the proposed technique which improves the computational runtime and speeds up the convergence rate.
- Investigating the different polarizations of scattered field and proposing a novel microwave tomography setup wherein a loop antenna is used to generate an electromagnetic incident field.
- Introducing a novel multi-level optimization technique for solving the inverse scattering problem which uses the real and binary coded GA. In this hybrid GA, RGA acts as a regularizer for BGA and rejects the non-true solutions. Therefore, the search space is very limited for RGA that make it converge quickly.
- Proposing a novel problem-dependent regularization approach which treats the ill-posedness of the inverse problem using *a-priori* information.
- Proposing a novel imaging technique for solving the inverse scattering problem using a microwave tomography method along with a microwave radar technique. In this technique, spatial information obtained from the radar method is used to initialize the microwave tomography technique in order to determine the accurate quantitative image.
- Discussing the fundamental role of the model and field calibrations required for pre-processing the measured scattered field before the use of inversion algorithms.

Overall, some significant advances have been made by the above contributions, but there is (as always) still room for much more research in this area. As far as the implementation of the algorithms is concerned, all the inversion algorithms were implemented by the author except the Neural-Network[1] and microwave radar method[2]. And also, the utilized forward solver was implemented by the author. The parallel version of that was developed in collaboration with the Computer Science Department[3].

---

[1] The utilized Neural-Network was implemented by Ali Ashtari.

[2] The utilized microwave radar method was implemented by Daniel Flories Tapia.

[3] Meilian Xu and Parimala Thulasiraman.

ACKNOWLEDGMENTS

First and foremost, I would like to thank my academic advisor Dr. Sima Noghanian for her support, direction, and encouragement of my education and research efforts for nearly a decade. Without her example and advice, I never would have entered graduate school.

I also recognize the direction and support given by my co-advisor, Dr. Lotfollah Shafai.

For their work in guiding my research throughout my PhD, I also recognize the efforts of my committee: Dr. Stephen Pistorius, Dr. Gabriel Thomas, and Dr. Atef Elsherbeni.

I would like to acknowledge the many colleagues without whom this research would not have been possible. More than is usually recognized, academic research is a group effort. Dr. Ali Ashtari, Meilian Xu, Dr. Daniel Flories Tapia, Dr. Parimala Thulasiraman, Dr. Joe LoVetri, Dr. Colin Gilmore, Majid Ostadrahimi, and Jonatan Aronsson have all significantly enriched my education.

I would like to thank the various agencies and individuals that have provided me (and many other researchers) with the funding necessary to live the academic life. Specifically, the CancerCare Manitoba, National Sciences and Engineering Research Council of Canada, Manitoba Hydro, North Dakota Experimental Program to Stimulate Competitive Research, and Mathematics of Information Technology and Complex Systems Canada, have all contributed to this research. Without this support, this research would have simply not been possible.

Finally, I would like to thank my family for all their love and encouragement. For my parents who raised me with a love of science and support me in all my pursuits. Their unconditional love and generosity have been the most precious blessings in my life. My brother, Farhad, and my sisters, Rozita and Farnoosh, have always been there for me and have kindly helped me to achieve my goals.

DEDICATION

To my parents

ABBREVIATIONS AND SYMBOLS

Abbreviation	**Description**
1D	One-dimensional.
2D	Two-dimensional.
3D	Three-dimensional.
ABC	Absorbing boundary condition.
AF	Antenna factor.
BGA	Binary-coded genetic algorithm.
CG	Conjugate gradient.
CSI	Contrast source inversion.
DBIM	Distorted born iteration method.
DLVA	Double-layer Vivaldi antenna.
dB	Desebell.
FDTD	Finite-difference time-domain.
$(\mathrm{FD})^2\mathrm{TD}$	Frequency-dependent finite-difference time-domain.
FDTD/GA	Finite-difference time-domain and genetic algorithm.
GA	Genetic algorithm.
GHz	Gigahertzes.
HGA	Hybrid binary and real coded genetic algorithm.
IE	Integral equation.
IDC	Infiltrating ductal carcinoma.
LM	Levenberg-marquardt.
MoM	Method-of-moment.
MR	Multiplicatively regularized.
MRI	Magnetic resonance imaging.
MWI	Microwave imaging.
MWT	Microwave tomography.
MWR	Microwave radar.
MPI	Message passing interface.
NN	Neural network.
NDE	Non-destructive evaluation.
OI	Object-of-interest.
PDE	Partial differential equation.
PML	Perfectly matched layer.

Abbreviation	**Description**
PGA	Parallel genetic algorithm.
PFDTD	Parallel finite-difference time-domain.
PEC	Perfect electric conductor.
RGA	Real-coded genetic algorithm.
RCS	Radar cross section.
RX	Receiver antenna.
RF	Radio frequency.
SNR	Signal-to-noise-ratio.
TE	Transverse electric.
TF/SF	Total field and scattered field.
TM	Transverse magnetic.
TX	Transmitter antenna.
TS	Tournament selection.
UWB	Ultra-wideband.
UPML	Uniaxial perfect match layer.
UM	University of Manitoba.
VNA	Vector network analyzer.
X-ray	X-radiation.

Symbol	**Description**
x, y, z	Coordinate stretching coefficients.
ϵ	Dielectric properties.
ϵ_0	Permittivity of free-space.
ϵ_r	Relative complex permittivity of the OI.
σ	Conductivity.
σ_s	Conductivity at low frequency.
δ	Penetration depth.
μ_0	Permeability of free-space.
ω	Radial frequency.
τ	Relaxation time.
f	Frequency of operation.
ρ	Percentage of water content.
Δt	Time increment.
Δx, Δy	Cell size in x, y direction.
E_{inc}	Incident field.
E_{scat}	Scattered field.
E_{total}	Total field.
E_{total}^{meas}	Measured total field.
E_{scat}^{sim}	Simulated scattered field.
E_{inc}^{meas}	Measured incident field.
E_{inc}^{sim}	Simulated incident field.
$\vec{r}$	Position vector in the Cartesian coordinates.
λ	Effective wavelength in the media.
D	Imaging domain.
V	Problem domain.
∇	Gradient operator.
$\nabla\cdot$	Divergence operator.
$\nabla\times$	Curl operator.

TABLE OF CONTENTS

Abstract i

Contributions ii

Acknowledgments iv

Abbreviations and symbols vi

1. Introduction 1
- 1.1 Electromagnetic imaging 1
- 1.2 Microwave imaging 3
- 1.3 Microwave imaging methods 4
  - 1.3.1 UWB microwave radar method 4
  - 1.3.2 Microwave tomography method 6
- 1.4 Qualitative linear inversion 7
- 1.5 Quantitative non-linear inversion 8
  - 1.5.1 Iterative approaches without using forward solver 8
  - 1.5.2 Iterative approaches using forward solver 10
- 1.6 Motivation 15
- 1.7 Outline of the thesis 18

2. Statement of the problem 21
- 2.1 Objective 21
- 2.2 Problem definition and assumption 22
  - 2.2.1 Geometry of the problem 22
  - 2.2.2 Two-dimensional MWT 23
  - 2.2.3 Background medium and scatterers 24
  - 2.2.4 Amplitude and phase 25
  - 2.2.5 Frequency bandwidth 25
  - 2.2.6 Search space 26
  - 2.2.7 Evaluating the results 27
- 2.3 Block diagram of the proposed technique 27

3. Microwave tomography algorithm 29
- 3.1 Maxwell's equations 29
  - 3.1.1 Inverse scattering problem from theoretical point of view . . . 34
- 3.2 Iterative technique 35
- 3.3 Optimization techniques 36
  - 3.3.1 Local optimization method 37
  - 3.3.2 Global optimization method 37
- 3.4 Genetic algorithm (GA) 38
  - 3.4.1 Advantage of GA 38
  - 3.4.2 GA parameters for the proposed MWT 40
  - 3.4.3 Real-coded GA (RGA) 40
  - 3.4.4 Binary-coded GA (BGA) 42
  - 3.4.5 BGA with knowledge about the number of scatterers 45
- 3.5 Fitness-function 47
  - 3.5.1 Multi-view/multi-illumination 48
  - 3.5.2 Multi-frequency 49
- 3.6 Dependent regularization 51
- 3.7 GA-based inverse solver 52
  - 3.7.1 The GA inversion procedure 53
- 3.8 Time domain algorithm 58
  - 3.8.1 Time domain forward scattering problem 58
- 3.9 Debye model 59
- 3.10 Frequency dependent FDTD 61
- 3.11 Preliminary validation 64
  - 3.11.1 Single scatterer 66
  - 3.11.2 Multiple scatterers 67
  - 3.11.3 Dispersive scatterers separated from each other 70
  - 3.11.4 Dispersive multiple adjacent scatterers 71
- 3.12 Hybrid real-coded GA and binary-coded GA (HGA) 74
- 3.13 Hybrid GA global optimization and Neural-Network training 76
- 3.14 Hybrid tomography and radar method (Hybrid MWR/MWT) 78
  - 3.14.1 Example of reconstructed image using the hybrid MWR/MWT technique 82
- 3.15 Parallel computing 85
  - 3.15.1 Parallel FDTD (PFDTD) 85
  - 3.15.2 Parallel GA (PGA) 87
  - 3.15.3 Integrating PGA and PFDTD algorithm 89
  - 3.15.4 Reconstructing a high resolution object using the PFDTD/PGA 91
- 3.16 Antenna effect on scattered field 92
  - 3.16.1 Dipole antenna 97
  - 3.16.2 Circular horn antenna 99

3.16.3 Microstrip patch antenna . . . 102

4. Microwave tomography for breast cancer detection . . . 106
4.1 Rationale . . . 107
4.2 MWI for breast cancer screening . . . 107
4.2.1 Active MWI for breast cancer screening . . . 109
4.2.2 UWB microwave radar imaging . . . 111
4.2.3 Microwave tomography imaging . . . 113
4.2.4 Hybrid active MWI . . . 116
4.3 Breast topology . . . 117
4.4 Electrical properties of the normal and malignant breast tissues . . . 117
4.4.1 *Ex-vivo* dielectric properties of breast tissues . . . 118
4.4.2 *In-vivo* measurement of dielectric properties of breast tissues . 122
4.5 Inclusion of the water content dependency of breast tissue in $(FD)^2TD$ forward solver . . . 123
4.6 Numerical breast phantom . . . 126
4.7 Penetration depth . . . 129
4.7.1 Simulation results of penetration depth . . . 132
4.8 Matching material . . . 133
4.9 Tumour response (tumour signature) . . . 139
4.9.1 Tumour signature for different breast types . . . 144
4.10 Reconstruction algorithm for breast cancer imaging . . . 145
4.11 Inversion results . . . 148
4.11.1 Binary GA . . . 148
4.11.2 Hybrid Genetic Algorithm (HGA) . . . 150
4.12 HGA/FDTD in the presence of noise . . . 160
4.13 Resolution in MWI for early stage breast cancer detection . . . 165
4.14 Comparing the electric and magnetic components of scattered fields for breast cancer detection . . . 168

5. Microwave tomography experimental system . . . 176
5.1 University of Manitoba MWT experimental setup and data acquisition 178
5.2 Calibration . . . 179
5.2.1 Field calibration . . . 179
5.2.2 Model calibration . . . 180
5.2.3 Model calibration using reference object . . . 184
5.3 Experimental inversion results . . . 188
5.3.1 Experimental data from UM MWT system . . . 188
5.3.2 Experimental data from Institut Frsenel's MWT system . . . 194

6. Conclusions and future work . . . 200
6.1 Future work . . . 203

Appendices 207

A. Instability of the inverse scattering problem 208
  A.1 Several local minima for the inverse scattering problem 208

B. Genetic algorithm operators 210
  B.1 Selection, crossover, and mutation 210
  B.2 Elitism 212
  B.3 Population and generation sizes and rates 212

C. FDTD formulations 214
  C.1 Fundamentals of FDTD method (Yee algorithm) 214

D. Parallel FDTD 225

E. Dielectric properties measurement of breast tissue 228
  E.1 *Ex-vivo* measurement at the hospital 228
    E.1.1 Dielectric properties vs. temperature 229
    E.1.2 Dielectric properties vs. time of excision 232

References 257

LIST OF TABLES

3.1 The Debye parameters of breast tissues. 43
3.2 Code representative for the breast tissues. 43
3.3 Parameters of GA program for first example. 66

4.1 Single-pole Debye parameters for breast tissues. 122
4.2 The value of area under the tumour response for various sizes of tumours at different angles. 142
4.3 Look-up table of the Debye parameters for the binary-coded GA. . . 151
4.4 Look-up table of the Debye parameters for the real-coded GA. 151

5.1 Total error in S_{n1} for UMMWT chamber. 191

C.1 Pulse duration versus bandwidth frequency. 217

D.1 Example of different parallel FDTD codes with different parameters. . 227

LIST OF FIGURES

1.1 Block diagram of the existing MWT methods. 7

2.1 Geometry of the MWT. 23
2.2 Discretizing the object, (a) without knowledge of the boundary for the object, (b) with knowledge of the boundary of the object. 26
2.3 Block diagram of the proposed MWT method. 28

3.1 Multiple scattering. 34
3.2 Flowchart of the iterative technique. 36
3.3 Discretized the imaging domain for MWT. 41
3.4 The 2D cross-section of the breast phantom with different patch sizes (a) 16 cells, (b) 64 cells, and (c) 400 cells. 45
3.5 Each chromosome contains hybrid of types and locations of scatterers. 46
3.6 Sample individual solution for the chromosome 3.14. 47
3.7 Illuminating a dielectric object at four incident angles when E_{inc} is radiated from the (a) west side, (b) north side, (c) east side, and (d) south side. 50
3.8 Block diagram of the inverse scattering solver based on GA optimizer. 54
3.9 2D dielectric shell cylinder with diameter of $12cm$ with a $1.5cm$ scatterer at the off-center (a) original structure, and (b) discretized structure. . 57
3.10 Dielectric shell cylinder with a scatter located off-center. 66
3.11 (a) Fitness value of the best individual in different generations, (b) comparison between forward and reconstructed field evaluated by FDTD. 67
3.12 (a) Real, and (b) reconstructed images of Fig. 3.10. 68
3.13 Dielectric shell cylinder with two scatterers. 68
3.14 (a) Fitness value of the best individuals in different generations, (b) comparison between forward and reconstructed field evaluated by FDTD at 2.5GHz. 69
3.15 (a) Real, and (b) reconstructed images of Fig. 3.13. 69
3.16 (a) Numerical breast phantom with a $1.5cm$ tumour inside the fatty tissue (top view), (b) map of dielectric constant, and (c) map of conductivity. 72

3.17 (a) Numerical breast phantom with a 1.5cm tumour inside the fatty and fibro-glandular tissues (top view), (b) map of dielectric constant, and (c) map of conductivity. 73
3.18 Block diagram of HGA optimization method. 75
3.19 Block diagram of the RGA (a) without NN classifier, and (b) with NN classifier. 77
3.20 Block diagram of the wavefront radar-based reconstruction method. . 81
3.21 Breast phantom with skin, breast tissue and a malignant tumor at an off-centered location ($-0.75cm$, $0.75cm$) with Debye parameters shown in Tab. 3.1 (top-view). 83
3.22 (a) Discretized the entire breast phantom of Fig. 3.21, and (b) reconstructed image obtained using radar technique. 83
3.23 (a) Discretized the breast phantom of Fig. 3.21 after radar focusing technique, and (b) total field distribution from the reconstructed image of a 0.9cm diameter malignant tumour inside a breast phantom using the FDTD method. 84
3.24 Breast phantom with skin, breast tissue, and 1cm diameter malignant. 86
3.25 (a) Parallel $(\mathrm{FD})^2$TD runtime vs. number of processors, (b) speed-up vs. number of processor for the FDTD algorithm. 87
3.26 Schematic of parallel GA program. 88
3.27 Parallel GA/FDTD runtimes for one generation of GA (120 chromosomes) vs. number of processors for the example of Fig. 3.24. 89
3.28 Parallel FDTD/Parallel GA configuration. 91
3.29 (a) Numerical breast phantom with a 7.5mm tumour in the lower right area, (b) fitness value of the best individual in different generations. . 92
3.30 Transmitted and scattered fields in an object. 93
3.31 Two receiver antennas around the object for collecting the scattered field. 94
3.32 The cross-section of the dielectric cylinder (a) 2D, and (b) 3D. 96
3.33 RCS of the dielectric cylinder at (a) 2GHz, and (b) 4GHz. 97
3.34 (a) Configuration of dipole antenna, and (b) directivity of the dipole antenna at different frequencies. 98
3.35 (a) Dielectric cylinder surrounded with dipole receiver antennas, (b) directivity pattern of the dipole antenna at different location. 98
3.36 Comparison of RCS and directivity pattern of the dipole antenna at two different positions (a) $\Phi = 0^o$, and (b) $\Phi = 135^o$. 100
3.37 Received power for dipole antenna at (a) $\Phi = 0^o$, and (b) $\Phi = 135^o$. . 100
3.38 (a) Conical horn antenna, (b) dielectric cylinder with conical horn receiver antennas around the cylinder. 101
3.39 Directivity of the conical horn antenna at different frequencies (a) rectangular pattern, and (b) polar pattern. 102

3.40 Received power with circular horn antenna at the same position and different frequency (a) 10GHz, and (b) 15GHz. 103
3.41 Microstrip patch antenna structure, (a) 3D, and (b) 2D. 103
3.42 (a) S_{11} of rectangular microstrip patch antenna in free space, (b) directivity of misrostrip patch antenna at different angles at resonance frequency. 104
3.43 Dielectric cylinder with microstrip patch receiver antennas around it. 104
3.44 (a) RCS of the dielectric cylinder at 4.64GHz, (b) received power for antenna at $\Phi = 0^o$ and $\Phi = 180^o$. 105

4.1 Clinical imaging system configuration for MWT. 115
4.2 Map of type of breast tissue (a) 3D image, (b) 2D images (coronal plane). 115
4.3 Frequency variation of electrical properties of malignant tumour, fibro-glandular, and fatty tissues. 119
4.4 Debye model of breast tissues dielectric properties (a) conductivity, (b) permittivity. 121
4.5 Dielectric properties of breast tissue (a) conductivity, (b) permittivity. 125
4.6 3D MRI breast images and 3D map of dielectric properties at 6GHz, mostly fatty: (a) map of density, (b) map of dielectric properties, scattered fibro-glandular: (c) map of density, (d) map of dielectric properties, heterogeneously dense: (e) map of density, (f) map of dielectric properties, very dense: (g) map of density, (h) map of dielectric properties. 127
4.7 2D sectional views of the different breast phantoms in terms of media type (a) mostly fatty, (b) scattered fibro-glandular, (c) heterogeneously dense, and (d) very dense. 128
4.8 2D sectional views of the different breast phantoms in terms of water content (a) mostly fatty, (b) scattered fibro-glandular, (c) heterogeneously dense, and (d) very dense. 130
4.9 The histogram of the permittivity for different numerical breast phantoms at 5GHz (a) mostly fatty, (b) scattered fibro-glandular, (c) heterogeneously dense, and (d) very dense. 131
4.10 Frequency variation of conductivity for different breast tissues. 132
4.11 $1/e$ penetration depth vs. frequency for different breast phantoms. . . 133
4.12 Breast phantom with $2mm$ tumour at the center. 135
4.13 Field distribution in the breast phantom Fig. 4.12 at different frequencies (a) at x=center and y-axis, and (b) in y=center and x-axis. . . . 136
4.14 Penetration depth for different permittivity values. 137
4.15 Field distribution inside the breast phantom matched to material with (a) $\epsilon_r = 30$ at f=6GHz, (b) $\epsilon_r = 80$ at f=10GHz for different values for conductivities. 137

4.16 Field distribution inside the breast phantom matched to material with different percentages of glycerine and saline at 6GHz. 138

4.17 Penetration depth vs. frequency for the breast phantom Fig. 4.12 using different matching material. 139

4.18 Summation of the difference between scattered fields at different frequencies from 1-10GHz, with different tumour sizes, for a heterogeneous numerical breast phantom. 142

4.19 Summation of the difference between scattered fields at different frequencies from 1-10GHz, with different tumour sizes, for a homogeneous fatty numerical breast phantom. 143

4.20 Summation of the difference between scattered fields at different frequencies from 1-10GHz, with different tumour sizes, for a homogeneous fibro-glandular numerical breast phantom. 143

4.21 Summation of the difference between scattering fields at different frequencies from 1-10GHz for each of the three scenarios, with and without a 2cm diameter tumour at the off-center location. 144

4.22 (a) Mostly fatty breast, (b) scattered fibro-glandular breast, (c) heterogeneous dense breast, and (d) very dense breast. 145

4.23 Tumour signature for (a) mostly fatty breast, (b) scattered fibro-glandular breast, (c) heterogeneous dense breast, and (d) very dense breast for different sizes of tumour at the center. 146

4.24 Block diagram of the proposed imaging system for breast cancer detection. 147

4.25 (a) Breast phantom with skin, breast tissue, and a malignant tumour (top view), (b) fitness value of the best individuals in different generations. 149

4.26 Map of dielectric properties for the breast phantom shown in Fig. 4.25 (a), (a) dielectric constant (b) conductivity. 150

4.27 Breast phantom with skin, breast tissue, and a square-shaped malignant tumour (top view). 152

4.28 (a) Fitness value of the best individuals in different generations of BGA for example shown in Fig. 4.27, (b) fitness value for RGA, for three of the possible solutions that result from the BGA optimization. 154

4.29 Map of dielectric constants for the breast phantom shown in Fig. 4.27. 154

4.30 (a) Relative permittivity and (b) conductivity of the numerical breast phantom obtained by sub-sampling the MRI. 155

4.31 (a) Trajectory of the fitness value of the best individual in the BGA, (b) trajectory of the fitness value of the 4 candidate solutions passed to RGA. 156

4.32 Result of the HGA method for the numerical phantom of Fig. 4.30 (a) permittivity, and (b) conductivity. 157

4.33 Result of the (a) RGA, and (b) BGA methods for relative permittivity. 158

4.34 Map of (a) permittivity, and (b) conductivity of the heterogeneously dense breast phantom. 159

4.35 Map of the (a) permittivity, and (b) conductivity of the heterogeneously dense breast with $7.5mm$ resolution. 159

4.36 Reconstructed image of (a) permittivity, and (b) conductivity for the breast phantom of Fig. 4.35. 160

4.37 Transects of the reconstructed permittivity image at (a) $y = 80$cell horizontal direction, and (b) $x = 64$cell vertical direction profiles compared with the actual distribution. 161

4.38 Tumour response for diverse SNR and different tumour sizes (a) scattered fibro-glandular breast, (b) heterogeneously dense breast, and (c) very dense breast. 162

4.39 Block diagram of adding noise in the proposed tomography method. . 163

4.40 (a) Histogram plot of the added white noise, (b) amplitude of white noise for each antenna at the observation point, and (c) power spectral density of the white Gaussian noise. 164

4.41 The average error in (a) dielectric constant, and (b) conductivity vs. SNR. 166

4.42 MWT system configuration. 169

4.43 Map of permittivity for heterogeneously dense breast at f=5GHz (each pixel is $0.5mm$). 170

4.44 3D breast phantom with skin, breast tissues excited by (a) circular-loop antenna, and (b) dipole antenna. 171

4.45 Antennas dimension (a) dipole antenna, and (b) circular-loop antenna. 172

4.46 Comparing the tumour signature (a) ΔE_Φ at 3GHz, (b) ΔE_z at 3GHz, (c) ΔE_Φ at 5GHz, (d) ΔE_z at 5GHz, (e) ΔE_Φ at 7GHz, and (f) ΔE_z at 7GHz. 174

5.1 University of Manitoba measurement setup. 179

5.2 3D modelling of the (a) $87mm$ diameter circular cylinder PEC, (b) $50mm$ diameter circular cylinder dielectric with permittivity 3.0. . . . 182

5.3 S_{j1} (a), (c) magnitude and (b), (d) phase comparison of the 3D simulation and measurement results for $87mm$ diameter PEC and $50mm$ diameter circular dielectric with permittivity of 3.0. 183

5.4 Comparing the S_{j1} amplitude and phase measurement and simulation for, (a), (b) $87mm$ diameter PEC, and (c), (d) $50mm$ diameter dielectric with permittivity of 3.0. 185

5.5 (a) Double-layer Vivaldi antenna, (b) comparing simulated and measured S_{11} for Vivaldi antenna. 189

5.6 UM microwave tomography system using 24 Vivaldi antennas (top view). 189

5.7 Simulation geometry of the MWT chamber with 24 Vivaldi antennas. 190

5.8 Amplitude of S_{n1} vs. antenna number at (a) 3GHz, and (b) 6GHz. . . 191

5.9 Magnitude comparison of simulated and calibrated electrical field for different reference objects at (a) 3GHz, and (b) 3.5GHz. 192
5.10 Reconstructed image of wooden block (map of permittivity), (a) 2D view, and (b) 3D view. 193
5.11 Geometry for Frsenel Data Set FoamDielint, (a) schematic of the scattering cylinders, b) comparing the calibrated and simulated scattered field at 8GHz where the transmitter antenna is positioned at 180^o. . . 195
5.12 Comparing the calibrated and simulated data at 8GHz where the transmitter antenna is positioned at (a) 90^o, and (b) 270^o. 196
5.13 Reconstruction of Fresnel Data Set FoamDielint (map of permittivity), (a) 2D view, and (b) 3D view. 197

A.1 Normalized scattered field of dielectric circular cylinder while observation point is at (a) $\Phi = 90^o$, (b) $\Phi = 270^o$. 209

C.1 Yee-cell schematic. 215
C.2 Gaussian pulse spectrum. 217
C.3 Different regions of solution space. 218
C.4 (a) Dielectric shell cylinder with 81 observation points, (b) distant scattering pattern of circular dielectric cylinder with plane-wave incident. 223
C.5 (a) Lossy circular cylinder, (b) TM plot of $2\pi|E_{scat}|^2/\lambda$ against Φ for case of lossy circular cylinder at 2.5GHz frequency. 224

D.1 Parallel FDTD configuration. 227

E.1 Measurement setup for breast tissues dielectric properties measurement (a) ENA network analyzer and Agilent 85070E dielectric probe kit, and (b) tissue under the performance probe measurement. 229
E.2 Breast tissue samples from mastectomy surgery (a) the entire breast sample, (b) benign tissue sample, and (c) malignant tissue. 230
E.3 Dielectric properties of breast tissue vs. frequency at different temperatures (a) permittivity when temperatures decreased from room temperature to freezing, (b) conductivity when temperatures decreased from room temperature to freezing, (c) permittivity when temperature increased from freezing to room temperature, and (d) conductivity when temperature increased from freezing to room temperature. . . . 231
E.4 Dielectric properties for fibro-glandular tissue from mastectomy surgery at different times after excision (a) permittivity, and (b) conductivity. 233

1. INTRODUCTION

I keep the subject of my inquiry constantly before me, and wait till the first dawning opens gradually, by little and little, into a full and clear light.
Isaac Newton

The first part of this chapter will introduce the reader to a brief overview of the extensive work that has been done in microwave imaging. The second part of this chapter will be devoted to the motivation behind this research and the scope of this work. Finally, at the end, the thesis organization will be described.

1.1 Electromagnetic imaging

Electromagnetic imaging, by means of Radio Frequency (RF), microwave, or optical signals, was always attractive due to its unique features as a diagnosis tool. Electromagnetic imaging has received intense attention, and therefore, extensive research has been conducted. This is due to the versatility and suitability of this imaging technique for a wide range of applications. For example, in the Non-Destructive Evaluation (NDE), MicroWave Imaging (MWI) has been proposed for on-line testing of material, in particular, the detection of possible defects and measurements of physical quantities (e.g. moisture content) on conveyed products [1–3]. It also can be used for material characterization, such as the determination of constituent, evaluation of porosity, and assessment of the curing state. In military application, microwaves' ability to penetrate into dielectric materials makes them useful for interrogating military composites [4–6]. In aerospace application, MWI may be useful for detection of cracks that may occur in aircraft fuselage [7]. In the geographical prospecting field, MWI has been used in remote detection of subsurface inclusions such as tunnels, landfill debris, and unexploded land mines [8–10]. In civil and industrial engineering application, MWI can be useful for evaluating the structural integrity of roadways, buildings, and bridges [11]. In medicine, currently, MWI systems have been proposed for non-invasive biological imaging applications [12, 13]. Significant progress in MWI has been accomplished in the last decade, with experimental prototypes capable of imaging excised pig's legs [14], heart disease such as ischemia and infraction [15–17], breast cancer imaging [18–30], brain imaging [31], bone imaging [32], and the detection of ischemia in different parts of the body [33]. A general review of different biomedical applications of MWI can be found in [12]. Furthermore, the applications of microwave techniques to medical imaging have been summarized in [34]. The above mentioned examples are just a few of electromagnetic imaging applications. One can imagine many other possible applications as long as there is enough penetration inside the target exist.

From this very short and incomplete list, it is apparent that the scope of electromagnetic imaging is extensive and applications can be found in many diverse fields. Some of these applications only require qualitative information about the object under test, whereas in many other cases, such as instance demining application, non-invasive archaeological survey, or medical imaging, there is a need for quantitative information of the object that can be obtained using information about its dielectric properties. In this thesis we are interested in creating quantitative images of objects using microwave signals which allow us recognize the material type of the internal structure of the object. Depending on the application, the frequency of operation and data acquisition can be different.

1.2 Microwave imaging

MWI is an active wave-based non-invasive imaging method [35]. It gives us an ability to see inside and through objects with radiation other than light, without direct contact, and it will expand humankind's sensory horizon. The physical quantities being imaged in MWI are the dielectric properties, i.e. the permittivity (ϵ) and the conductivity (σ) of the target[1]. The value of the permittivity is related to the molecule's dipole moment per volume while the conductivity is related to the free path length and speed of the electrons inside the material [38]. When the object is induced by external stimulations (microwave signal), the microscopic processes can deviate from their normal state and impact the overall dielectric properties. MWI techniques

---

[1] We consider non-magnetic objects; however, the simultaneous determination of the dielectric and magnetic properties of a magnetic object has been reported in [36, 37].

use microwave radiation with frequencies ranging from approximately 0.3-30GHz [39], and therefore, the image pixel size may vary from meter to sub-millimeter.

1.3 Microwave imaging methods

Current research in MWI can be divided mainly into Ultra-WideBand (UWB) radar imaging and Microwave Tomography (MWT). In the MWT image reconstruction, a non-linear inverse scattering problem must be solved to predict a map of the dielectric properties of the target. In this technique, the scattered field is measured at the observation points outside the object of interest. In contrast to tomography technique, the UWB radar approach solves a simpler computational problem (linear inverse problem) by seeking only the significant scatterers. In this technique, the reflected fields are measured. This technique is useful for non-quantitative (qualitative) imaging application, such as determining the shape of the object or localizing an unknown scatterer.

1.3.1 UWB microwave radar method

In this method of imaging, the transmitter antenna (TX) irradiates a UWB electromagnetic waveform into the scan area, and the magnitude and phase of backscattered signals from the Object of Interest (OI) are then recorded by receiver antennas (RX). The scan can be in a circular or rectangular path. This method involves analyzing reflections from the OI to identify the presence of target. The UWB signal may be generated physically as a time-domain impulse or synthetically by using a swept frequency input. The time-domain image-formation algorithms (beamformers) are used to spatially focus the backscattered signals to discriminate against clutters that caused by the heterogeneity of OI (different travel time and noise), while compensating for path dependent attenuation and phase effects. The beamformers can be divided into two distinct categories: "data-independent" and "data-adaptive beamformers". Data-independent beamformers typically use an assumed channel model to compensate for path-dependent propagation effects. Conversely, data-adaptive beamformers attempt to directly estimate the actual channel based on signals reflected from the OI. The data-independent beamformers include mono-static and multi-static Delay-And-Sum (DAS) [21, 40–42], Delay-Multiply-And-Sum (DMAS) [43], and Improved-Delay-And-Sum (IDAS) [44]. Data-adaptive beamformers include Robust Capon Beamforming (RCB) [45] and Multi-static Adaptive Microwave Imaging (MAMI) [46].

The measurements for these techniques require wideband multi-frequency data acquisition. The main advantage of microwave radar is the fast runtime [21, 47, 48]. These are actually Fourier-based imaging techniques, which linearize the inverse problem [49] and make specific simplifications regarding the wave propagation within the scatterer. They might not be accurate enough for complex structures. In order to know more about the radar imaging methods, we recommend the paper by Cheney [50] and the references therein. Thus, these types of MWI techniques are not considered in this thesis.

1.3.2 Microwave tomography method

In MWT, one attempts to reconstruct the electric properties of an unknown OI immersed in a known background medium. To reconstruct the OI's properties, the OI is illuminated by various known sources of microwave radiation, and field scattered by the OI is measured at various locations surrounding it. There are two parts associated with the MWT: forward simulation and inverse solution. In the forward simulation, both the medium properties and the domain of inhomogeneity are assumed to be known and the Maxwell's equations are solved to obtain the scattered electric field. In the inverse scattering problem, scattered fields are measured at discrete points and the medium properties are the unknowns to be determined.

In the last few years, several approaches have been proposed for solving non-linear inverse scattering problems. Except for One-Dimensional (1D) problems that have analytic solutions [51], in general computational methods are utilized. Fig. 1.1 summarizes the block diagram of the existing methods for solving the inverse scattering problems. These methods are categorized into linear and non-linear algorithms. The non-linear inverse scattering algorithms are more computational intensive and complex than linear ones. However, non-linear methods take into account more accurate physical properties of the problem and hence, are more appropriate for complex media. The following sections of this chapter are devoted to briefly overview each block of Fig. 1.1.

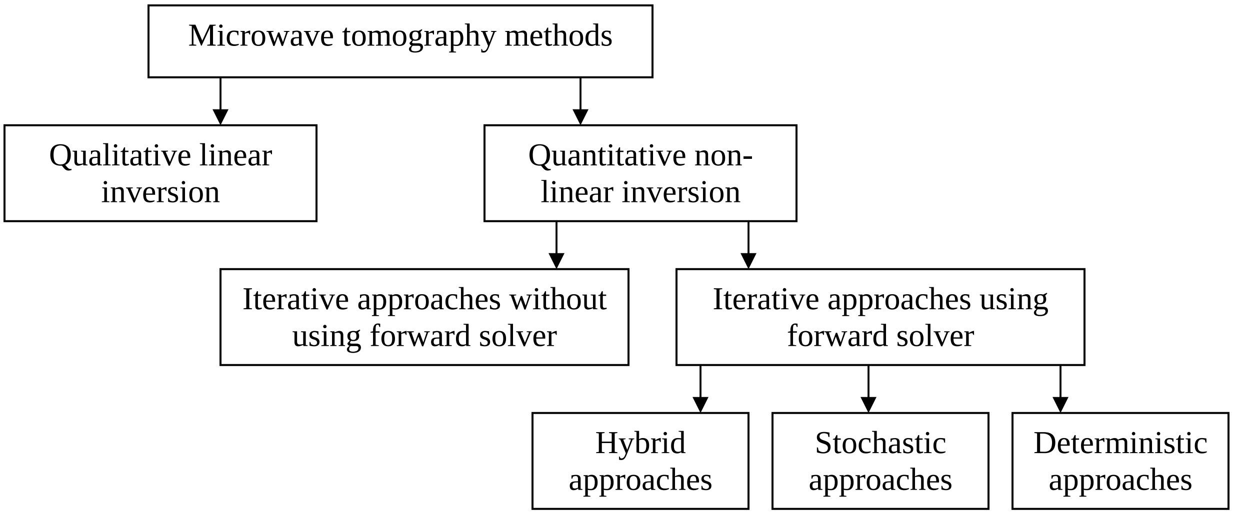

Fig. 1.1: Block diagram of the existing MWT methods.

1.4 *Qualitative linear inversion*

The simplest and fastest way to linearize the inverse scattering problems is to use the first-order Born approximation [52, 53]. In the Born approximation, the total field inside the imaging domain is approximated by the incident field. In this case, the unknown is the solution of a linear first-kind Fredholm integral equation [52, 54]. This approximation is only valid for smaller objects with low contrast[2] (the object represents a weak discontinuity in the propagation medium). This is a very restrictive approximation, which a vast majority of interesting inverse scattering problems do not satisfy [55]. Despite the fact that the problem is now linear, it is important to realize that it still remains ill-posed (the ill-posed condition for inverse scattering problem will be discussed in Chapter 3). This means that regularization is required [52].

---

[2] Contrast is the difference between the relative complex permittivity of the OI and background.

1.5 Quantitative non-linear inversion

For simple structures where inverse scattering require solving a convex optimization problem, linearization can be applied without a big scarifies in correctness and/or accuracy. However, as the complexity of structure increases it is advisable to use non-linear methods. Iterative techniques are currently one of the best options for solving the non-linear inverse scattering problem and for performing quantitative imaging of the two parameters such as permittivity and conductivity. In iterative techniques, the solution is found iteratively by minimizing the norm of the error with respect to the scattered field's value (cost-function). There are two different categories of iterative approaches that have been successfully used to solve the inverse scattering problem. The first approach uses conventional cost-function which is based on the difference between the measured and predicted scattered fields for a particular choice of the material parameters. The second approach, uses the same conventional cost-function, formulated in terms of the "contrast sources", added to an error functional involving the domain equation, which relates the fields inside the imaging domain to the contrast of the unknown OI. These two approaches are also distinguished by the use of a forward solver or the absence of a forward solver.

1.5.1 Iterative approaches without using forward solver

This approach does not use a forward solver and the cost function is defined based on both scattered fields outside of the OI and total fields inside the OI. This method is in the category of the "modified gradient" methods. In this approach, the optimization process is formulated in terms of an unknown contrast and an unknown total field (contrast source). At each iteration of the optimization procedure, these two unknowns have to be updated. In order to update these parameters, different techniques have been suggested. For example, in [56] the contrast and the total field are updated simultaneously as one unknown vector in the discrete domain successively using a Conjugate Gradient (CG) method. Another approach is that these two parameters (contrast and total field) are treated separately. This means that when optimizing over the total field, the contrast is assumed to be known (e.g. Modified Gradient Method (MGM) [57]) and when optimizing over the contrast, the total field is assumed to be known (e.g. Contrast Source Inversion (CSI) method [58–60]). In order to increase the robustness to noisy data and enhance the quality of reconstructions from the CSI algorithm, regularization is introduced to the cost-functional at each step of the optimization process in the form of a weighted L^2-norm multiplicative constraint [60,61]. This method is called the Multiplicative Regularized CSI (MR-CSI) method. The two methods are applied successfully in several applications [62–64]. Although CSI and MRCSI have been successful, these methods are very efficient only if the Green's function is available and can be computed easily. The latter two conditions are applicable if the background medium is homogeneous and if the problem boundary can be easily defined within the Green's function (e.g. unbounded problem domains). In order to solve this problem and consider the inhomogeneous background medium, recently a Finite-Difference CSI (FDCSI) method has been introduced. The multiplicative regularization also has been applied in the FDCSI method (FD-MRCSI), and it has successfully been utilized in wall-through imaging, geophysical surveying, and biomedical applications [65, 66]. The integration of Tikhonov regularization and projection-based regularization has also been applied to CSI as hybrid regularization CSI [67, 68]. The number of unknowns in this approach is greater than that in conventional iterative approach, and therefore it requires much more iterations to converge.

1.5.2 Iterative approaches using forward solver

In conventional cost-function approach, which is the one followed in this thesis, minimizes the differences between measured scattered fields (only outside the OI) and the scattered fields that are calculated from a possible solution. This approach is computationally complex because the system of equations has to be built at each iteration. In order to calculate the scattered field, when the electric contrast or the size of the OI is small, one may use the well-known Born approximation [69]. Another popular approximation is the Rytov approximation [69]. The Rytov approximation gave better results in imaging an object with high contrast. Basically, the result of linearizing the inverse problem is a significant loss of accuracy in predicting dielectric properties. These methods are computationally efficient and can obtain images in a short runtime, but they usually fail when a complex media with high contrast scatterers exist [70–72]. Forward solver based on Integral Equations (IE) such as the the Born Iterative Method (BIM) [73], Distorted Born Iteration Method (DBIM) [74], Local Shape Function (LSF) [75, 76] have also been implemented. Various attempts were made to reduce the reconstruction problem complexity by taking into account different approximations and simplifications, such as the dual-mesh scheme [77], conformal mesh reconstruction [23], adjoint technique [24], frequency-hopping reconstruction algorithms [78], and iterative multi-scaling approach [79–81]. In addition, methods for solving nonlinear Partial Differential Equations (PDE) such as Finite-Difference Time-Domain(FDTD) method appears to be more appropriate model for the EM scattered fields and it has been used in this thesis.

In order to minimize the cost-function and retrieve the unknown objects from the measurements, different deterministic (local optimization) and stochastic (global optimization) approaches have been proposed.

i. Deterministic approaches

These techniques proceed by minimizing the cost-function using the Newton type minimizations. These techniques always require the selection of some kind of regularization terms. Examples of such deterministic algorithms are the Modified-Newton method [20, 82], Gauss-Newton (GN) inversion [83–87], Inexact-Newton (IN) [88, 89], Quasi-Newton method [90], Newton-Kantorovich (NK) [91], and Levenberg-Marquardt (LM) inversion [92]. The Gauss-Newton technique (or NK method) is also equivalent to the DBIM, as shown in [93]. The ill-posedness is usually treated by employing different regularization techniques. Various regularization techniques such as Tikhonov Regularization [54, 74, 92, 94–98], Krylov subsurface regularization [20, 99], Maxwell regularizer (physical regularizer) [57], and MR [84] have been used. These traditional regularization methods, which facilitate the inversion of ill-conditioned matrices are application-independent, which enables these methods to be used for a variety of applications. In addition, these traditional regularizations work well when only a few scatterers with small difference in dielectric properties (contrast) exist. From a computational point of view, deterministic techniques are attractive, however, they can be trapped in local minimum. This means that the local-based optimization imaging techniques are only accurate if the starting trial solution is not far from the real solution or the regularization keeps the search around the global minimum. In many practical cases, it is not possible to guess the proper initial point or regularization term, and therefore some inaccuracies in the resulting reconstructed image may appear. In terms of number of frequencies, both multiple frequencies [100–103] or single frequency [76, 104–106] approach have been used. The main advantages of deterministic algorithms is their convergence speed. This imaging procedure works well when only a few scatterers with small difference in dielectric properties (contrast) exist. Including *a-priori* information in theses approaches is quite complex.

ii. Stochastic approaches

In contrast to deterministic approaches, a number of global optimization methods have been utilized in solving non-linear inverse scattering problems. The stochastic approaches are potentially able to obtain global minimum which most probably corresponds to a true solution. Without dependency on initial guess they are a better choice when multiple scatterers inside heterogeneous objects are presented. The stochastic approaches include the stochastic search base, such as the Simulated Annealing techniques [107, 108], Ant Colony Optimizer (ACO) [109] and population-based evolutionary algorithms such as Neural-Networks (NN) [110], Genetic Algorithms (GAs) [13, 111–118], Differential Evolution Strategy (DES) [119–122], Particle Swarm Optimization (PSO) [123–126], and more recently the Evolutionary Algorithms (EAs) [127]. These global optimization methods can be evaluated based on different parameters such as the ability to deal with complex cost-functions, the simplicity of use, the number of control parameters, convergence rate, and the possibility of the exploitation of the parallelism by modern PC clusters. One of the advantages of using global optimization methods is that they can escape from local minima through randomization, and there is no need for the rigorous regularization (which often results in smoothing effects). Furthermore, including some *a-priori* information such as physical and geometrical structure is quite easy and very flexible. Despite all the advantages the heavy computational load is a major drawback inherent in stochastic approaches. Therefore, mainly they have been utilized in Two-Dimension (2D) imaging approaches;

however, there has been same efforts initiated for implementing Three-Dimensional (3D) imaging using these approaches [64, 96, 128–130].

iii. Hybrid approaches

Besides "bare" techniques, a number of hybrid approaches have been implemented to improve the convergence and accuracy. Basically, hybrid methods are integrating the stochastic and deterministic approaches. Moreover, the stochastic approach starts from trial solution to find the right solution and then the deterministic approach starts from this initial data and the solution is quickly reached. Some examples for these approaches include the hybrid GA and LM [131] and hybrid GA and CG [113]. In [132] we used the multi-resolution strategies and zooming procedure with hybridization of qualitative and quantitative techniques in order to enhance spatial resolution only in those regions of interest (this hybrid technique will be explained in Chapter 3). Hybrid methods also include the combination of two stochastic methods such as GA and NN [133] or two deterministic methods such as hybrid extended Born approximation and a gradient procedure [134]. Furthermore, the hybrid methods can be devised by combining the qualitative and quantitative stochastic method such as the hybrid of linear sampling and Ant Colony [135, 136]. The integration of the stochastic and deterministic methods can be made stronger optimization. For example, the Memetic Algorithm (MA) [137–139] is the result of combining the stochastic and deterministic methods.

1.6 Motivation

In spite of the efforts and research in the field of inverse scattering, still many important analytical and computational challenges have remained untouched. Therefore, further efforts are necessary to allow their massive employment in real applications. From a practical point of view, there are difficulties in designing efficient illumination and measurement apparatuses. On the other hand, from a computational point of view, the heterogeneous and dispersive media cause a high computational load. Most of the above mentioned algorithms are very effective when the object under the test is simple. But for applications with complicated structures (such as breast imaging which has a high degree of heterogeneity and high dielectric properties contrast), the result may lead to non-real solutions. To deal with these complicated objects, we chose to make no simplification into non-linear equations. We proposed to solve Maxwell's equations directly, without any assumption, and to solve the time domain inverse scattering problem based on FDTD numerical method and GAs in order to reconstruct an image of heterogeneous and dispersive objects to determine the shape, location, and dielectric properties of profile.

The solution is obtained by minimizing the cost-function by means of a binary-coded GA, real-coded GA, or hybrid GA, which, in principle, ensures the convergence to the global minimum and prevents the solution from being trapped in local minima. Moreover, the proposed approach prevents the problems due to inaccuracies in near-field phase measurements since only the amplitude of the scattered fields are considered in the inversion process. The effectiveness of the MWT approach is assessed by means of some numerical examples (with synthetic and measured input data) concerning a realistic cross-section of a phantom exposed to an electromagnetic illumination. The presence of noise in the synthetic data is also considered and the dependence of the reconstruction accuracy on the signal-to-noise ratio (SNR) is investigated. To the best of our knowledge, this is the first attempt in using the combination of FDTD and GA to reconstruct the location, shape, and dielectric properties of heterogeneous and dispersive media with an arbitrary shape.

There are many advantages of using the differential equations solver such as FDTD over the IEs ones. In differential equations, it is much easier to add new scatterers and materials to the problem and meshing is very simple, but in the IE methods, adding scatterers and materials involves the need for reformulating a complex IE. This can become burdensome for inverse scattering problems, when the scatterers are unknown and are constantly changing based on the optimization process. The dispersive characteristic of material can be easily taken into account in FDTD simulation. The main problem associated with FDTD is the requirement of large amounts of computer memory to store field values at large number of mesh points and subsequently calculate the updated values at each time step. However, with the ever increasing amounts of computer power and memory, this problem is not a terminal one. The main advantage of FDTD over frequency domain formulations, considering the nature of this thesis, is the wideband analysis. In the frequency domain, the simulation must run at each single-frequency to provide wideband results. However, in FDTD the system can model an impulse response and hence track the system features over a wide frequency range. When the scattered field is required for a wide frequency band, FDTD is clearly the best choice as it provides all of them with a single run.

In this thesis, we decided to utilize the GA approach rather than any other global optimization methods for solving inverse problem. The reason stems from the fact that the GA is simple and is ables to deal with discrete cost-functions with multiple minima. The complexity of the cost-function is due to the non-linear relation between the scattered field and the dielectric properties of the scatterers. The GA allows for on easy implementation on parallel computers which can be a very good option for dealing with a large number of unknowns. Furthermore, the capability of including *a-priori* information in the GA technique is a fundamental factor and makes it a suitable approach where such information exists. In addition, the GAs can be combined easily (we introduce four types of hybrid GA in this thesis). These features, along with the accuracy of the FDTD as a forward solver, were our motivation to focus on FDTD/GA method for inverse scattering.

The disadvantage of this method is the long runtime. In general, the iterative procedures such as FDTD and GA are very slow. To remedy this problem, we suggest different solutions. First, by using hybrid algorithms we reduce the search space and speed-up the optimization process. Second, the parallel algorithms as well as *a-priori* knowledge are used to significantly reduce the computation time. The wideband, multi-view, multi-incident plan waves as well as a multi-level of optimization will be used to improve the image quality in the future. This configuration is considered with the assumption that measurements can be performed around the object under test. In fact, using a multi-view/multi-illumination algorithm decreases the effect of ill-conditioning, as the number of views increases and this results in a better accuracy compared to mono-view images. The greater the amount of data, the less the chance of being stuck in local minima and ending up with a non-real image.

Breast cancer detection is chosen as a primary application for the proposed technique due to the heterogeneous structure and dispersive characteristic of the breast. However, the proposed technique can be applied to many other applications.

1.7 Outline of the thesis

This dissertation is divided into six chapters:

In Chapter 1, a brief review of the ongoing research in the field of MWI is given with a focus on the microwave inverse scattering problem. In this chapter, we provide the outline of contributions presented in this thesis.

In Chapter 2, the methodology of the proposed algorithm for solving the inverse problem is explained in detail. It starts with the problem statement and is followed by the block diagram of the MWT system. In this chapter, we provide the notation that is used in this thesis.

In Chapter 3, we present, in detail, the theoretical background of the wavefield forward and inverse problems and methods of solving these equations. In particular, Chapter 3 focuses on the forward solver using FDTD and different GAs as optimization methods for minimizing the cost-function. The details of frequency dependence FDTD that have been developed for simulating the dispersive structure and calculating the scatter field are explained. We gave different examples of dispersive and non-homogeneous objects for evaluating the proposed non-linear inverse scattering techniques. The parallel version of the proposed algorithm is implemented in order to overcome the computation runtime and improve the convergence rate.

In Chapter 4, we first present a brief introduction to breast cancer imaging modalities and illustrate the importance of MWI as a breast cancer imaging modality by reviewing its advantages over other imaging techniques. A subsection focuses on breast topology and dielectric properties of the breast tissues as the fundamental factor for MWT. In this chapter, inclusion of the dispersive characteristics and water content into FDTD formulation will be explained in detail. The principle limiting factor in penetration depth of the microwave is attenuation of the electromagnetic wave in the breast tissues. The penetration depth will be calculated for different breast types, and the optimized dielectric properties of matching material to improve the penetration depth will be discussed. The “tumour response” is the difference between scattered fields of a specific tissue composition with and without the tumour. This parameter is investigated for different breast tissue compositions for different tumour sizes. In the last section of this chapter, the robustness of the proposed imaging method with respect to signal-to-noise ratio has been investigated.

In Chapter 5, we explain the hardware setup required to collect the necessary field for MWT imaging and also the different calibrations needed to be performed before inverting the scattered field data. We present some results from the experimental setup from the University of Manitoba MWT system and the Fresenel Insitute in this chapter.

In Chapter 6, we present the conclusions and provide recommendations for the future work.

2. STATEMENT OF THE PROBLEM

We cannot solve our problems with the same thinking we used when we created them.
Albert Einstein

2.1 Objective

The objective of this thesis is to develop an efficient reconstruction algorithm for MWT in order to obtain a quantitative images of the penetrable and dispersive objects in a non-invasive manner. The *"quantitative image"* is a quantitative pixel intensity which relates to some physical parameters from a cross-section of the object, hereafter referred to as the Object of Interest (OI). In order to solve this problem some assumptions have been considered. The four most important assumptions are as follows:

1. the effects of transmitter antennas are neglected and the incident field is modeled by a plane-wave.

2. the 3D OI is modeled by 2D slices.

3. the phase information is ignored.
4. the dielectric properties of the background medium surrounding the OI is assumed to be known.

These assumptions will be discussed in the following sections.

2.2 Problem definition and assumption

2.2.1 Geometry of the problem

The problem geometry is depicted in Fig. 2.1 where D is the imaging domain (or search space domain) which is occupied by single or multiple scatterers and V is the problem domain where the scattered field is collected. In order to create an image of the unknown object, the OI needs to be located inside the imaging domain and irradiated by known microwave incident waves. The presence of inhomogeneities in the dielectric properties affects the incident pattern of the microwave signal throughout the OI by altering its amplitude, phase, and polarization which results in distortions of the microwave field which is called "scattered field". The OI is surrounded by measurement probes that are able to acquire the sample of scattered field outside the imaging domain at the observation points. The region D is illuminated by a set of transverse magnetic fields (incident fields), denoted by $E_i^{inc},\ i = 1, 2, 3, ..., T$ (T is the maximum number of illumination directions). The scattered field is measured around the object. The value of scattered field is denoted by $E_{ij}^{scat}(r),\ j = 1, 2, ..., M$, and

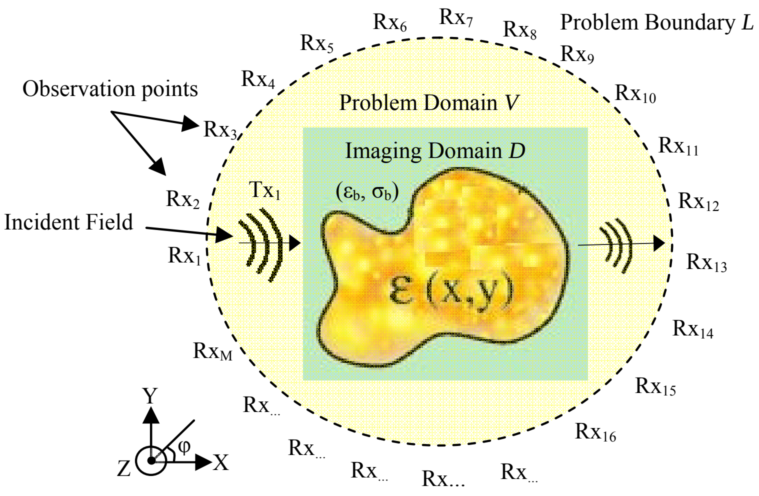

Fig. 2.1: Geometry of the MWT

$i = 1, 2, 3, ..., T$, where the index j denotes the j^{th} measurement points (observation points), located at different angles around the object. Since there are M measurements points and T incident angles, then the scattered field can be stored in a matrix of size $T \times M$. This is a typical tomographic[1] imaging configuration. Within this thesis, we focus on the MWT method as MWI.

2.2.2 Two-dimensional MWT

Within this thesis, we consider the OI to be infinitely long in z-direction (this creates a 2D problem). This approximation is made for efficiency in terms of runtime and memory. In fact, the behavior of the electric field within a 2D environment can be repeatedly evaluated very quickly, while this evaluation is much slower for 3D problems. This allows the iterative imaging algorithm to converge to a solution in a

---

[1] Tomography is derived from the Greek word *tomo* which means "a slice".

reasonable amount of time. From a practical prospective, currently there is no 3D MWT system capable of collecting all the field components required in 3D solvers. In the framework of 2D inversion algorithms, we consider the Transverse Magnetic (TM) polarization for illumination. In particular, we consider TM to z (TMz). In the TMz polarization, the OI is illuminated with the electric field parallel to the z-axis. This polarization is often used for 2D MWT.

2.2.3 Background medium and scatterers

Within this thesis, the objects which are going to be imaged are called "scatterers" (targets, defects, or obstacles). "*Resolution*" refers to the minimum size of the object which may be detected. The heterogeneous[2] background includes homogeneous[3] scatterers that can be made of dispersive[4] and lossy dielectric materials and are described by the spatial distributions of their electromagnetic properties, i.e., the relative permittivity (denoted by $\epsilon(\omega, x, y)$) and the conductivity (denoted by $\sigma(\omega, x, y)$). We also assume that the background medium and scatterers are non-magnetic which implies that the permeability of the media is identical to that for free space ($\mu = \mu_0$).

---

[2] The heterogeneous background has electrical properties that vary in all directions.

[3] In homogeneous scatterers' dielectric properties in all directions are constant.

[4] The dependency of the permittivity and conductivity values on the frequency content of the wave is called frequency dispersion. Frequency dispersion happens when different frequency components of the wave travel at different velocities.

2.2.4 Amplitude and phase

Collecting the fields requires a complex and expensive hardware setup. In particular, the measurement of the phase distribution turns out to be very important when high frequencies are considered. However, measuring the phase with acceptable error is one of the most difficult tasks at high frequencies. Therefore, in this thesis, we only consider the amplitude. Although this reduces the useful information in the inverse algorithm, but makes the method applicable to practical measuring systems. The amplitude of the scattered electric field (denoted by E_{scat}) can be measured by measuring the amplitude of the incident electric field (denoted by E_{inc}) for the case of object free and the amplitude of the total electric field (which is denoted by E_{total}) when the OI is present. The amplitude of the scattered field is defined as:

$$|E_{scat}| = |E_{total}| - |E_{inc}| \tag{2.1}$$

2.2.5 Frequency bandwidth

In MWT, in order to reconstruct images with high resolution, high frequency is desired. On the other hand, depending on the application, the penetration depth may decrease as the frequency increases. Finding the optimum frequency band and good attenuation is still a challenge and depends on many factors such as: the conductivity of OI, the bandwidth of the sensors (TX and RX), the size of the OI, and the matching material. In this thesis, we consider the frequency bandwidth of UWB imaging as defined by

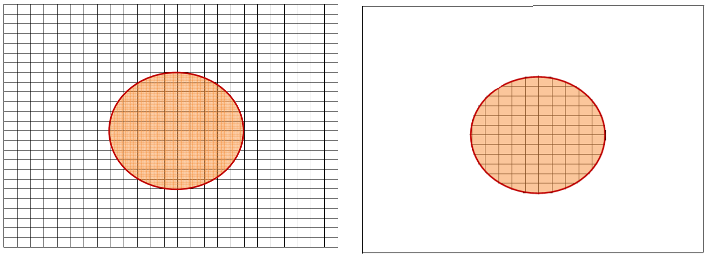

(a) (b)

Fig. 2.2: Discretizing the object, (a) without knowledge of the boundary for the object, (b) with knowledge of the boundary of the object.

Federal Communications Commission (FCC), which is 3.1-10.6GHz.

2.2.6 Search space

In the proposed inversion algorithm, in order to create an image, we discretize the entire imaging domain into n sub-domains and assume that the dielectric properties for each sub-domain is unknown. However, we are interested in creating an image of the inner structure of objects. Therefore, we limit our search space to only the interior of the object. In order to do this, some information about the position, dimensions, orientation, and surface of the object is required. This information can be found using surface detection methods. For instance, laser has been used for accurately estimating the surface of the object [140]. This information will be used in the inverse program in order to discretize only inside the object. This will significantly decrease the computation time. Fig. 2.2 (a) and (b) show discretizing the same object with and without knowledge of surface.

2.2.7 Evaluating the results

In MWT, the image can be obtained by solving the inverse scattering problem. In the proposed technique an iterative approach has been used to solve the inverse scattering problem. In the iterative approach, it is common to compare the difference between the field due to trial solution and the measured scattered field (i.e. fitness value at different iterations) [141]. In this thesis, we compare fitness value to show the quality of the images. We will use two terms, namely *reconstruction* and *inversion* for the results. These two terms are used interchangeably within this thesis and have the following meaning: "determination of the shape, location, and dielectric properties of the OI using microwave measurements collected outside the OI".

2.3 Block diagram of the proposed technique

Fig. 2.3 shows the block diagram of the MWT method considered for this thesis. The proposed MWT technique requires some *a-priori* information about OI and measured scattered field. As can be seen in this figure, the quality of the images are determined by the accuracy of input information, measured fields, the numerical simulation, and the inverse algorithm. These blocks will be explained in detail, in the Chapters 3 and 5.

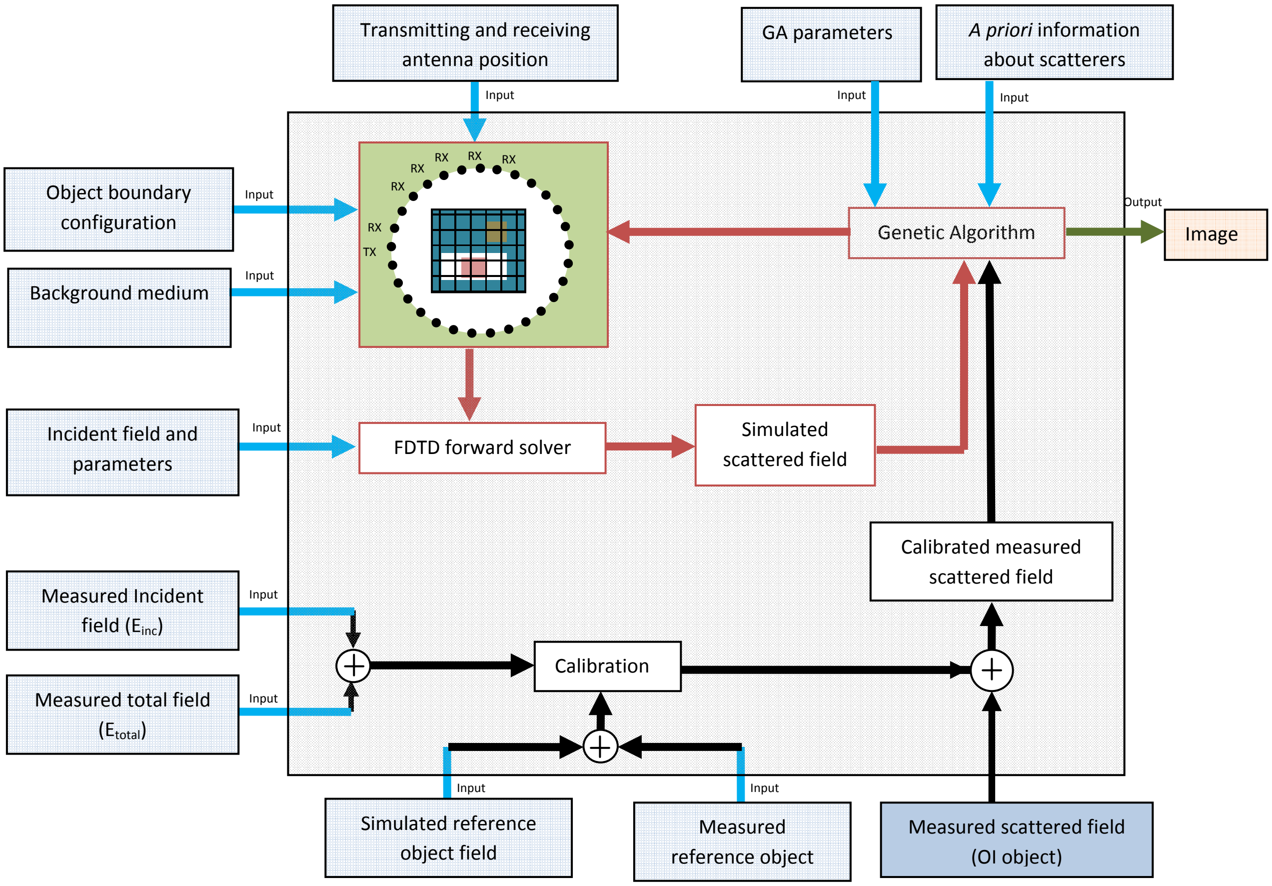

Fig. 2.3: Block diagram of the proposed MWT method.

3. MICROWAVE TOMOGRAPHY ALGORITHM

> *From a long view of the history of mankind, seen from, say, ten thousand years from now, there can be little doubt that the most significant event of the 19th century will be judged as Maxwell's discovery of the laws of electrodynamics.*
> Richard Phillips Feynman

In this chapter, the theory of the inverse and direct (forward) scattering problem is explained. A method for solving the inverse problem is developed in detail, and the results of some numerical simulations are used to make an in-depth analysis of the capabilities and effectiveness of the proposed approach.

3.1 Maxwell's equations

MWT is the process of creating the image of dielectric properties from measured electric field qualities. The dielectric properties and measured field are related by a non-linear relationship that is modelled by Maxwell's equations. The time-harmonic Maxwell's equations describe the electromagnetic phenomena in macroscopic media and are given by [142]:

$$\nabla \times \vec{\mathbf{E}}(\vec{r}) = -j\omega\vec{\mathbf{B}}(\vec{r}) \quad \text{Farady's law} \tag{3.1}$$

$$\nabla \times \vec{\mathbf{H}}(\vec{r}) = j\omega\vec{\mathbf{D}}(\vec{r}) + \vec{\mathbf{J}}(\vec{r}) \quad \text{Ampere's law} \tag{3.2}$$

$$\nabla \cdot \vec{\mathbf{B}}(\vec{r}) = 0 \quad \text{Gauss' law} \tag{3.3}$$

$$\nabla \cdot \vec{\mathbf{D}}(\vec{r}) = \rho \quad \text{Gauss' law} \tag{3.4}$$

where $\vec{\mathbf{E}}$ (V/m) is the electric field intensity, $\vec{\mathbf{H}}$ (A/m) is the magnetic field intensity, $\vec{\mathbf{B}}$ (T) is the magnetic flux density, $\vec{\mathbf{D}}$ (C/m^2) is the electric flux density, $\vec{\mathbf{J}}$ (A/m^2) is the electric current density (we consider it as a source term), ρ (C/m^3) is electric charge density, denotes the position vector, $j = \sqrt{-1}$ is the imaginary unit, and $\omega = 2\pi f$ (rad/Hz) is the radial frequency (f is the frequency). In order to include the information about the media in which electromagnetic phenomena occur, the *constitutive relations* has been used. Thus, for an isotropic and linear medium (background and OI) the relationships between the vector-field and the medium become:

$$\vec{\mathbf{D}}(\vec{r}) = \epsilon_r\epsilon_0\vec{\mathbf{E}}(\vec{r}) \tag{3.5}$$

$$\vec{\mathbf{B}}(\vec{r}) = \mu_0\mu_r\vec{\mathbf{H}}(\vec{r}) \tag{3.6}$$

$$\vec{\mathbf{J}}(\vec{r}) = \sigma\vec{\mathbf{E}}(\vec{r}) \tag{3.7}$$

where ϵ_0 (F/m) is the permittivity of free space, ϵ_r (unit-less) is the relative permittivity (dielectric constant), μ_0 (H/m) is the permeability of free space, μ_r (unit-less) is the relative permeability, and σ (S/m) is the electrical conductivity. We consider non-magnetic media in this thesis ($\mu_r = 1.0$). The value of permittivity and conductivity may depend on the operating frequency. This dependency can be modeled by different formulas. In this thesis the Debye model has been used (see Section 3.9). Substituting the equations (3.5-3.7) into equations (3.1-3.4), what can be seen is the dependency of the electric field on dielectric properties of the background. Solving the Maxwell's equations in order to determine the electric field ($\vec{\mathbf{E}}$) from the knowledge of the source ($\vec{\mathbf{J}}$), obstacles, and medium dielectric properties (ϵ_r, σ) is called the forward scattering problem. The forward problem may be solved based on either IE formulation [143] or PDE formulation. In contrast, in an inverse scattering problem, the goal is to determine the physical quantities of the media (ϵ_r, σ) from the knowledge of the electric field ($\vec{\mathbf{E}}$) at a set of receiver points and knowledge of the source ($\vec{\mathbf{J}}$).

In the following sections, some challenges associated with the inverse scattering problem are explained, and some solutions are provided for them. The inverse scattering problem is always associated with ill-posedness and non-linearity. The next section is devoted to introducing these two characteristics for the inverse problem.

i. Ill-posedness of the inverse problem

In regards to ill-posedness, in the sense of Hadamard [144], any problem is considered a well-posed problem if the solution is:

I. In Existence: For the existence of the solution (i.e. map of dielectric properties of scatterers), as long as the best approximations are made for solving the mathematical model, we can guarantee that a solution exists.

II. Unique: For the uniqueness of the solution, based upon the Maxwell's equations, the scattered fields are continuous functions of incident field and dielectric properties of the background. Therefore, the solution is unique if the knowledge of the field scattering at all positions and frequencies outside of the scatterers is available [52]. Practically speaking, we can only measure the field at a finite number of locations as well as a limited number of frequencies. As a result, the solution is always non-unique for practical problems [52]. In order to overcome the non-uniqueness of the solution, a fast, accurate, and inexpensive apparatus for the generation of the interrogating field and the measurement of a large number of samples of the scattered field is necessary.

III. Stable: The inverse scattering problem maybe unstable because a small arbitrary change in the incident field may result in an arbitrarily large change in the material parameters. From a practical perspective, the measured scattered field is always corrupted by noise, and therefore the solution might become unstable. Beside noise, the solution is very dependent on the observation point locations and the measurement accuracy.

After all, because of the non-uniqueness and instability of the inverse scattering problem, it is considered an ill-posed problem.

ii. Non-linearity of the inverse scattering problem

In an inverse scattering problem, the aim is to determine the dielectric properties in the imaging domain from the knowledge of the scattered field. In equation (3.2), the second term represents the multiplication of the field and material properties which means there is a non-linear relation between field and material properties. When the scattered fields are only available at discrete points, this problem becomes more severe. Another reason for non-linearity is the multiple reflections from different boundaries (Fig. 3.1). Significant absorption of the incident field may occur in heterogeneous object with high conductivity. For dispersive objects, different components of the signal travel at different speeds, thus the shape of the original waveform is altered. The above mentioned characteristics make the inverse problem non-linear and complicated to solve.

In summary, any algorithm used in order to solve the inverse scattering problems needs to consider three fundamental factors:

1. How to deal with the ill-posed and the ill-conditioned inverse scattering problems which is possible by using an iterative algorithm.
2. Developing an efficient accurate numerical method as forward solver, can be computationally intensive.

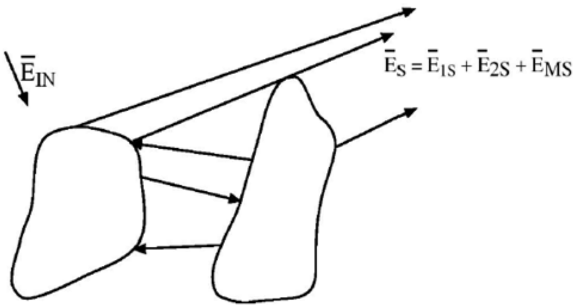

Fig. 3.1: Multiple scattering

3. Overcoming the drawbacks of two previous factors can be done using parallel computing power.

Our proposed methods deal with, and handle, all of the above three factors.

3.1.1 Inverse scattering problem from theoretical point of view

Consider an OI inside the imaging chamber. The cross-section of the OI successively is irradiated by a number of $E_{inc}(\vec{r}, \omega, \Phi)$. The electric field is calculated at the receivers and can be expressed in functional form as $E_{total}(\vec{r}, \omega, \epsilon(\vec{r}, \omega), \sigma(\vec{r}, \omega))$ where functions $\epsilon(\vec{r}, \omega)$ and $\sigma(\vec{r}, \omega)$ are the unknown distributions of permittivity and conductivity, respectively. $\vec{r}$ is the spatial coordinate. The goal is to find a set of dielectric properties of the material that can generate the same scattered fields as the measured ones. The following condition needs to be satisfied:

$$\sum_{i=1}^{M} \left| E_{total}^{estimated}(\vec{r_i}, \omega, \epsilon(\vec{r}, \omega), \sigma(\vec{r}, \omega)) - E_{total}^{measured}(\vec{r_i}, \omega) \right| = 0 \tag{3.8}$$

where $E_{total}^{measured}(\vec{r_i},\omega)$ is the measured total field at the M number of receiver points and the $E_{total}^{estimated}(\vec{r_i},\omega,\epsilon(\vec{r},\omega),\sigma(\vec{r},\omega))$ is the total field computed by the forward solver. The next section is devoted to introducing an iterative technique in order to find the permittivity and conductivity profiles that satisfies equation (3.8).

3.2 Iterative technique

Iterative techniques are currently one of the the best options for solving the non-linear inverse scattering problem. These techniques have a greater probability of converging to the right solution. In this approach the scattered field outside the object is measured and the differences between this field and the scattered field of a possible solution calculated by a forward solver is minimized. Therefore, this approach needs an iterative minimization process. Fig.3.2 shows the flowchart of the iterative technique for the image reconstruction method. This method is based on optimizing a fitness-function (3.8):

$$\begin{aligned}\min_{\vec{r},\omega,\epsilon(\vec{r},\omega),\sigma(\vec{r},\omega)}\alpha\left\|E_{total}^{estimated}(\vec{r_i}\,|_{i=1}^{M},\omega,\epsilon(\vec{r},\omega),\sigma(\vec{r},\omega))\right\| \\ -\beta\left\|E_{total}^{measured}(\vec{r_i}\,|_{i=1}^{M},\omega)\right\|+R(\omega,\epsilon(\vec{r},\omega),\sigma(\vec{r},\omega))\end{aligned} \tag{3.9}$$

The constants α and β can be heuristically determined for a certain class of scatterers. This kind of calibration is based on the assumption that can be inspected and the optimal values for these constants are used for a class of similar scatterers (see Chapter 5). In the third term of the equation (3.9), the function $R(\omega,\epsilon(\vec{r},\omega),\sigma(\vec{r},\omega))$ is a term

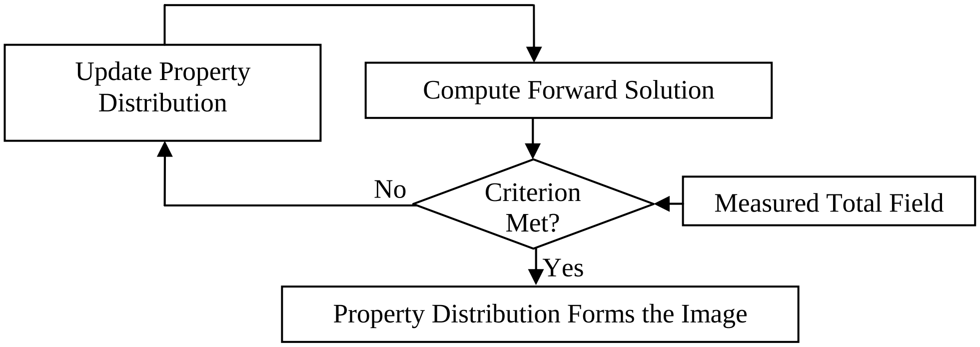

Fig. 3.2: Flowchart of the iterative technique

that can include *a-priori* information (constraints of dielectric properties) or their gradient configuration to be inspected and can play the role of regularization. The general approach for regularizing an ill-posed problem is to set "appropriate" constraints on the solution, e.g. limiting the norm of the solution or enforcing the solution to lie in an appropriate subspace [86]. This term is needed because of the ill-posedness of the inverse problem, and in this thesis, *a-priori* information is used as regularization term.

3.3 Optimization techniques

To date, in order to solve the inverse problem using the iterative method and to retrieve the unknown objects from the measurements, different deterministic (local optimizations) and stochastic (global optimizations) approaches have been proposed. These two kinds of optimization will be introduced in the following section.

3.3.1 Local optimization method

In deterministic approaches in particular gradient-based methods (first derivatives), Newton methods (first and second derivatives), Conjugate Gradient methods, and quasi-gradient methods have been used for solving the inverse scattering problem (see Section 1.5.2). The optimization starts from an initial guess and iteratively flows the direction of derivative to end up with the nearest minimum point in the search space. If the initial guess is close enough to the global minimum, the methods find the global minimum point. From a computational point of view, deterministic techniques are attractive. However, they can be trapped in local minimum. It means that the local based optimization imaging techniques are not accurate, and reliable results can be obtained only if the starting trial solution (initial solution) is not far from the real solution. In many practical cases, such a knowledge is not available and some inaccuracies or artifacts in the resulting reconstruction image appear. These methods are fast and a good choice for objects with no complex shapes, but is not proper for heterogeneous and complex objects.

3.3.2 Global optimization method

A number of global optimization methods have been developed for solving the non-linear inverse scattering problems related to MWT (see Section 1.5.2). A general review of different evolutionary optimizations (population-based optimizations) and stochastic optimizations for MWT can be found in [109, 127]. Global optimization methods are chosen because MWT problems have several local minima (see Appendix A). These algorithms tend to move toward the most attractive region of the solution space by means of an "almost" blind search technique since the operators are applied in a probabilistic way, instead of considering definite rules. They have been used in a wide range of applications. In the following part, we explain the capability of the GA as the global optimization method for MWT imaging.

3.4 Genetic algorithm (GA)

The GA is a robust stochastic (randomized), population-based global search technique inspired by the Darwinian theory that has its roots in the principle of genetics. In the late 1960s and early 1970s, John Holland first proposed the basic idea of GA [145]. It was used by Haupt in 1995 [146] and Rahmat-Samii in 1997 [147] in the area of computational electromagnetics.

3.4.1 Advantage of GA

A GA has several advantages over the traditional optimization method for MWT applications because of many features:

1. It can be used for optimizing continuous or discrete problems,
2. It does not require derivative (differentiability) information or analytical knowledge of objective function, but only the values of the fitness are needed to pursue

the evolutionary process,

3. It can work with a large number of variables,
4. It is easy to combine it with other methods,
5. It is very robust in terms of capability to reach global minima and not getting stuck in local minima,
6. It uses random transition rules not deterministic ones,
7. It works with coding of the parameters not with the parameters themselves,
8. It can deal with non-linearity and optimizes extremely complex fitness-functions,
9. It is well suited for parallel algorithms,
10. It has the ability to work with numerically generated data and experimental data,
11. It allows a simple and efficient inclusion of *a-priori* information into the model.

All of these advantages of the GA make it a very useful technique in solving constrained problems. However, it inherently takes a long time to converge. We proposed to use dependent-regularization as well as the parallel computing to overcome the long runtime.

3.4.2 GA parameters for the proposed MWT

Different parameters need to be defined in any GA. These included the type of GA (real or binary), the fitness-function, and the operators. The solution for each iteration is called an “individual” or a “chromosome”. Each chromosome consists of an array of “genes,” and the gene is the parameter to be optimized. The coding and decoding of the chromosome is different for binary or real GA. Each chromosome corresponds to a value of the objective function, referred to as the fitness value of the chromosome. A collection of the chromosomes forms a population. The GA iteratively modifies the population by applying three types of operators: selection, crossover, and mutation. These operators will be explained in more detail in Appendix B. The chromosome is a finite-length string of code corresponding to a solution (image) of a given problem. Basically, each unknown array (chromosome) obtained concatenates the code of each parameter (gene) from a specific material and belongs to a finite set of values (*a-priori* information). The chromosome can be a real or binary number. In this thesis, we have implemented the real-coded GA and binary-coded GA, differing only by chromosome and equivalent otherwise. In the next two sections, the configuration of the chromosome for the real and the binary GAs is explained.

3.4.3 Real-coded GA (RGA)

In RGA optimization, the chromosome is a floating point number. In the RGA program for the proposed MWT, the enclosed imaging domain is discretized into a

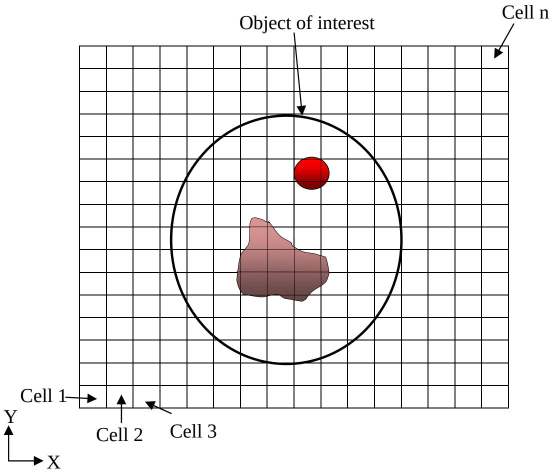

Fig. 3.3: Discretized the imaging domain for MWT.

number of small patches and a dielectric permittivity and conductivity pair (ϵ_j, σ_j) is assigned to each patch, where j is the index to the patch location (Fig.3.3). In RGA, each element is initialized within the desired range. Depending on the application, the boundary of the permittivity and conductivity is determined. Each gene is a random number picked from a uniform distribution: ($\epsilon_1 < \epsilon_j < \epsilon_2$) and ($\sigma_1 < \sigma_j < \sigma_2$), where ϵ_1 and ϵ_2 are the minimum and maximum possible values of the permittivity and σ_1 and σ_2 are minimum and maximum values for conductivity. It should be noted that this maximum and minimum number can be defined at a single-frequency for the dispersive object.

For each cell of the imaging domain, random values within the range of the permittivity and conductivity are assigned and considered as a gene:

$$\text{Gene} : (G_j) = (\epsilon_j, \sigma_j) \tag{3.10}$$

where j is the cell number. In fact, each gene represents a variable of the problem without any coding or decoding procedure. An array of genes that shows the dielectric properties distribution for an entire imaging domain is considered as a chromosome (3.11). The chromosome is an array of unknowns that needs to be determined.

$$\text{Chromosome} : [G_1,\ G_2,\ G_3, ...,\ G_n] \tag{3.11}$$

where n is the total number of patches of the imaging domain. Increasing n means that the resolution of imaging domain, and therefore, the search space are increased. RGA is very powerful, since it is able to find the dielectric properties values within a large range. The disadvantage is that RGA has slow convergence.

3.4.4 Binary-coded GA (BGA)

In BGA optimization, the discretization of the region stays the same as RGA; however, the chromosome's structure is different. In BGA, the gene is the type of the specific materials and they are distinguished by the Debye parameters (see Section 3.9). We designed a BGA that considers only limited material types taken from a look-up table, instead of randomly selecting the dielectric properties. The look-up table is

Tab. 3.1: The Debye parameters of breast tissues [148].

Medium	ϵ_∞	ϵ_s	$\sigma(S/m)$	$\tau_0(S)$
Skin	4.00	37.00	1.10	7.23e-12
Tumour	3.99	54.00	0.70	7.00e-12
Fatty tissue	7.00	10.00	0.15	7.00e-12
Fibro-glandular tissue	6.14	21.57	0.31	7.00e-12

created based on *a-priori* information and can be modified for different applications. For example, for water-tree detection, which is searching for water inside the power cable, the look-up table only consists of water and air. For breast cancer detection the look-up table consists of specific breast tissue types (Tab. 3.1) [148].

Since the parameter to be optimized is discrete with an integer value, a coding procedure is needed. Each parameter is represented by a string of q bits, where $q = log_2(L)$ and L is the number of different values that discrete variable can assume [114]. For example, in Tab. 3.1, the discrete variable can assume four cases; therefore, two bits can represent all four cases (Tab. 3.2). After the discretization of the investigation domain (Fig. 3.3), the number of cells multiplied by the number of the bits (that is assigned to each material) will be the size of one chromosome. For example, if the

Tab. 3.2: Code representative for the breast tissues.

Medium	Code represent
Fatty	00
Transitional	01
Fibro-glandular	10
Tumour	11

search space area is divided into n cells and in the look-up table for each material two binary strings are assigned, then the size of the chromosome will be $2n$ bits. As an example, the configuration of a chromosome for breast cancer detection before and after coding are shown in (3.12) and (3.13), respectively.

$$\text{Chromosome before coding} =$$

$$\{(\text{fatty})_1, (\text{fatty})_2, (\text{transitional})_3 ... (\text{fibro-glandular})_{n-1}, (\text{tumour})_n\} \tag{3.12}$$

$$\text{BGA chromosome after coding} = \left\{ \underbrace{00}_{\text{fatty}} \; \overbrace{00}^{\text{fatty}} \; \underbrace{01}_{\text{transitional}} \; ... \; \overbrace{10}^{\text{fibro-glandular}} \; \underbrace{11}_{\text{tumour}} \right\} \tag{3.13}$$

The number of unknowns for optimization depends on the number of cells in the investigation domain. For example, Fig. 3.4 shows the 2D cross-section of the breast phantom with different patch sizes. In Fig. 3.4 (a), the search space is divided into 16 cells in order to create an image with a $1.5cm$ resolution. If we want to find a tumour with a diameter less than $1.5cm$, for example $7.5mm$, we have to divide the search space into 64 cells (Fig. 3.4 (b)). If we divide the search space into 64 cells (considering four types of possible scatterers and two bits for each gene), then the size of the chromosome becomes 128 bits which takes a lot of time to converge to the best solution. Generally, in BGA, as the number of parameters increases, the convergence rate and the memory requirement increases. In order to mitigate this problem, we proposed to use the knowledge about the number of scatterers inside the imaging

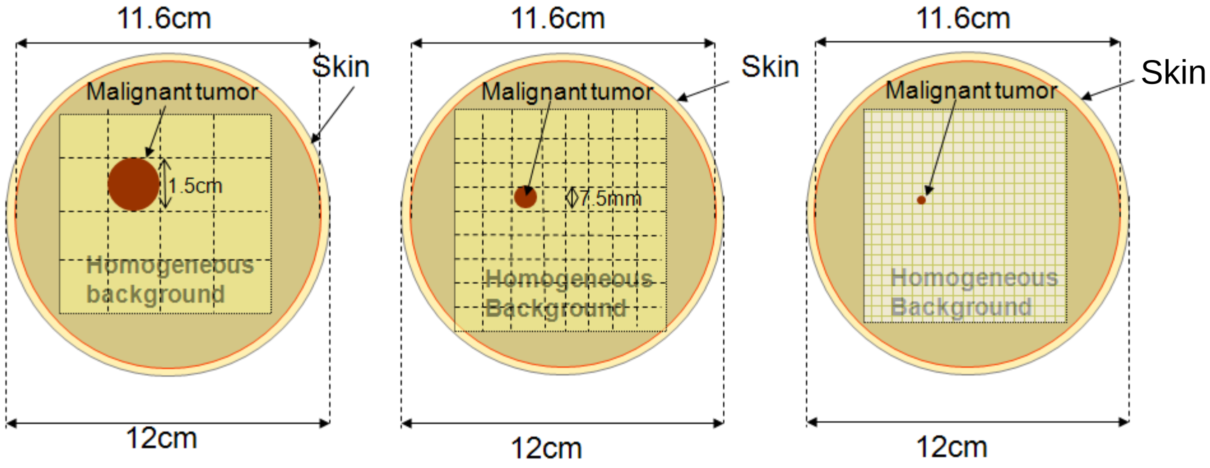

Fig. 3.4: The 2D cross-section of the breast phantom with different patch sizes (a) 16 cells, (b) 64 cells, and (c) 400 cells.

domain which will improve the convergence rate.

3.4.5 BGA with knowledge about the number of scatterers

Here, in order to increase the convergence rate of BGA, the new configuration for the chromosome is suggested. In this structure, knowledge of the maximum number of scatterers inside the imaging domain is required. This information of the OI significantly decreases the number of parameters to be optimized.

In this structure, each chromosome consists of two parts: the first part includes the type of scatterers, and the second part represents the location of the scatterers. For instance, a sample chromosome with four different homogeneous materials is shown in Fig. 3.5, where $D_j|_{j=1}^{4}$ is the Debye parameters and $P_j|_{j=1}^{4}$ is the location of the patch. In this chromosome, the first four numbers are the type of the material index and the

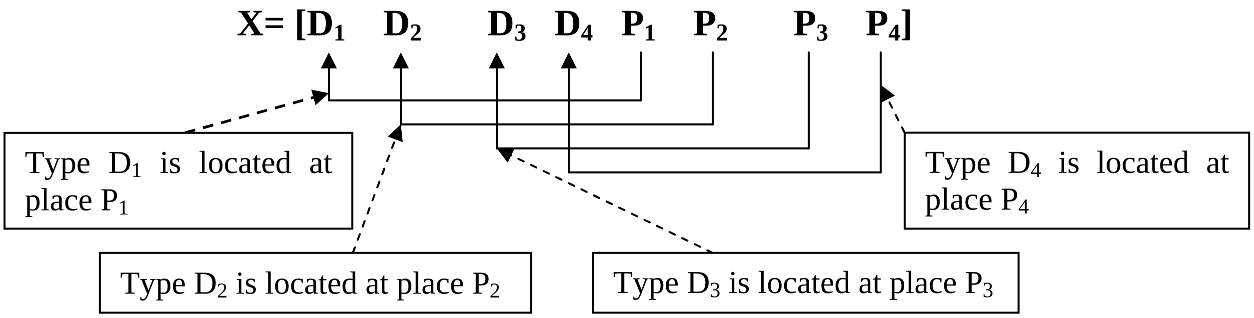

Fig. 3.5: Each chromosome contains hybrid of types and locations of scatterers.

next four numbers are the patch index. For example, a sample of a chromosome for breast cancer application can be: X = [1 3 0 2 - 4 7 9 13]. After coding this array using Tab. 3.2, the chromosome becomes:

$$\text{BGA Individual} = \left\{ \underbrace{01}_{\text{Transitional}} \overbrace{11}^{\text{Tumour}} \underbrace{00}_{\text{Fatty}} \overbrace{10}^{\text{Fibro-glandular}} \quad - \underbrace{0100}_{\text{cell 4}} \overbrace{0111}^{\text{cell 7}} \underbrace{1001}_{\text{cell 9}} \overbrace{1101}^{\text{cell 13}} \right\} \tag{3.14}$$

The chromosome (3.14) creates the map of the dielectric properties inside a cylinder as shown in Fig. 3.6. This type of coding decreases the runtime substantially compared with traditional BGA that was explained in the previous part. The drawback of this coding is the possibility of missing some scatterers, because we need to know the maximum number of scatterers beforehand. This information can be easily made available by the use of some other inexpensive deterministic methods (see Section 3.14). Two major disadvantages of the BGA approach for MWT are as follows:

1. When experimental data is used, the measurement data is contaminated by noise

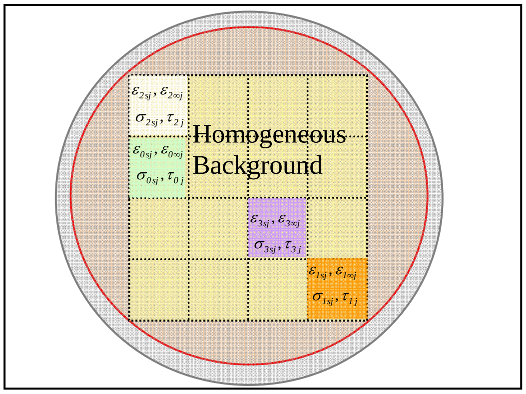

Fig. 3.6: Sample individual solution for the chromosome 3.14.

and thus there might be a false solution. In order to decrease the possibility of false solution, the hybrid RGA/BGA method is developed (see Section 3.12).

2. The GA operator representation of the solution (chromosome) does not ensure that the chromosome of the next generation is an admissible solution. Therefore, additional procedure is necessary to check if the proposed offspring is accepted. To overcome this problem, the hybrid Neural-Network/GA is suggested (see Section 3.13 and [133]).

3.5 Fitness-function

The fitness-function is used to distinguish the quality of the represented solution. A fitness-function is evaluated for every individual to check how good it is. It is the only way to measure the closeness of the proposed solution (or trial solution) to the actual solution. In fact, this function is composed of an error term representing the discrepancy between the measured and estimated values of the electromagnetic field at the observation points. Equation (3.15) shows the fitness-function we proposed:

$$fitness = 1 - \left\| \sum_{\phi=1}^{M} \frac{(E_\phi^{measurement} - E_\phi^{simulation})^2}{(E_\phi^{measurement})^2} \right\| \tag{3.15}$$

where $E_\phi^{measurement}$ is the measured scattered electric field, $E_\phi^{simulation}$ is the estimated scattered field obtained by performing a forward simulation, M is the total number of observation points, and ϕ is the angle of the observation point from the axis of the incident wave.

3.5.1 Multi-view/multi-illumination

Due to the ill-posedness of the inverse problem, it is necessary to collect a sufficient amount of data. Increasing the number of observation points increases the accuracy; however, there is a practical limit on the number of observation points. This is due to limited space and mutual coupling between antennas. To mitigate the ill-posedness of the problem, a multi-view/multi-illumination system is adopted to collect a sufficient amount of data. The multi-view/multi-illumination algorithm is commonly used in diffraction tomography. This approach is based on the use of an illuminating electromagnetic source that rotates jointly with the observation domain where the scattered electromagnetic field is measured. Mainly, by changing the positions of the scatterers and illuminating them with a source at multiple directions, the number of effective propagation modes increases and different values of the scattered field are measured [149]. In this case, the value of the fitness-function is given by:

$$fitness = 1 - \frac{1}{T}\sum_{i=1}^{T}\left\|\sum_{\phi=1}^{M}\frac{(E_{\phi,i}^{measurement} - E_{\phi,i}^{simulation})^2}{(E_{\phi,i}^{measurement})^2}\right\| \tag{3.16}$$

where T is the total number of transmitters.

Fig. 3.7 shows a dielectric object illuminated by an incident wave at four angles. M number of receiving points are considered in which the observation domain jointly rotates with the pulse illuminating source. For each set of solutions, the scattered fields are evaluated using the forward solver. It should be pointed out that the number of the transmitters is proportional to the computation time because the forward solver should run once per transmitter for each individual solution in each generation of GA. However, increasing the number of transmitters provides more information about the object.

3.5.2 Multi-frequency

The scattered field is a function of frequency [150]. By including the frequency term into the equation (3.16) we increase the information for image reconstruction. In this case the fitness-function becomes:

$$fitness = 1 - \frac{1}{T}\sum_{i=1}^{T}\left\|\sum_{f=f_1}^{f_2}\sum_{\phi=1}^{M}\frac{(E_{\phi,i,f}^{measurement} - E_{\phi,i,f}^{simulation})^2}{(E_{\phi,i,f}^{measurement})^2}\right\| \tag{3.17}$$

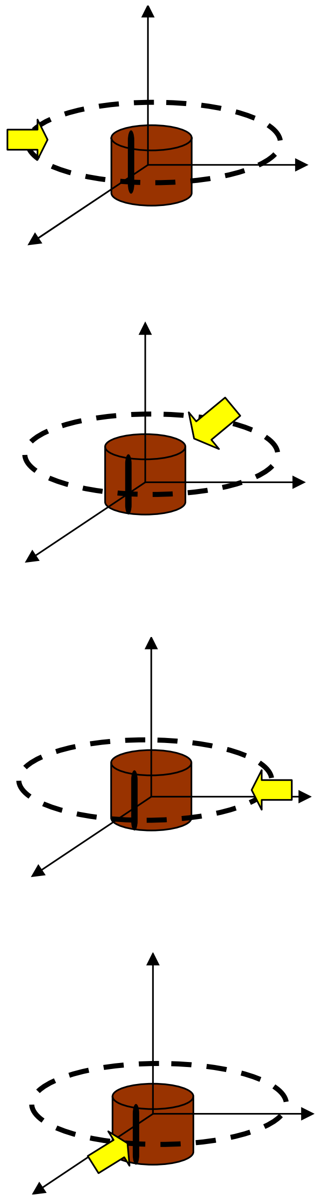

$$fitness\,T_1 = 1 - \left\| \sum_{\phi=1}^{M} \frac{(E_\phi^{\text{measurement}} - E_\phi^{\text{simulation}})^2}{(E_\phi^{\text{measurement}})^2} \right\|$$

(a)

$$fitness\,T_2 = 1 - \left\| \sum_{\phi=1}^{M} \frac{(E_\phi^{\text{measurement}} - E_\phi^{\text{simulation}})^2}{(E_\phi^{\text{measurement}})^2} \right\|$$

(b)

$$fitness\,T_3 = 1 - \left\| \sum_{\phi=1}^{M} \frac{(E_\phi^{\text{measurement}} - E_\phi^{\text{simulation}})^2}{(E_\phi^{\text{measurement}})^2} \right\|$$

(c)

$$fitness\,T_4 = 1 - \left\| \sum_{\phi=1}^{M} \frac{(E_\phi^{\text{measurement}} - E_\phi^{\text{simulation}})^2}{(E_\phi^{\text{measurement}})^2} \right\|$$

(d)

Fig. 3.7: Illuminating a dielectric object at four incident angles when E_{inc} is radiated from the (a) west side, (b) north side, (c) east side, and (d) south side.

f refers to different frequencies within f_1 and f_2. Note that the data at each frequency are equally weighted in the inversion process.

3.6 Dependent regularization

Local optimization methods require rigorous regularization (which often results in smoothing effects) in order to escape the local minima. In contrast, global optimization methods can escape from local minima through randomization. As a consequence, there is no need for global optimization-based inverse scattering methods to use the same regularization approaches as the local optimization methods [133]. Global optimization methods are more flexible regarding the regularization strategy. However, the existing global optimization methods, used for microwave image reconstruction, mainly use similar regularization approaches as the local optimization methods do; i.e., they smoothen sharp changes in the dielectric properties' profiles [112,113,124,151,152]. In this thesis, we propose to use a dependent-regularization approach which simply uses *a-priori* information.

In most applications of MWI, the range of possible physical parameters of OI are known. When this information is available, it is possible to limit the search to a specific range. *A-priori* information is, in fact, fundamental in limiting the set of admissible solutions and also in improving the efficiency and effectiveness of the inversion procedures. For instance, for breast cancer detection, because of the physical constraint for biological tissues $\epsilon_r > 1$, $\sigma > 0 S/m$, and depending on the types of the tissue, ϵ_r and σ have certain boundaries. Another example is using MWI for NDE applications; the OI is often a defect in an otherwise known structure. The defect can be represented by a given material, filling a hole or slot, such as ice, water, or rust. This information can be successfully integrated with the inverse solver in which there are significant possible solutions and the reconstruction method can consider only limited possible solutions. As it has been noted, one of the advantages of using GA as the optimizer for solving the inverse scattering problem is that *a-priori* information about the scatterer can be easily incorporated into the reconstruction algorithm. This information can lead the GA to the right solution, significantly reduce the number of possible answers, and improve the convergence speed.

3.7 GA-based inverse solver

The GA has been proposed previously by many researchers such as Pastorino, Caorsi, and Massa for solving the inverse scattering problem [13, 111–118]. The key difference among various approaches reported in literature concerns not only the adopted version of GA, but also the inverse scattering formulation and the procedure used, the forward solver, and definition of the fitness-function. In most cases, the GA is dealing with those problems which can be linearized using the first-order or second-order Born approximation [153, 154]. These problems can be used for low-contrasted bodies. To image high-contrasted bodies, the complete non-linear nature of the problem must be taken into account. In 2000, Pastorino *et al.* used a non-linear operator such as the

Lippman-Schwinger IE [155] in order to model the relation between the dielectric object and the field scattered [111]. For the optimization part, he used the standard GA. In most cases these techniques aim to solve the equation for the inverse scattering in its integral form by using matrix approaches. This technique seems to be very promising because it may allow the inverse scattering problem to be solved in exact complete form. The GA has been effectively employed with IE formulations for determining the inverse scattering of 2D homogeneous objects located in free space [113, 156, 157].

In this thesis, we have implemented a variety of inverse solvers based on GA, and they will be discussed throughout the rest of this chapter. We will discuss various search methods that are global in nature in the sense that they are attempting to search throughout the entire feasible set and optimize the fitness-function (3.17). To the best of our knowledge, the GA has not been applied with a full non-linear solver for solving the inversion scattering problem except in a paper [117] which has used non-dispersive and homogeneous structures. In general this is not valid for most MWI applications.

3.7.1 The GA inversion procedure

The proposed algorithm contains different steps. Fig. 3.8 shows the steps of the GA optimizer. The strategy of these steps that allows the GA optimization to create image from the scattered field data are described here.

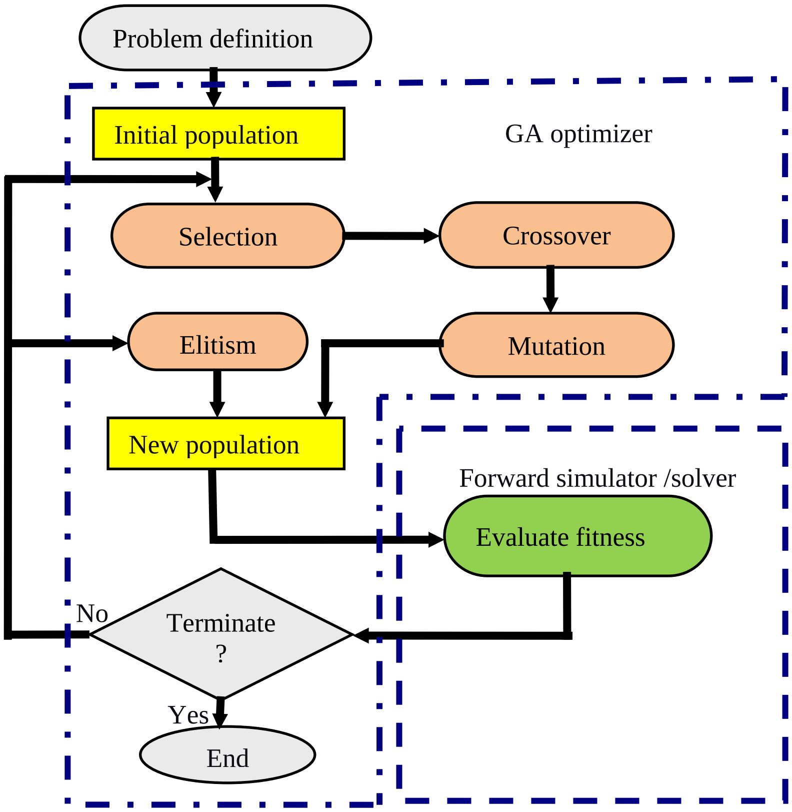

Fig. 3.8: Block diagram of the inverse scattering solver based on GA optimizer.

Step I. Define parameters

Defining some parameters such as the number of populations (P), number of generations (G), stopping criteria, probability of the crossover, mutation, and elitism is critical.

Step II: Representation scheme

The choice of type of GA, chromosome length, and encoding is called the representation scheme for the problem.

Step III. Initialization

Once a suitable representation scheme has been chosen, the next step is to initialize the first population of chromosomes. This is done by a random selection of a set of chromosomes considering the limitation of *a-priori* information. It is also possible to generate all individuals at the same time due to the independence of each individual.

Step IV. Calculating the fitness-function

After forming the initial population of chromosomes, we apply the operations of crossover and mutation on the population. During each iteration of the process, we evaluate the fitness value for each individual of the generation using the fitness-function. Calculating the fitness-function is the most time consuming part of the optimization. Using the parallel machines in order to solve the forward problem and calculate the fitness value significantly improves the computation time (see Section 3.15).

Step V. Saving the fitness values and chromosomes

The calculation of the forward problem is the most time-consuming part of the process. Therefore, the fitness value for each individual is stored to avoid repeating the forward simulation for those individuals that frequently appear in different generations.

Step VI. Selection, evolution, and mutation

When the fitness value for the entire population is evaluated, we form a new population using the selection process. Then, the crossover and mutation are applied (based on their probability).

Step VII. Repeat the procedure

The procedures of selection, crossover, and mutation are repeated for all generations until the maximum number of generations is reached or the threshold on the fitness measure is met.

Example of GA process

Here, we provide an example to show the process of the GA for the proposed MWT technique. Fig. 3.9 (a) illustrates a shell cylinder as an OI, and a small cylinder as a target is located inside the shell cylinder. Since we have assumed that the location of the surface of the cylinder is known, therefore we consider the investigation domain

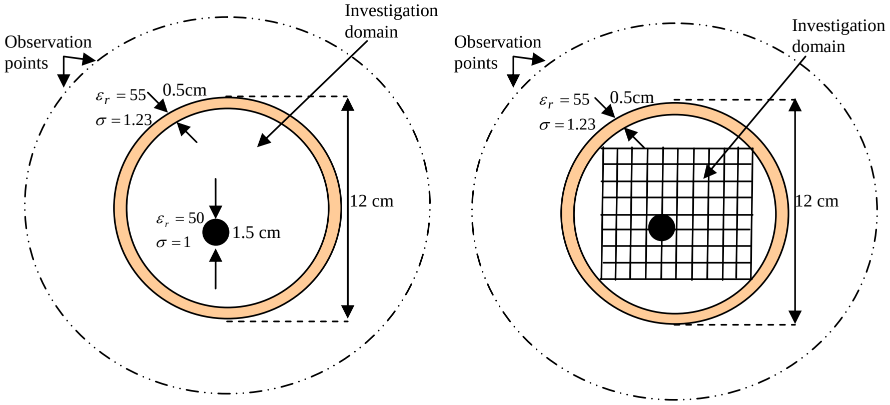

(a) (b)

Fig. 3.9: 2D dielectric shell cylinder with diameter of $12cm$ with a $1.5cm$ scatterer at the off-center (a) original structure, and (b) discretized structure.

only inside the cylinder. Fig. 3.9 (b) shows that inside the cylinder (the search space) has been discretized into small patches. The size of each patch depends on the smallest target size that we are interested in. The smaller the patch size, the more laborious and time consuming the process of GA can be.

After discretizing the search space area depending on the number of possible materials, the number of bits for each gene is selected. In GA, the solution starts from a homogeneous background such as air (for this example). Then the GA selects a random combination of these pairs, and as it evolves it gets closer and closer to the actual solution.

3.8 Time domain algorithm

The majority of the proposed inverse scattering algorithms have used monochromatic (single-frequency) excitation [57, 74, 92, 105, 113, 158–163]. Although using monochromatic incidences has been applied successfully to different applications of MWI, it has a significant shortcoming. It has been proven that due to the ill-posedness and non-linearity of the problem the inverse algorithms fail if they only use monochromatic incidences [164]. The frequency-hopping algorithm has been proposed to overcome this problem [78, 165–169]. In this method, for the data acquisition, a continuous incident wave spectrum is necessary to illuminate the object at different frequencies and also UWB probe is required to collect the electric field. Consequently, for analyzing such a measurement setup with multiple frequencies, it is better to use a time domain solver. This is the reason that we select the time domain numerical method as the forward solver.

3.8.1 Time domain forward scattering problem

The goal is to calculate the scattered fields when the object, background medium, and source are completely known. This is called the forward scattering problem. In order to solve this problem, the same as the inverse problem, Maxwell's equations need to be used. For calculating the scattered field in some problems the analytical solutions, in the form of eigenfunction expansions are available. However, when the geometry of the scatterer is complex, these analytical methods are not applicable. In such cases, we have to use approximations and/or numerical methods. Throughout this work, the FDTD numerical method has been used as a forward solver. FDTD is a numerical method used to solve Maxwell's equations in the time domain by applying central difference to time and space derivation in a wide range of applications [170]. One benefit of the time domain approach is that it yields a broadband output from a single execution of the program. However, the main reason for using the FDTD approach is its effectiveness as a technique for calculating electromagnetic fields in multilayer inhomogeneous objects. With a large number of unknown parameters related to the object under the test, the FDTD approach outpaces other methods in efficiency and provides accurate results of the field penetration into objects. The details of the FDTD formulation have been discussed in Appendix C. In FDTD methods, Maxwell's equations are solved in a closed area. This means that the solution area for scattering problems in an infinite space, such as the one that we are dealing with, needs to be truncated by an Absorbing Boundary Condition (ABC) [170]. We chose to use the Uniaxial Perfectly Match Layer (UPML) which is a very efficient ABC [171]. The UPML ABC is based on an artificial absorbing layer surrounding the simulation region (see reference [170] for more details).

3.9 Debye model

The frequency dependence of materials can be efficiently described in the time domain using Debye or Lorentz models [170]. These models can be expressed in different orders. The higher order models can accurately represent arbitrary dispersive medium at the expense of computational cost and complexity [172]. The Debye equation is given by:

$$\epsilon_r(\omega) = \epsilon_\infty + \sum_{p=0}^{p_{max}} \frac{(\epsilon_s - \epsilon_\infty)}{1 + (j\omega\tau_p)^{1-\alpha_p}} - j\frac{\sigma_s}{\omega\epsilon_0} \tag{3.18}$$

where α_p is a dimensionless weight, τ_p is the relaxation time of the p^{th} Debye function, ϵ_0 is the permittivity of the free space, ϵ_s and ϵ_∞ are the dielectric constants at zero (static) and infinite frequencies, respectively. σ_s is the conductivity at low frequency, and ω is the angular frequency. In order to maintain the simplicity of the method and to reduce computational cost, the first-order Debye model is employed [41, 148]. If $p = 0$ and $\alpha_0 = 0$ therefore

$$\epsilon_r - j\frac{\sigma}{\omega\epsilon_0} = \epsilon_\infty + \frac{\epsilon_s - \epsilon_\infty}{1 + j\omega\tau_0} - j\frac{\sigma_s}{\omega\epsilon_0} \tag{3.19}$$

$$\epsilon = \epsilon_0(\epsilon' - j\epsilon") = \epsilon_0(\epsilon' - \frac{j\sigma}{\omega\epsilon_0}) = \epsilon_0\epsilon'(1 - tan\delta) \tag{3.20}$$

$$\epsilon = \epsilon_0(\epsilon_\infty + \frac{\epsilon_s - \epsilon_\infty}{1 + j\omega\tau_0} - j\frac{\sigma_s}{\omega\epsilon_0}) \tag{3.21}$$

From equation (3.21), it is evident that the permittivity is a function of frequency as well as conductivity.

3.10 Frequency dependent FDTD

The conventional FDTD has been previously used for the modelling of non-dispersive material using constant material parameters. Frequency Dependent Finite-Difference Time-Domain ($(\mathrm{FD})^2\mathrm{TD}$) is an extended version of the conventional FDTD that incorporates the Debye model into the difference equations and can handle dispersive materials more accurately [173]. In this section it is explained how the Debye model has been implemented into the FDTD numerical model. by taking the inverse Fourier transform of (3.21), (3.5) and (3.6), one obtained $\epsilon(t)$, $B(t)$, and $D(t)$:

$$\epsilon(t) = \epsilon_\infty \delta(t) + \frac{\epsilon_0 - \epsilon_\infty}{\tau_0} e^{-t/\tau_0} u(t) \tag{3.22}$$

$$B(t) = \mu_0 H(t) \tag{3.23}$$

$$D(t) = \int_{-\infty}^{+\infty} \epsilon(t-\beta) E(\beta) d\beta \tag{3.24}$$

Therefore, the electric flux density is

$$D(t) = \epsilon_\infty E(t) + \frac{\epsilon_0 - \epsilon_\infty}{\tau_0} \int_{-\infty}^{+\infty} e^{-(t-\beta)/\tau_0} u(t-\beta) E(\beta) d\beta \tag{3.25}$$

By differentiating the above equation twice with respect to t, we obtain the first and second derivatives of $D(t)$

$$\frac{\partial D(t)}{\partial t} = \epsilon_\infty \frac{\partial E(t)}{\partial t} + \frac{\epsilon_0 - \epsilon_\infty}{\tau_0}\left[E(t) - \frac{\Delta t}{\tau_0} S(t)\right] \tag{3.26}$$

$$\frac{\partial^2 D(t)}{\partial t^2} = \epsilon_\infty \frac{\partial^2 E(t)}{\partial t^2} + \frac{\epsilon_0 - \epsilon_\infty}{\tau_0}\left[\frac{\partial E(t)}{\partial t} - \frac{1}{\tau_0} E(t) + \frac{\Delta t}{\tau_0^2} S(t)\right] \tag{3.27}$$

where

$$S(t) = \frac{1}{\Delta t}\int_{-\infty}^{+\infty} e^{-(t-\beta)/\tau_0} u(t-\beta) E(\beta) d\beta \tag{3.28}$$

$S(t)$ can be reduced to recursive form which is

$$S(t) = e^{-\Delta t/\tau_0} S(t-\Delta t) + \frac{1}{2}\left[e^{-\Delta t/\tau_0} E(t-\Delta t) + E(t)\right] \tag{3.29}$$

Applying equation (3.26) and (3.27) to the time domain form of (3.1) and (3.2), we obtained the magnetic field, H, and electric field, E, in finite difference form as:

$$\begin{aligned} E_z^{n+1}(i,j) &= [1 - \Delta t(\frac{\sigma_s}{\epsilon_\infty} + \frac{\epsilon_0 - \epsilon_\infty}{\epsilon_\infty \tau_0})] E_z^n(i,j) \\ &\quad + \frac{\Delta t}{\epsilon_\infty \Delta x}[H_y^{n+\frac{1}{2}}(i+\frac{1}{2}, j) - H_y^{n+\frac{1}{2}}(i-\frac{1}{2}, j)] \\ &\quad - \frac{\Delta t}{\epsilon_\infty \Delta y}[H_x^{n+\frac{1}{2}}(i, j+\frac{1}{2}) - H_x^{n+\frac{1}{2}}(i, j-\frac{1}{2})] \\ &\quad + (\frac{\epsilon_0 - \epsilon_\infty}{\epsilon_\infty})(\omega_0 \Delta t)^2 S_z^n(i,j) \end{aligned} \tag{3.30}$$

$$S_z^{(n)}(i,j) = e^{-\Delta t/\tau_0} S_z^{(n-1)}(i,j) + \frac{1}{2}\left[e^{-\Delta t/\tau_0} E_z^{(n-1)}(i,j) + E_z^n(i,j)\right] \tag{3.31}$$

The magnetic field equations remain unchanged as

$$\begin{aligned} H_x^{n+\frac{1}{2}}(i,j+\frac{1}{2}) &= H_x^{n-1/2}(i,j+\frac{1}{2}) \\ &\quad -\frac{\Delta t}{\mu_0 \Delta x}\left[E_z^n(i,j+1) - E_z^n(i,j)\right] \qquad (3.32) \\ H_y^{n+\frac{1}{2}}(i+\frac{1}{2},j) &= H_y^{n-1/2}(i+\frac{1}{2},j) \\ &\quad +\frac{\Delta t}{\mu_0 \Delta y}\left[E_z^n(i+1,j) - E_z^n(i,j)\right] \qquad (3.33) \end{aligned}$$

Since we used the first-order Debye equation to describe the dispersive material, the electric field values only at the previous step are needed to be stored. However, using a higher-order Debye model requires storing a large number of electric field values at previous time steps which consequently increases the computational complexity. An $(\mathrm{FD})^2$TD program was developed to simulate the interaction of the plane-wave with materials, and evaluate the scattered field. The program is written for a 2D Cartesian coordinate system. Unless otherwise noted, all forward simulations in this thesis are performed by the $(\mathrm{FD})^2$TD numerical method. From a computational point of view, the inverse scattering program has a long runtime because it is computationally heavy. By using a parallel computer and through Message Passing Interface (MPI) method, the runtime can be decreased in inverse proportion to the number of parallel processors used for the $(\mathrm{FD})^2$TD solver. The parallel $(\mathrm{FD})^2$TD will be explained in Section 3.15.

3.11 Preliminary validation

While the ultimate test of any inversion algorithm must involve experimentally collected scattered fields, it is very useful for comparison purposes to have a synthetic data set where the true contrast is known. We have created a synthetic data set obtained by running a forward simulation using $(\mathrm{FD})^2\mathrm{TD}$. To prevent the "inverse crime" [174], the discretization used in the inversion algorithm to invert E^{scat}_{meas} is chosen to be different than the discretization used in the forward solver to generate E^{scat}_{sim}. In some of the examples presented in this thesis, we have assumed the unknown scatterers are enclosed in a cylinder. This makes the problem more challenging and closer to real cases.

In all examples considered herein, unless otherwise stated, the following parameters have been used. 100 observation points are uniformly distributed around the investigation domain. A TMz Gaussian plane-wave successively illuminates the OI and penetrates in the investigation domain, and the scattered fields are measured at the observation points around it. To enhance the accuracy of the image and reduce the ill-posedness of the inverse problem, the procedure is repeated for four different incident angles (0^o, 90^o, 180^o, and 270^o). In these examples the measurement scattered field values are replaced by simulated data (hypothetical measured data) obtained by running a forward simulation using $(\mathrm{FD})^2\mathrm{TD}$ with a $0.1mm$ resolution. To prevent the inverse crime, a $0.5mm$ resolution mesh has been used for the inverse solver. *A-priori* information about the scatterers, such as possibility of material and maximum number of scatterers, could be available. In order to decrease the computation time and to speed-up the convergence rate, those information have been used. As a proof of concept, we have considered the noise-less scenarios for all simulations in this chapter.

I. Reconstruction algorithm using BGA

In the first two examples, we want to investigate the capabilities of the proposed technique using BGA, in reconstructing the high contrast homogeneous scatterers inside a shell dielectric cylinder. We assumed that a maximum of four scatterers can be found inside the cylinder and also four types of material can exist inside the investigation domain. The investigation domain is partitioned into $n = 16$ patches. The BGA with two bits is selected for each gene; therefore each individual consists of 24 bits. The initial value for the background depends on *a-priori* information of that specific application. Here in these examples, the majority of the material inside the object is filled by air. Therefore, for each cell of background, the dielectric properties of free space are attached. The GA parameters are defined in Tab. 3.3. The assumed value seems to be a reasonable choice for the configuration assumed in these examples after running the GA several times. It should be noted that for these two examples only one single-frequency has been used for reconstruction procedure. A regular 3GHz personal computer with 1GB RAM has been used to run these simulations.

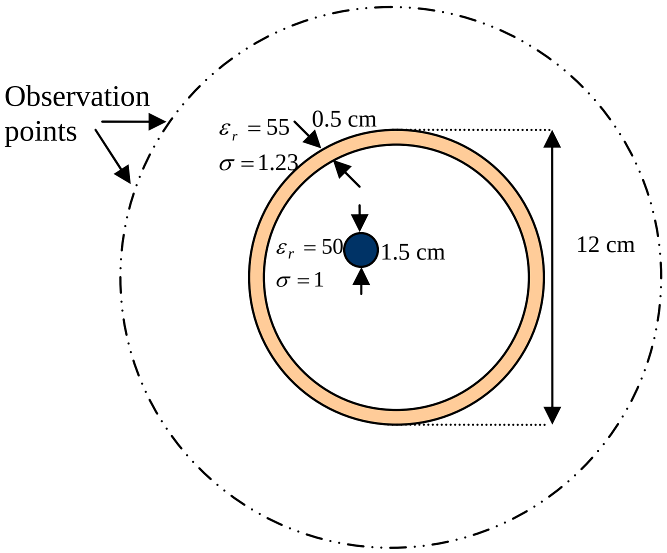

Fig. 3.10: Dielectric shell cylinder with a scatter located off-center.

Tab. 3.3: Parameters of GA program for first example.

Number of generations	10
Number of populations	60
Probability of crossover	0.7
Probability of mutation	0.03
Elitism	0.0

3.11.1 Single scatterer

The first example illustrates a cylinder with a diameter of $12cm$ with a $0.5cm$ skin layer with a dielectric material of relative dielectric constant 55 and conductivity 1.23. This cylinder is filled with dielectric material with $\epsilon_r = 1.0$ and $\sigma = 0.0S/m$. A small cylinder with a diameter of $1.5cm$, $\epsilon_r = 50$, and $\sigma = 1.0S/m$ is located inside the outer cylinder (Fig. 3.10). Basically in the iterative techniques, it is common to monitor the behavior of the fitness value at different generations in the GA-based

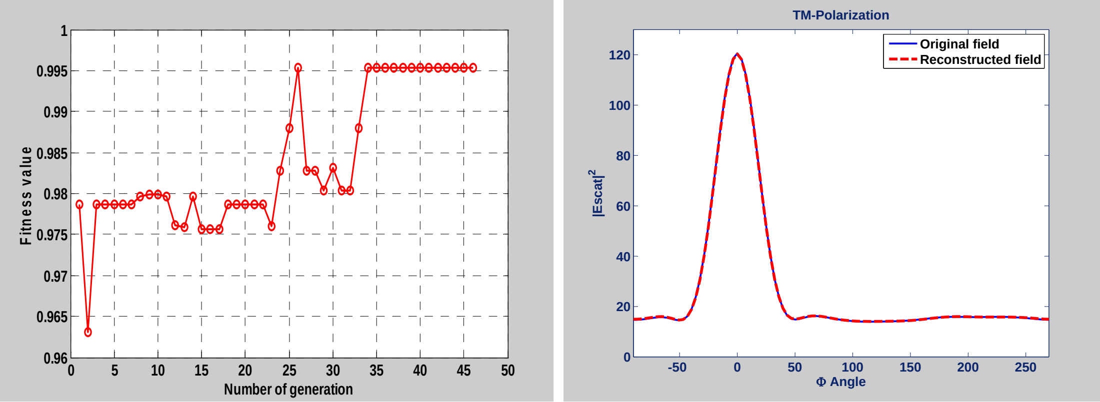

(a) (b)

Fig. 3.11: (a) Fitness value of the best individual in different generations, (b) comparison between forward and reconstructed field evaluated by FDTD.

optimization for evaluating the results [141]. Fig. 3.11 (a) shows the best fitness value and its convergence at different iterations. From this figure one can observe that as the generation evolves, the population gets close to the real solution. For this example, no elitism was considered; therefore, through different iterations the best solution might be lost. In order to better evaluate the reconstruction and true image, the scattered field of the reconstructed image and the true image are shown in Fig. 3.11 (b). In terms of the shape, the reconstructed image shows a square shape for a circular scatterer (Fig. 3.12).

3.11.2 Multiple scatterers

In the second example, the same outer cylinder as in the first example is considered, but this time a second smaller cylinder with $\epsilon_r = 90$ and $\sigma = 0.0S/m$ is located very close to the skin layer (Fig. 3.13). Both scatterers have the same size of $1.5cm$

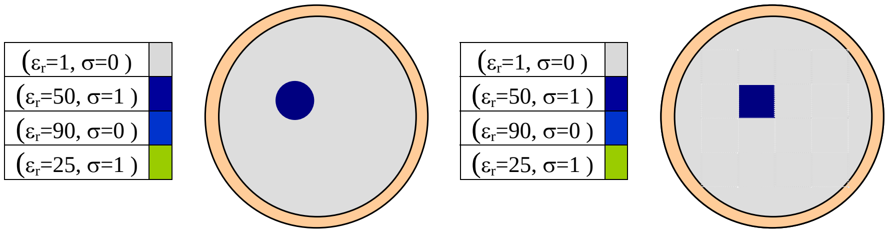

(a) (b)

Fig. 3.12: (a) Real, and (b) reconstructed images of Fig. 3.10.

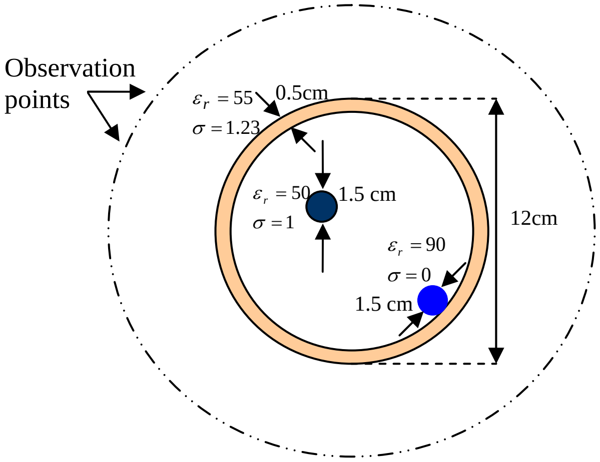

Fig. 3.13: Dielectric shell cylinder with two scatterers.

diameter. This configuration is selected to investigate the capability of the proposed method when a strong scatterer exists next to the skin layer. The GA parameters were the same as the first example shown in Tab. 3.3. Fig. 3.14 (a) reports the behavior of the fitness-function. Surprisingly, the GA optimizer was faster than the previous example, and after the 5^{th} iterations, no further convergence occurs. Fig. 3.14 (b) shows the validation of the reconstructed image obtained at a frequency of 2.5GHz.

What we can observe from these two examples is that the proposed approach is able

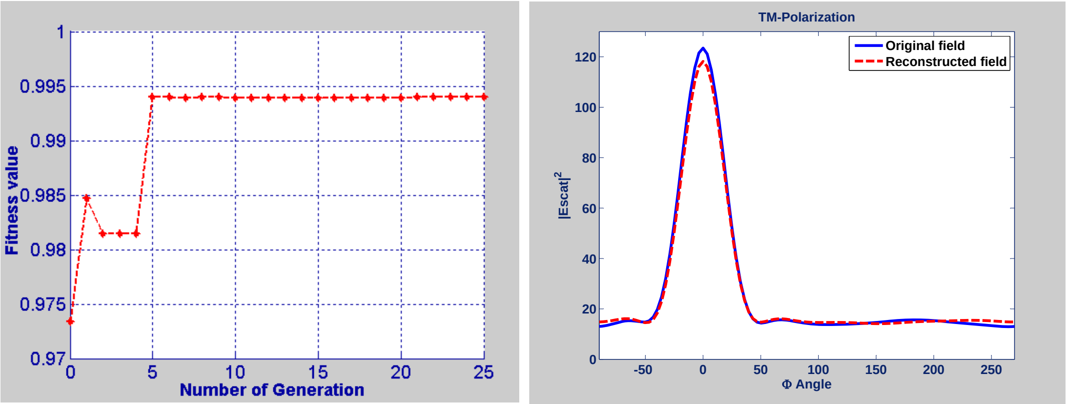

(a) (b)

Fig. 3.14: (a) Fitness value of the best individuals in different generations, (b) comparison between forward and reconstructed field evaluated by FDTD at 2.5GHz.

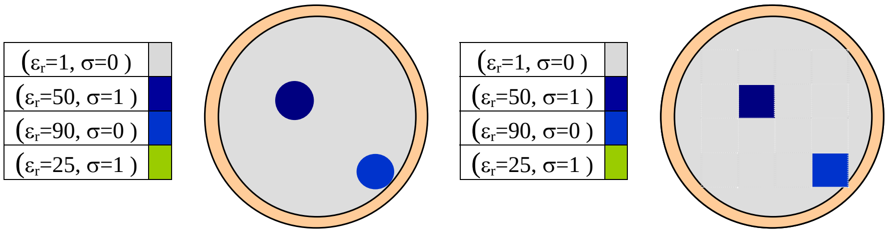

(a) (b)

Fig. 3.15: (a) Real, and (b) reconstructed images of Fig. 3.13.

to accurately find strong scatterer. It should be pointed out that in the reconstructed images, the scatterers have rectangular shapes while the actual images are circular (Figs. 3.12 and 3.15). The reason is that the discretization is done in squared shape patches. If the investigation domain is discretized with small square patches, then the non-rectangular shape of scatterers can be modeled. However, in this case, the number of patches increase and eventually the computational load, time, and memory for reconstruction images will increase.

3.11.3 Dispersive scatterers separated from each other

In order to illustrate the feasibility of MWT using the $(FD)^2TD/GA$ tomography method, we present three experimental examples with dispersive scatterers. These dispersive scatterers are considered as the biological breast tissues. The Debye parameters of biological breast tissue such as normal and cancer breast tissues used in these examples are given in Tab. 3.1 [148]. A simplified breast phantom will be presented here in order to show the capability of the proposed MWT for detecting the malignant tissue inside the normal tissues. Breast cancer imaging is our first primary application and will be explained in detail in the next chapter with realistic cases using Magnetic Resonance Imaging (MRI) data. The first example of the numerical breast model is shown in Fig. 3.16 (a). It has a diameter of $12cm$, is filled with fatty tissue, and has a square-shaped tumour with a size of $1.5cm$. The skin thickness and the size of the fibro-glandular regions are $2mm$ and $1.5cm$, respectively. Since we used elitism here, in the process of reconstructing an image, the fitness value increases from generation to generation. In a sample experiment, we found that with 120 individuals in each generation, the fitness-function reached the optimum value. In this experiment, the best match between the hypothetical data from the $(FD)^2TD$ forward simulation and the calculated scattered field was reached after the 64^{th} generation and did not change for 10 generations. The fitness value corresponding to the correct solution might be different in real situations where noise is present. Such a match corresponds to a successful recovery of the location and dimension of the breast tissues, as well as the type of material representing the breast tissues. Fig. 3.16 (b) and (c) show the map of the dielectric properties of the recovered image at 6GHz with the x and y axes representing the 2D search space inside the numerical breast phantom, and the z-axis showing the permittivity (Fig. 3.16 (b)) and conductivity (Fig. 3.16 (c)). The GA's outputs are the Debye parameters which completely reconstruct the dielectric properties profile at any given frequency.

3.11.4 Dispersive multiple adjacent scatterers

Fig. 3.17 (a) shows the second phantom used to illustrate the robustness of this method for different breast compositions. The numerical breast phantom size and optimization procedure are the same as the previous example, except that this time a tumour is located adjacent to fibro-glandular regions. Fig. 3.17 (b) and (c) show the dielectric property map at 6GHz, again showing a successful recovery of all tissue

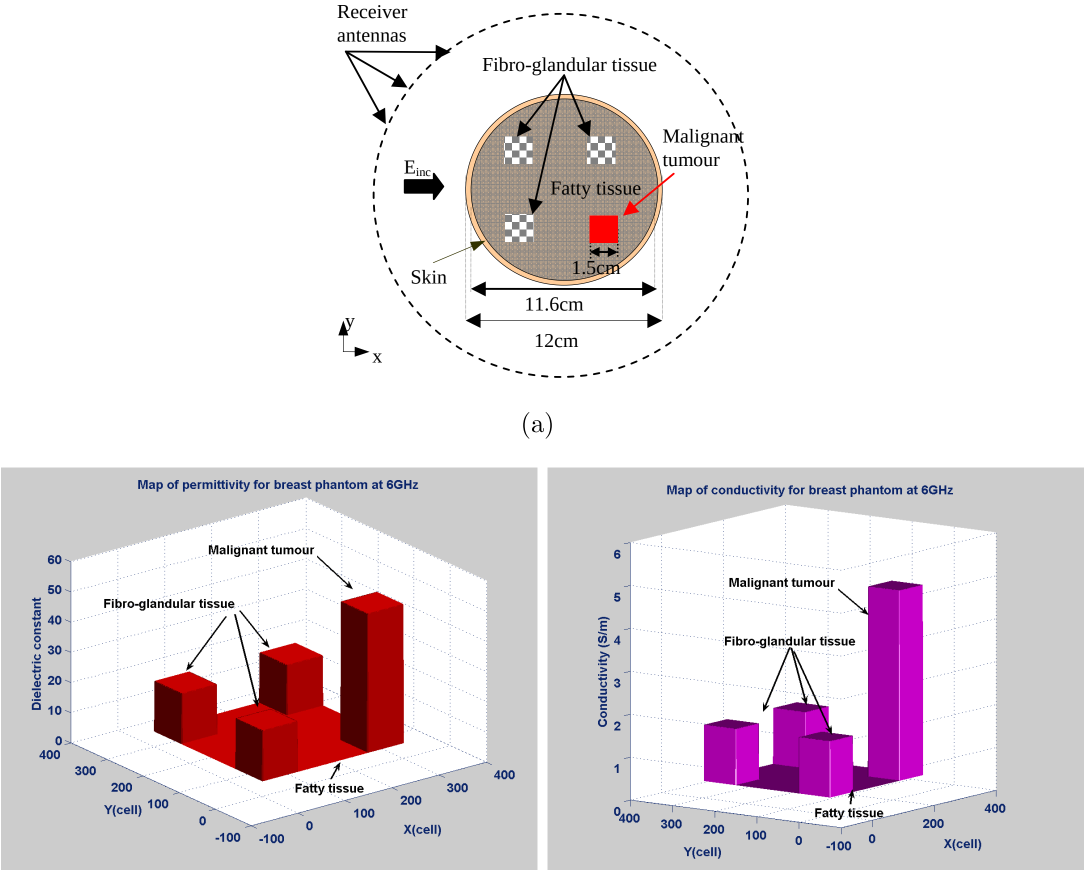

(a)

(b) (c)

Fig. 3.16: (a) Numerical breast phantom with a 1.5*cm* tumour inside the fatty tissue (top view), (b) map of dielectric constant, and (c) map of conductivity.

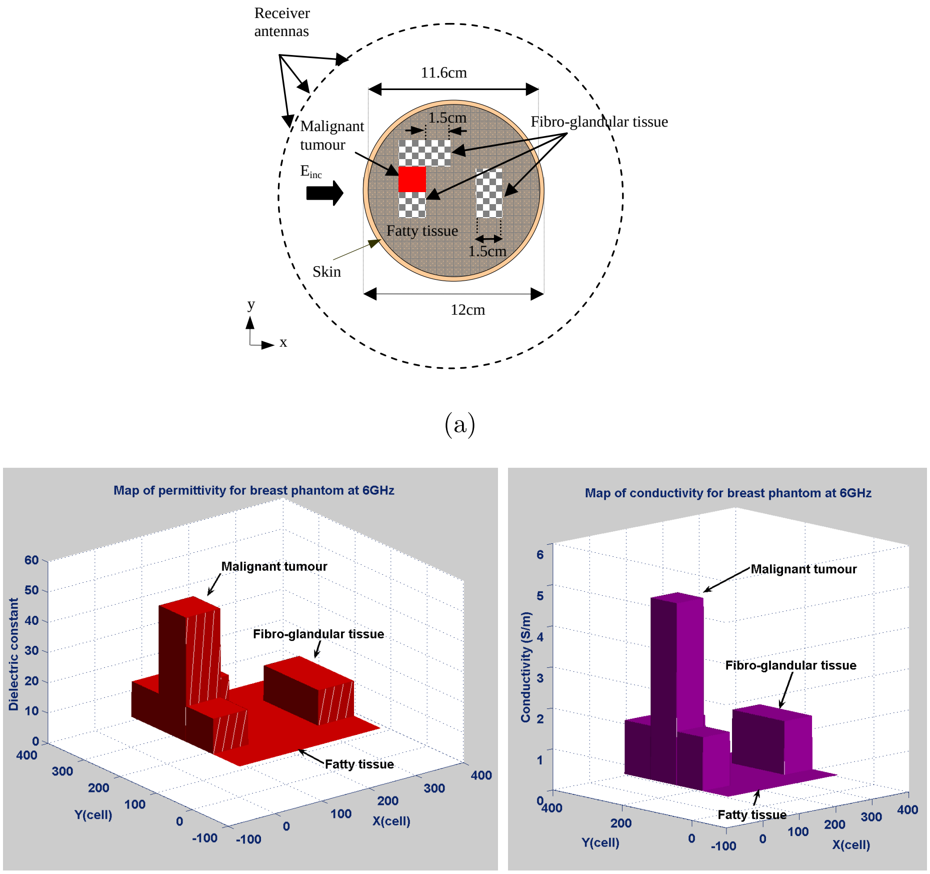

(a)

(b) (c)

Fig. 3.17: (a) Numerical breast phantom with a 1.5*cm* tumour inside the fatty tissue (top view), (b) map of dielectric constant, and (c) map of conductivity.

types. These examples illustrate that the proposed (FD)^{2}TD/GA method is capable of detecting lesions in environments where they are surrounded by fibro-glandular tissue, which happens in most cases of breast cancer. Higher resolution images of the realistic phantom can be obtained by using longer chromosomes which result in a longer runtime. An example of such images with high resolution are given in Section 3.15.

3.12 Hybrid real-coded GA and binary-coded GA (HGA)

The RGA[1]-based procedure is very slow to converge, and the BGA procedure is not able to “fine-tune” the optimum solution. Each of them has some advantages and disadvantages. Combining the BGA/RGA takes the advantages of these two stochastic approaches. In fact, the RGA alone might be able to finally converge to the solution, but it is a laborious and time consuming process. On the contrary, the proposed BGA requires a limited number of possible dielectric properties that may not be possible in some applications. To overcome these problems, a hybrid method including the BGA and RGA is introduced.

Fig. 3.18 shows the block diagram of the HGA optimization method. Since the inverse scattering poses an ill-posed problem, the solution is non-unique. Therefore, to reduce the search space and regularize the problem, a combination of BGA and RGA is proposed. First, the proposed inversion procedure starts with a BGA procedure until a given stop condition is reached, and then those best solutions are chosen as an initial estimate for the next step of optimization which is RGA. The RGA uses the best solutions as initial individual in its first generations. Then, the best solution that converges is considered the best result.

One of the most critical points for accuracy in image reconstruction is the ability to accurately measure the field at the observation point. Moreover, measurement is always under the influence of external electromagnetic artifacts which might change

---

[1] The RGA code is written by Ali Ashtari.

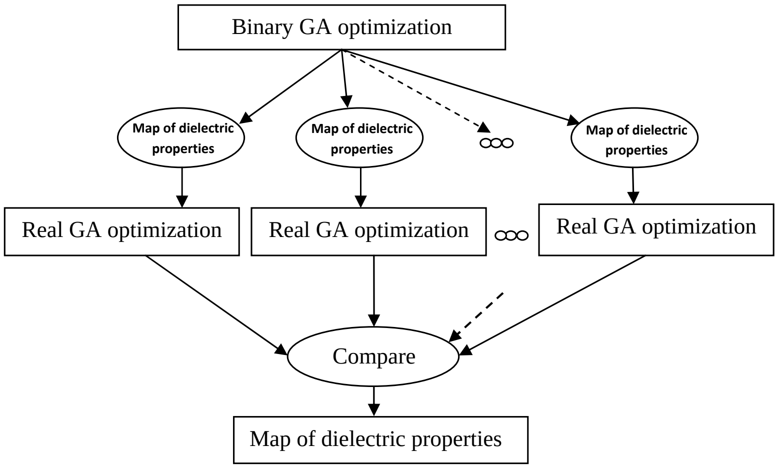

Fig. 3.18: Block diagram of HGA optimization method.

the measured scattered field. As well, due to the instability of the inverse problem, the image accuracy might decrease and non-real solution might be given by reconstruction methods. However, the fine-tune capability of RGA in hybrid BGA/RGA improves the image accuracy while the noise appears in the measurements. We recommend the HGA inverse solver, for those applications that deal with complex and large distribution of dielectric properties. An example of using the Hybrid BGA/RGA for solving the inverse scattering problem for microwave breast cancer image reconstruction will be discussed in the next chapter.

3.13 Hybrid GA global optimization and Neural-Network training

[2] One of the problems with GA for solving the inverse scattering problem is that the GA operators do not assure that the chromosomes of the next generation are admissible solutions. In order to mitigate this problem, a training procedure is added to the optimization procedure. In this technique, the RGA for optimization and feed forward Neural-Network (NN) for training the system have been applied [175]. This method will be referred to as Neural-Network Real-coded GA (NNRGA) throughout this thesis. In each RGA iteration, *a-priori* information about the shape of the object profile is checked by a NN classifier to reject the solutions that cannot be a map of the dielectric properties of the object profile. Fig. 3.19 shows the block diagram of the proposed technique with and without the NN block. Mainly, a NN classifier is applied to each individual which is created by the RGA, and any profile that does not "look like" an OI profile is disregarded. Therefore, we need to define the NN classified from *a-priori* information about the OI. The main advantage of the NN is increasing the convergence rate. In fact, in the regular GA (RGA or BGA)/(FD)^{2}TD technique, for any individual, the forward solver is running in order to calculate the fitness value, regardless of whether or not the temporary solution looks like an image for that specific application. Therefore, suitable genetic operators such as NN classifiers have to be defined in order to obtain admissible solutions and to enhance the convergence process. In the NNRGA technique, at each step a new temporary

---

[2] The Neural-Network classifier was developed by Ali Ashtari [175].

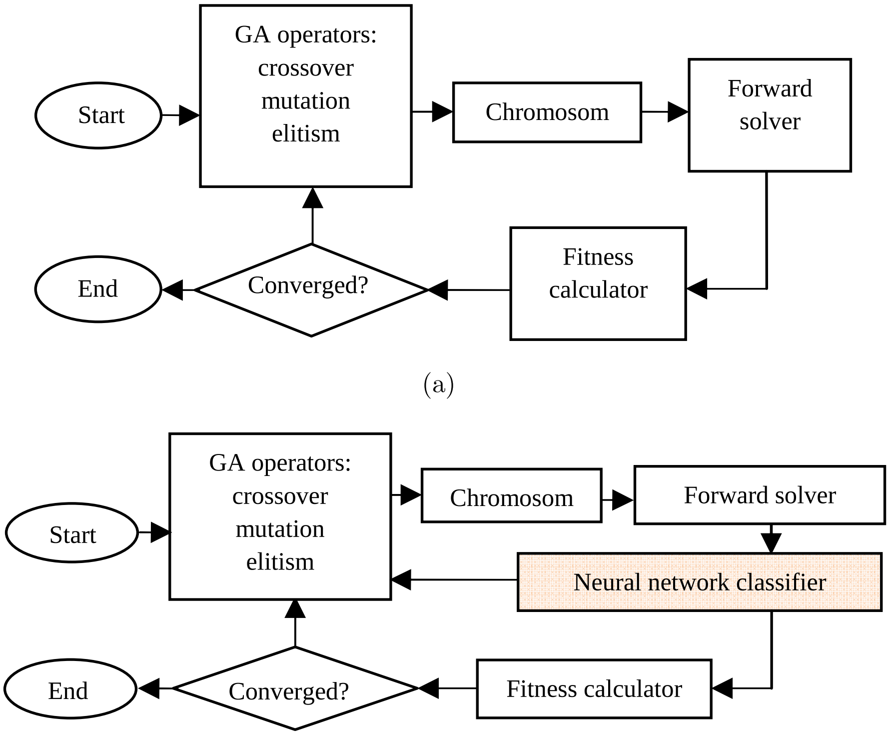

(a)

(b)

Fig. 3.19: Block diagram of the RGA (a) without NN classifier, and (b) with NN classifier.

population is generated applying the crossover, mutation, and elitism operator to ensure a monotonic decrease of the best fitness in the population during the iterative process, and then it goes to the NN evaluation procedure to check different features. If the temporary population meets the NN criteria, it will go to the next step which is the fitness-function calculation. Otherwise, the temporary population will be replaced with another one and go through the same procedure. The NN features have been extracted depending on the application beforehand. Basically, the ill-posedness of the inverse problem creates many solutions for an inverse problem. By merging the NN procedure with the GA approach, the possible solutions decrease, and eventually the ill-posed condition for the inverse scattering problem decreases.

For example, for breast imaging application, 12 features are extracted for each profile in the search area such as the percentage of tissue in the fatty groups, the fibro-glandular groups, the transitional group, and the total percentage of the fatty tissue. The number of connected fatty regions and connected fibro-glandular regions are two additional features used for the classification. For more details about these features and how to extract them see [133]. The proposed technique was able to remove ill-posed answers without smoothing the reconstructed profile and also significantly decreased the computational runtime. This technique has been evaluated for four types of breasts and were able to reconstruct both high contrasts (between the fatty and fibro-glandular tissue) and low contrasts (between the fibro-glandular tissue and tumour). It should be noted that the method was able to provide a $4mm$ resolution on realistic numerical breast phantoms [133].

3.14 Hybrid tomography and radar method (Hybrid MWR/MWT)

[3] It has been fully demonstrated that the GA is very powerful in searching for the identification of the profile. However, the search is extremely time consuming, in particular for high resolution images, which is one of the basic disadvantages of using GA for MWT purposes. The convergence rate can be improved by hybridizing the GAs with some fast algorithms (see Section 1.5.2). We proposed to use a hybrid

---

[3] The microwave radar method was developed by Daniel Flores Tapia [176].

approach, which combines radar and tomography, to provide more information and stronger signals. While radar has the advantage of computational simplicity in image reconstruction, it cannot provide information about the type of scatterer. The tomography method attempts to solve an inverse scattering problem imposed by the non-linear relationship between the measured scattered fields and dielectric properties of the scatterers. Although tomography is numerically intensive, it provides a map of the dielectric properties of the object, from which the scatterer type can be recognized.

To the best of our knowledge, this is the first time that a Hybrid MWR/MWT imaging method for the detection and reconstruction of dielectric objects has been proposed. In most applications of the MWI technique, the object to be imaged is completely known except for a defect. The localization of the defect may constitute sufficient information which will be useful to identify the defect. Therefore the MWR technique uses the reflections from the defects present in the scanned area in order to determine their spatial location and dimensions. On the other hand, MWT techniques try to recreate the dielectric properties map of the scan area from measurements of the microwave energy transmitted through it. Therefore, combining a qualitative method such as the radar-based approach and a quantitative method such as the tomography method increases the rate of the convergence of the iterative approach. In the hybrid MWR/MWT technique, the following sequence of steps is performed:

1. Detection

First, we check whether something suspicious exists in the structure by using the following objective function:

$$F = \sum_{i=1}^{4} \left(\frac{\sum_{\phi} \left(E_{i\phi}^{reference} - E_{i\phi}^{measurement} \right)^2}{\sum_{\phi} \left(E_{i\phi}^{measurement} \right)^2} - \sum_{\phi} N_{\phi} \right) \qquad \phi = 1, 2, ...M \tag{3.34}$$

where the $E_{i\phi}^{reference}$ is the total field at observation points for the case of the reference object present and the $E_{i\phi}^{measurement}$ is the total field for a case while OI is under the test; i is the number of the illuminations at different directions, and N is the measurement of the noise for each antenna which is define as:

$$N_{\phi} = \frac{\left(E_{i\phi}^{reference(measurement)} - E_{i\phi}^{reference(simulation)} \right)^2}{(E_{i\phi}^{reference(simulation)})^2} \tag{3.35}$$

the $E_{i\phi}^{reference(measurement)}$ and $E_{i\phi}^{reference(simulation)}$ represent the total field for the reference object from measurement and simulation, respectively. If the value of the F is less than a fixed threshold, the object is defect-free; otherwise, the localization procedure (focusing and identification) takes place. Note that the value of the detection threshold is a function of the sensitivity of the measurement system.

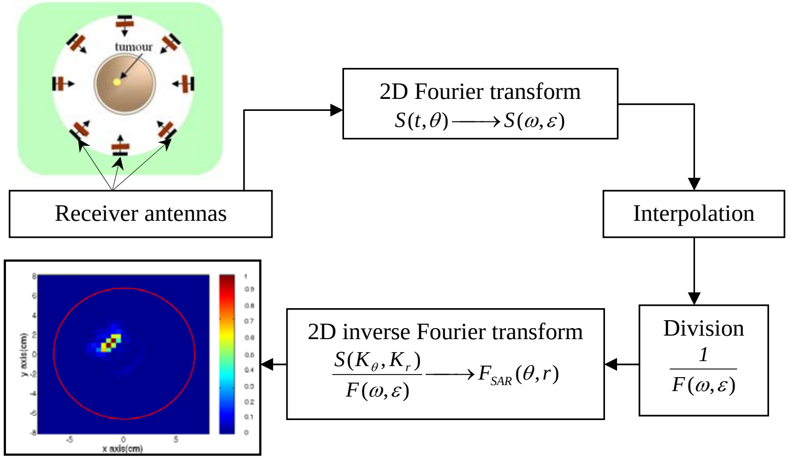

Fig. 3.20: Block diagram of the wavefront radar-based reconstruction method.

2. Focusing

Fig. 3.20 shows the block diagram of the wavefront radar-based reconstruction method. The plane-wave impinges on the OI and the reflected field is collected by the receiving antenna. Then, the same procedure is repeated for individual antennas/probes around the OI. The collected reflected fields are used as a source of data for the radar reconstruction method. The collected reflections are focused using a wavefront reconstruction approach [176, 177]. When the target signatures are labeled and their spatial locations and dimensions are stored, identification takes place at the next step of the optimization procedure.

3. Identification

For identification, the proposed MWT technique based on the $(FD)^2TD/GA$ method is utilized (only around the identified objects) to obtain the exact location and dielectric properties of the OI.

3.14.1 Example of reconstructed image using the hybrid MWR/MWT technique

In this example, the effectiveness of the hybrid method of tomography and radar reconstructed method for early breast cancer detection is discussed. Fig. 3.21 illustrates the multi-layer breast phantom used in this research which is considered to consist of skin, normal breast tissue, and malignant tumour tissue. The model includes a $2mm$ thick skin layer, a $11.6cm$ diameter circle for a normal breast, and a $0.9cm$ diameter circular malignant tumour at an off-centered location $(-0.75cm, 0.75cm)$. The data acquisition process in the MWT imaging scenario is quite similar to MWR scan. After the data is collected, the FDTD procedure is utilized with a rough estimate of the imaging area with dielectric properties. The Debye parameters of dielectric properties of skin, breast, and tumour are assumed to be those given in Tab. 3.1. There are 72 receiving antennas positioned at $64cm$ away from the skin. While starting with BGA to find a $0.9cm$ tumour, the investigation domain needs to be divided into 72 patches and to optimize the dielectric properties for all patches, which is a very time consuming process and might not be managed within a reasonable time (Fig. 3.22 (a)). However, after running the MWR technique, the spatial location of the high

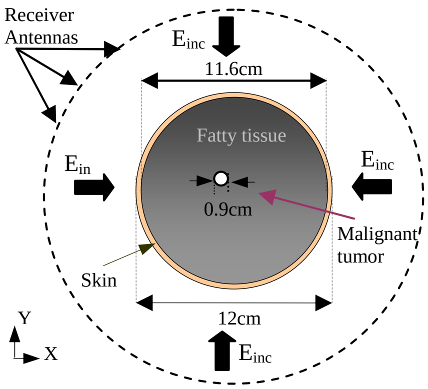

Fig. 3.21: Breast phantom with skin, breast tissue and a malignant tumor at an off-centered location ($-0.75cm$, $0.75cm$) with Debye parameters shown in Tab. 3.1 (top-view).

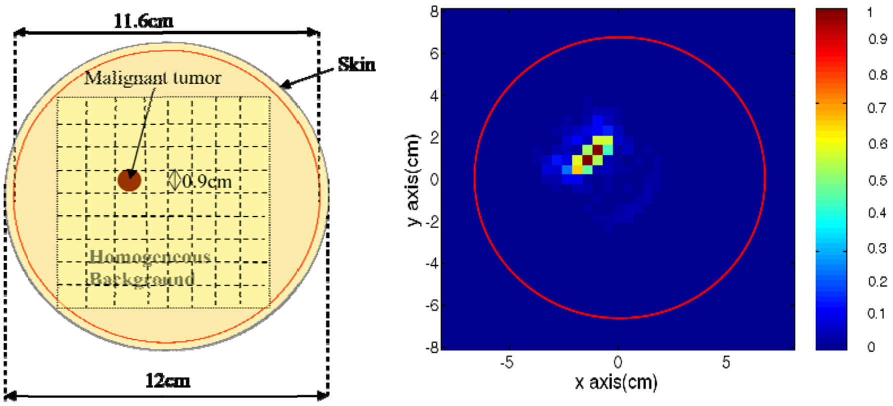

(a) (b)

Fig. 3.22: (a) Discretized the entire breast phantom of Fig. 3.21, and (b) reconstructed image obtained using radar technique.

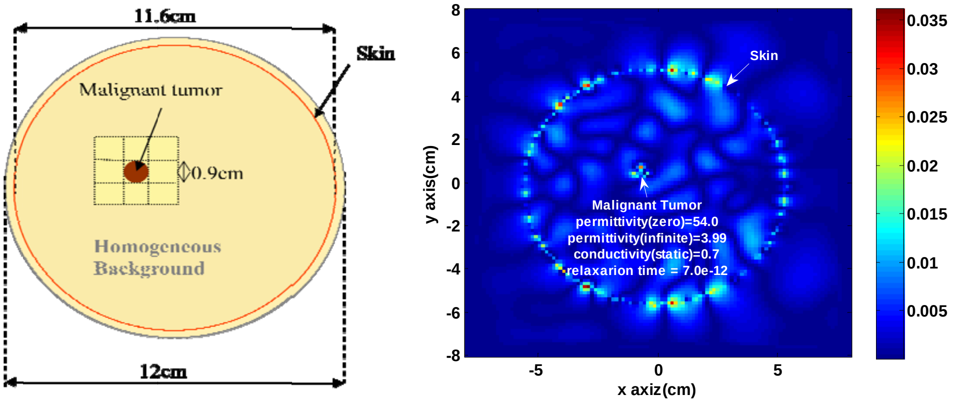

(a) (b)

Fig. 3.23: (a) Discretized the breast phantom of Fig. 3.21 after radar focusing technique, and (b) total field distribution from the reconstructed image of a 0.9cm diameter malignant tumour inside a breast phantom using the FDTD method.

reflectivity region is obtained (Fig. 3.22 (b)). This estimated region will be used to initialize the BGA-based MWT reconstruction technique that will determine a dielectric map of the scan area. The MWT method indeed focuses on a specific area and discretizes it into small patches. Fig. 3.23 (a) shows the discretization of this specific area. The suspicious area is discretized into small patches, and the proposed BGA algorithm optimizes the map of the dielectric properties for respective patches. A BGA optimization program runs for 30 generations, each with a population of 10. Fig. 3.23 (b) shows the total field distribution of the exact locations and dielectric properties of the tumour. The hybrid MWT and MWR can still be considered a work in progress, and further assessments are to be performed.

3.15 Parallel computing

[4] MWT techniques have been investigated for a long time; however, the progress in this field has been slow for a number of reasons - mainly insufficient computer power. In recent years, tremendous research has been done on fast solver computing techniques and has opened up unique opportunities for future research in MWT.

3.15.1 Parallel FDTD (PFDTD)

The major time consuming part of the proposed MWT algorithm is the forward solver which needs to run for several times (depending on the resolution). In order to overcome the runtime problem, we have proposed to employ the parallel algorithm for the FDTD forward solver. The parallelization of FDTD is based on the distributed heartbeat algorithm. This algorithm allows separate processors to compute blocks of the problem space at each time step. The processors then exchange the boundary values to/from adjacent processors using standard MPI technology [178]. The use of MPI allows for the simulation of very large problems by distributing the problem across multiple machines in addition to speeding the execution of the simulation by using more CPUs. More details about the parallel $(FD)^2TD$ solver are provided in Appendix D. To evaluate the efficiency of a 2D $(FD)^2TD$ using MPI, the setup in Fig. 3.24 is used. Fig. 3.24 shows a breast phantom with a $12cm$ diameter region and a $2mm$ thickness of skin and a $1cm$ diameter tumour at an off-center position. The

---

[4] The parallel programming was completed with help of Meilian Xu and Parimala Thulasiraman.

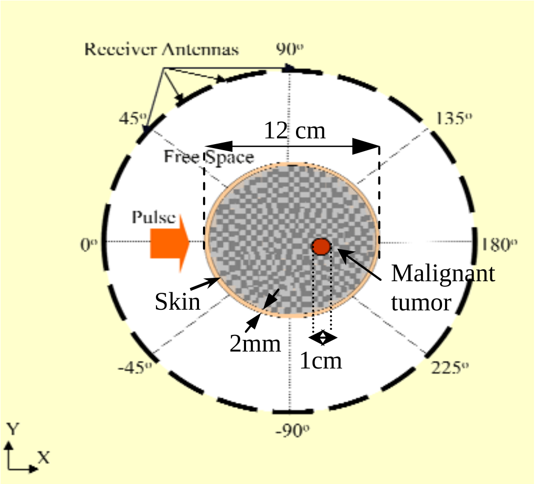

Fig. 3.24: Breast phantom with skin, breast tissue, and $1cm$ diameter malignant.

plane-wave impinges the structure at $\Phi = 0^o$, and receivers collect the scattered fields at different angles in the far-field zone. The efficiency obtained for parallel $(\mathrm{FD})^2\mathrm{TD}$ is portrayed in Fig. 3.25 (a) with a speed-up of 6.25 by 16 processors. As it can be seen in this graph, the computation time decreases when the number of processes increases. The computations were performed on the AMD machines with 8 nodes, and there are two processors in each node. Fig. 3.25 (b) shows the speed-up for the FDTD algorithm when the number of processors increases. This figure shows that the increase in speed-up is not linearly dependent on the number of computers. The greater the number of operating computers, the more communication time is spent. This is called "communication latency".

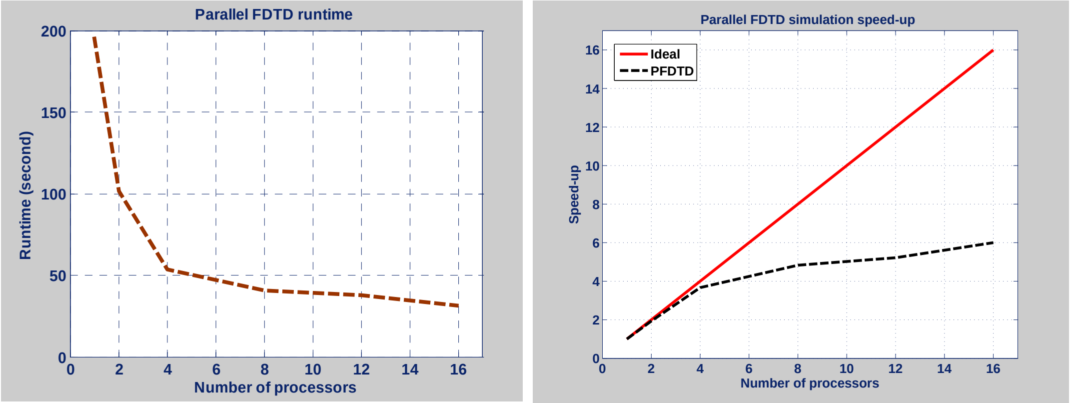

(a) (b)

Fig. 3.25: (a) Parallel $(FD)^2TD$ runtime vs. number of processors, (b) speed-up vs. number of processor for the FDTD algorithm.

3.15.2 Parallel GA (PGA)

In the GA-based reconstruction methods depending on the number of unknown parameters, the size of the reconstruction problem, and the numerical methods used for evaluated fitness-function; the computation time for solution convergence varies from a few hours to several days. Therefore, in order to achieve images with high resolution, the overall runtime can easily become unacceptable using serial implementation. With parallel computations of the GA, we are able to reduce the time required to reconstruct the images. A key advantage of the GA is that at each generation the fitness-function for each individual can be evaluated independently, and hence simultaneously, on a parallel computer system. In the GA optimization, we need sufficient individuals per generation to accelerate the convergence of the algorithm.

The implementation of PGA is based on a master/slave protocol [179]. A schematic

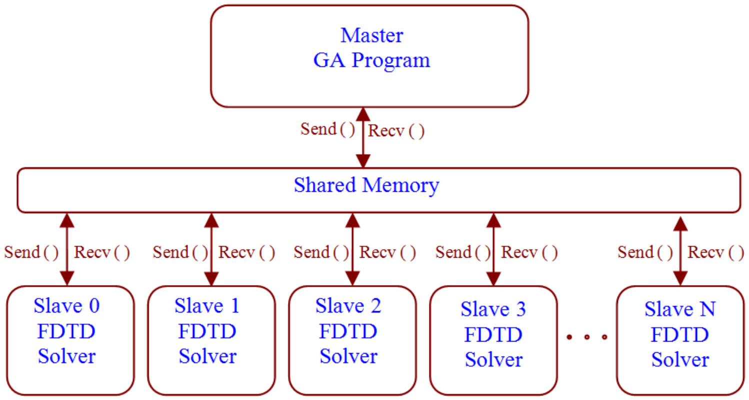

Fig. 3.26: Schematic of parallel GA program.

of a Parallel GA (PGA) is provided in Fig. 3.26. The master processor is dedicated for scheduling and assigning tasks one by one to slave processors. Each slave processor executes the forward problem of the FDTD code for individuals and returns the results of the FDTD codes for all populations in each generation to the master processor, which then performs the GA optimization. Each computer node receives an identical copy of the FDTD program through MPI and runs it independently, using a unique input data set. MPI then orchestrates the gathering of pertinent output data to the master processor, on which the GA is running. In the context of the PGA, this means that the individual fitness evaluations are distributed across the slave nodes, each of which performs the simulation on an individual in the population. Fig. 3.27 shows the runtime of one generation of the GA with a population of 120 for different numbers of processors for the phantom structure illustrated in Fig. 3.24. This graph shows that the computation time decreases when the number of processes increases. From this

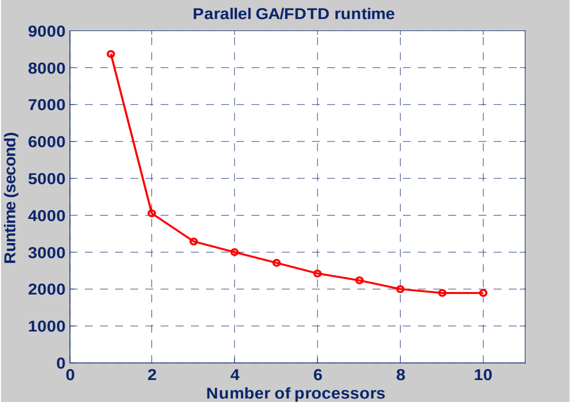

Fig. 3.27: Parallel GA/FDTD runtimes for one generation of GA (120 chromosomes) vs. number of processors for the example of Fig. 3.24.

comparison, one observes that a great deal of computer time has been saved through the parallel computation.

3.15.3 Integrating PGA and PFDTD algorithm

Image reconstruction using the proposed MWT technique involves GA and FDTD. In this section, we integrate parallel versions of these two algorithms. In this type of implementation, a master-slave and MPI parallelization are considered for GA and FDTD, respectively. Parallelizing the optimization part only requires negotiating between master and slave computers and not among master computers. While, in order to parallelize the FDTD forward solver for calculating the fitness-function, we need to negotiate among slaves. Fig. 3.28 illustrates the algorithm for the master and slave processors computing GA and FDTD.

In the PGA/PFDTD method, the master processor stores the initial population (which consists of different combinations of the patch's properties) and applies to the GA operation. The same GA operation parameters - including selection, crossover, mutation, and elitism - as in the serial implementation procedure explained in Section 3.4 is employed in PGA. The PGA master processor sends each individual solution to the PGA slave processors and waits until it receives the fitness values.

The slave processors are used in parallel to evaluate the fitness-function. All PGA slave processors evolve their own subpopulations simultaneously. Each PGA slave processor transmits the profiles to a number of processors which act as the master processor for computing FDTD (PFDTD master processor). They operate in parallel on different profiles. The PFDTD master processor in turn dispatches the calculation to other processors which are called PFDTD slave processors following the procedure explained in Appendix D. The PFDTD master processors are responsible for collecting the final results and communicating with PGA slave processors. The PGA slave processors compare the FDTD calculation results with the measurement results using the fitness-function in (3.17). If the results are not close enough, the computation procedures are repeated. Note that during the entire process, the master computer interrogates the slaves node by using handshake signals to make sure that all slaves are available.

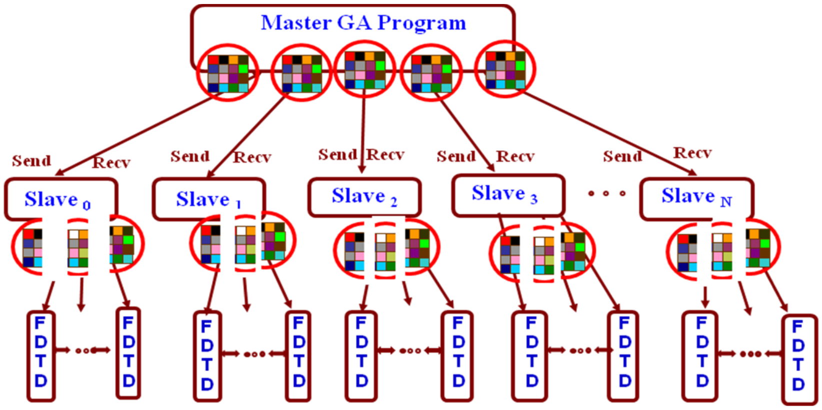

Fig. 3.28: Parallel FDTD/Parallel GA configuration.

3.15.4 Reconstructing a high resolution object using the PFDTD/PGA

In this example, there is a 2D structure of the breast phantom with a $12cm$ diameter and a $2mm$ thickness of skin and a $7.5mm$ diameter square-shaped tumour in the lower right area (Fig. 3.29 (a)). We used the FDTD data as hypothetically measured data, then we started the optimization method without assuming any information about the inside of the cylinder to find out the map of the dielectric properties. Here, in order to find a $7.5mm$ malignant tumour, we must divide the search space into at least 64 cells. Fig. 3.29 (b) shows the GA performance to converge to the right answer. At least 600 iterations are required to achieve the best solution in this example (Fig. 3.29 (a)). The runtime for the serial method in this example is expected to be approximately two months, but, parallel processing reduces the time consumption to two weeks. We unable to calculate the runtime because it requires to run the program on dedicated machine. In addition, we must start with small size patches, since the

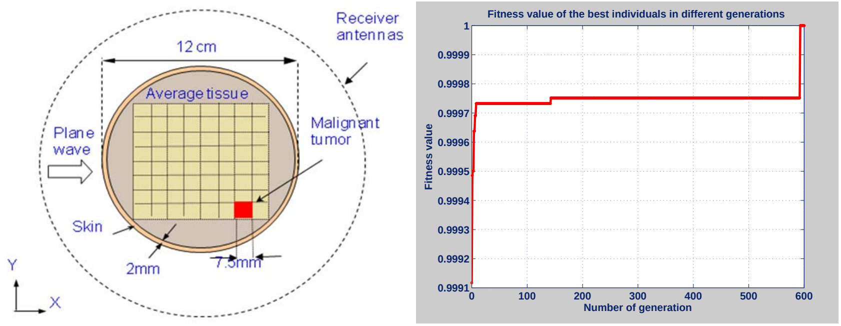

(a) (b)

Fig. 3.29: (a) Numerical breast phantom with a 7.5mm tumour in the lower right area, (b) fitness value of the best individual in different generations.

exact size of the tumour is unknown. In conclusion, the demand for faster simulation enables higher functionality of MWT techniques. The author believes that the fast forward solver and Moore's Law will eventually make this a viable technology for imaging processing.

3.16 Antenna effect on scattered field

So far we assumed that the receiver antennas only detect z-polarized field. However, if the cross-polarization level of the antenna is not negligible, the x and y polarized components of field seriously degrade the resultant images. Therefore, the directivity pattern of the antenna must be taken into account in the inversion solver.

Here, we address the effect of receiver antennas used for collecting the electric field from a 2D dielectric object. In order to do so, first we need to measure the Radar

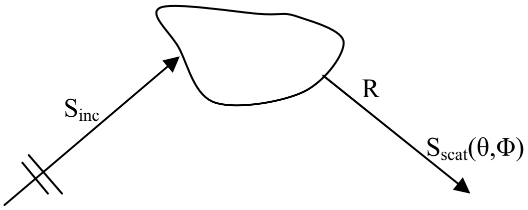

Fig. 3.30: Transmitted and scattered fields in an object.

Cross Section (RCS)[5] of the object. Then, by multiplying the RCS with the incident power, the total power captured by the object can be determined. Then, this captured power should be considered as an isotopic incident power which is scattered around the object. This scattered field is then picked up by the receiver antennas at the observation points. Depending on the frequency, distance of the receiver antenna from the object, and the gain pattern of the antenna, the received power at the observation points might change. Therefore, by using this method, we take the gain pattern of the antennas into consideration for calculating the scattered field. Fig. 3.30 shows the configuration of the transmitted and scattered waves. The scattered field is a function of Φ and θ components in a spherical coordinate. The incident power flux density (S_{inc}) at the object location is given by:

$$S_{inc} = \frac{1}{2}(E_{inc} \times H^*_{inc}) = \frac{|E_{inc}|^2}{2\eta_0} \tag{3.36}$$

---

[5] The RCS is the equivalent area, which when multiplied by the incident power density, and which if it then scatters this power isotropically in all directions, will produce the same incident returned power at the antenna as the target actually does [180].

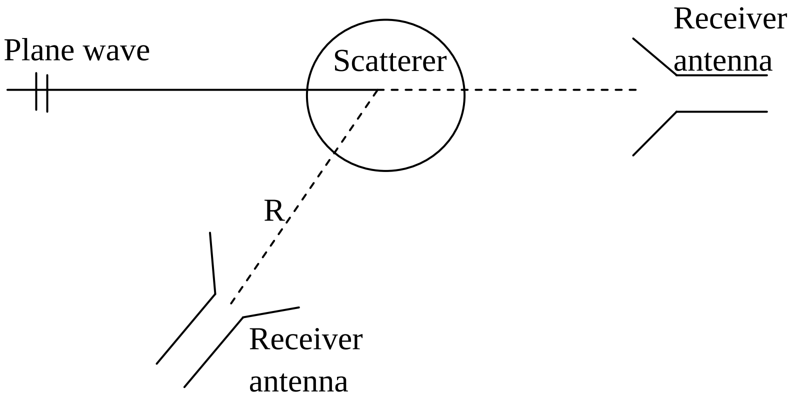

Fig. 3.31: Two receiver antennas around the object for collecting the scattered field.

while the scattered power flux density S_{scat} at a distance R from the object in the direction of θ and Φ is given by:

$$S_{scat} = \frac{1}{2}(E_{scat} \times H^*_{scat}) = \frac{|E_{scat}|^2}{2\eta_0} \tag{3.37}$$

where η_0 is the impedance of free space. Our interest is to calculate the electric field at the antenna's location around the object. After calculating the RCS for the object, the captured power P_c at the object location is obtained by multiplying the incident power density by the RCS. If we assume the received power at the input of the object is P_t, then the power captured by the object at its terminal (P_c) is equal to RCS multiplied by P_t, and this captured power is considered to radiate isotropically. The scattered power density can be written as:

$$W_s = \frac{P_c}{4\pi R^2} = \frac{P_t \cdot RCS}{4\pi R^2} \tag{3.38}$$

The amount of power delivered to the receiver antenna is given by:

$$P_r = A_r \cdot W_s = A_r \frac{P_t \cdot RCS}{4\pi R^2} \tag{3.39}$$

where A_r is the effective area of the receiving antenna as defined by:

$$A_r = G(\theta, \Phi) \frac{\lambda^2}{4\pi} \tag{3.40}$$

where $G(\theta, \Phi)$ is the gain of the antenna at different angles at λ wavelength. To use the above formula, it is assumed that the antenna is situated in the far-field zone, therefore $R \geq 2D^2/\lambda$ where the D is the largest dimension of the receiver antenna. Equation (3.39) can be written as the ratio of the received power to the input power:

$$\frac{P_r}{P_t} = A_r \frac{RCS}{4\pi R^2} = G(\theta, \Phi) \frac{\lambda^2}{4\pi} \frac{RCS}{4\pi R^2} = RCS \cdot G(\theta, \Phi) (\frac{\lambda}{4\pi R})^2 \tag{3.41}$$

Expression (3.41) shows the received power is a function of the input power and gain of the receiving antenna. However, it does not include reflection losses due to mismatching and polarization losses. If these two losses are also included, then (3.41) must be expressed as [180]:

$$\frac{P_r}{P_t} = RCS(1 - (|\mu_r|)^2) G(\Phi) (\frac{\lambda}{4\pi R})^2 \times |\hat{\rho}_w \cdot \hat{\rho}_r|^2 \tag{3.42}$$

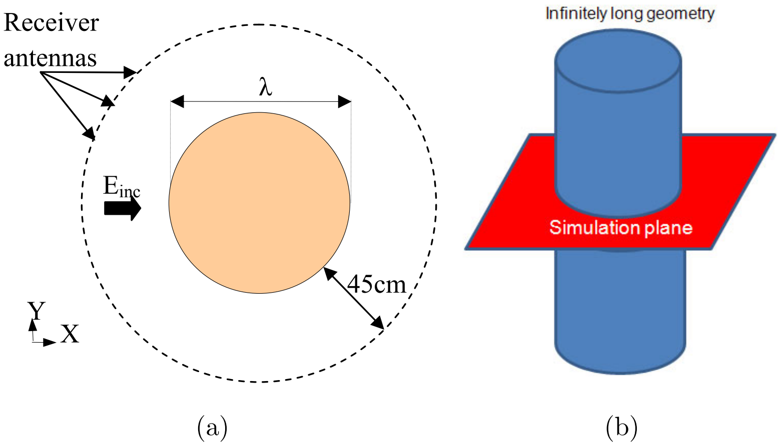

Fig. 3.32: The cross-section of the dielectric cylinder (a) 2D, and (b) 3D.

where ρ_w is the polarization unit vector of the scattered waves and ρ_r is the polarization unit vector of the receiving antenna. In this section, it is assumed that the power input delivered to the object is 1 ($P_t = 1$), the antenna is matched ($\mu_r = 0.0$), and the polarization-matched antenna is aligned for maximum directional radiation and reception ($|\hat{\rho}_w.\hat{\rho}_r|^2 = 1$). For the next part of this section, we simulated different types of antennas such as dipole, circular horn, and microstrip patch antennas around the dielectric object and calculated the scattered field at the observation points. We also considered the 2D pattern of the antenna in the x-y plane. In order to avoid the mutual coupling between antennas, it was assumed only one antenna rotates around the object and collects the scattered field. In all the examples in this section, we considered the dielectric homogeneous circular cylinder as an object of interest (scatterer). Fig. 3.32 illustrates the 2D of dielectric cylindered with dielectric constant of 55, conductivity of $1.23 S/m$, and diameter of λ. We have utilized the FDTD

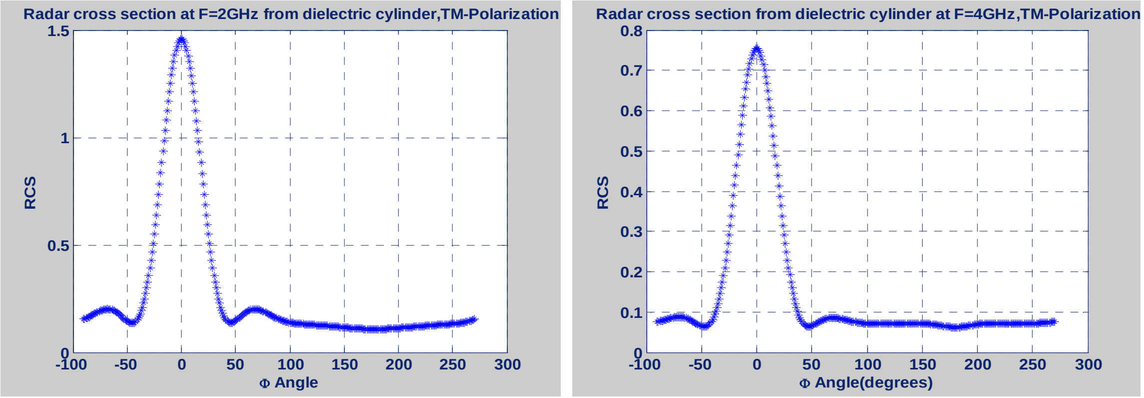

(a) (b)

Fig. 3.33: RCS of the dielectric cylinder at (a) 2GHz, and (b) 4GHz.

method for calculating the RCS. Fig. 3.33 shows the RCS for the 2D dielectric circular at 2 and 4GHz.

3.16.1 Dipole antenna

In the first example, we used a dipole antenna at the observation points. Fig. 3.34 (a) depicts the geometry of a dipole antenna with a length of $1cm$ and a diameter of $1mm$. The dipole is excited using a probe feed from the middle. The dipole antenna has been analyzed using the MININEC software [181]. The antenna lies in the x-y plane and is placed at the far-field zone that is $22.5cm$ away from the center of the object. Fig. 3.34 (b) shows the maximum directivity of the dipole antenna at different frequencies. From the figure, it is observed that as the frequency changes, the directivity pattern also changes. Fig. 3.35 (a) shows the configuration and directivity pattern of the dipole antennas around the dielectric object at 1GHz. Fig. 3.35 (b) shows that if

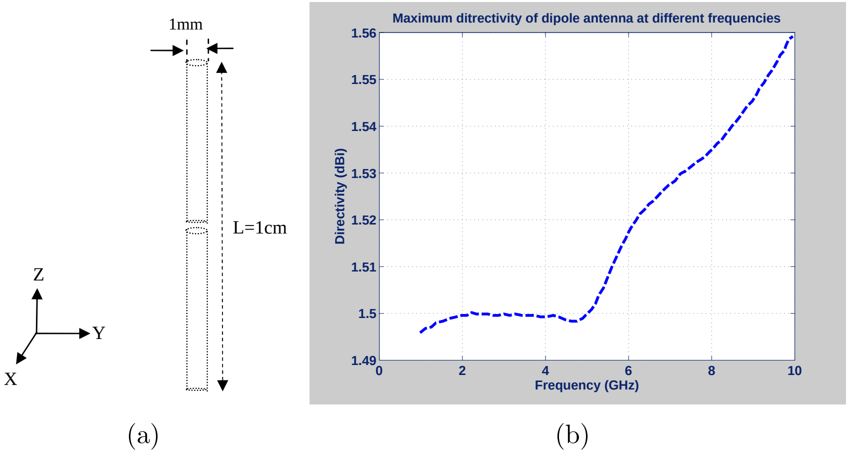

(a) (b)

Fig. 3.34: (a) Configuration of dipole antenna, and (b) directivity of the dipole antenna at different frequencies.

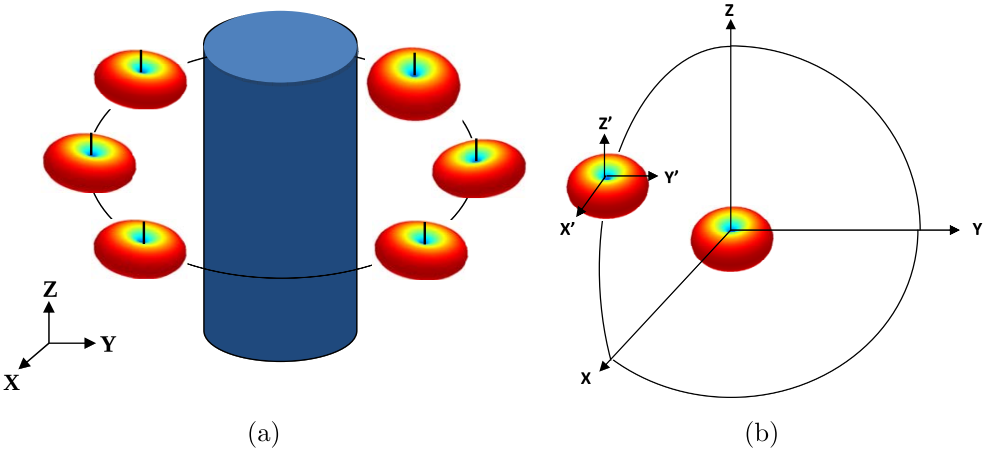

(a) (b)

Fig. 3.35: (a) Dielectric cylinder surrounded with dipole receiver antennas, (b) directivity pattern of the dipole antenna at different location.

the dipole antenna is placed at the observation point on a circle around the object, the radiation pattern for each antenna at the constant frequency is the same but the coordinate system for each antenna is different. In other words, the radiation pattern for the antenna that is located at $\Phi = 0^o$, has the maximum pattern at $\Phi = 0^o$, but for the antenna that is located at $\Phi = 45^o$, the maximum pattern is at $\Phi = 45^o$ with respect to the object coordinate (x, y, z). Therefore, we need to know the position of each antenna in order to map the antenna coordinate to the object coordinate. Fig. 3.36 shows the RCS and the directivity pattern of the dipole antenna at $\Phi = 0^o$ and $\Phi = 135^o$ at 2GHz. In this simulation, we avoided the back side-lobe of the antenna and only considered the pattern between $-90^o < \Phi < 90^o$. At $\Phi = 0^o$ the antenna and object have the same coordinate and mapping of the coordinate does not take place. But for the antenna at $\Phi = 135^o$, we need to map the antenna coordinate to the object coordinate. Fig. 3.37 shows the received power at 2GHz for the antenna located at $\Phi = 0^o$ and $\Phi = 135^o$. As expected, when the RCS has a maximum at $\Phi = 0^o$, the antenna located at $\Phi = 0^o$ receives a strong signal. On the other hand, when the antenna is placed at $\Phi = 135^o$, where the main lobe of the antenna is not the same main lobe of scattered field, it receives a small amount of scattered field.

3.16.2 Circular horn antenna

For the second example, we utilized a conical horn antenna in order to measure the field from the same dielectric circular cylinder as the previous example. The configuration

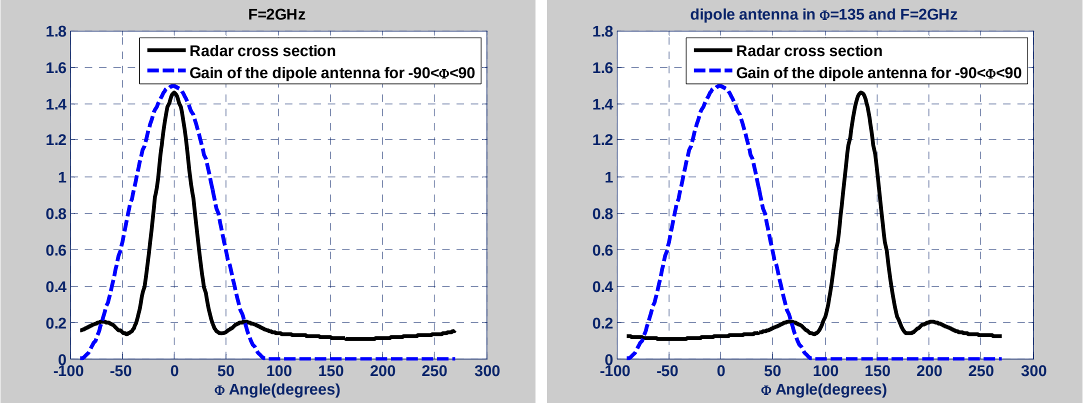

(a) (b)

Fig. 3.36: Comparison of RCS and directivity pattern of the dipole antenna at two different positions (a) $\Phi = 0^o$, and (b) $\Phi = 135^o$.

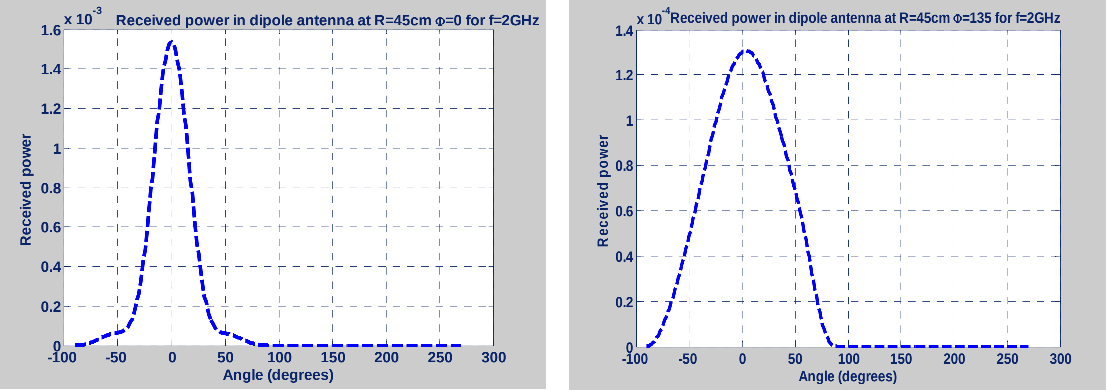

(a) (b)

Fig. 3.37: Received power for dipole antenna at (a) $\Phi = 0^o$, and (b) $\Phi = 135^o$.

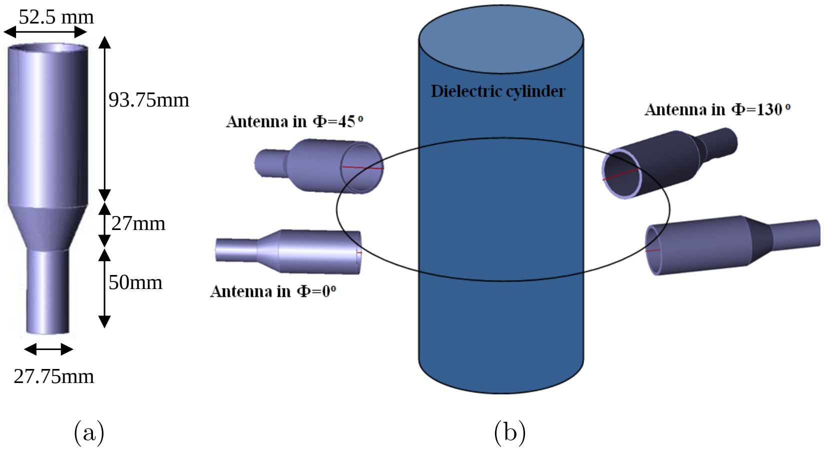

Fig. 3.38: (a) Conical horn antenna, (b) dielectric cylinder with conical horn receiver antennas around the cylinder.

of the horn antenna is illustrated in Fig. 3.38 (a). For simulating this antenna, the GEMS software based on the FDTD method has been used [182]. The radiation pattern and directivity of the horn antenna are shown in Fig. 3.39. Advantages of this type of antenna are high directivity and a low side-lobe level. As can be seen in Fig. 3.39, the back lobe level of the directivity pattern is almost zero. Fig. 3.38 (b) shows the 3D configuration of the dielectric cylinder with circular horn antennas located on the circle around the cylinder. In order to measure the field of the dielectric cylinder at the observation points, we repeat all steps of the previous example. Fig. 3.40 shows the received power as a function of angle at 10 and 15GHz. By comparing the amplitude of both Fig. 3.40 (a) and (b), one can observe that due to the higher directivity of the receiver antenna at 15GHz frequency, the amplitude of the signal has been amplified by the directivity of the receiver antenna. Therefore, depending

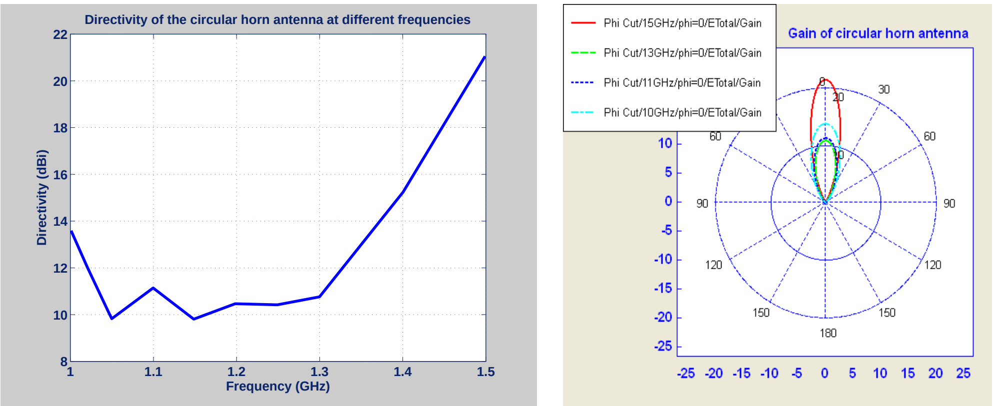

(a) (b)

Fig. 3.39: Directivity of the conical horn antenna at different frequencies (a) rectangular pattern, and (b) polar pattern.

on the application, if the scattered field is weak, we must use the antenna with higher directivity. In addition, the pattern of the horn antenna is very directive, so by using this type of antenna in an array, the mutual coupling between the antennas will be very low. The disadvantage of this antenna is the dependency of the directivity on the frequency.

3.16.3 Microstrip patch antenna

The third example for this study uses the square microstrip patch antenna, which has a side length of $20mm$ and is etched on a dielectric substrate with a thickness of $1.57mm$ and a relative permittivity of 2.33 (Fig. 3.41). A coaxial probe is used to feed the antenna. The microstrip patch antenna has been simulated using the Ansoft Designer Software ver. 2.0. The microstrip antenna resonances at at 4.64GHz frequency, and the feed probe is $3mm$ from its center. The reflection coefficient of the

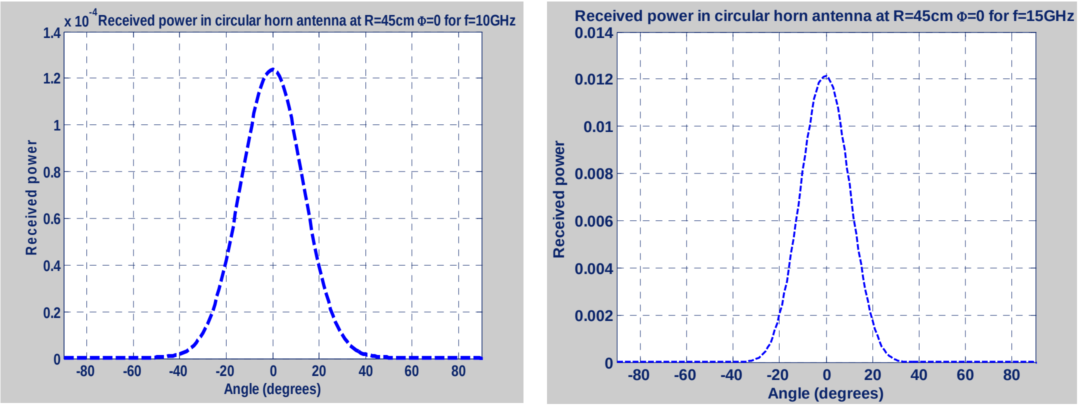

(a) (b)

Fig. 3.40: Received power with circular horn antenna at the same position and different frequency (a) 10GHz, and (b) 15GHz.

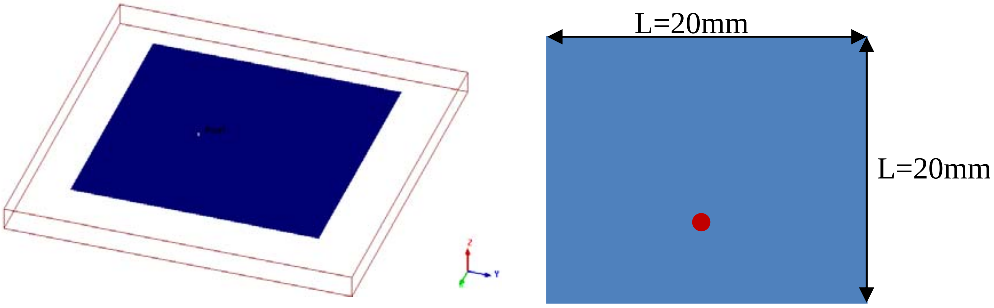

(a) (b)

Fig. 3.41: Microstrip patch antenna structure, (a) 3D, and (b) 2D.

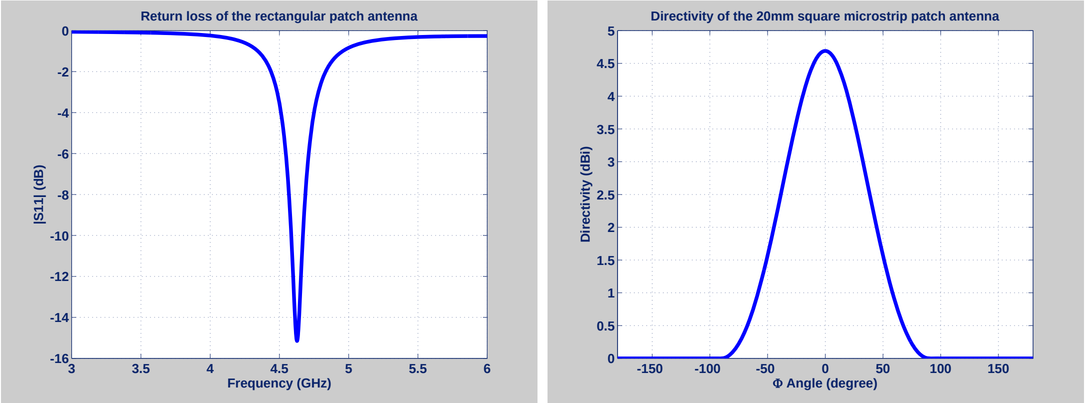

(a) (b)

Fig. 3.42: (a) S_{11} of rectangular microstrip patch antenna in free space, (b) directivity of misrostrip patch antenna at different angles at resonance frequency.

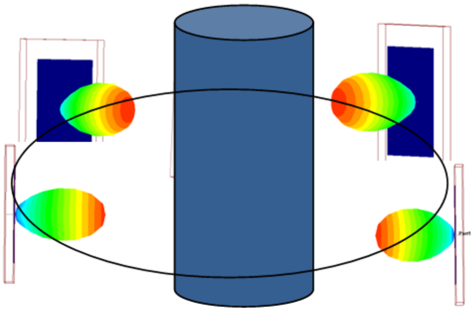

Fig. 3.43: Dielectric cylinder with microstrip patch receiver antennas around it.

antenna with respect to the frequency and the directivity versus different angles in the x-y plane are illustrated in Fig. 3.42. In this example, the microstrip patch antenna was used as a receiver antenna in order to collect the scattered field of the dielectric cylinder shown in Fig. 3.32. The same procedure used in the two previous examples is repeated for this type of antenna. The 3D configuration for these antennas located in the far-field zone with their antenna directivity pattern is illustrated in Fig. 3.43. Fig.

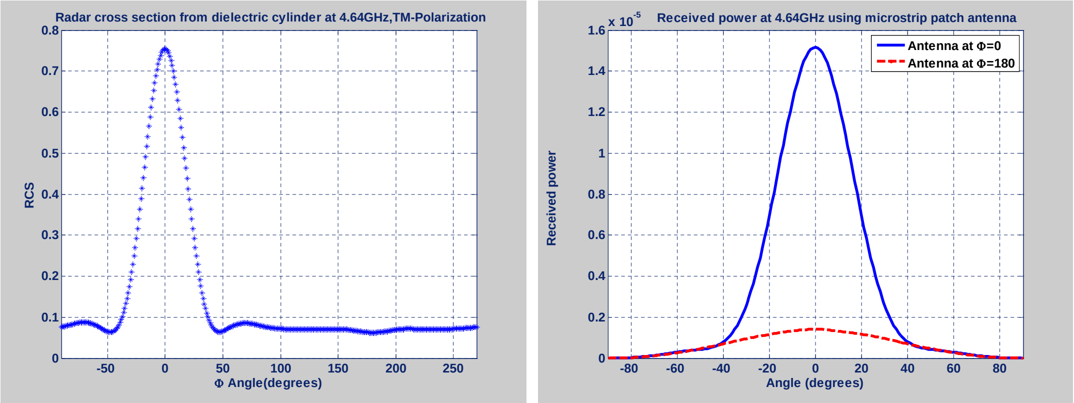

(a) (b)

Fig. 3.44: (a) RCS of the dielectric cylinder at 4.64GHz, (b) received power for antenna at $\Phi = 0^o$ and $\Phi = 180^o$.

3.44 (a) shows the RCS pattern of the dielectric cylinder at the resonance frequency of the microstrip antenna (4.64GHz). The amplitude of the received power by the microstrip antenna located at $\Phi = 0^o$ and 180^o at different angles is shown in Fig. 3.44 (b). Moreover, the scattered field received by the antenna at the $\Phi = 0^o$ has a high amplitude compared to the antenna located at the back of the object at $\Phi = 180^o$. To summarize, the directivity pattern of the antenna needs to be included in the program and the proposed MWT technique has the capability to substitute the antenna pattern in the program and accurately calculate the scattered field. While including the directivity patterns of the receiver antenna is feasible, it needs substantial additional work that is beyond the scope of this thesis and we did not include them into the inverse algorithm.

4. MICROWAVE TOMOGRAPHY FOR BREAST CANCER DETECTION

> *Every woman needs to know the facts. And the fact is, when it comes to breast cancer, every woman is at risk.*
> Debbie Wasserman Schultz

This chapter introduces the breast cancer imaging modalities and in particular an emerging technology for breast cancer detection which is called "microwave imaging". This application has been selected because of the dispersive as well as heterogeneous characteristics of the object of interest (breast) for evaluating the proposed imaging technique. Microwave imaging has the potential to exploit the translucent nature of the breast and obtain maps of the dielectric properties of the breast. We are attempting to examine the performance of the proposed technique using anatomically accurate breast models. 2D MRI derived breast models with varying levels of dielectric heterogeneity are utilized to evaluate the proposed technique. Before utilizing the proposed MWT technique for breast cancer detection, we briefly introduce the rational for breast cancer detection and discuss a range of the topics related to MWI that illustrate the importance of this work and summarize related previous work.

4.1 Rationale

According to the American Cancer Society (ACS) [183], breast cancer is a leading cause of death among women in North America, next only to lung cancer. In 2009, an estimated 40,610 (40,170 women, 440 men) people died from breast cancer. Excluding cancers of the skin, breast cancer is the most common cancer diagnosed among U.S. women, accounting for more than one in four cancers. One out of eight American women who live to be 85 years of age will develop breast cancer, a risk that was one out of 14 in 1960. In the United States, breast cancer is newly diagnosed every three minutes, and a woman will die from breast cancer every 13 minutes. Breast cancer is also the most invasive cancer among women in the U.S., accounting for nearly one out of every three cancers diagnosed. Therefore by detecting breast cancer in its early stages, it can be identified and treated before it spreads and becomes potentially lethal.

4.2 MWI for breast cancer screening

In recent years MWI has attracted significant interest for biomedical applications. This is due to the fact that the microwave signals are able to transmit through and be absorbed and reflected by biological tissues. The basic motivation for MWI is improved physiologic and pathophysiologic correlation with the presence of cancer, especially in soft tissue. This expectation arises from molecular-(dielectric) rather than atomic-(density) based interactions of the microwave radiation with the target when compared with X-radiation (X-ray) imaging.

These factors make microwaves suitable to be used for diagnosis in medicine, especially for the imaging of the biological structures which depend on the tissue's dielectric properties. For example, for breast cancer imaging, when the breast tissue is exposed to microwaves, the high-water content of malignant breast tissues causes scattering that is significantly stronger than that for normal fatty breast tissues that have a low-water content. The concept of MWI is the same basic physical principle as Computed Tomography (CT) or ultrasound tomographic techniques, but it probes for information using energy in the microwave region of the electromagnetic spectrum. This technique uses microwave radiation with frequencies ranging from the high-MHz to low-GHz frequency range. Therefore, the longer wavelengths of microwave radiation makes it more susceptible to higher-order interaction with malignant cells and causes multiple time refraction through and diffraction around the other tissues and does not follow the simple linear optics approximation that is made in X-ray based tomography imaging.

Microwave breast imaging techniques can be divided into three main categories: passive, hybrid, and active methods [184]. Passive methods, such as microwave radiometry, take advantage of the temperature difference between normal tissue and cancer tissue [185]. The hybrid method makes use of microwave illumination to selectively heat and then map parameter changes like pressure to the proper tissue. Different heating and expansion characteristics of the tumour relative to the host medium are the principle factors behind this method [186]. In active imaging approaches, transmitters illuminate the region of interest, and the resulting scattered fields are measured to locate the tumour as well as to map the internal structure of the breast tissue in terms of its electrical parameters. This active MWI is of our particular interest in this thesis.

4.2.1 Active MWI for breast cancer screening

In active MWI, the microwave signals penetrate into the body, and structural and functional information of the tissues is extracted from the scattered and reflected signals. Although the heterogeneous nature of the breast complicates the imaging, the high contrast of electrical properties between tumor and normal tissue makes active MWI a promising method for tumour detection. The potential benefits of using active MWI for breast cancer detection are:

- its non-ionizing radiation (ionizing radiation can directly damage DeoxyriboNucleic Acid (DNA) and cellular molecules and eventually cause cancer);
- its low illumination power levels (having a low health risk, the level of the microwave field used in imaging procedures will be comparable to the level of the microwave field used in cell phones at the same GHz portion of the EM

spectrum);

- its non-invasive nature;
- its less cumbersome nature;
- its availability at the bedside of patients;
- its user-friendly operation (while great care should be exercised when using X-rays);
- its relatively low cost;
- its ability to provide greater patient comfort because there is no need for breast compression (required for mammographic imaging).

From the point of view of safety, the only concern about MWI is related to the heating effects of this type of radiation. Zastrow *et al.* [187] investigated the absorption of short microwave pulses in anatomically realistic numerical breast phantoms in an effort to formally evaluate the safety of UWB microwave breast cancer detection technology. They found that a typical UWB imaging system poses no health risk to the patient. From a practical point of view, designing the equipment might be difficult, and the 3D MWT may require a very long data acquisition time. In spite of this, the MWI technique is feasible and preferable for breast cancer screening, and it remains a research interest for diagnostic medicine. Three approaches for using active MWI for breast cancer detection are currently under investigation: UWB Microwave Radar (MWR) Imaging, Microwave Tomography (MWT), and hybrid imaging techniques.

4.2.2 UWB microwave radar imaging

In this approach, the breast is illuminated with a UWB frequency signal from a transmitter antenna [184]. Backscattered signals are recorded over a UWB frequency range by the same (mono-static [21, 41, 188]) or different (bi-static or multi-static [46, 189, 190]) antennas, to determine the presence and location of significant dielectric scatterers, which may be representative of cancerous tissue within the breast. This scattered field must be focused in order to properly visualize the target [21, 40–46]. The radar method cannot predict the type of tissue, but it has the advantages of not needing complex inversion techniques and of having a fast image reconstruction. Interest in UWB technology started during the 1980s, when it was anticipated that UWB radars could detect small-sized targets better than conventional narrow-band radars. Two specific configurations of antenna array that are currently being used by researchers for UWB breast cancer detection are planar and circular configurations. The planar configuration involves placing a conformal array of antennas on the naturally flattened breast with the patient is lying in the supine (planar) position. Hagness *et al.* first introduced a UWB radar imaging technique for breast cancer detection and used this antenna configuration with resistively loaded bow-tie antenna [40]. The planer antenna configuration is also used by other researchers [28, 42, 189, 191].

On the other hand, the circular configuration involves the patient is lying in the prone (circular) position, with the breast surrounded by a circular array of antennas. Fear *et al.* [21, 184] developed the Tissue Sensing Adaptive Radar (TSAR) system using a cylindrical configuration of resistively loaded dipoles. Other researchers have used the same antenna configuration [44, 46, 192–196]. A comparison of these two configurations shows that the circular antenna configuration is much more effective in terms of tumour localization as well as more robust to natural variations in dielectric heterogeneity [197].

In UWB radar imaging, which ignores the high-order of interactions and uses the linearized assumption about wave propagation, only the qualitative images can be generated. This technique has been shown to be successful in many experiments using simple simulated breast models [41, 192, 198, 199]. In [48, 200] the authors have developed a UWB microwave radar system for breast imaging, with promising initial clinical results. However, in a clinical situation it may be hard to diagnose a tumour since the radar method provides qualitative images. The solution to this problem is to use statistical methods to confirm the results [201]. In the radar-based technique, when the microwave signal impinges the breast, due to the high contrast between the skin and the outer layer (free space), the reflected field is strong. In order to remove the input signal and reflection from the skin-breast interface, in [201] the breast model was first measured without a tumour and then the field in presence of breast was subtracted channel by channel from the field in the presence of tumour. In reality, however, this situation is impossible, because the breast tissue distribution is different from person to person and even different for left and right breasts for the same person. It is impossible to find two identical breasts in order to use one as a reference a tumour. In a study at the University of Bistrol, Dr. Craddock stated, *"We've seen about 65 patients so far and I think it would be fair to say that no two women have been the same shape or size"* [202]. In addition, recent studies demonstrated the range of properties of healthy tissues and indicated small differences between glandular tissue and malignancies (see Section 4.4). This low contrast between healthy glandular tissues and a tumour creates a small reflection field which will be dominant with high reflection from complex distribution of dielectric properties as well as significant reflection from the skin. To do this, sensitive microwave measurement equipment is required. Thus, these methods, in their current state of development, may not be appropriate for breast cancer detection. The method of MWI based on the radar approach is not discussed in this thesis, but an adequate review of this technique was published in 2005 [198].

4.2.3 Microwave tomography imaging

The second approach to active microwave imaging is MWT. In this imaging method, the patient lies in the prone position and the transmitter and receiver antennas are located around the breast (Fig. 4.1). A transmitter antenna is fixed at the specific radius from the breast and transmits a signal; the scattered field is collected by receiver antennas around the breast at a specific radius while they are at the same plane of transmitter antenna. While a realistic model of the numerical breast phantom should be 3D, 2D models are quite prevalent mainly due to their simplicity [16, 159]. By putting 2D cross-sectional images together one can provide a 3D image (Fig. 4.2 (a)). The antennas collect the scattered field at different cross-sections where the interest is the 3D image. In the case of using matching material, the breast and antennas are immersed in a tank filled with liquid material (for more details about matching material see Section 4.8). With the knowledge of input and recorded signals, the unknown dielectric properties of the breast tissue are determined. This information can be used for tissue density characterization, cancer detection, treatment monitoring, contrast agents, and propagation models. In this approach, the map of the dielectric properties is provided by solving an inverse scattering problem [23, 77, 159, 203]. The only actual clinical system developed based on tomography is by a group at Dartmouth College [22, 204, 205]. This system is operating in the frequency range of 0.3-1GHz. Two dimensional images obtained by the system that consist of 16 monopole antennas located vertically along a circular path with the data acquisition system consisting of 32 channels. The patient lies with the breast pendant through a hole in the examination table and immersed in a tank of saline water. A sinusoidal signal is transmitted from one antenna and recorded by the others, and this procedure is repeated for 12 different frequencies. Multi-slice illuminations of the breast are achieved by raising and lowering the antenna array with a computer-controlled linear actuator. The inverse scattering

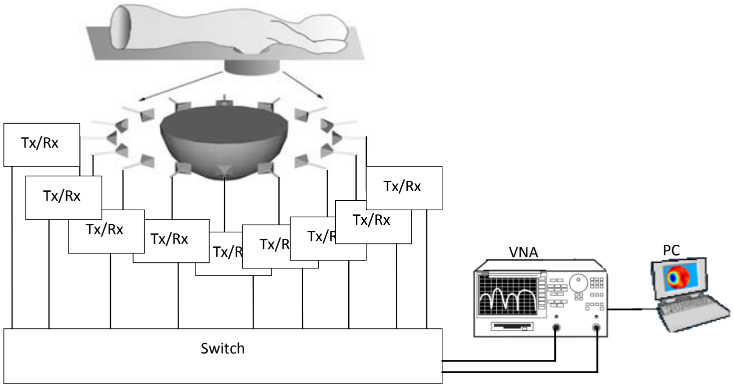

Fig. 4.1: Clinical imaging system configuration for MWT.

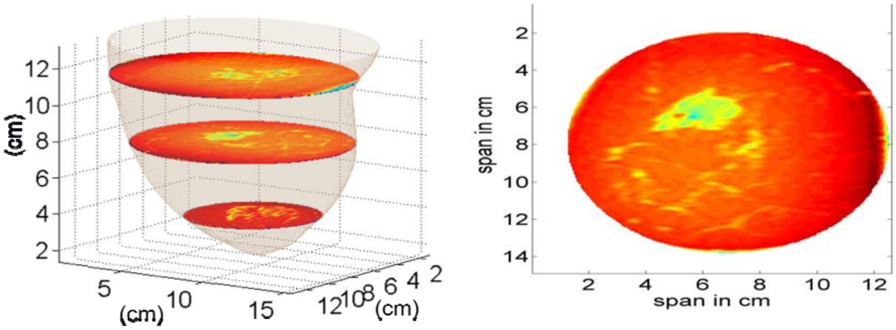

(a) (b)

Fig. 4.2: Map of type of breast tissue (a) 3D image, (b) 2D images (coronal plane).

problem is solved based on finite element and boundary element methods. Results show that this imaging system can detect tissue abnormalities. Rubaek *et al.* recently introduced a computational method based on a similar setup for 3D imaging that uses a single-frequency and 32 dipole antennas [206]. One potential downside of this approach is the need to solve the inverse scattering problem, since the reconstruction methods are computationally intensive and require a long runtime.

The time-reversal algorithm is also considered as an MWT method and recently was utilized for breast cancer detection which is based on time-reversing the FDTD equations. This implies that if a point source radiates and the time-reverse FDTD equations are applied to all points of the grid, the wave will converge back to the source at the time corresponding to the maximum of the initial excitation [207, 208].

4.2.4 Hybrid active MWI

Induced thermo-acoustic imaging is a very promising hybrid technique that combines elements of microwave and ultrasound imaging methods. The breast tissue is irradiated by pulse waves. The energy from the microwaves is absorbed and converted to heat, which slightly raises the temperature of the tissue, causing the tissue to expand in volume. This expansion produces an acoustic wave that propagates outward in all directions from the site of energy absorption. These acoustic (pressure) waves (which are typically ultrasonic) are then detected by an array of transducers and used to reconstruct images [209, 210]. Another hybrid method has been introduced by Zhao *et al.* which combines microwave and acoustic approaches for breast cancer detection [211]. In this method, the hybrid approach applies mechanical excitation to induce tissue-dependent displacements within the heterogeneous breast while low power microwave signals are transmitted into the breast and the scattered microwave signals are measured using an antenna array. This hybrid method takes advantage of both electric and elastic tissue property-contrasts and reveals the potential for enhancing the overall microwave scattering contrast between normal and malignant fibro-glandular tissues.

4.3 Breast topology

The human breast contains different tissue types including the fatty or adipose (small ϵ_r and σ), fibro-glandular or fibro-connective tissues (ducts and lobules, large ϵ_r and σ), benign and malignant (i.e. breast carcinomas), and skin which are contiguous with each other. The fibro-glandular tissues include lobules that produce milk and connective tissue. The benign tissue includes fibroadenoma and mastitis. According to the American Cancer Society [183], among all breast cancer cases in the U.S., Invasive/Infiltrating Ductal Carcinoma (IDC) accounts for roughly 80% of the total. IDC is a breast cancer which is still within fibro-glandular tissue and has spread to surrounding fatty tissue and other parts of the body. If the MWI is going to be used for detecting the tumour in early stages, the cancer needs to be detected while it is growing inside the fibro-glandular tissue, which has similar dielectric properties to cancer. Dection of IDC using MWI is very challanging.

4.4 Electrical properties of the normal and malignant breast tissues

By monitoring the variations of the dielectric properties and comparing them with those for the healthy tissues, one may be able to diagnose abnormalities. This is the basic rationale for microwave medical imaging. From the scattering point of view, the dielectric properties determine the attenuation, reflection, and transmission of microwave signals. In the breast tissues, these properties might be related to other physiological conditions such as temperature, density, molecular constituents, ion concentration, mobility, blood content, blood oxygenation, blood vessel occlusion, myocardial ischemia, and water content [212, 213]. Basically, when the biological tissues undergo physiological changes, such as those due to the presence of diseases, those induced by external stimulations, or even by variations in the environmental temperature, the microscopic processes can deviate from their normal state and impact the overall dielectric properties. Low-water content tissues such as skin and fat have permittivity values that are estimated to be less than half of those of high-water content tissues such as blood and cancerous tissues [214–221].

4.4.1 Ex-vivo dielectric properties of breast tissues

Dielectric properties of biological tissue have been investigated for almost eighty years [214–223]. It has been twenty-six years since Chaudhary *et al.* measured the dielectric properties of healthy and malignant tissues within 3MHz-3GHz [214]. Their studies generated interest in the possibility of using non-ionizing electromagnetic waves to image the breast in order to detect tumours. In 1994, a similar study was repeated by Joins *et al.* [219]. A literature survey by Gabriel *et al.* reports the characterization of breast tissue over the range of 0.01-20GHz also shows the contrast in dielectric

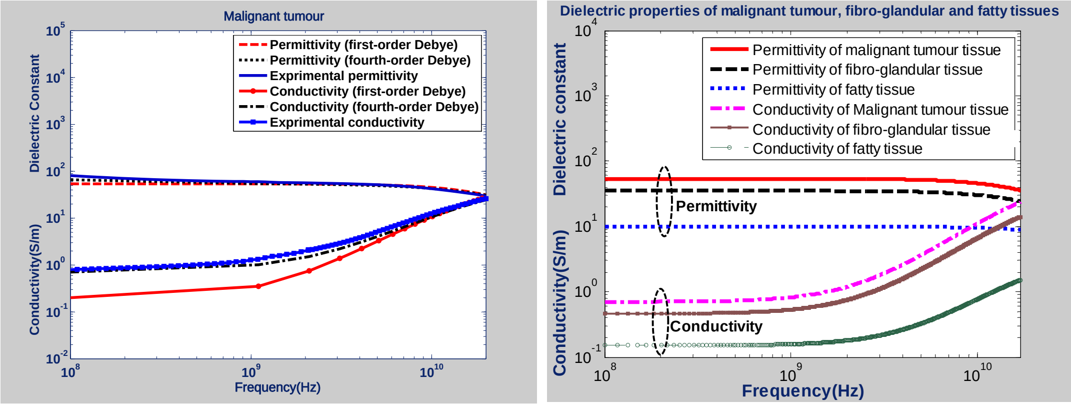

(a) (b)

Fig. 4.3: Frequency variation of electrical properties of (a) malignant tumour [216], (b) malignant, fibro-glandular, and fatty tissues [148].

constant and conductivity between normal tissue and a malignant tumour (Fig. 4.3 (a)) [217, 218]. This report shows that there are significant differences (approx. 10:1) between the dielectric properties of fatty and malignant breast tissues. In 1988, Surowiec *et al.* [224] found that the tissue at the infiltrating edge of the tumour had increased dielectric properties, and even small tumours could still induce significant microwave back scattering. In a paper by Converse *et al.* [148], the available data as well as the approximated values at higher frequencies are summarized, as shown in Fig. 4.3 (b). This figure shows that the electrical property contrast between the normal and malignant breast tissue is more than 3:1. Recent extensive characterization of the dielectric properties of different tissue types, including normal, malignant, and benign breast tissues obtained from woman undergoing breast reduction and cancer surgeries, in the frequency range of 0.5-20GHz, has been performed by Lazebnik *et al.* [220, 221].

This study shows that:

1. The dielectric properties of breast tissues are dispersive, and they change with the water content amount.

2. There is a large variation in the dielectric properties of normal breast tissue due to substantial tissue heterogeneity.

3. The dielectric properties of cancerous tissue are consistently 40-50% larger than the dielectric properties of normal adipose tissue, when measured at 5GHz. On the other hand, the dielectric properties of cancerous tissue are no more than 10% larger than those of normal glandular/fibro-connective tissue. The median dielectric properties at other frequencies for the other tissue types exhibit a similar trend to their behaviour at 5GHz.

4. The dielectric properties are independent of the location of measurement and age of the patient.

5. The dielectric properties' variability between breasts is not larger than the variability between samples; however, the dielectric properties' variability between patients is larger than the variability between samples.

6. Malignant lesions are typically attached to the glandular tissue rather than adipose tissue.

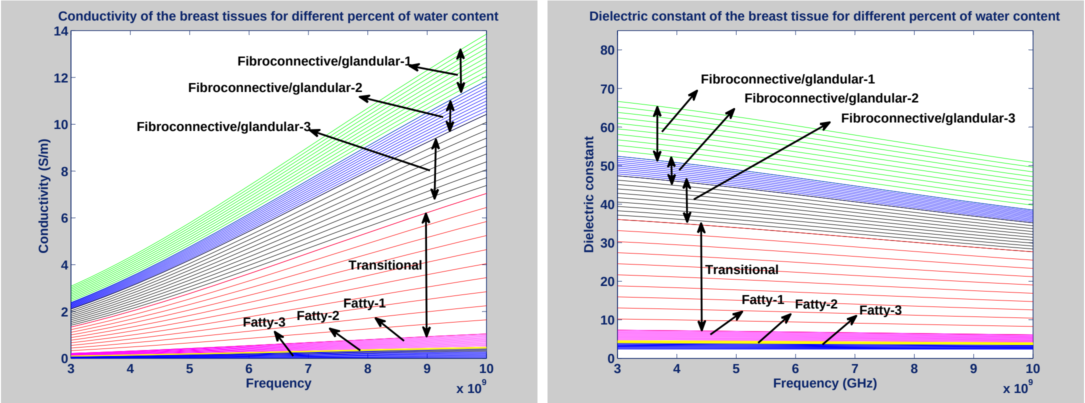

(a) (b)

Fig. 4.4: Debye model of breast tissues dielectric properties (a) conductivity, (b) permittivity.

Fig. 4.4 shows the dielectric properties of different breast tissues having different levels of water content, while the related Debye parameters are specified in Tab. 4.1 for 3-10GHz. The conclusion that can be drawn from these figures is that, for example, in 5GHz the relative permittivity of breast tissues varies between 9.8 and 63. The conductivity of breast tissue also changes between 0.1 and $6.0 S/m$. This study of breast tissue dielectric properties presents a much more difficult than expected imaging problem due to the variation in dielectric properties. Previously, the dielectric heterogeneity of breast tissue was significantly underestimated. Although recent studies show a low contrast between malignant and fibro-glandular tissues, the properties measured by other imaging techniques have even smaller contrast. Mammography, for example, uses X-ray that relies on contrast in density which is less than 2% [34]. For ultrasound, the contrast is less than 10% [34]. For microwave imaging, even a 10% contrast can be large enough to create scattering signals and

Tab. 4.1: Single-pole Debye parameters for breast tissues [225].

Medium	ϵ_∞	ϵ_s	$\sigma(S/m)$	$\tau_0(ps)$
Skin	15.93	39.76	0.83	13.0
Glandular 1	23.20	69.25	1.306	13.0
Glandular 2	14.20	54.69	0.824	13.0
Glandular 3	13.81	49.36	0.738	13.0
Transitional	12.99	37.19	0.397	13.0
Fatty 1	3.987	7.535	0.080	13.0
Fatty 2	3.116	4.708	0.050	13.0
Fatty 3	2.848	3.952	0.005	13.0

potentially detect malignancies.

4.4.2 *In-vivo measurement of dielectric properties of breast tissues*

The MWT method is a non-invasive imaging modality, and it is necessary to know the dielectric properties of the breast tissue at the condition where the temperature and blood pressure are as close as possible to the situation when the imaging is being performed. This means it is necessary to know the dielectric properties of breast tissue when they are functioning inside the body and under the same conditions. Besides a few papers that were recently published to investigate the *in-vivo* tissue properties [226], the majority of the research studies have been based on the *ex-vivo* dielectric properties measurements. In fact, dielectric properties depend strongly on the physiological state of the tissue. Therefore, when the physiological conditions change, the dielectric properties also change. These physiological conditions include temperature, blood content, blood oxygenation, blood vessel occlusion, and water content. Since the physical characteristics change significantly almost immediately following the removal of the tissue from the body, the *ex-vivo* data can cause errors in the resulting images. Meany *et al.* showed that the average relative permittivity value at 900MHz for normal versus malignant tissue was significantly higher than that previously published [226]. This study was based on the *in-vivo* measurements during partial and full mastectomy surgeries. The *in-vivo* measurements were performed during open surgeries using a needle probe. According to this study, when a tissue or organ is devascularized, its electrical properties will change. Since any changes in the temperature and blood pressure can cause changes in the dielectric properties, even the *in-vivo* measurements performed using needle probes can be inaccurate.

In order to study the dependency of dielectric properties on temperature and water content, we have completed different measurements in collaboration with the Pathology department at the Altru Hospital with actual samples from breast cancer surgery. The results of these measurements have been provided in Appendix E.

4.5 Inclusion of the water content dependency of breast tissue in $(FD)^2TD$ forward solver

As explained in Section 4.4, breast tissues can exhibit very low or very high loss at microwave frequencies. These variations depend on the type of tissue and, more precisely, on the water content. In addition, the dielectric properties of breast tissues are also very dispersive in terms of frequency. In this section, inclusion of the dispersive characteristics and water content into the FDTD program will be explained in detail. The frequency dependence of dielectric properties of breast tissues can also be efficiently described in FDTD numerical method by using the single-pole Debye model as described in Chapter 3, equation (3.21). In order to simplify the problem, the breast tissues are divided into seven groups: three different groups of fibro-glandular tissues, three different groups of fatty tissues, and one transitional group (Fig. 4.5). Each group has an upper bound and a lower bound value of dielectric properties, depending on the amount of water content and the frequency. The dielectric properties can be given by:

$$\epsilon(\omega) = p\epsilon_u(\omega) + (1-p)\epsilon_l(\omega) \tag{4.1}$$

$$\sigma(\omega) = p\sigma_u(\omega) + (1-p)\sigma_l(\omega) \tag{4.2}$$

where the parameter p is a coefficient showing the percentage of water content and it can be changed between [0 - 1], ϵ_u and σ_u are the dielectric constant and conductivity at the upper bound, respectively, and ϵ_l and σ_l are the dielectric constant and conductivity at the lower bound of the corresponding group at a specific frequency, respectively. Therefore by substituting equations (4.1 and 4.2) into equation (3.21) the parameters of the Debye model become functions of both water content and the dielectric properties of the lower and upper bounds of each group, and can be defined

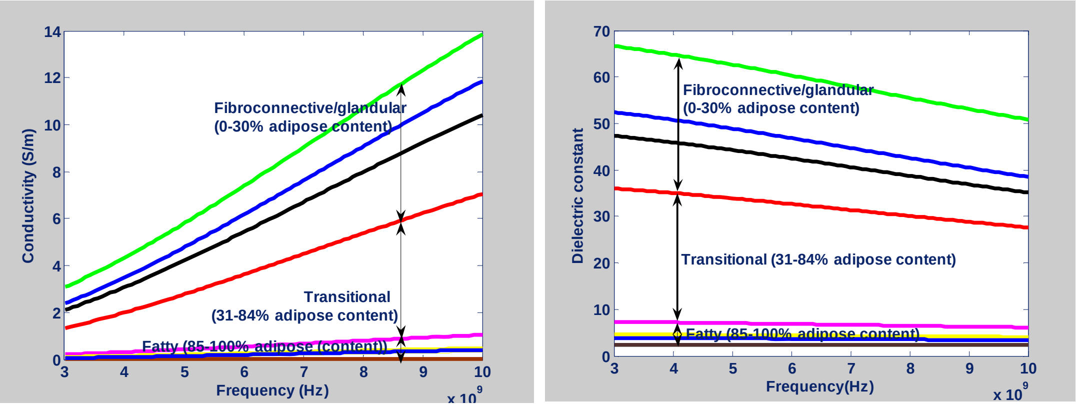

(a) (b)

Fig. 4.5: Dielectric properties of breast tissue (a) conductivity, (b) permittivity.

as:

$$\sigma_s = p\sigma_{su} + \sigma_{sl} - p\sigma_{sl} \tag{4.3}$$

$$\epsilon_\infty = p\epsilon_{\infty u} + \epsilon_{\infty l} - p\epsilon_{\infty l} \tag{4.4}$$

$$\epsilon_s = p\epsilon_{su} + \epsilon_{sl} - p\epsilon_{sl} \tag{4.5}$$

where σ_{su} and σ_{sl} are conductivity at the upper and lower bounds of the corresponding group, respectively, $\epsilon_{\infty u}$ and $\epsilon_{\infty l}$ are permittivity at infinite frequency for the upper and lower bounds of the corresponding group, and ϵ_{su} and ϵ_{sl} are dielectric constant at zero frequency for the upper and lower bounds of the corresponding group, respectively. The single-pole Debye parameters for the breast tissues are based on the results described by Zastrow *et al.* [225, 227]. At this point, by inserting the new parameters of the Debye model, the water content dependency has been included in $(\text{FD})^2$TD program (see Section 3.10)

4.6 Numerical breast phantom

For simulating the breast, in this thesis, we used a numerical breast phantom. Fig. 4.6 depicts an MRI in 3D and maps of dielectric properties for the spatial distribution of media numbers for different breast phantoms in terms of X-ray mammography descriptors: mostly fatty, scattered fibro-glandular, heterogeneously dense, and very dense. These were derived from a series of T1-weighted MRIs of the patient in a prone position, provided by the University of Wisconsin-Madison [228]. Fig. 4.6 (b), (d), (f), and (h) are comprised of four types of breast phantoms in terms of dielectric properties. Each phantom contains three variations of both fibro-glandular and adipose tissues, as well as transitional tissues. Dimensions within the 3D region of the breast are described according to each axis. The z-axis signifies the depth, and the x and y-axes represent the span and breadth of the breast, respectively. In order to create the dielectric properties map from the MRI, the range of MRI pixel densities in the breast interior have been linearly mapped to the range of the percentage of water content and to tissue type, such as skin, muscle, fatty, fibro-glandular, and transitional, for each voxel. Fig. 4.7 shows the cross-sectional view in the x-y plane of tissue types for different breast phantoms in terms of X-ray descriptors. The color bar in this figure indicates the different tissue types; the red color shows the fatty tissue, the orange color shows the transitional tissue, the yellow color shows the fibro-glandular

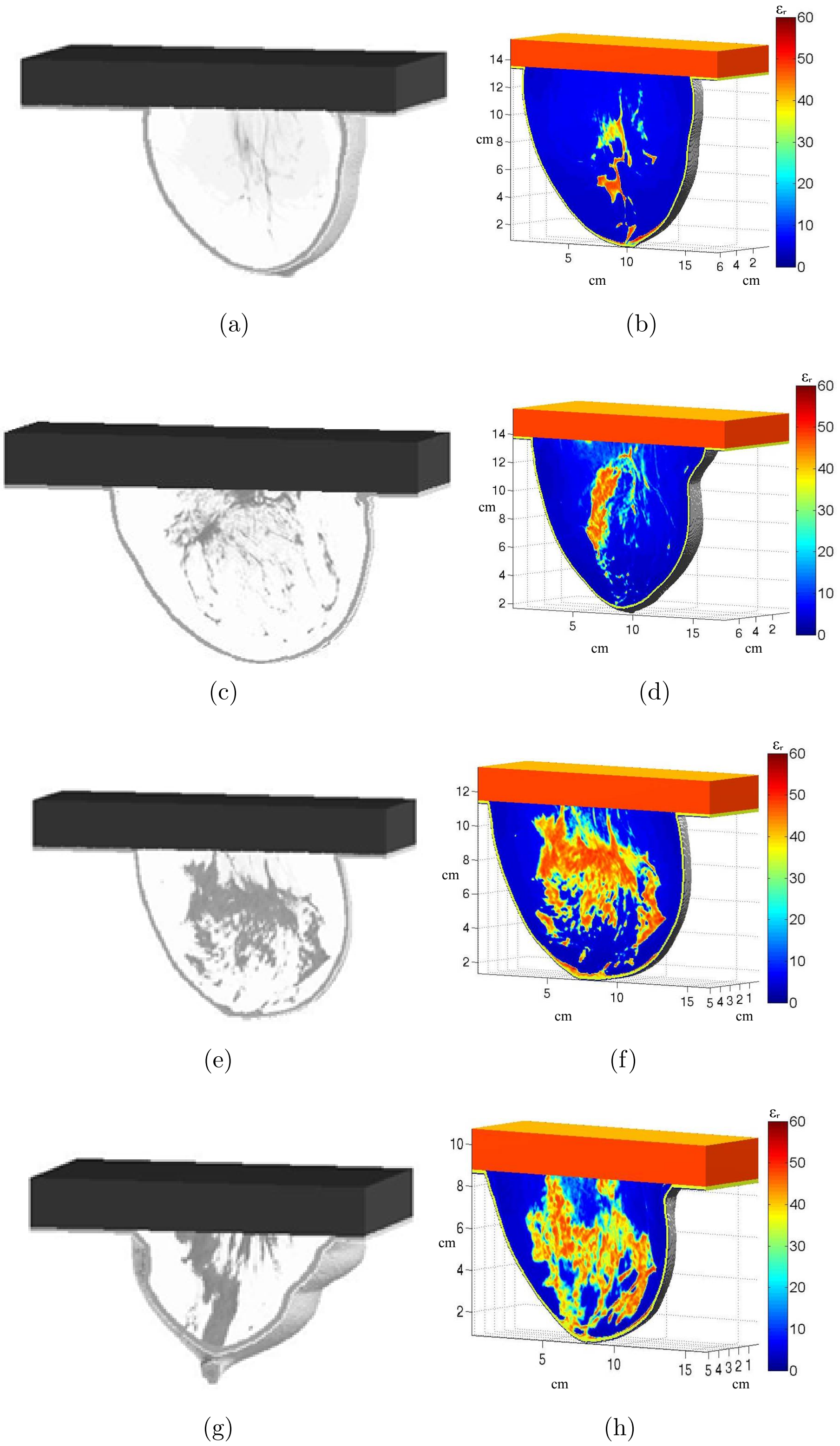

(a) (b)

(c) (d)

(e) (f)

(g) (h)

Fig. 4.6: 3D MRI breast images and 3D map of dielectric properties at 6GHz, mostly fatty: (a) map of density, (b) map of dielectric properties, scattered fibro-glandular: (c) map of density, (d) map of dielectric properties, heterogeneously dense: (e) map of density, (f) map of dielectric properties, very dense: (g) map of density, (h) map of dielectric properties [228].

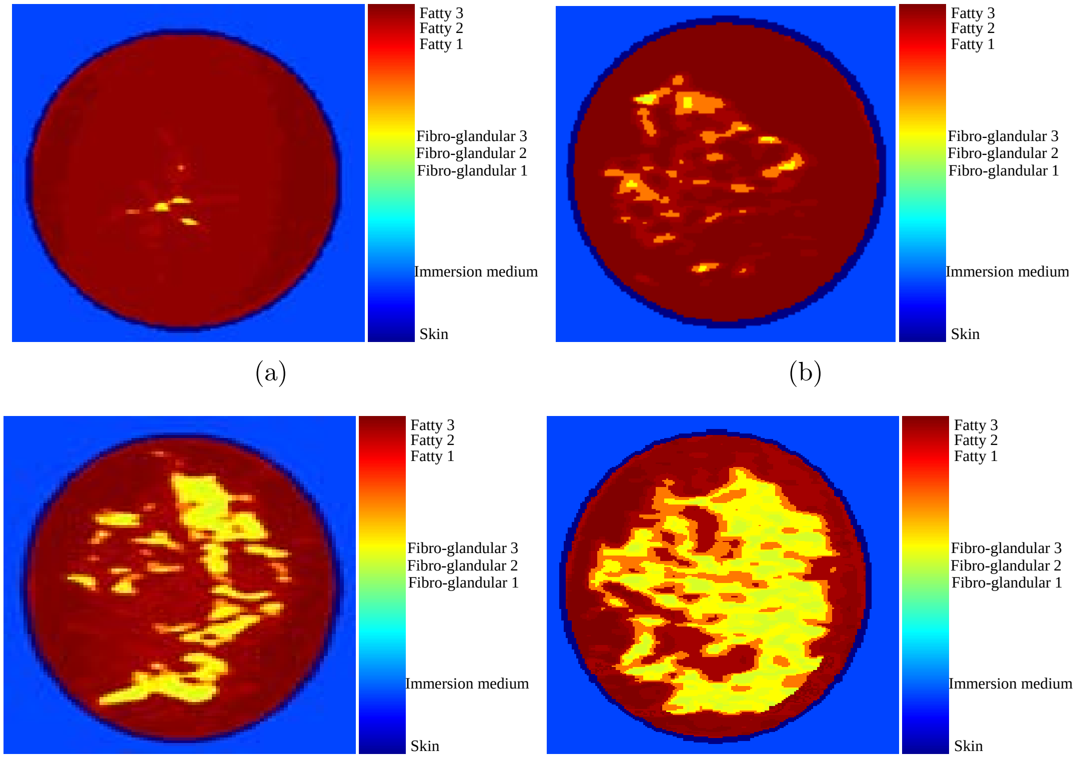

(a) (b)

(c) (d)

Fig. 4.7: 2D sectional views of the different breast phantoms in terms of media type (a) mostly fatty, (b) scattered fibro-glandular, (c) heterogeneously dense, and (d) very dense [228].

tissue, and dark blue represents the skin, while the medium blue color represents the immersion medium. Fig. 4.8 shows the cross-sectional view in the x-y plane in terms of water content for four types of breast phantoms. The color bar illustrates the water content over a pixel range of zero to one. As explained in Section 4.5, fatty and fibro-glandular tissues were divided into three different groups. Therefore, in each group the water content varies within a range of values from zero to one. We used these two pieces of information (type and water content), for each voxel and mapped them to appropriate Debye parameters (see Section 4.5). In order to show the majority of fatty tissue in all types of breast phantoms and how the amount of fibro-glandular tissue changes in these four types of breast tissue, we performed a data analysis. Fig. 4.9 shows the histogram of the permittivity for different numerical breast phantoms at 5GHz. Several observations can be drawn from these graphs. First, as we move from mostly fatty to the very dense breast phantom, the percentage of fatty tissue decreases, and the percentage of fibro-glandular tissue increases. Second, each breast phantom almost covers the entire range of dielectric properties, and furthermore, the distribution of dielectric properties is not uniform.

4.7 Penetration depth

The principal limiting factor in penetration depth of the microwave is attenuation of the electromagnetic wave in the breast tissues. The attenuation predominantly results from the conversion of electromagnetic energy to thermal energy due to the high conductivities of the skin and breast tissue at high frequencies. Fig. 4.10 illustrates that the conductivities of the skin, the fibro-glandular tissue, and the malignant tumour increase by increasing the frequency with a constant amount of water. In this section, we focus on the investigation of the penetration depth of the microwave pulse into the numerical breast phantom, and we compare the scattered fields for each case of Fig. 4.6. The penetration depth is the distance that the propagation wave will travel before the power density is decreased by a factor of $1/e$. The absorbed power

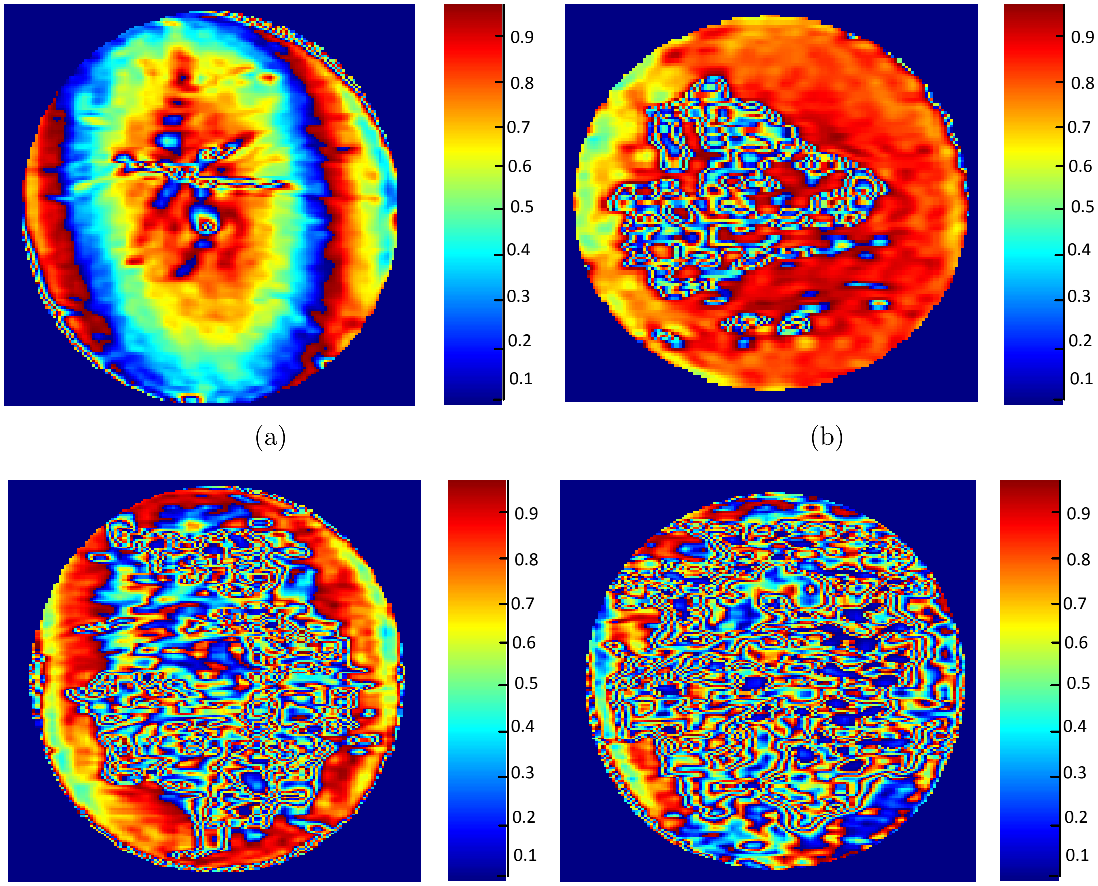

(a)

(b)

(c)

(d)

Fig. 4.8: 2D sectional views of the different breast phantoms in terms of water content (a) mostly fatty, (b) scattered fibro-glandular, (c) heterogeneously dense, and (d) very dense [228].

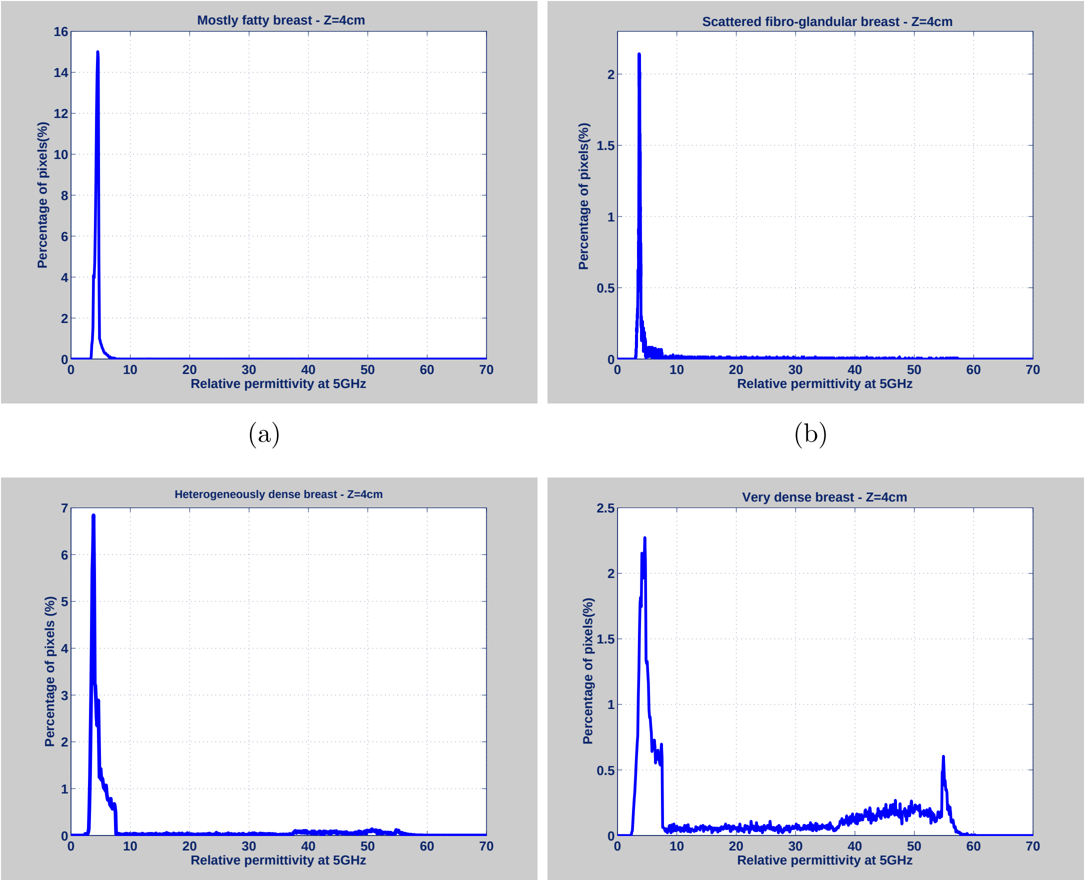

(a) (b)

(c) (d)

Fig. 4.9: The histogram of the permittivity for different numerical breast phantoms at 5GHz (a) mostly fatty, (b) scattered fibro-glandular, (c) heterogeneously dense, and (d) very dense.

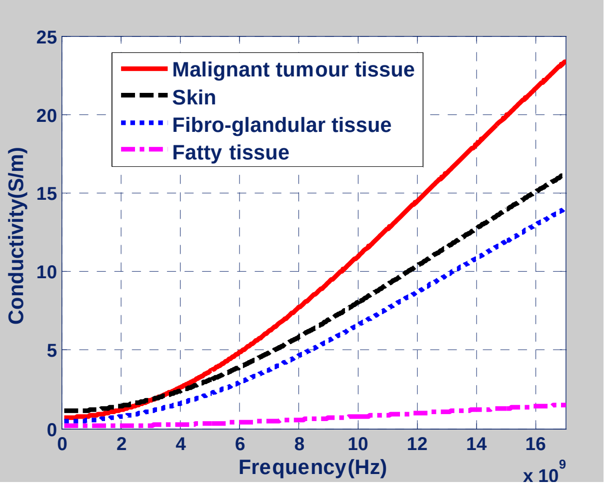

Fig. 4.10: Frequency variation of conductivity for different breast tissues.

density is given by:

$$\text{Absorb power density} = \frac{\sigma_{average}}{2} \left|E_{total}\right|^2 \tag{4.6}$$

where $\sigma_{average}$ is the average of conductivity for breast tissues and E_{total} is the total field.

4.7.1 Simulation results of penetration depth

In order to calculate the penetration depth, we used 2D $(FD)^2TD$ that includes the water content as explained in the previous section. The breast model is based on an MRI data taken from the breast phantom repository [228] as explained in Section 4.6. Each cell of the $(FD)^2TD$ contains its own tissue type and percentage of water content. For the study of penetration depth, the breast is surrounded by free space. Fig.

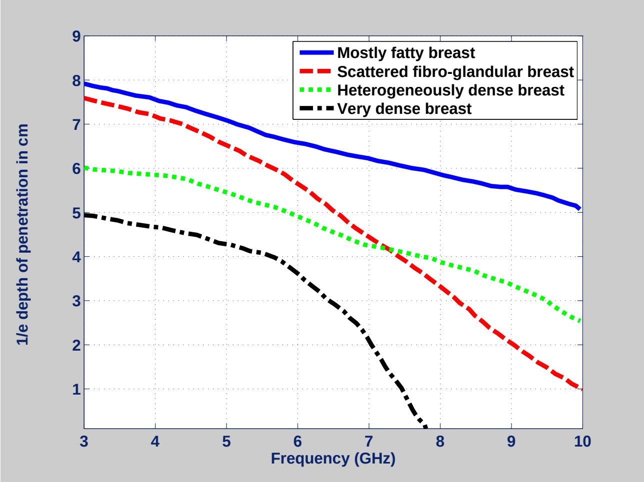

Fig. 4.11: $1/e$ penetration depth vs. frequency for different breast phantoms.

4.11 shows the depth of penetration as a function of frequency for different types of numerical breast phantoms. As can be seen in this graph, the $1/e$ depth of penetration is different for each case. This is due to different tissue compositions in different types of numerical breast phantoms. The penetration depth inside the dispersive lossy biological media decreases as the frequency increases. Therefore, employing higher frequencies to obtain better resolutions and improved imaging accuracy remains a challenge.

4.8 Matching material

The MWI chamber is usually filled with a liquid called “matching material”, and the breast is immersed into this liquid. Proper selection of a matching material is essential for minimizing the reflection, and to enhance the coupling of the electromagnetic energy to the breast. The matching material is also essential for creating a better resolution of the reconstructed images [205]. In a near-field microwave medical imaging environment, when the antennas are located close to the breast, a suitable matching fluid make the breast to be considered in the far-field zone. This medium helps to avoid antenna-object mismatch. In MWT, we assumed an infinite region of the background medium, which means that the interactions between the antennas, the surrounding system, and the object were ignored. This approximation is very useful as long as the background medium is a lossy dielectric. Furthermore, a contrast in the dielectric properties of the object and the coupling medium decreases the measurement accuracy, due to increase in attenuation, which causes a small signal-to-noise ratio. In addition, it is desirable to reduce antenna-object distance in order to decrease the total attenuation or minimize the temperature drift. The temperature drift might change the dielectric properties of the matching material. In biomedical imaging, the matching materials should meet the requirements for use in clinical applications. The background medium should be readily disposable, inexpensive, and environmentally safe. Furthermore, the background medium should exhibit low contrast with the predominantly high-water content of the body and electrical properties can be controlled by dilution with varying fractions of saline or any material. The challenge is finding the optimum material to increase penetration depth, and to be safe for the body. This section addresses the optimum value for the permittivity and conductivity of a matching material which provides more penetration depth of the electromagnetic wave into the body. We

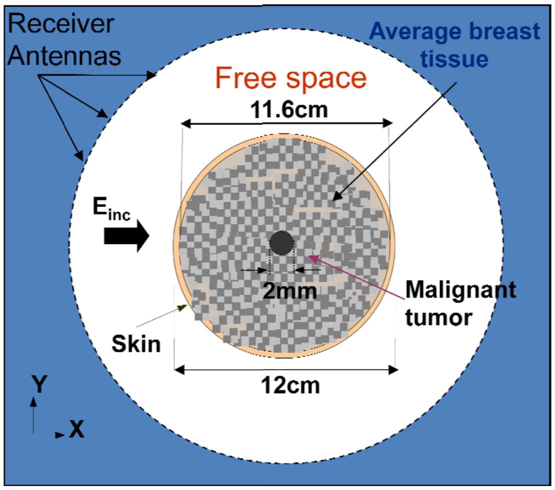

Fig. 4.12: Breast phantom with $2mm$ tumour at the center.

illustrate this procedure using 2D cylindrical configurations of a breast phantom in the spatial domain. Fig. 4.12 shows a breast phantom that includes a $12cm$ diameter cylinder with background tissue, $2mm$ thickness of skin, and a $2mm$ diameter tumour at the center. The cylinder is filled with average breast tissue with $\epsilon_\infty = 6.57$, $\epsilon_s = 16.29$, $\sigma_s = 0.23S/m$, and $\tau = 7.0ps$ [148]. The cylinder is illuminated by a plane-wave, and the total electric field is measured inside the cylinder. Fig. 4.13 (a) shows the total field in the y-axis and Fig. 4.13 (b) indicates the electromagnetic field in the x-axis at five frequencies (2, 5, 6, 7, 9, and 12GHz). As illustrated, penetration depth inside the dispersive lossy biological media decreases as the frequency increases. Now, in order to show the effect of the permittivity of the matching material on the penetration depth at two different frequencies (6 and 10GHz), the above mentioned breast phantom was immersed into a loss-less material while the permittivity value

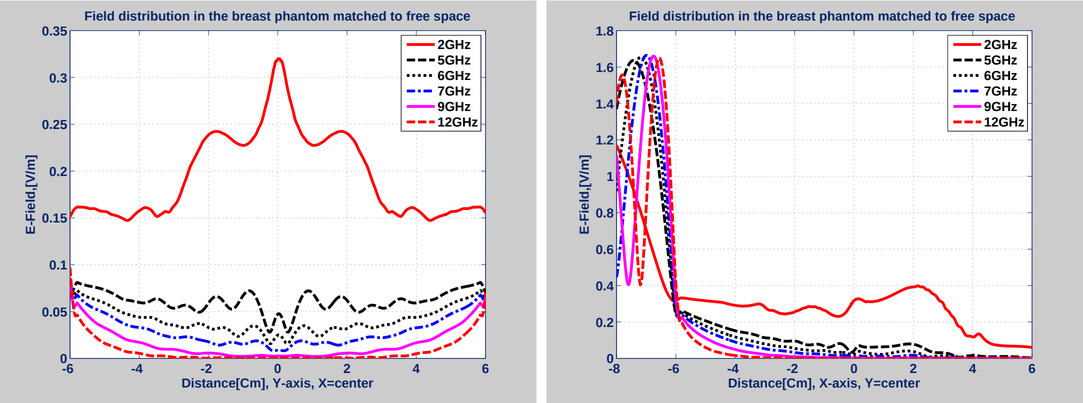

(a) (b)

Fig. 4.13: Field distribution in the breast phantom Fig. 4.12 at different frequencies (a) at x=center and y-axis, and (b) in y=center and x-axis.

changes from 1 to 50. Fig. 4.14 shows that as the permittivity of the matching material increases, the penetration depth increases. One observation that can be drawn from this graph is that the penetration depth does not change much after the permittivity of the matching material approaches that of the permittivity of the skin. The importance of conductivity to penetration depth is apparent. In order to show the effect of the conductivity of the matching material on the penetration depth, we used the same breast phantom (Fig. 4.12) while it is immersed in the material with a permittivity of 30 and with different values for conductivity. As can be seen in Fig. 4.15, the penetration depth decreases as the conductivity increases. As a result, a suitable coupling medium with a high dielectric constant and a low attenuation accomplishes wavelength contraction without the propagation loss penalty at high frequencies. Recently, a mix of glycerin and water or glycerin and saline has

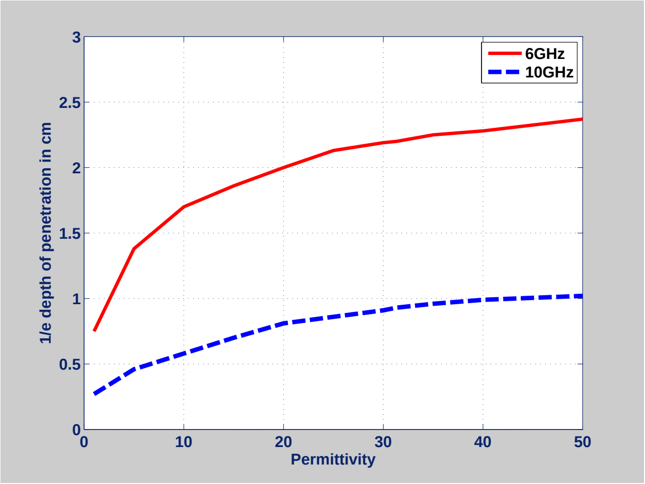

Fig. 4.14: Penetration depth for different permittivity values for Fig. 4.12.

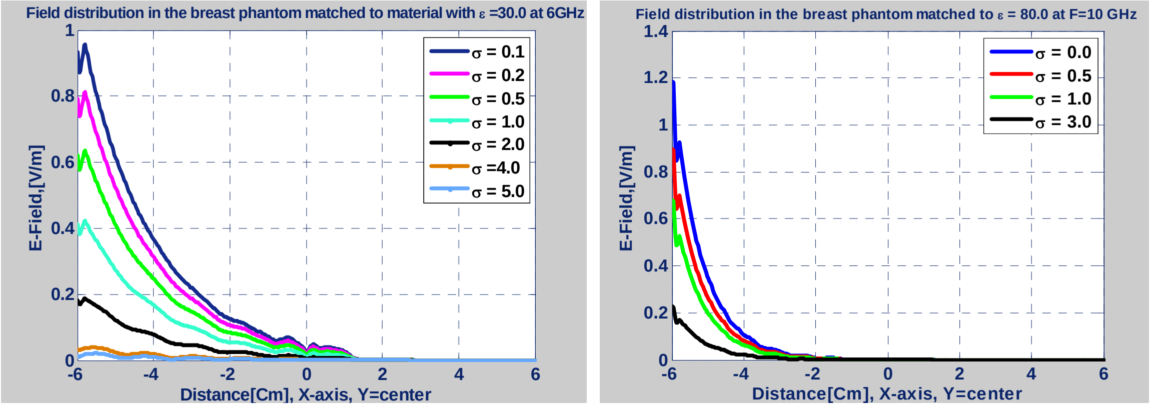

(a) (b)

Fig. 4.15: Field distribution inside the breast phantom matched to material with (a) $\epsilon_r = 30$ at f=6GHz, (b) $\epsilon_r = 80$ at f=10GHz for different values of conductivities.

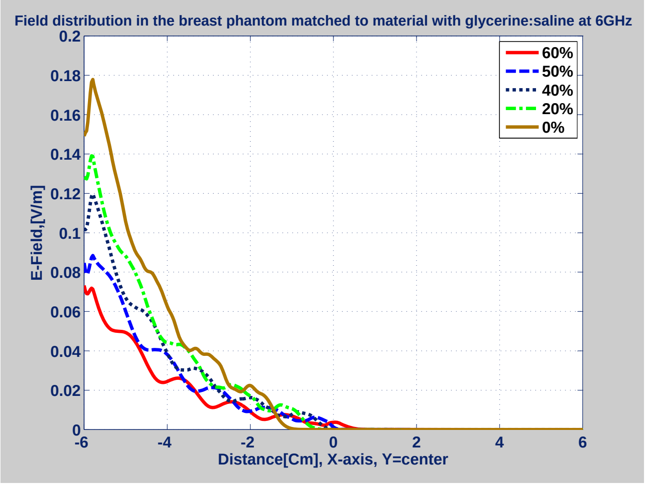

Fig. 4.16: Field distribution inside the breast phantom matched to material with different percentages of glycerine and saline at 6GHz.

been used as a matching material [205]. Here, we calculate the penetration depth for the breast phantom (Fig. 4.12) using a mix of glycerin and saline with different ratios. Fig. 4.16 illustrates the total field inside the breast phantom at 6GHz. From the figure, it is observed that the maximum penetration depth is obtained around $6cm$. Fig. 4.17 compares the penetration depth for the breast phantom (Fig. 4.12) immersed in different materials for the frequency band of 1-12GHz. These materials include free space, vaseline, mineral oil, a loss-less material with permittivity close to skin (optimum value), and deionized water. These are common materials used by other researchers as coupling medium; they are safe and their dielectric properties were available at high frequencies. Fig. 4.17 shows that none of these materials are ideal in terms of electrical properties; however, they are low cost and easy to use. As the results indicate, if we can find the materials with high permittivity and low

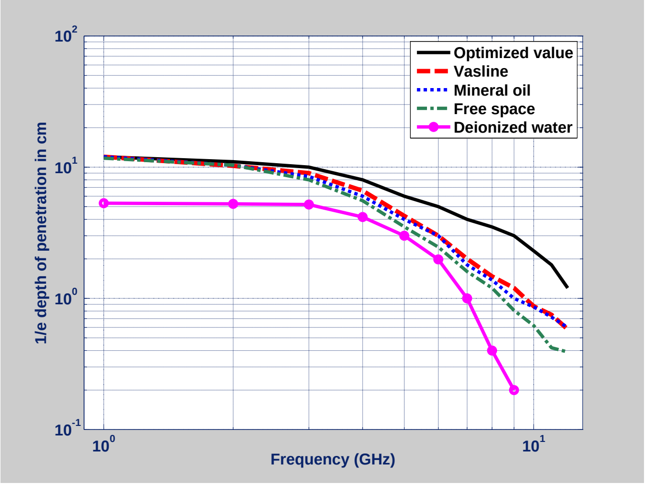

Fig. 4.17: Penetration depth vs. frequency for the breast phantom Fig. 4.12 using different matching material.

conductivity, the penetration depth will improve.

4.9 Tumour response (tumour signature)

In MWI (both radar and MWT methods) the imaging is based on the scattered field caused by an incident field. The difference between the permittivity of the tumour and that of the surrounding tissue creates more scattering. If the tumour response is weak, the scattered field can be easily obscured by background noise, and the probability of detecting the tumour decreases. Therefore, to compare different tissue compositions, we define the *"tumour response"* as the difference between scattered fields for the same tissue compositions with and without a tumour. The tumour response is given by:

$$\text{Tumour response} = \int_{\Phi=0^o}^{360^o} \int_{f=1GHz}^{10GHz} \left(\frac{\left|E_{scat(\text{with tumour})}\right|^2}{\left|E_{inc}\right|^2} - \frac{\left|E_{scat(\text{without tumour})}\right|^2}{\left|E_{inc}\right|^2} \right) df\, d\Phi \qquad (4.7)$$

where f is the frequency, $E_{scat(\text{with tumour})}$ and $E_{scat(\text{without tumour})}$ are scattered electric fields with and without tumour, respectively. E_{inc} is the incident field illuminated to the object, and Φ is the angle of observation from the axis of the incident wave. The effect of different tissue compositions on the tumour response will be discussed in this section for different numerical breast phantoms as well as different tumour sizes. The tumour signature can be easily masked by clutter from adjacent breast regions. In order to illustrate how the scattered field varies with different breast tissue compositions, three cases with various arrangements of adipose (fatty) and fibro-glandular tissues are simulated. In the first scenario, the breast phantom is assumed to be heterogeneously dense with a background of fatty tissue and masses of fibro-glandular tissue and a $2cm$ diameter tumour located in an off-center location. In the second case, the background is homogeneously fatty tissue, while a tumour at the same location as in the first scenario exists, and in the third scenario the fatty tissue of the second case is replaced by fibro-glandular tissue. It is noted that a homogeneous dielectric profile is obtained by setting all regions within the breast to a specific tissue. The Debye parameters set for breast tissues of interest for this simulation are based on Tab. 3.1 [148]. For all of the above scenarios, the diameter of the numerical breast phantom is $12cm$ and the thickness of the skin is $2mm$ (the configurations of these scenarios are illustrated in Figs. 4.18-4.20. The $(FD)^2TD$ forward simulation was performed to illuminate each numerical breast phantom and to collect the scattered field at the observation points. For this simulation, 100 observation points are considered at the far-field zone around the breast with the uniform spacing. It was assumed the phantom was surrounded by free space in all three scenarios. Fig. 4.21 illustrates the differences between the far-field scattered fields with and without the tumour, summed over all frequencies from 1-10GHz, for each of the three scenarios. The tumour response was evaluated as 0.75, 0.97, and 0.14 for the first, second, and third scenarios, respectively. The tumour response for a $1.5cm$ tumour is found to be 6.7 and 5.2 times larger when it is embedded within homogeneously uniform fatty tissue or a heterogeneous mix of fibro-glandular and fatty breast tissues, respectively, than when it is embedded within homogeneously uniform fibro-glandular tissue. Since the dielectric properties of the tumour and the adipose tissue are significantly different, the tumour response is stronger for the first two cases where a significant percentage of adipose tissue is present. As the area under the curve of tumour response versus different angles (Fig. 4.21) decreases, the detection will be harder. This indicates that it is harder to detect the difference between the cancerous and fibro-glandular tissues than it is to detect the difference between the fatty and cancerous tissues. However, it is easier to detect the cancerous tumour where fibro-glandular tissues are clustered than where they are uniformly distributed. Tab. 4.2 illustrates the value of the area under the curve of

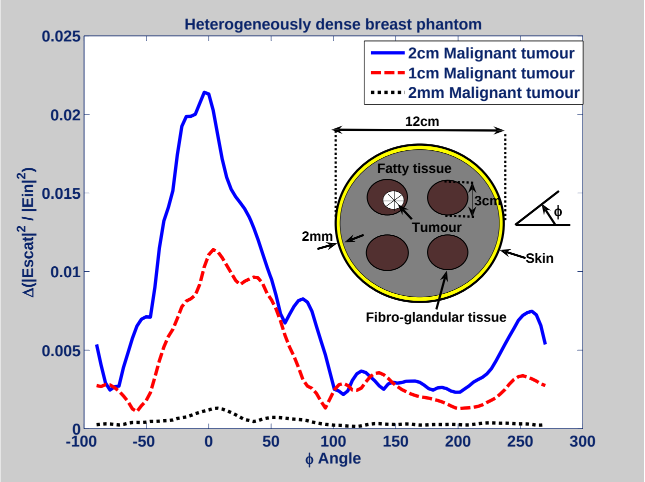

Fig. 4.18: Summation of the difference between scattered fields at different frequencies from 1-10GHz, with different tumour sizes, for a heterogeneous numerical breast phantom.

Tab. 4.2: The value of area under the tumour response for various sizes of tumours at different angles.

Tumour size	Heterogeneous phantom	Homogeneous fatty phantom	Homogeneous fibro-glandular phantom
$2cm$	0.7527	0.9710	0.1438
$1cm$	0.4243	0.5316	0.0701
$2mm$	0.0455	0.1137	0.0429

the tumour response for various tumour sizes. These results show that the tumour response becomes smaller as the tumour size decreases, and for homogeneous fatty and homogeneous fibro-glandular breasts the tumour response decreases by a factor of 8.5 and 3.3, respectively, as the tumour decreases in size from $2cm$ to $2mm$. These results also show that for a heterogeneous breast, the tumour response is reduced by a factor of 16 for the same decrease in tumour size.

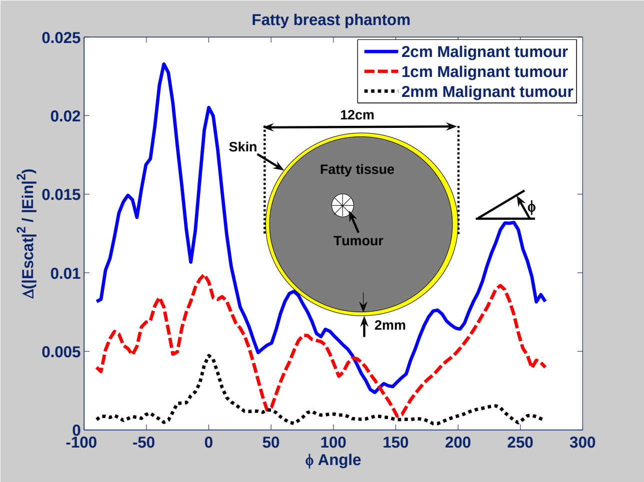

Fig. 4.19: Summation of the difference between scattered fields at different frequencies from 1-10GHz, with different tumour sizes, for a homogeneous fatty numerical breast phantom.

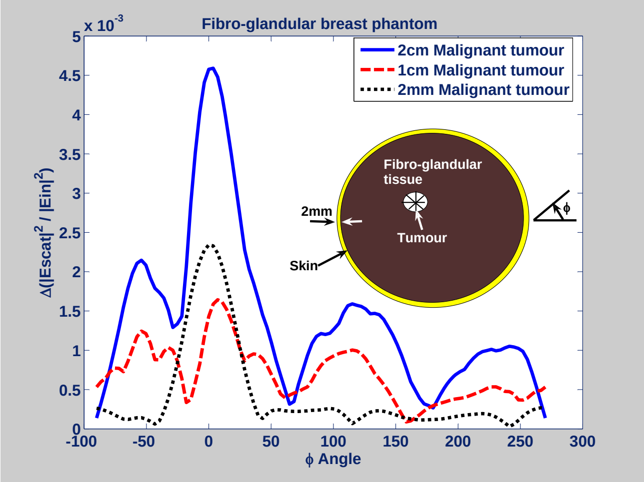

Fig. 4.20: Summation of the difference between scattered fields at different frequencies from 1-10GHz, with different tumour sizes, for a homogeneous fibro-glandular numerical breast phantom.

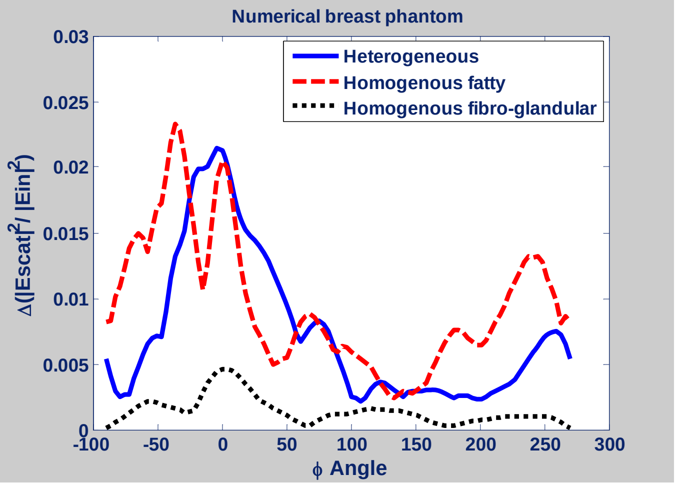

Fig. 4.21: Summation of the difference between scattering fields at different frequencies from 1-10GHz for each of the three scenarios, with and without a $2cm$ diameter tumour at the off-center location.

4.9.1 Tumour signature for different breast types

Here, as in the previous section, the tumour response has been calculated for four types of breasts (Fig. 4.22). Fig. 4.23 shows the difference between the scattered fields in the case of no tumour at the center and the cases with tumours of different sizes ($1cm$, $5mm$, $2mm$, and $1mm$ diameters). This graph shows that as the size of the tumour decreases, the tumour response is also decreased. This means that the detection of the tumour becomes more difficult for early stage cancer detection. Moreover, the power of the maximum tumour response for the case of mostly fatty breast at $\Phi = 0^o$ is around 2.5 and 1.2, 0.2, and 0.06 for the scattered fibro-glandular breast, heterogeneous dense breast, and very dense breast, respectively. This means that the tumour response changes based on the breast type, and as the power of the

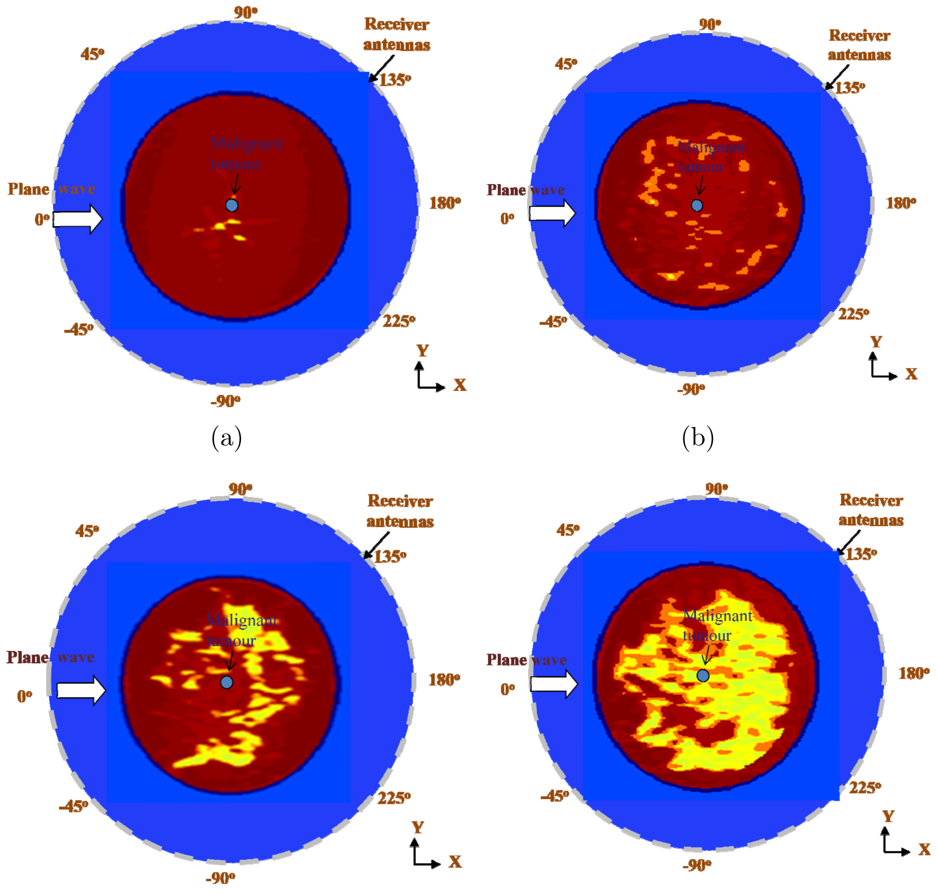

(a) (b)

(c) (d)

Fig. 4.22: (a) Mostly fatty breast, (b) scattered fibro-glandular breast, (c) heterogeneous dense breast, and (d) very dense breast.

tumour signature decreases, it becomes more sensitive to the noise. This problem will be discussed in Section 4.12.

4.10 Reconstruction algorithm for breast cancer imaging

For the simulations in this section, the following parameters have been used. The FDTD mesh consists of 600 × 600 pixels depending on the size of the breast cross-

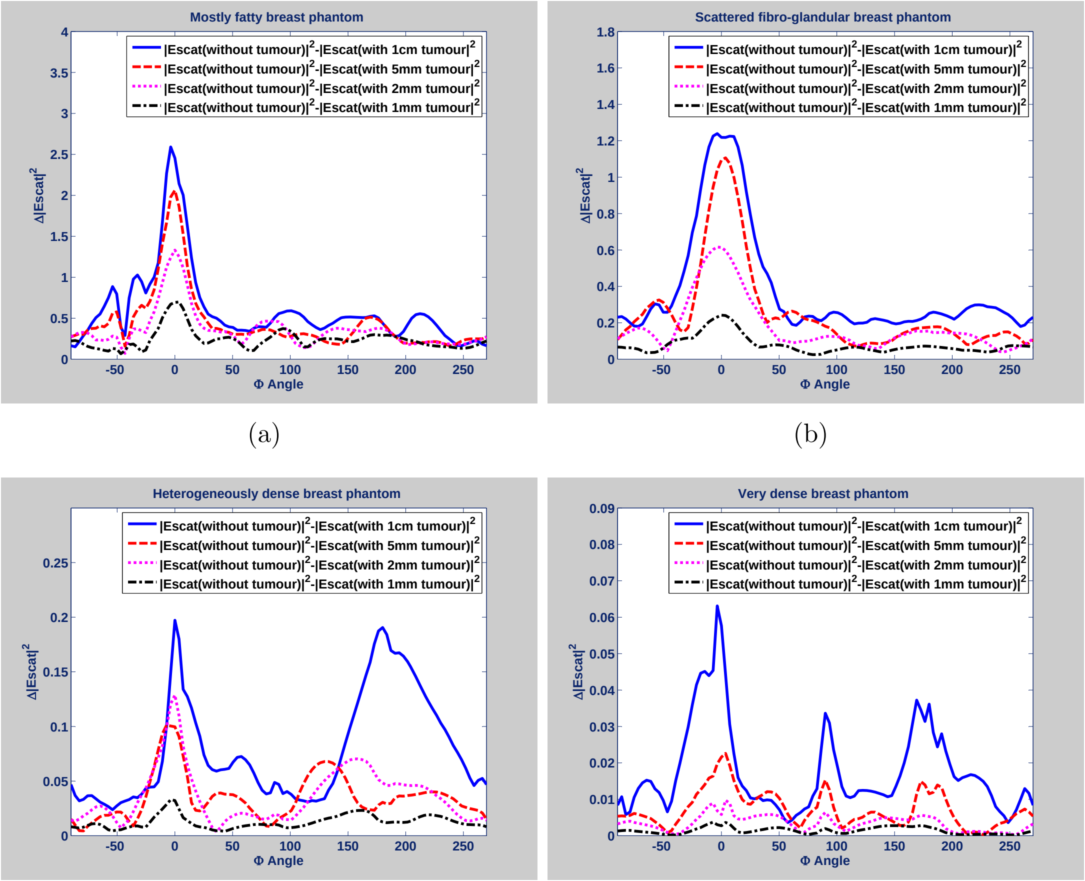

(a) (b)

(c) (d)

Fig. 4.23: Tumour signature for (a) mostly fatty breast, (b) scattered fibro-glandular breast, (c) heterogeneous dense breast, and (d) very dense breast for different sizes of tumour at the center.

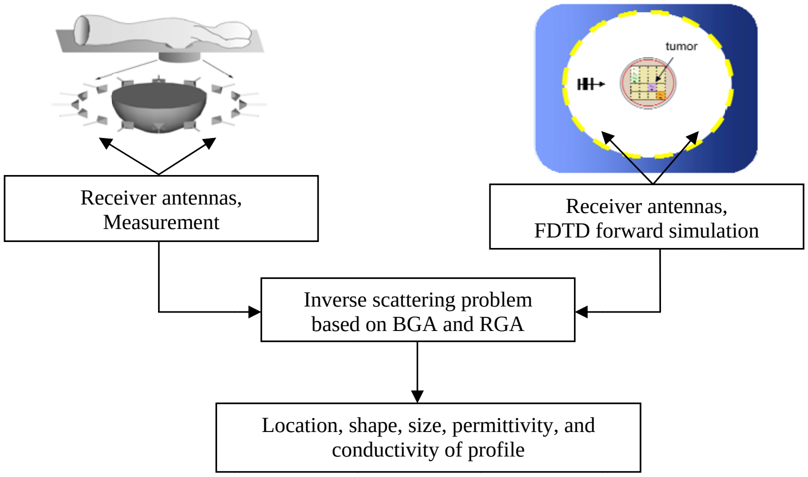

Fig. 4.24: Block diagram of the proposed imaging system for breast cancer detection.

section. The cell size (for inversion) is $\Delta = 0.5mm$ which is $\lambda/10$ (where λ is the effective wavelength in the fibro-glandular tissues at f=7GHz), and the time step is $\Delta t = 0.8ps$. A higher resolution for the inversion will increase the size of the search space and consequently the computational cost. The measurement data is replaced by simulated data (hypothetical measured data) obtained by running a forward simulation using (FD)^{2}TD with $\lambda/50$ cell size which is equal to $0.1mm$ resolution, to avoid the inverse crime. Fig. 4.24 shows the block diagram of the proposed method based on an inverse scattering method. To enhance the accuracy of the image and reduce the ill-posedness of the problem, four different incident angles (0^o, 90^o, 180^o, and 270^o) have been used (the plane-wave rotates 90^o for each measurement). With respect to the number of the receivers, increasing the number of receivers provides more information about the object at almost no computational cost. There are 100 observation points located in the far-field zone, and the time domain scattered field is measured on a circle around the numerical breast phantom with uniform spacing in the step of 3.6^o. From a practical point of view, using 100 probe positions at the observation points around the breast may not be possible in reality due to the size of antenna and mutual coupling between them. We chose this number for the proof of concept. In the optimization procedure for all of the following examples, it is assumed that the location of the breast surface is already known and we were only interested in creating an image of the dielectric properties inside the breast phantom.

4.11 Inversion results

4.11.1 Binary GA

In order to investigate the ability of the proposed technique for early stage cancer detection, we present an experimental example. Fig. 4.25 (a) depicts a cross-sectional view in the x-y plane of this phantom. It has a diameter of $12cm$, is filled with fatty tissue, and has a square-shaped tumour with a side of $7.5mm$. The skin thickness and the fibro-glandular region sizes are $2mm$ and $7.5mm$, respectively. Fig. 4.25 (b) shows the process for the GA and illustrates how the fitness value improves for different generations in order to reconstruct the image of Fig. 4.25 (a). At the 410^{th} generation with 120 chromosomes in each generation, the fitness value reaches 1, which represents a perfect match between the hypothetical data and the calculated scattered

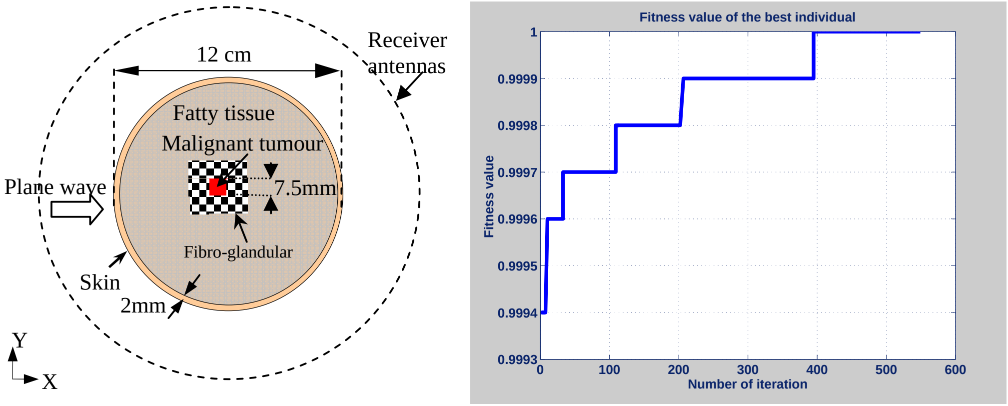

(a) (b)

Fig. 4.25: (a) Breast phantom with skin, breast tissue, and a malignant tumour (top view), (b) fitness value of the best individuals in different generations.

field. The fitness value corresponding to the correct solution can be other than 1 in real situations where noise is present, but in this example, we assumed a noiseless case. Fig. 4.26 shows the map of the dielectric properties of the recovered image at 6GHz. The x and y axes represent the 2D search space inside the breast phantom, and the z-axis shows the permittivity (Fig. 4.26 (a)) and conductivity (Fig. 4.26 (b)) at 6GHz. Such a match corresponds to a successive recovery of the location and dimension parameters, as well as the type of material representing the breast tissues. By monitoring the variations of the dielectric properties with respect to those for the healthy tissues, one may be able to identify abnormalities and use this information for treatment of the disease.

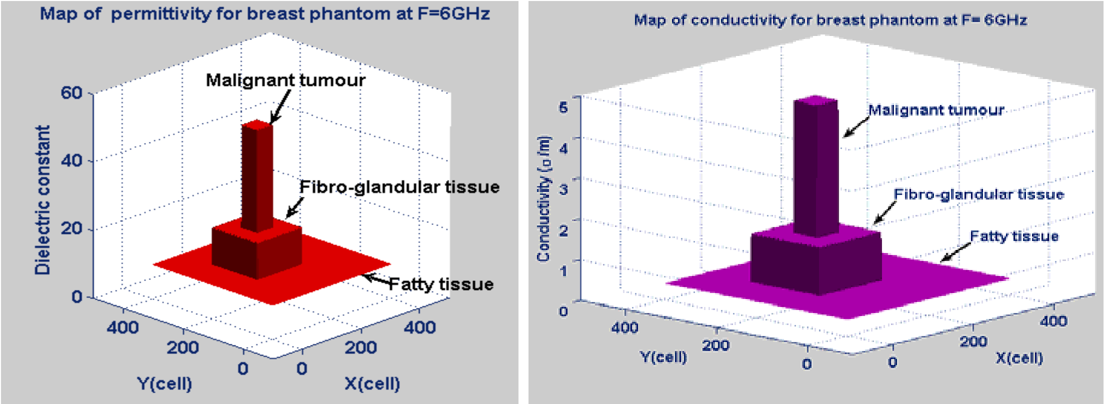

(a) (b)

Fig. 4.26: Map of dielectric properties for the breast phantom shown in Fig. 4.25 (a), (a) dielectric constant (b) conductivity.

4.11.2 Hybrid Genetic Algorithm (HGA)

In this part, we examined the HGA for solving the inverse scattering problem for breast cancer imaging. The HGA is the combination of binary and real-coded GA (see Section 3.12). One of the advantages of using the HGA for reconstruction is that it can provide information about the percentage of the water content. The HGA is divided into two steps of optimization. At the first step, the BGA is employed in order to determine the type of the tissue for each patch of search space. In the second step, by using RGA, the candidate solutions will search for different percentages of water content. In the BGA, the look-up table consists of first-order Debye parameters for four different tissue types: fibro-glandular, fatty, transitional, and malignant tissues with the water content percentage of 50%, given in Tab. 4.3. The BGA optimization stops when the average quality of the population does not improve after some number

Tab. 4.3: Look-up table of the Debye parameters for the BGA [220, 221].

Medium	Fat	Transitional	Fibro-glandular	Malignant
ϵ_∞	4.33	22.46	52.02	76.17
ϵ_s	2.98	8.488	14.0	25.52
$\sigma_s(S/m)$	0.027	0.23	0.78	1.2
$\tau_0(ps)$	13.0	13.0	13.0	13.0

Tab. 4.4: Look-up table of the Debye parameters for the RGA [220, 221].

Medium	Fat	Transitional	Fibro-glandular	Malignant
$\epsilon_{\infty u}$	3.987	12.99	23.20	9.058
ϵ_{su}	7.535	37.19	69.25	60.36
$\sigma_{su}(S/m)$	0.080	0.397	1.306	0.899
$\epsilon_{\infty l}$	2.309	3.987	12.99	23.20
ϵ_{sl}	2.401	7.535	37.19	69.25
$\sigma_{sl}(S/m)$	0.005	0.080	0.397	1.306
$\tau_0(ps)$	13.0	13.0	13.0	13.0

of generations. Then, the best individuals of the last generation in terms of fitness value are passed to the second step of optimization, which is RGA. For the RGA, the look-up table consists of first-order Debye parameters from the upper to lower end of the range for four different types of breast tissue (Tab. 4.4). In this step, for those individuals that are chosen by BGA, the tissue types remain constant, but the percentage of water content can vary between 0 and 100%. After the process of BGA, the behavior of the best fitness values at different generations for each individual are studied to choose those individuals that show an increase in the fitness value consistently, and they were passed to RGA. This selection can decrease the chances of getting stuck in a local minimum and can increase the chance of finding the global

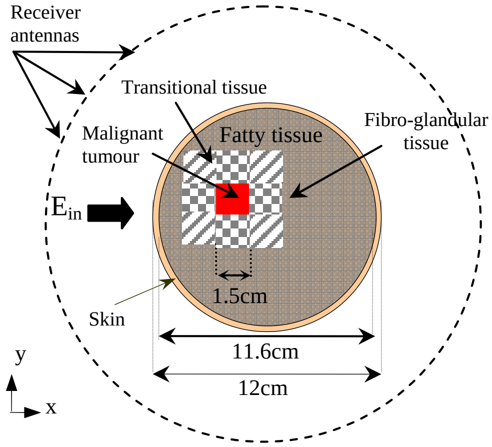

Fig. 4.27: Breast phantom with skin, breast tissue, and a square-shaped malignant tumour (top view).

optimum solution. For the rest of the thesis, the fitness-function is the same as equation (3.17) except the first term was removed. Then, the fitness-function becomes:

$$fitness = \frac{1}{T}\sum_{i=1}^{T}\left\|\sum_{f=f_1}^{f_2}\sum_{\phi=1}^{M}\frac{(E_{\phi}^{measurement}-E_{\phi}^{simulation})^2}{(E_{\phi}^{measurement})^2}\right\| \tag{4.8}$$

Fig. 4.27 depicts a cross-sectional view in the x-y plane of the breast phantom. The inhomogeneous background has a diameter of $12cm$, filled with fatty tissue. A square-shaped tumour is located inside a region of fibro-glandular and transitional tissues. This tumour has a side of $1.5cm$. The thickness of the skin layer is $2mm$. The dispersive dielectric properties of normal breast tissue used in this example are given in Tab. 4.1. The hypothetical measured data obtained by running a forward simulation using (FD)^{2}TD with dielectric properties of breast tissue containing 70% water content is utilized to mimic the measured data. It was assumed that the contrast between fibro-glandular and malignant tissues persists at around 10% within the frequency range of 3-10GHz [220, 221]. In the first step, the BGA optimization starts from a homogeneous fatty tissue background and fills in some inhomogeneous patches of possible materials inside the area. The BGA at 115 generations provides many possible solutions of which we choose the best three (none of them reaches the fitness value of "1".) Then, for the next step of the optimization, each possible solution is sent to the RGA optimization process which finds the optimum percentage of water content for each point inside the breast phantom. Fig. 4.28 (a) shows the process for the BGA and illustrates how the fitness value improves for different generations. Fig. 4.28 (b) shows the fitness values versus generation for RGA, for three possible solutions that were passed to it from BGA optimization. Fig. 4.29 shows the map of dielectric constants of the recovered image at 6GHz. As can be seen in Fig. 4.28 (b), the best solution has a different growth trajectory than the other solutions.

The next three examples are based on a realistic numerical breast phantom (MRI data). Fig. 4.30 shows a sub-sampled version of a cross-section of an MRI in the numerical breast phantoms repository of [228]. A numerical phantom of the breast is used to obtain the synthetic measured data by applying the Richmond method [229]. A 2D cross-section of a breast is divided into 18 equal regions. We considered only one transmitter as incident field at $\Phi = 0^o$ and single-frequency in this example. In the first stage of the optimization process, typical Debye parameters are assigned to

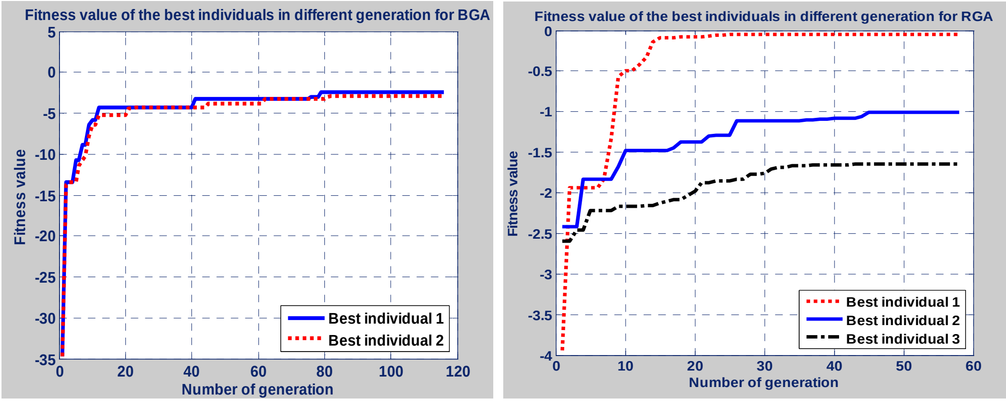

(a) (b)

Fig. 4.28: (a) Fitness value of the best individuals in different generations of BGA for example shown in Fig. 4.27, (b) fitness value for RGA, for three of the possible solutions that result from the BGA optimization.

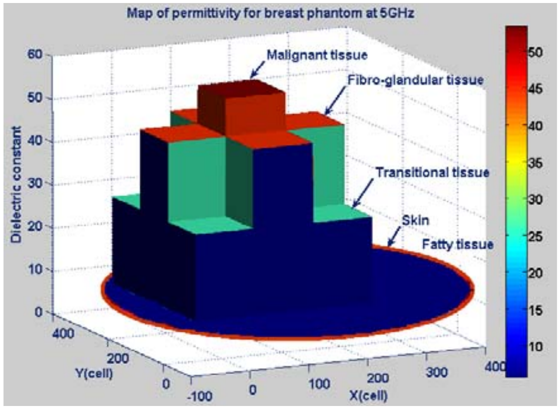

Fig. 4.29: Map of dielectric constants for the breast phantom shown in Fig. 4.27.

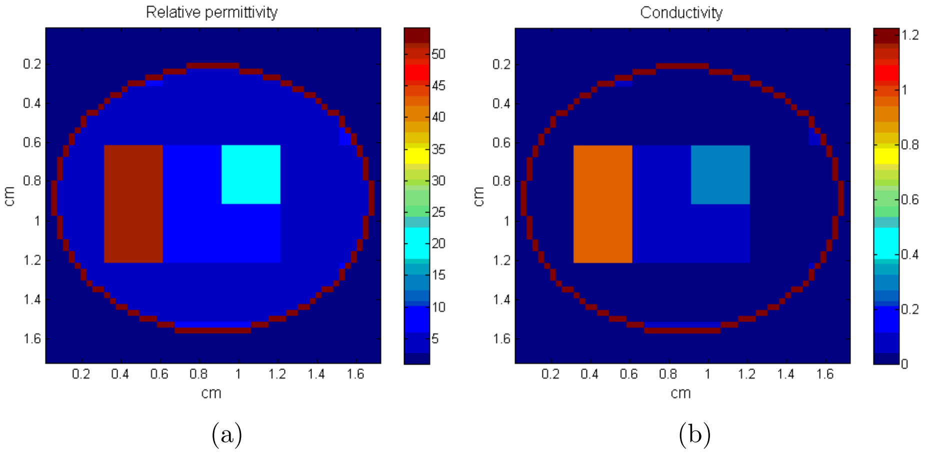

(a) (b)

Fig. 4.30: (a) Relative permittivity and (b) conductivity of the numerical breast phantom obtained by sub-sampling the MRI.

each category of the tissue type (fatty, transitional, fibro-glandular) assuming 50% water content (Tab. 4.3). Then, the BGA is used to find the tissue type. The best 4 solutions are then passed to the second stage where the RGA is used to find the water content. In this stage, the search space is limited to the range of the dielectric properties of each tissue type. After 200 generations of the RGA, the best candidate is chosen for further calibration and the other three candidates are removed from the optimization process. For the winning candidates, the GA runs for 300 more generations to obtain the final result. Parallel programming is used in both BGA and RGA. Each parallel job runs on 8 processors with the first optimization stage using 8 processors, simultaneously. The second optimization block uses 32 processors in the first 200 generations and 8 processors in the remaining 300 generations. Fig. 4.31 (a) shows the average fitness value of the solutions of the BGA over 1000 generations. Fig.

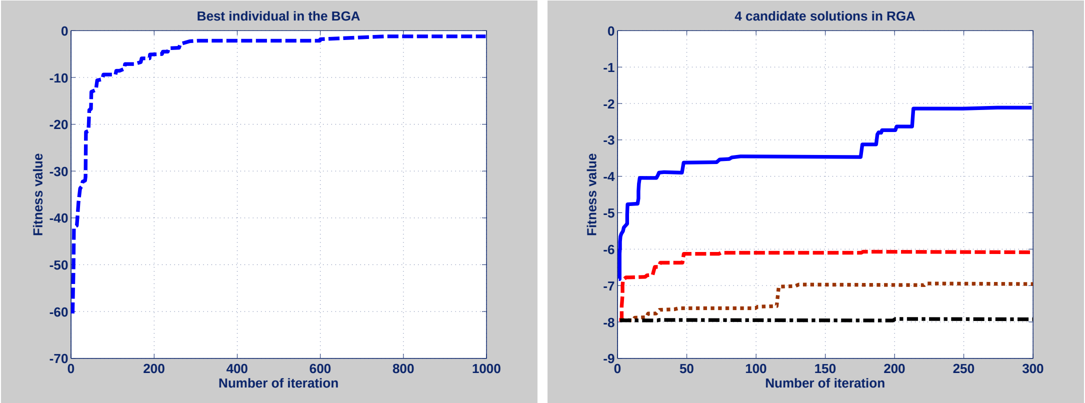

(a) (b)

Fig. 4.31: (a) Trajectory of the fitness value of the best individual in the BGA, (b) trajectory of the fitness value of the 4 candidate solutions passed to RGA.

4.31 (b) shows the improvement of the 4 candidates after 300 generations. Typically, the fitness of only one of the candidates significantly improves while the other 3 do not show a significant improvement. This implies that for those candidates, the tissue type was not predicted correctly in the first stage. Fig. 4.32 shows the reconstructed dielectric properties of the phantom shown in Fig. 4.30. Two other optimization methods using BGA only and RGA only are implemented for comparison purposes. The hybrid method overall performs $(4 \times 30 \times 200) + (4 \times 30 \times 300) = 60,000$ function evaluations. In order to be comparable with the hybrid method, the BGA and the RGA run for 2000 generations with 30 individuals in each iteration. This results in 60,000 function evaluations. Fig. 4.33 shows the result of the BGA and the RGA. Neither of these methods was able to converge to a right solution in 500 iterations. In addition, because the four RGA implementations can run in parallel, the hybrid

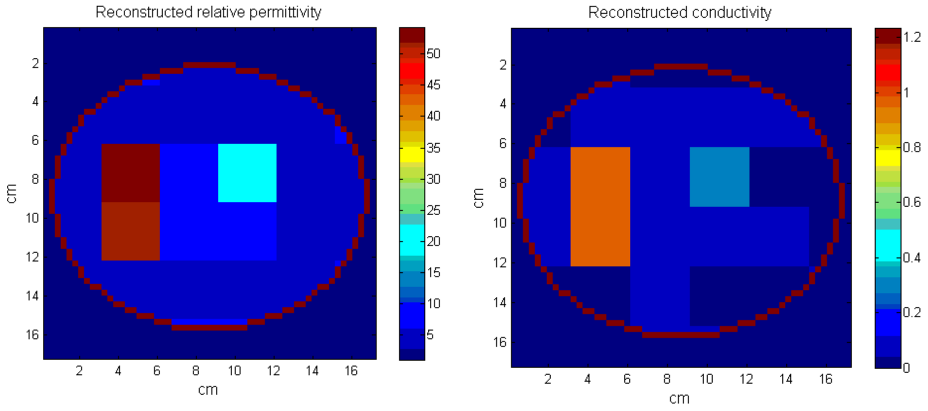

(a) (b)

Fig. 4.32: Result of the HGA method for the numerical phantom of Fig. 4.30 (a) permittivity, and (b) conductivity.

method is faster than both BGA and RGA alone. In breast imaging, the typical range of the dielectric properties is limited and is determined by *a-priori* knowledge about the tissues existing in the breast. By limiting the search space to first finding the tissue type and then finding the water content for a specific tissue type, the proposed method removes the non-physical solutions from the search space. This is an advantage over many of the local optimization methods used in inverse scattering, and those that uses a regularization terms with smoothing effects. Additionally, the proposed method is potentially able to reconstruct sharp profiles which occur frequently in breast imaging.

In order to show the ability of the proposed method in terms of resolution, the breast phantom derived from MRI [228] data with a $7mm$ resolution has been selected for the third example. Cross-sectional maps of the dielectric constant and effective conductivity distribution at 5GHz for a "heterogeneously dense" breast phantom are

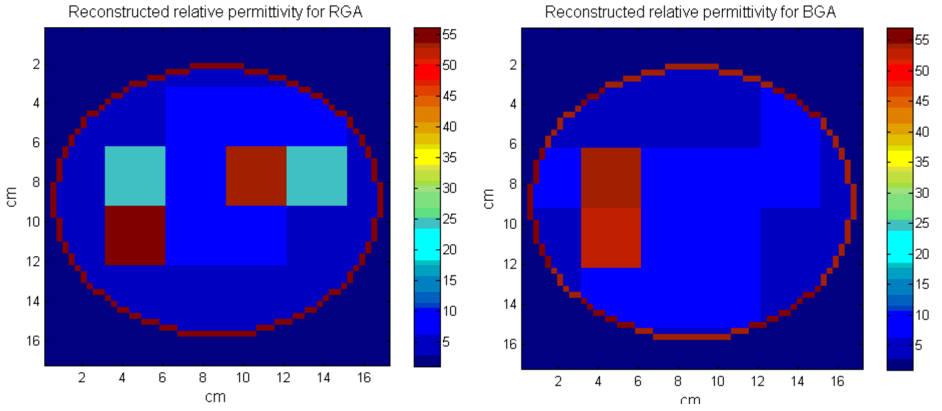

(a)

(b)

Fig. 4.33: Result of the (a) RGA, and (b) BGA methods for relative permittivity.

shown in Fig. 4.34. The physical diameter of the breast phantom is approximately $8cm$. The phantom contains heterogeneous breast tissue, including different tissue types ranging from the highest water content (fibro-glandular) tissue to lowest water content (fatty) tissue, and also a transitional region with various water content levels. Fig. 4.35 shows the map of the dielectric properties at $7.5mm$ resolution of the numerical breast phantom shown in Fig. 4.34. A $7.5mm$ square-shaped tumour was inserted inside the fibro-glandular tissue introduced into the FDTD model. The tumour is placed at a $x = 60cm$ and $y = 80cm$ position. This numerical breast phantom is discretized into a uniform grid cell size of $0.5mm$. The breast is surrounded by the free space.

Fig. 4.36 shows the reconstructed image of permittivity and conductivity. Transects of the reconstructed permittivity and conductivity at 5GHz in the horizontal direction at line $y = 80$ cell and $x = 64$ cell, compared with the actual distribution, are shown in

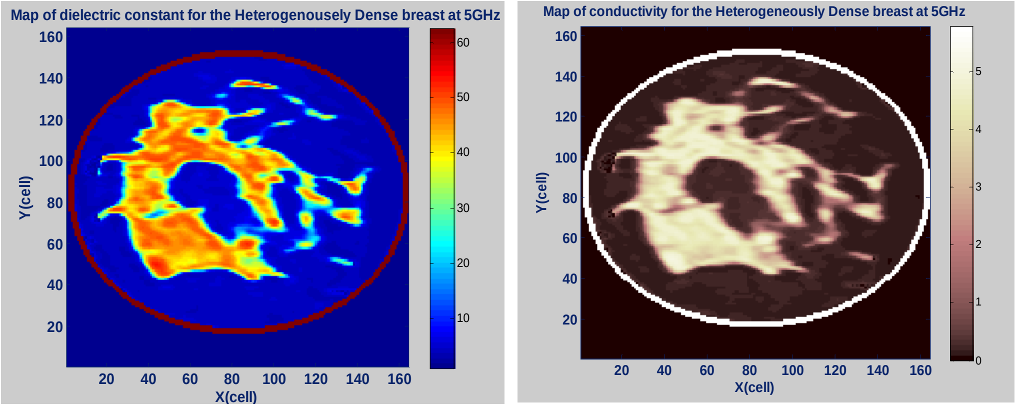

(a) (b)

Fig. 4.34: Map of (a) permittivity, and (b) conductivity of the heterogeneously dense breast phantom.

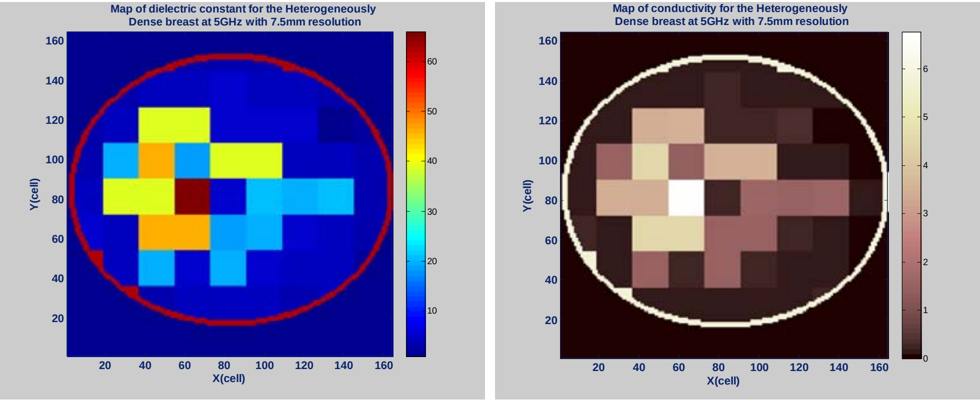

(a) (b)

Fig. 4.35: Map of the (a) permittivity, and (b) conductivity of the heterogeneously dense breast with 7.5mm resolution.

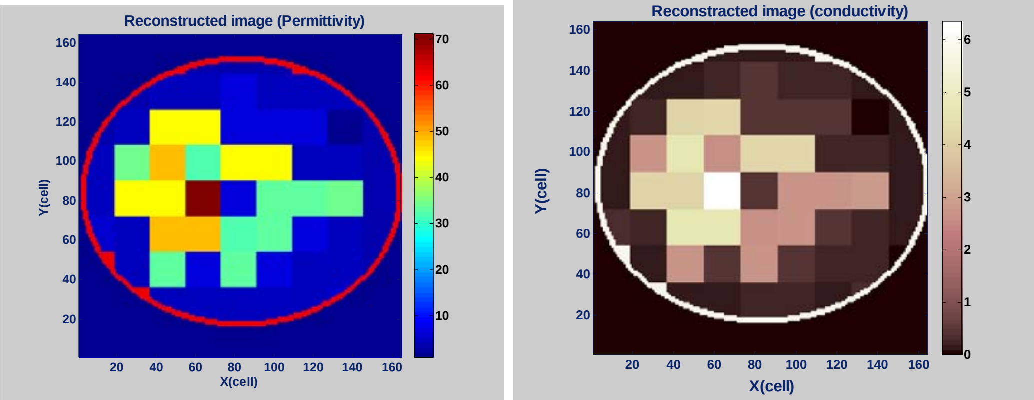

(a) (b)

Fig. 4.36: Reconstructed image of (a) permittivity, and (b) conductivity for the breast phantom of Fig. 4.35.

Fig. 4.37. One observation apparent in these images is the small degree of inaccuracy in the recovered permittivity and conductivity compared with the actual image, since the percentage of water content, which affects dielectric properties, is not known precisely. However, the estimated percentage of water content is within the range for each tissue type to recognize the right tissue composition.

4.12 HGA/FDTD in the presence of noise

Background noise is always present in any measurement and it must be taken into account. This is particularly important in biomedical applications, since for safety reasons, it is not possible to increase the energy of the incident field to overshadow the background noise. It is shown in this section that the proposed method is efficient and provides adequate accuracy even when the Signal-to-Noise Ratio (SNR) is low.

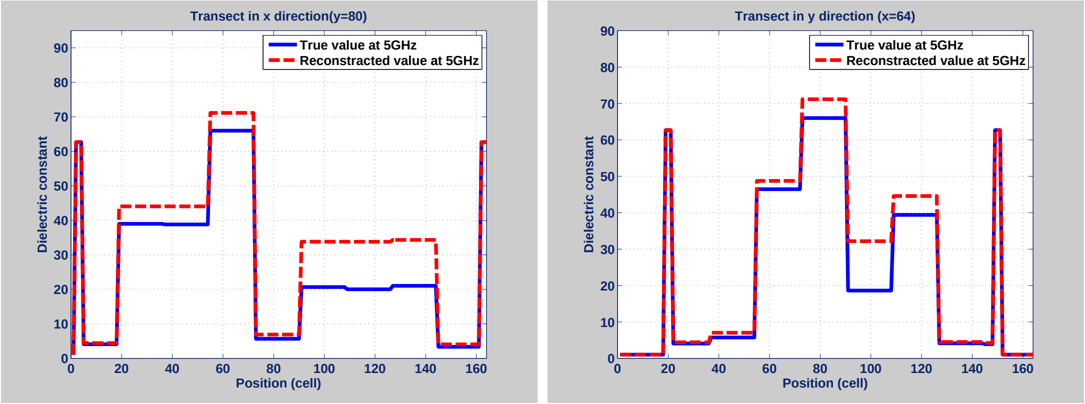

(a) (b)

Fig. 4.37: Transects of the reconstructed permittivity image at (a) $y = 80$cell horizontal direction, and (b) $x = 64$cell vertical direction profiles compared with the actual distribution.

SNR is given by [102]:

$$SNR = 10log\left(\frac{P_s}{P_n}\right) \tag{4.9}$$

in which P_s is the total power of scattered field and is equal to $\frac{1}{2}\sum_{f_1}^{f_2}|E_z|^2$ (E_z is the scattered field at the different frequencies within $f_1 - f_2$ range), and P_n is the noise power. Fig. 4.38 shows the tumour response for different types of breasts and different tumour sizes while the noise has been added for different SNRs. (For detail about the tumour response, see Section 4.9.) It can be seen that the power of the tumour response for the heterogeneous breast and the very dense breast is weak compared with the scattered fibro-glandular breast. This means that the scattered field for dense breast type is very sensitive to the noise, and the image reconstruction of this breast

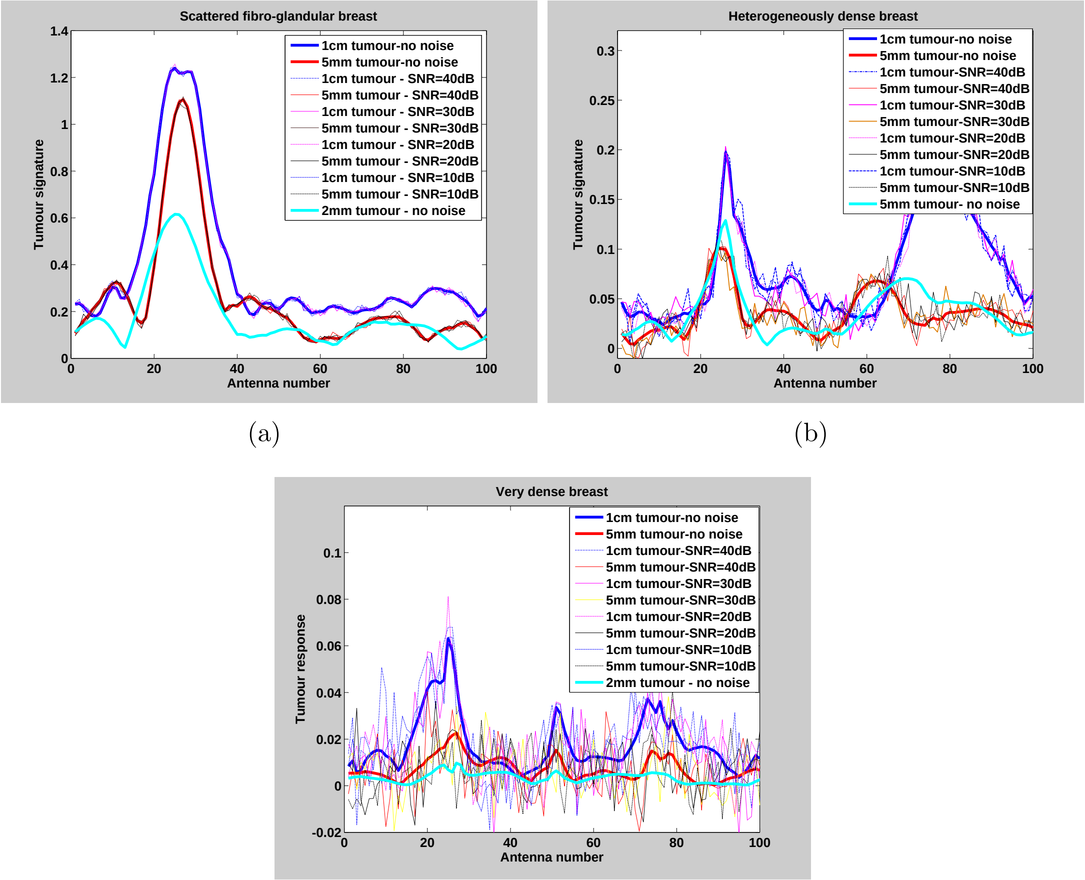

(a) (b)

(c)

Fig. 4.38: Tumour response for diverse SNR and different tumour sizes (a) scattered fibro-glandular breast, (b) heterogeneously dense breast, and (c) very dense breast.

type is more difficult than other types.

In this section, we investigate the performance of the proposed method at different SNR levels. Fig. 4.39 shows the block diagram of the process of adding the noise to the measurement signal. After recording the scattered fields at the observation points by using the $(FD)^2TD$ solver, an additive white Gaussian noise was added to simulate the noise which is present in real measurements. The HGA optimization

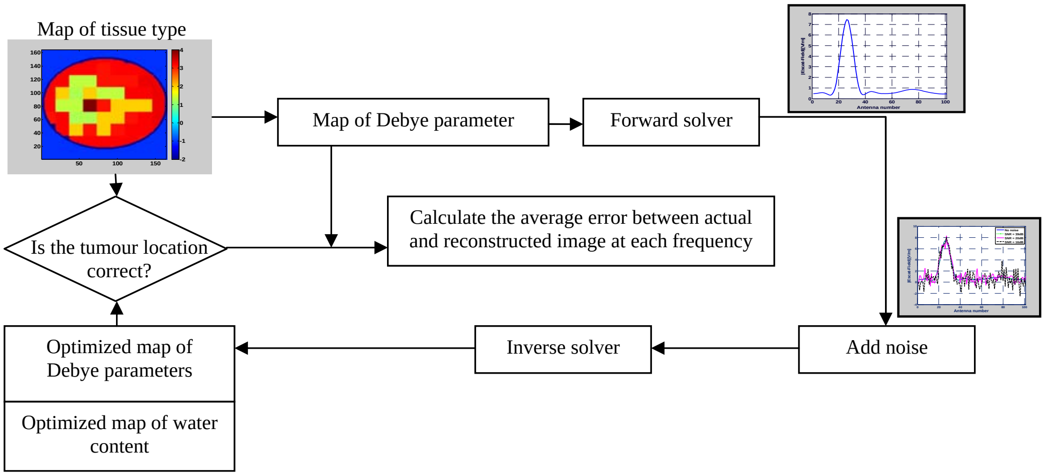

Fig. 4.39: Block diagram of adding noise in the proposed tomography method.

technique was then used to reconstruct the dielectric property map of the breast tissue inside the numerical breast phantom. Background noise generally qualifies as white noise, that is, having a constant power spectral density [102]. Fig. 4.40 (a) shows the histogram plot of white noise. Fig. 4.40 (b) shows the amplitude of white noise for each antenna at the observation point. Fig. 4.40 (c) presents the power spectral density of the white Gaussian noise. The white noise was artificially added to all measurements of the scattered field at different frequencies in such a way that the power of noise was constant at all frequencies, but the power of the noise changed randomly with Gaussian distribution at each observation point. To illustrate the ability and robustness of the proposed HGA method, we added different levels of noise to the scattered field of the breast phantom of Fig. 4.35 by using the process shown in Fig. 4.39. Figs. 4.41 (a) and (b) show the average error of the dielectric constant and

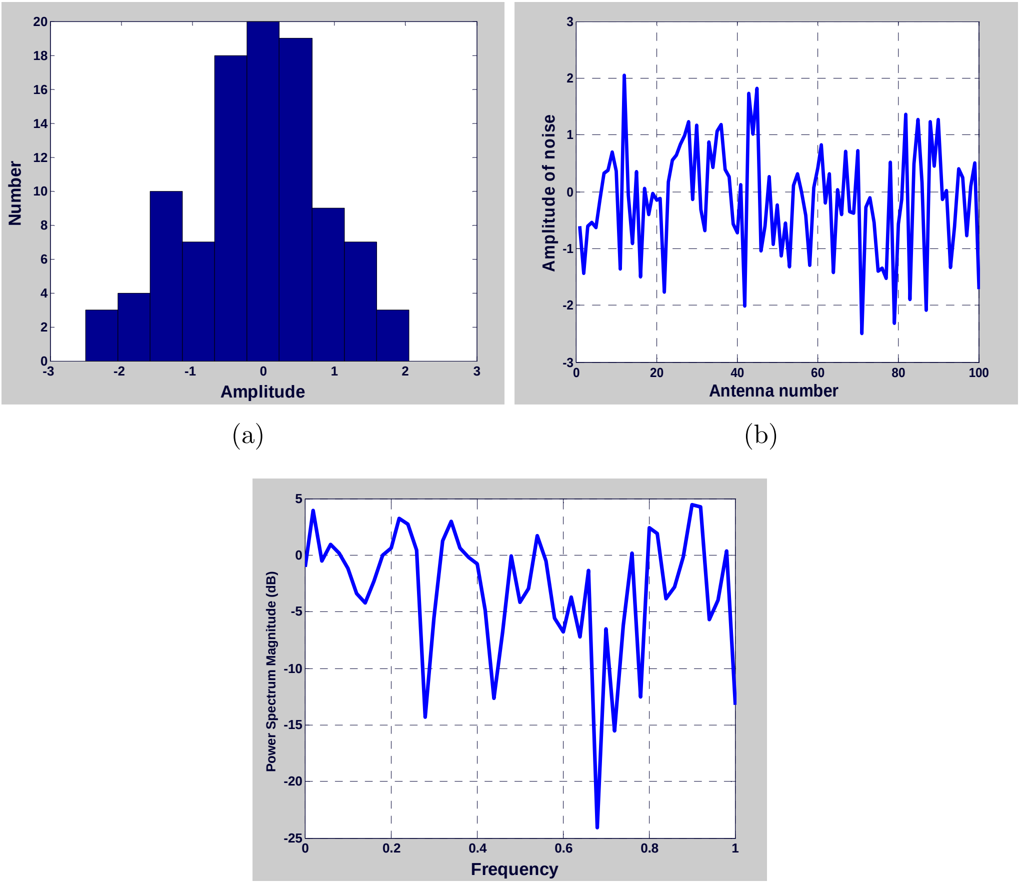

(a) (b)

(c)

Fig. 4.40: (a) Histogram plot of the added white noise, (b) amplitude of white noise for each antenna at the observation point, and (c) power spectral density of the white Gaussian noise.

conductivity versus SNR, respectively. These errors are averaged over the differences between the actual and the reconstructed permittivity (5.10) and conductivity (4.11).

$$\text{Average error in permittivity} = \sum_{f_1}^{f_2} \frac{\sum_i \sum_j |\epsilon_{r(\text{reconstructed image})} - \epsilon_{r(\text{real image})}|}{\text{number of cells}} \tag{4.10}$$

$$\text{Average error in conductivity} = \sum_{f_1}^{f_2} \frac{\sum_i \sum_j |\sigma_{(\text{reconstructed image})} - \sigma_{(\text{real image})}|}{\text{number of cells}} \tag{4.11}$$

where f_1 and f_2 refer to different frequencies of reconstruction and i and j are the cell numbers in the x and y directions, respectively. These figures demonstrate that as the SNR decreases (noise level increases), the average error increases. It was observed that the proposed method still can find the tissue types of the heterogeneous structure even when the SNR is 23dB which is equivalent to 15% background noise. When the background noise is greater than 15%, the optimization program did not converge. It was also noticed that by increasing the noise level, the optimization time for convergence was significantly increased.

4.13 Resolution in MWI for early stage breast cancer detection

MWT is on the edge of becoming a useful clinical tool for the detection and subsequent treatment of breast cancer. Early clinical work with a leading MWT system has shown statistical evidence of a conductivity image contrast of $\approx$ 200% for malignant tissue [230]. However, in order to obtain this result, the researchers had to restrict themselves to lesions $1cm$ in size or greater [230]. If MWT is to become competitive

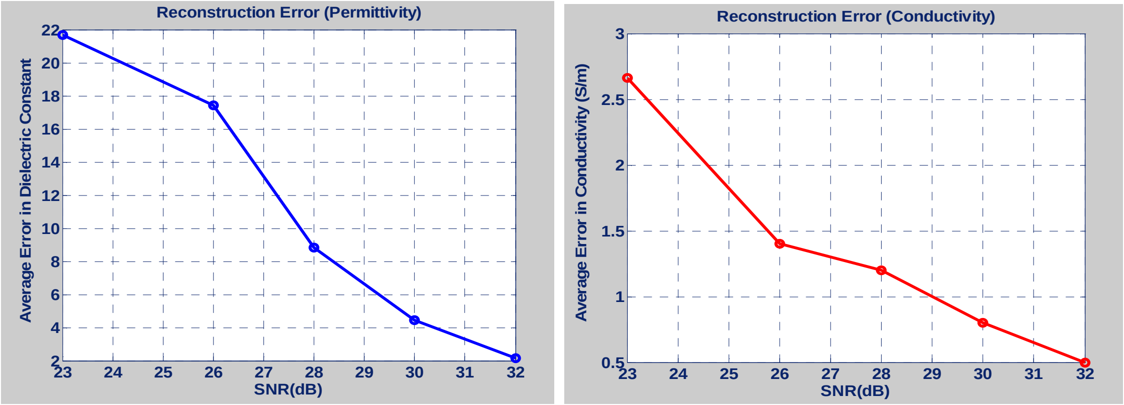

(a) (b)

Fig. 4.41: The average error in (a) dielectric constant, and (b) conductivity vs. SNR.

with the current gold-standard of mammography, the minimum lesion size must be reduced (to $\approx 3mm$), which implies that the resolution capabilities of this technology must improve. The spatial resolution that we achieved by using HGA was about $7.5mm$. However, a $4mm$ resolution for different breast tissue was also achieved by NNGA/FDTD [133]. Despite the fact that in a radar-based imaging technique the resolution is limited by half-wavelength, in the MWT technique, because of the non-linearity of the algorithms, the spatial resolution of the image was limited by noise rather than by the half-wavelength diffraction limit. It is important to note that the noise is not only the receiver thermal noise. The "modelling errors" are much more important sources of noise. The modelling calibration will be discussed in Chapter 5. Different factors might change the resolution:

1. increasing the number of transmitters (in terms of multi-view and multi-frequency)

due to providing sufficient information during the optimization procedure,

2. increasing the number of receiving antennas in order to measure more scattered fields due to heterogeneities,
3. increasing the accuracy of the forward solver and calibration procedures.

In summary, although there has been enormous progress in MWT for biomedical imaging applications, ranging from advances in the inverse algorithm to better data collection technology that has led to preliminary clinical results, state-of-the-art MWT systems are still at the pre-clinical or early clinical stages and are not yet competitive as compared with other more consolidated imaging modalities. One of the reasons might be that the *in-vivo* dielectric property values of breast tissues are not readily available for evaluating the MWT techniques for breast cancer detection. In MWT methods, the values of these properties are used as diagnosis indices; therefore, the accurate data based on *in-vivo* measurement can validate the imagining modalities and accelerate this technique to be transferred into a clinical trial. In addition, the MWI is going to be a complementary method to X-ray and MRI to avoid the unnecessary biopsies. Unfortunately, there is not much information available about dielectric properties of benign tumours yet. Hence, it is too early to make any comments about false positive and negative percentages for the MWT methods. It should be stressed that, in spite of the work and effort that has been done for using the microwave for breast cancer imaging, most researchers who have no strong intersections with the medical community do not consider the actual model of the breast in their techniques. A recent study of the dielectric properties of breast tissues shows that in addition to the dielectric contrast 10:1 between adipose and malignant tissues, there is only a 10% contrast between fibro-glandular and malignant tissues [220, 221]. Therefore, any microwave breast imaging needs to consider both of the dielectric contrasts in their model, and not only consider high contrast which is easy to image due to a high scattered field. The goal of this chapter was to apply the proposed inverse scattering solver to the media that is close to the breast tissue composition. In this chapter, we utilized TM field for the inversion algorithm. However, the scattered field also includes Transverse Electric (TE)-polarized component. These two polarizations are physically uncoupled: they provide independent information about the object being imaged and their combination may eventually improve the reconstruction in tomographic configurations. In the last part of this chapter, we investigate this issue by comparing the tumour response for the TE and TM polarizations.

4.14 Comparing the electric and magnetic components of scattered fields for breast cancer detection

In this section, we compare different components of scattered fields when different polarizations have been used for illumination. For this purpose, a circular-loop antenna is used for illuminating the TE mode. The tumour signature is compared when the

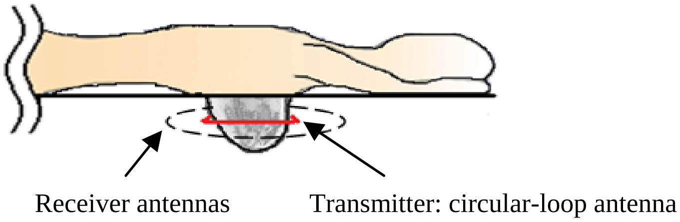

Fig. 4.42: MWT system configuration.

dipole and circular-loop antennas were used as transmitters. The arrangement of the MWT system while the loop antenna is used as a transmitter is shown in Fig. 4.42. A loop antenna was placed around the breast as a transmitter. An array of antennas was positioned around the breast as receivers. Receiver and transmitter antennas are all located on the same plane. We investigated the differences in the simulated scattered fields (ΔE) between a numerical breast phantom with and without tumour. ΔE is calculated as $\Delta E = |E_r - E_s|$, where E_r is the electric field intensity evaluated in a 3D simulation, at the receiver points, without a tumour, and E_s is the electric field intensity measured at the same receiver points in 3D, when a tumour is present. In this section, ΔE is called "tumour signature". This term will be calculated for the z and Φ components of E-field. Practically speaking, these two terms are best received by a dipole antenna as a receiver, when the dipole is located along the axis of the receiver antennas and oriented parallel to the long axis of the breast phantom for E_z measurement or orthogonal to the long axis of breast phantom for E_Φ measurement. For evaluating the loop antenna and comparing it with the

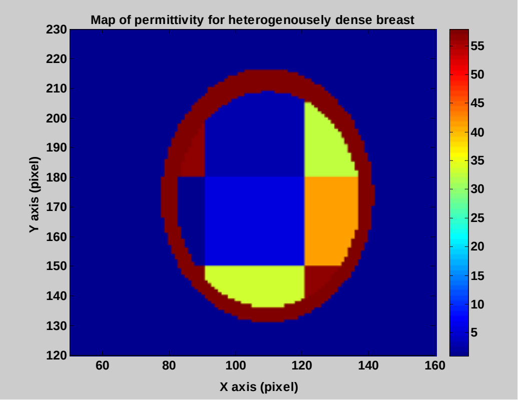

Fig. 4.43: Map of permittivity for heterogeneously dense breast at f=5GHz (each pixel is 0.5mm).

dipole antenna for illuminating the breast in a realistic environment, a cross-section of the numerical breast phantom has been used. Cross-sectional maps of the dielectric constant and effective conductivity distribution with a 1.5cm resolution at 5GHz for a "heterogeneously dense" breast phantom are shown in Fig. 4.43. The breast phantom is derived from MRI data and incorporates realistic dispersive dielectric properties of normal breast tissue in the microwave frequency range [228]. This cross-section has been extended in the z-direction by 7.5cm for a 2.5D simulation[1]. The numerical breast phantom consists of a region of fatty, fibro-glandular, and transitional tissues and also includes a thin layer of skin. This is considered as a "breast without a tumour". A 7mm square shaped malignant tumour is inserted in the plane of the antenna attached to the fibro-glandular tissue in the numerical breast phantom, and it is considered as a "breast with a tumour". The permittivity of biological materials

---

[1] The 2.5D simulation because one axis was extended to some length but not ∞.

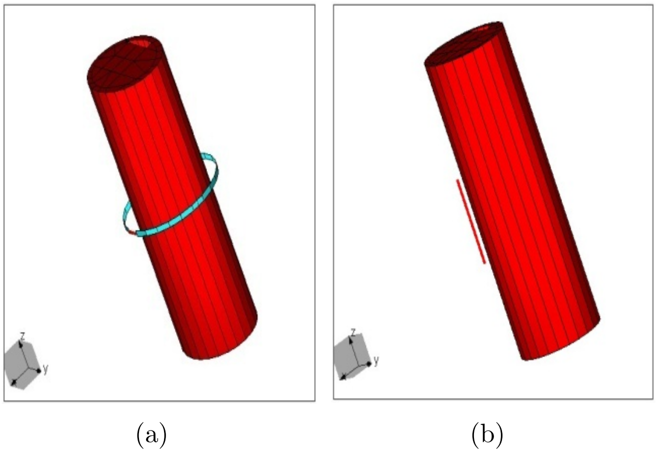

(a) (b)

Fig. 4.44: 3D breast phantom with skin, breast tissues excited by (a) circular-loop antenna, and (b) dipole antenna.

generally changes with the frequency as well as the water content. The electrical properties used for breast tissues can be found in Tab. 4.1. The coupling medium is assumed to be air in this study. The ability of the circular loop antenna compared with the dipole antenna in illuminating the object and increasing the sensitivity is explored. To simulate the structure and calculate the scattered field, a Method of Moments (MoM)-based electromagnetic simulation package, WIPL-D is used [231]. The simulation setup is shown in Fig. 4.44. The breast phantom is located at the center of the circular loop antenna (Fig. 4.44 (a)) and in front of the dipole antenna (Fig. 4.44 (b)). The 2.85cm long dipole antenna is designed to operate at the frequency of 5GHz; however, the radius of the circular loop antenna is determined based on the size of the breast. In this study, the radius of 2.2cm is considered for the loop antenna. The dipole antenna is located at a distance of 7mm from the skin, but the

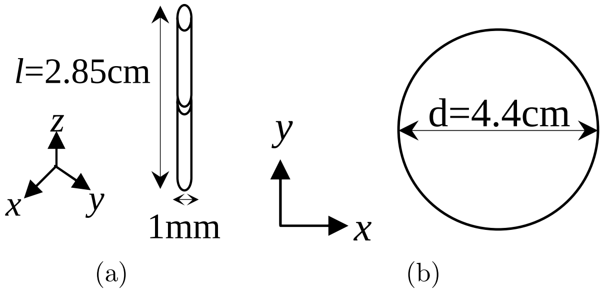

Fig. 4.45: Antennas dimension (a) dipole antenna, and (b) circular-loop antenna.

loop antenna is positioned around the breast, and due to the non-symmetric shape of the breast, the distance might change. The dimensions of the loop and dipole antennas are shown in Fig. 4.45. In order to compare the tumour signatures, the input power must be the same for both transmitter antennas. Therefore, the differential voltage at the input terminal of the dipole antenna for each frequency has been adjusted to generate the same power as the loop antenna. In addition, 24 observation points are considered around the breast. The scattered field collected at each observation point is determined by taking an average for the points from 3.2-4cm away from the center and within the angle of $\pm 7.5^o$ from the center. The comparison of the tumour signatures for both TM (the measured field component being E_z and TE (the measured field component being E_Φ) polarizations are considered. The scattered fields for three different frequencies are obtained at each receiver point as shown in Fig. 4.46. It should be noted that the amplitudes of the scattered field in all simulations are not normalized by any coefficient. Fig. 4.46 (a, c, and e) represent the case where the loop or dipole antennas are used as transmitters and E_Φ components are measured as the tumour signature. This figure shows the tumour signature in the Φ direction is significantly higher while the loop antenna is chosen as a transmitter. On the other hand, the tumour signature for the transmitter dipole antenna is very weak. From a practical point of view, if the signature of the tumour is weak, the scattered field can be easily obscured by the background noise, and the probability of detecting the tumour decreases. Fig. 4.46 (b, d, and f) represents the case where the loop or dipole antennas are transmitters and the signature of the tumour is found by measuring E_z. It can be observed that even though the polarization of the incident field at the receiver antenna is the same as the polarization of the radiated field, the received scattered field is quite weak, approximately two times less in comparison to the first scenario where the circular-loop antenna was used as a transmitter and E_Φ component of scattered field was measured. This indicates that the breast tissue's composition causes changes in the polarization of the scattered field. It has been realized that the TE comportments of the scattered field is significantly greater while the loop antenna is used for illuminating the breast. The simulation results from the breast phantom suggest that the circular-loop antenna is a promising candidate for use as a transmitter in breast cancer tomography. The most important effect of the proposed method is the ability to achieve similar results using only one fixed radius loop antenna for a wide range of frequencies, while for dipole antennas the size of the dipole antenna has to be adjusted for the frequency range, or a resistively loaded dipole antenna should be used. Despite the fact that the inversion algorithm based on TE and TM components

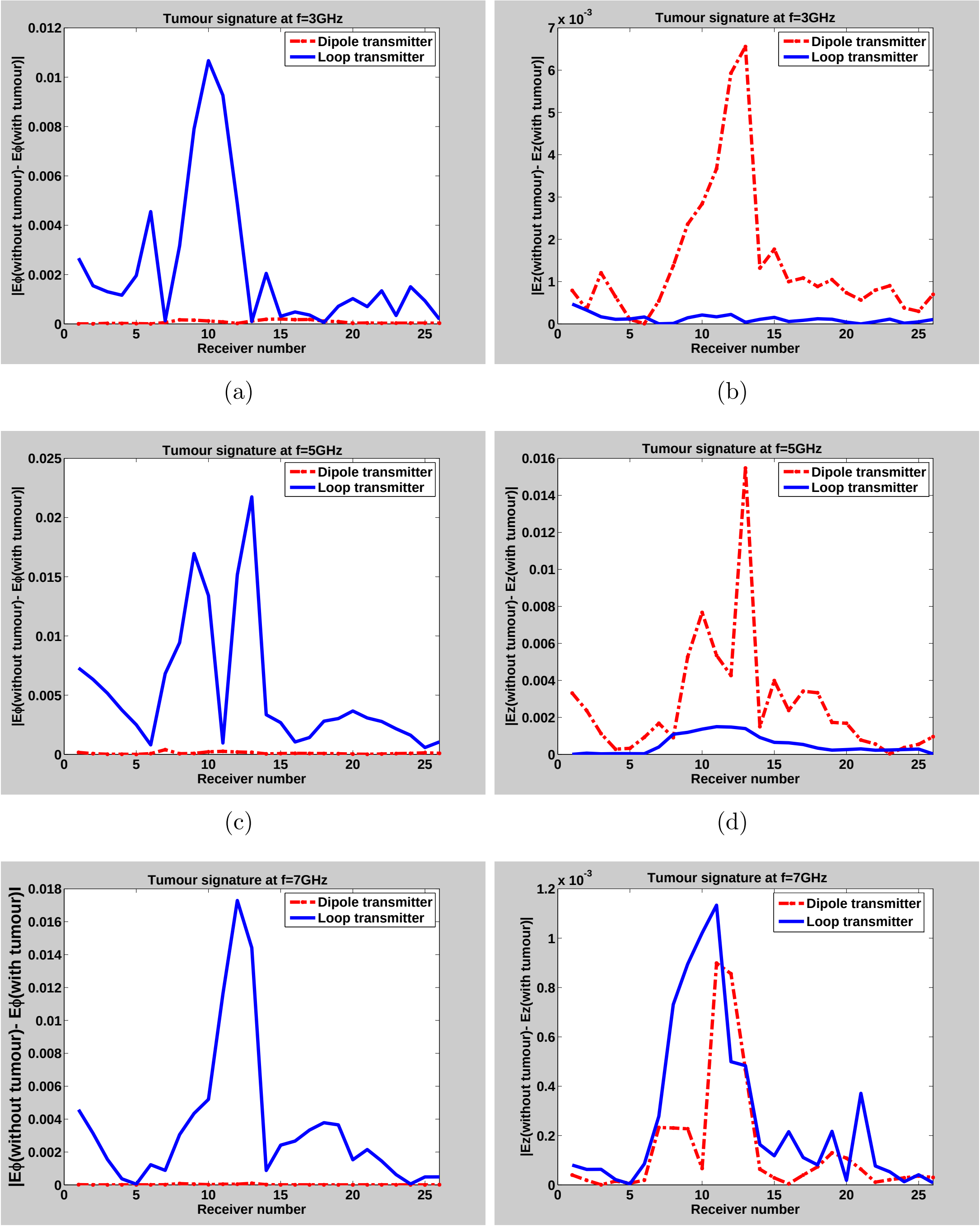

(a) (b)

(c) (d)

(e) (f)

Fig. 4.46: Comparing the tumour signature (a) ΔE_{Φ} at 3GHz, (b) ΔE_z at 3GHz, (c) ΔE_{Φ} at 5GHz, (d) ΔE_z at 5GHz, (e) ΔE_{Φ} at 7GHz, and (f) ΔE_z at 7GHz.

in near-field will improve the image quality by using independent information, most of the inversion algorithms proposed so far are based on TM excitation. The current near-field MWT systems have no, or limited, capability of collecting vectorial field data. In fact, for TE measurement, two orthogonal electric field components need to be measured independently.

5. MICROWAVE TOMOGRAPHY EXPERIMENTAL SYSTEM

> *In every branch of knowledge the progress is proportional to the amount of facts on which to build, and therefore to the facility of obtaining data.*
> James Clerk Maxwell

For almost 30 years, different experimental systems have been developed for data acquisition for microwave imaging systems. A comprehensive review of all of those experimental systems including frequency and time domain systems can be found in [232, 233]. For all of these experimental setups, there has been a discrepancy between measurement and simulation. This discrepancy is not only due to the thermal noise or inherent systematic error in the measurement equipment; the most important source of the noise is "model noise". Therefore, calibrating the raw measured data before the inversion process is a fundamental factor for obtaining good quantitative images in MWT. This chapter describes some of these experimental errors affecting field measurement such as field error and model error for MWT systems.

As mentioned earlier in Chapter 3, inversion algorithms for reconstructing the permittivity and conductivity profiles of the OI typically require measuring the electric field intensity within the imaging domain with and without the OI present. In most inversion methods, including our proposed technique, the unknown dielectric properties are determined using a cost-function that is proportional to the norm of the difference between the measured and simulated electric field intensity. Accurately determining the electric field intensity strongly depends on the calibration. Calibration can be divided into "hardware calibration", "field calibration", and "model calibration". Hardware calibration is the process to compensate the systematic errors in the network analyzer, adapters, and cables during measurements [204, 234]. Hardware calibration has a significant role in the reliability and repeatability of the measured data sets and is an important prerequisite of field calibration. Field calibration is used to determine the electric field intensity values from measurements of S-parameters by the Vector Network Analyzer (VNA), and model calibration is the process of applying a correction coefficient to the calibrated field to correct the assumed model in the inversion algorithm. In fact, after the field calibration, we cannot use the measured data directly in the inversion algorithms without calibrating it to the model utilized in the inverse algorithm. This correction coefficient can be obtained by comparing the simulated field values at the observation points for an assumed model with the measured field value from the same model at those receiver points. This correction factor is then applied to the measured scattered field data to compensate for the discrepancy between the measured and simulated field values. In order to calculate this factor, either the incident field or the scattered field of a known reference object has been suggested and used by researchers. Different reference objects such as an empty chamber (incident field) [22], a metallic cylinder [235, 236], nylon, or polyvinyl chloride [237] have been successfully used for different imaging algorithms. In the following section, our focus will be on model and field calibrations. We examine these two calibrations for the current experimental system that was developed by the imaging group at the University of Manitoba.

5.1 University of Manitoba MWT experimental setup and data acquisition

The University of Manitoba (UM) imaging group recently developed and constructed an MWT prototype. This system includes a plexiglass cylindrical shell with $44cm$ diameter and $50.8cm$ height. A circular array of 24 antennas is mounted inside the plexiglass cylinder. A two-port Agilent 8363B PNA-Series Network Analyzer is used to measure the S-parameters between each antenna pairs, and a 2×24 mechanical switch is used for connecting two ports of network analyzer into 24 antennas. The entire system is capable of moving vertically using an elevator, but the moving part is not functioning yet. The data acquisition is automated, and for each frequency the measurement takes about one minute. For more details about this system see [235]. A photo of the system is shown in Fig. 5.1.

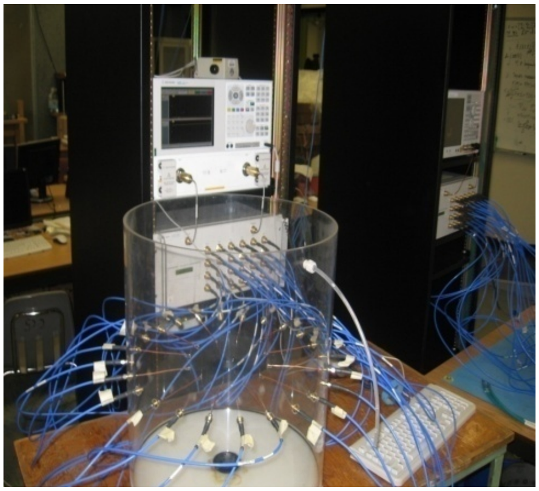

Fig. 5.1: University of Manitoba measurement setup.

5.2 Calibration

5.2.1 Field calibration

In MWT system, we are interested to measure the electric field. But, the fundamental quantities measured by VNA are S-parameters. Therefore, the field calibration is used to determine the electric field intensity values from measurements of S-parameters by VNA. The S-parameters are in the form S_{nm} (the ratio of received signal as measured at port n to the incident signal from port m). $|S_{nn}|$ is commonly known as the reflection coefficient at the port n and $|S_{nm}|$ as the transmission coefficient from port m to port n. The electric field value needs to be derived from the S-parameter given by:

$$E_{21}^{measured} = AF.\left(S_{21}^{measured}\right) \tag{5.1}$$

where $E_{21}^{measured}$ is the electric field when the antenna number 1 is transmitting and antenna number 2 is receiving the signal. $S_{21}^{measured}$ is the transmission coefficient collected by VNA when the transmitting antenna is connected to port 1 and receiving antenna is connected to port 2. AF is the antenna factor which is used to convert measured voltage at the terminal of the antenna into the electric field and will be calculated in the following section.

5.2.2 Model calibration

The second step of calibration is model calibration. In 2D simulation, the antennas are not usually modeled. For example, the infinite line source is considered as a transmitting source to replace the antenna used in real measurements. This approximation can be accurate enough if the antennas are dipole. However, in most MWT systems when the object is in the antenna's near-field and inside a small imaging chamber and in the presence of the non-active antennas, the approximation can cause significant errors and prevent us from finding the real image of the OI. In addition, usually the boundary around the imaging chamber is another cause of mismatch between the 2D model and 3D measurement. Therefore, the model calibration is required to reduce the error. Model calibration is the process of adjusting the raw 3D scattered field data such that it can be effectively employed by the approximate 2D models upon which the inversion algorithms are based. There have been a number of model calibration methods suggested by researchers [22, 235–237], but they only calculate the correction coefficient between measurement and the 2D model. In the following section, we simulate the 3D model which will be useful to determine the correction coefficients for model calibration. Besides calculating the model calibration coefficients from the 3D simulation, it can be used for different purposes such as: (i) investigating the best frequencies where the 2D and 3D models do not significantly differ, (ii) finding the optimum frequency for maximum penetration depth and resolution, (iii) estimating the incident field to be used in the imaging algorithm, and (iv) studying polarizations of the scattered field when the object is present.

I. 3D simulation model

In this stage, we compare the results of a 3D simulated data with measured data. We simulated the University of Manitoba (UM) MWT system using a MoM-based electromagnetic simulation package, WIPL-D [231]. Fig. 5.2 shows the 3D simulation of the UM MWT system using 24 dipole antennas (designed for $f = 2.05$GHz). Fig. 5.2 (a) shows the MWT while a Perfect Electric Conductor (PEC) circular cylinder with 87mm diameter is placed in it. Fig. 5.2 (b) shows the simulation setup of the same system with a 50mm diameter loss-less circular cylinder dielectric with permittivity of 3.0 as OI.

The transmission coefficient (S_{j1}) (j is an index showing the receiver antenna number) simulation and measurement results at the frequency of 2.05GHz (dipole's resonance frequency) for two models of Fig. 5.2 (a) and (b) are shown in Fig. 5.3.

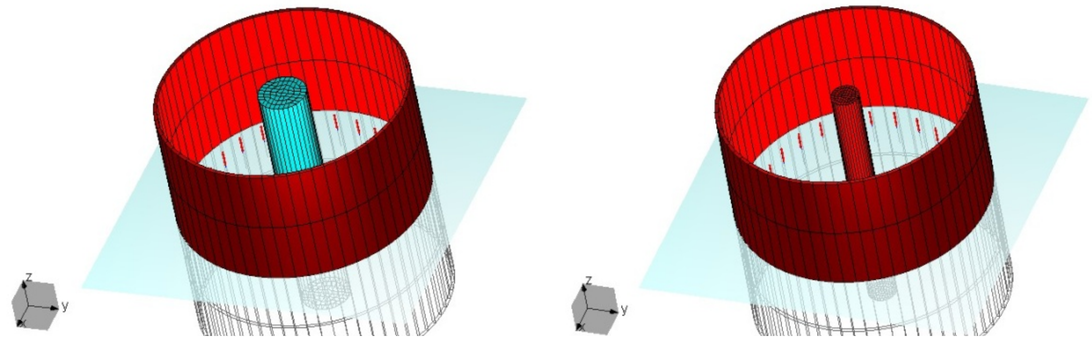

(a) (b)

Fig. 5.2: 3D modelling of the (a) 87mm diameter circular cylinder PEC, (b) 50mm diameter circular cylinder dielectric with permittivity 3.0.

Fig. 5.3 (a) and (c) show the amplitude of S_{j1}, and Fig. 5.3 (b) and (d) depict the phase of S_{j1} for different receiver antennas. As the results clearly show, even though we considered a full 3D model for simulation, there was still a discrepancy between the simulation and measurement results. This is due to the fact that the transmission coefficient is more affected by the interference from outside sources and imperfection in the placement of the transmitting and receiving antennas. Obviously the interference and multi-paths from outside of the chamber can make a significant change in the results, which is different than thermal noise. In order to compensate for the discrepancy between the simulation and measurement results, we defined a correction coefficient for amplitude and phase for each antenna. Since in the simulation it is easy to use free space, the correction coefficient was calculated based on free

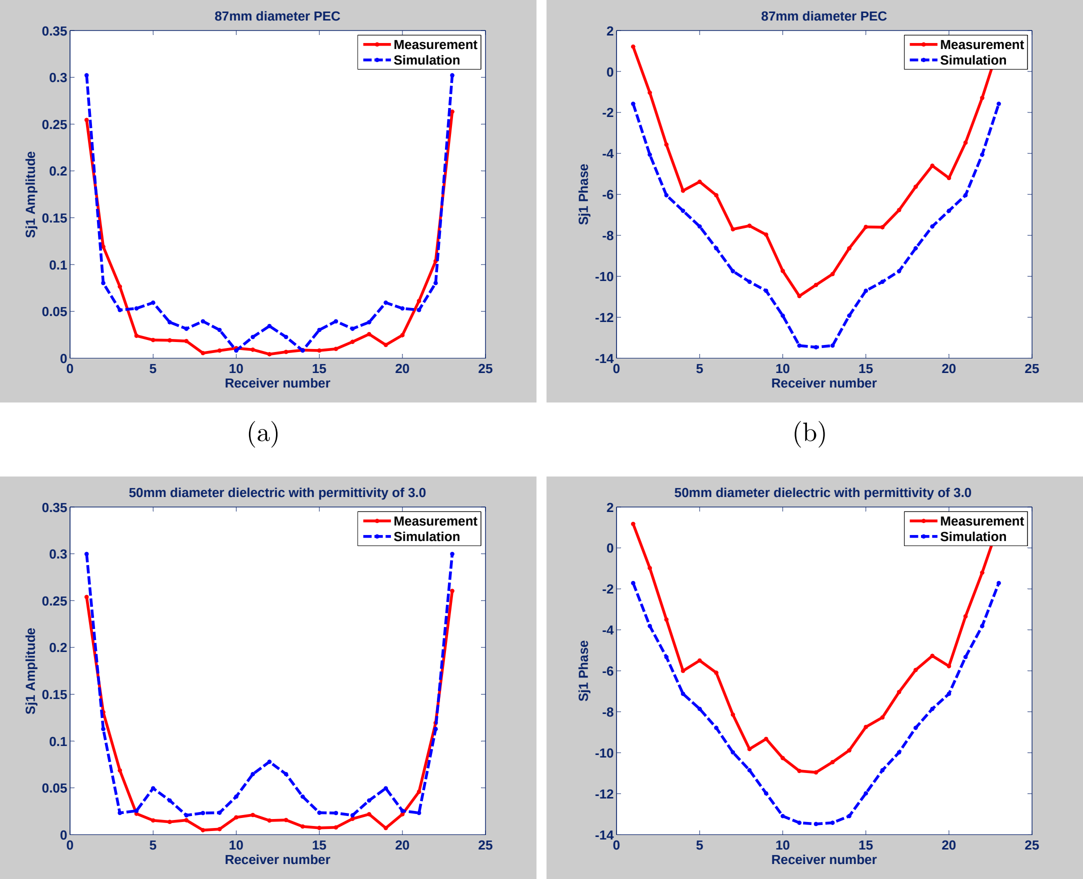

(a) (b)

(c) (d)

Fig. 5.3: S_{j1} (a), (c) magnitude and (b), (d) phase comparison of the 3D simulation and measurement results for $87mm$ diameter PEC and $50mm$ diameter circular dielectric with permittivity of 3.0.

space measurements:

$$\text{Amplitude correction coefficient} = \frac{\text{Amplitude of } S_{j1}(\text{Measurement without object})}{\text{Amplitude of } S_{j1}(\text{Simulation without object})} \tag{5.2}$$

$$\text{Phase correction coefficient} = \frac{\text{Phase of } S_{j1}(\text{Measurement without object})}{\text{Phase of } S_{j1}(\text{Simulation without object})} \tag{5.3}$$

Fig. 5.4 compares the simulated and calibrated data using the above incident field calibration factor for each antenna individually. As can be seen in this figure, the discrepancy between the calibrated and the simulation data decreases significantly. This type of calibration compensates for the differences in amplitude and phase due to the interference and multi-path caused by scatterers outside of the imaging chamber and the environment's noise. However, the presence of the OI to be imaged causes perturbation in the near-field (if the antenna is close to the OI) and affects antenna's behavior (antenna loading) that should also be considered. Therefore, finding an appropriate reference object for microwave tomography systems is necessary. The next step of calibration is to calibrate the system with a proper reference object.

5.2.3 Model calibration using reference object

In order to calibrate the measured data, ideally it is better to use a reference object which is similar in size, shape, and dielectric properties to the OI. In fact, calibrating the measured data ($E^{measured}_{scattered}$) means that for every receiver antenna a single correction factor ($F_{i,m(ref)}$, where i is the transmitter number and m is the receiver number)

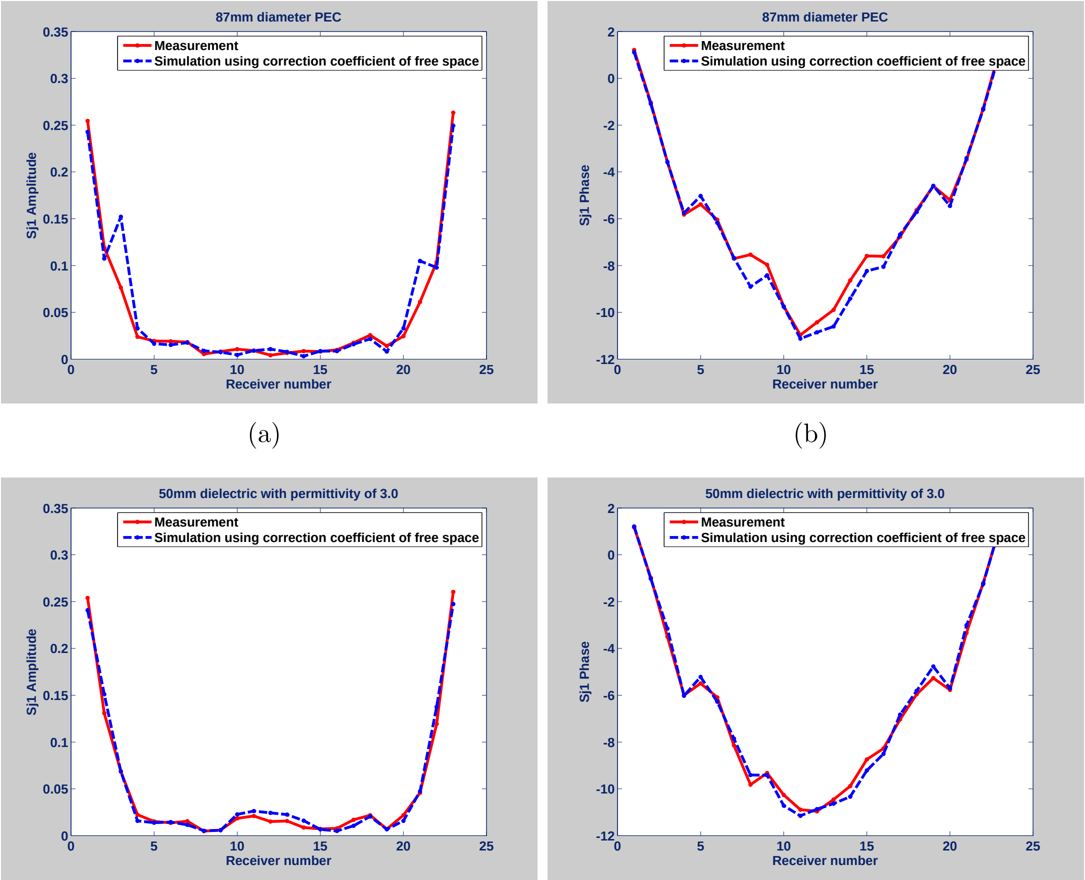

(a) (b)

(c) (d)

Fig. 5.4: Comparing the S_{j1} amplitude and phase measurement and simulation for, (a), (b) $87mm$ diameter PEC, and (c), (d) $50mm$ diameter dielectric with permittivity of 3.0.

needs to be defined for its respective transmitter.

$$E_{scattered}^{calibrated} = F_{i,m(ref)}.E_{scattered}^{measured} \tag{5.4}$$

The $E_{scattered}^{calibrated}$ is the simulated field data obtained for the same receiver point. Therefore, for each MWT system and for every frequency, an array of calibration factors needs to be calculated. For example, for n transmitter and m receiver antenna, an $n \times m$ correction coefficient is needed. The $F_{i,m(ref)}$ is the ratio of the simulated field over the measured field for a model state. Therefore:

$$F_{m(ref)} = \frac{E_{ref}^{simulation}}{E_{ref}^{measured}} \tag{5.5}$$

where $E_{ref}^{simulation}$ and $E_{ref}^{measured}$ is the electric field simulation and measurement for a reference object. By replacing (5.5) into (5.4):

$$E_{scattered}^{calibrated} = \frac{E_{ref}^{simulation}}{E_{ref}^{measured}}.E_{scattered}^{measured} \tag{5.6}$$

Again, as noted earlier, the VNA has a unity output voltage and the field component of interest can be assumed to be proportional to the induced voltage at the port of the antenna. Therefore:

$$E_{21}^{measured} = AF.\left(S_{21}^{measured}\right) \tag{5.7}$$

where AF is the antenna factor. By inserting the (5.7) into (5.6):

$$E_{scattered}^{calibrated} = \frac{E_{ref}^{simulation}}{AF_{ref}.\left(S_{21}^{measured}\right)_{ref}}.AF_{OI}.\left(S_{21}^{measured}\right)_{OI} \tag{5.8}$$

where AF_{ref} and AF_{OI} are the antenna factors when the antenna is in front of the reference object and the OI, respectively. If $AF_{ref} = AF_{OI}$, then a field calibration process can be used to effectively cancel the antenna factor, from the measurements. Therefore:

$$E_{scattered}^{calibrated} = \frac{E_{ref}^{simulation}}{\left(S_{21}^{measured}\right)_{ref}}.\left(S_{21}^{measured}\right)_{OI} \tag{5.9}$$

However, the condition ($AF_{ref} = AF_{OI}$) dictates that the reference object should have known dimensions and dielectric properties and be similar to the OI. This method of calibration has eliminated any errors which are constant over the two measurements (measurement of OI and measurement of the reference object). If the condition of $AF_{ref} = AF_{OI}$ is not satisfied, then there will be some systematic error between measurement and simulation due to the mismatches at the connector, phase shift, and cable losses, as well as mutual coupling between antennas.

5.3 Experimental inversion results

5.3.1 Experimental data from UM MWT system

In this section, we present an example to illustrate the image reconstruction capability of the $(\mathrm{FD})^2\mathrm{TD}$/GA using experimental data from the UM MWT system. In the MWT system, it is necessary to reduce the cross-polarization level of the antenna as much as possible in order to use the 2D assumption from the 3D model. To reduce the polarization, we utilize a Double-Layer Vivaldi Antenna (DLVA) (Fig. 5.5 (a)). This antenna is designed and optimized for the bandwidth of 2-10GHz [238]. The high directivity of the antenna also minimizes the coupling between transmitting and non-active antennas. The detail of the antenna design has been reported in [238]. Fig. 5.5 (b) shows the results of comparing the S_{11} from measurement and simulation for one single DLVA using the WIPL-D software. As can be seen in Fig. 5.5 (b) there is a disagreement between measurement and simulation results. The disagreement in S_{11} appeared as a shift of frequency between simulation and measurement which is usual for WIPL-D results. The source of this error is mostly computational error in modelling the excitation, and fabrication accuracy. Fig. 5.6 shows the UM microwave tomography setup with 24 Vivaldi antennas.

As an initial phantom experiments, we utilized a wooden block with square cross-section and $87 \times 87 \times 300mm^3$ dimensions. The dielectric constant of the wood is around 1.8 at 3.5GHz, and the conductivity is very low. We considered the wooden

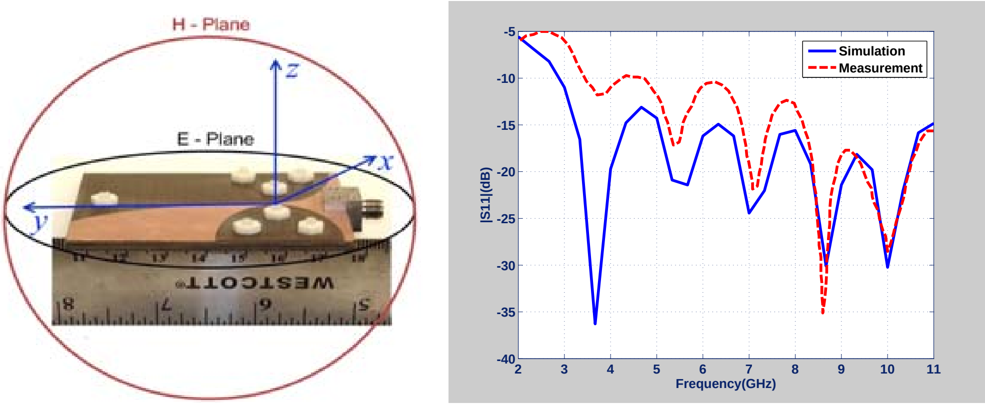

(a) (b)

Fig. 5.5: (a) Double-layer Vivaldi antenna [238], (b) comparing simulated and measured S_{11} for Vivaldi antenna.

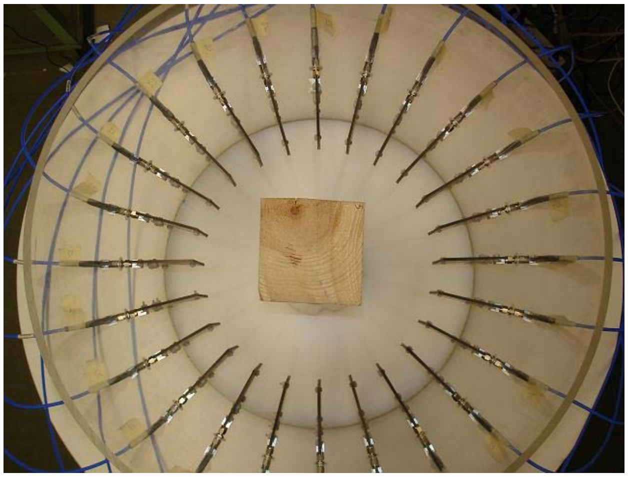

Fig. 5.6: UM microwave tomography system using 24 Vivaldi antennas (top view) [235].

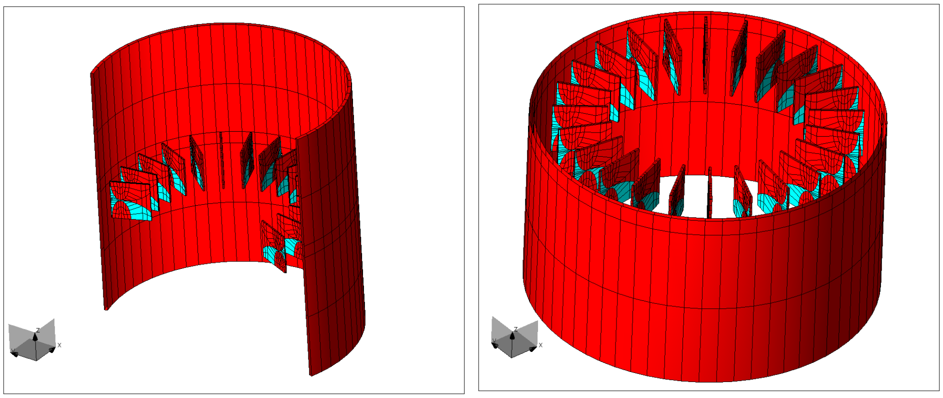

(a) (b)

Fig. 5.7: Simulation geometry of the MWT chamber with 24 Vivaldi antennas.

block as a loss-less material in simulation. The wood was placed at the center of the UM MWT chamber within air, as shown in Fig. 5.6. The measurement was taken at the frequencies between 3-7GHz, with step of 0.5GHz. This data must then be calibrated as explained in the previous part. To perform the calibration, we first calibrated the MWT system using the correction coefficient (5.2). For this purpose, the entire MWT system has been simulated using the 3D WIPL-D solver (Fig. 5.7). Fig. 5.8 compares the transmission coefficient values for the 3D simulation data and the raw measured data at 3 and 6GHz. From the Fig. 5.8, it is observed that the simulation and measurement results do match at a 3GHz frequency, but not at a 6GHz frequency. This means that the calibration factor is a function of frequency, as expected. Tab. 5.1 shows the average error between the transmission coefficient values from simulation and measured data at different frequencies. After calibrating the MWT system without an object, in order to consider the loading effect of antennas, we

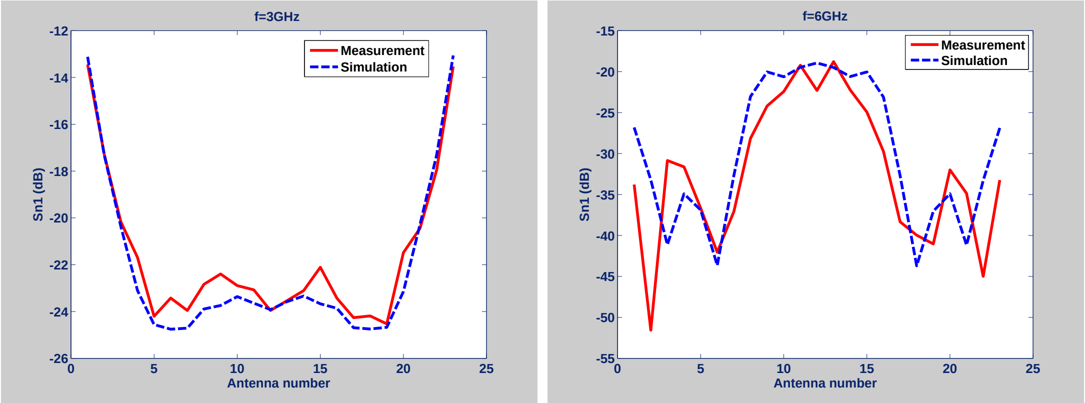

(a) (b)

Fig. 5.8: Amplitude of S_{n1} vs. antenna number at (a) 3GHz, and (b) 6GHz.

Tab. 5.1: Total error in S_{n1} for UMMWT chamber.

Frequency (GHz)	3	3.5	4.5	5	6	8
Amplitude (dB)	0.47	2.25	1.54	0.54	2.42	3.81
Phase (^{o})	0.8	1.65	1.12	1.74	1.36	1.91

calibrated the MWT system using a reference object. For this purpose, we measured the S-parameters for a reference object with a known radius and known dielectric properties. As an example, we have utilized two metallic cylinders with diameters of 38.4mm and 50.9mm, as well as incident field as a reference object. We used these reference objects due to the ease of characterization. The Fig. 5.9 compared the simulated and calibrated data for different reference objects at 3 and 3.5GHz. It should be noted that at 3GHz, where the coupling between antennas is low, the calibrated data is quite matched with the simulation compared to the 3.5GHz. However, even at 3GHz where the coupling seems to be minimal, there is still some discrepancies between simulated and measured fields which might be due to the assumption of a

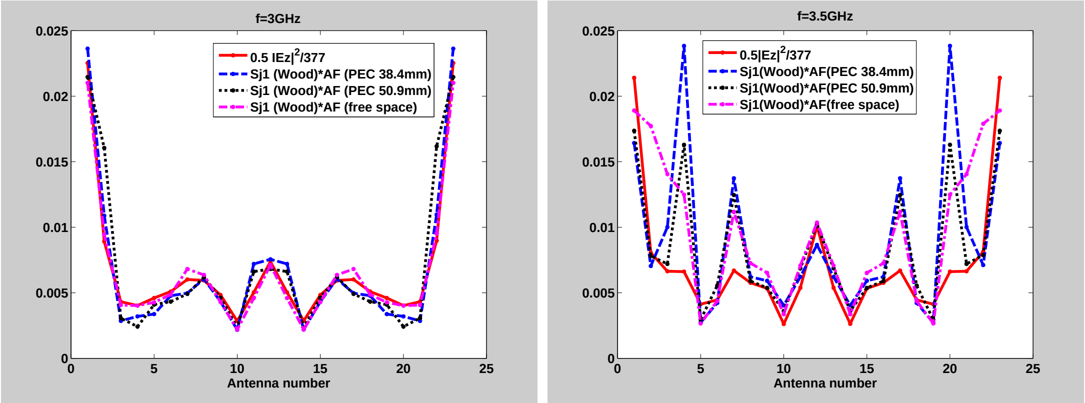

(a) (b)

Fig. 5.9: Magnitude comparison of simulated and calibrated electrical field for different reference objects at (a) 3GHz, and (b) 3.5GHz.

plane-wave source based incident field. Another reason might be due to the loading effect of the reference object on the antenna behavior. Besides, at other frequencies where the antenna-coupling was high the results were much worse. This means that the antenna coupling effects are not entirely removable by the calibration procedure, and they are major sources of error. To obtain usable frequencies for our inverse scattering experiment, we selected those frequencies where the coupling was minimum. We expect that when the MWT system is filled with a matching material, the antenna coupling will become significantly less noticeable due to losses in the material. As *a-priori* information, we considered the reconstructed relative complex permittivity within physical ranges $\epsilon_r \geq 1.0$ and $\sigma = 0.0 S/m$, with 1 decimal point accuracy and a known geometry of OI and background material. The single-frequency 3.5GHz reconstructed image is shown in Fig. 5.10. When inverting the data, we considered

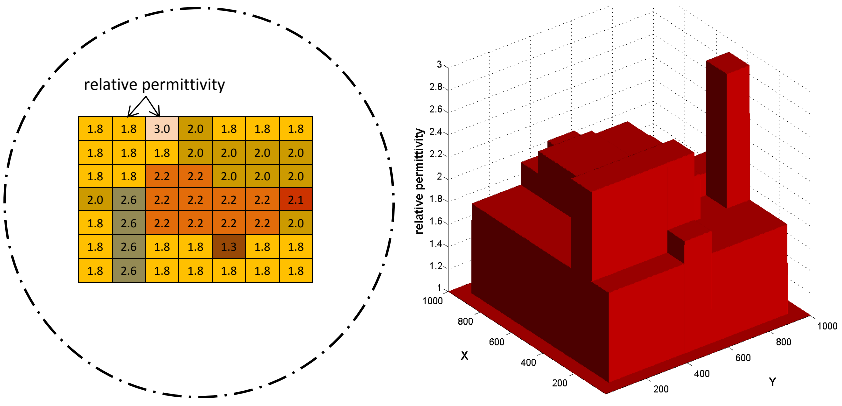

1.8	1.8	3.0	2.0	1.8	1.8	1.8
1.8	1.8	1.8	2.0	2.0	2.0	2.0
1.8	1.8	2.2	2.2	2.0	2.0	2.0
2.0	2.6	2.2	2.2	2.2	2.2	2.1
1.8	2.6	2.2	2.2	2.2	2.2	2.0
1.8	2.6	1.8	1.8	1.3	1.8	1.8
1.8	2.6	1.8	1.8	1.8	1.8	1.8

(a) (b)

Fig. 5.10: Reconstructed image of wooden block (map of permittivity), (a) 2D view, and (b) 3D view.

four different transmission angles (0^o, 90^o, 180^o, and 270^o) and 23 receiver antennas at $15^o \leq \Phi \leq 345^o$ respect to the transmitter. The reconstructed map of permittivity is generally correct; however, in some parts the exact values are not obtained, but the results are close to real values. As a quality indicator, we define the error between the true image and the reconstructed image as follows:

$$E_{error} = \frac{\sum_i \sum_j \frac{|\epsilon_{r(\text{reconstructed image})}(i,j) - \epsilon_{r(\text{true image})}(i,j)|^2}{|\epsilon_{r(\text{true image})}(i,j)|^2}}{\text{number of cells}} \tag{5.10}$$

where i and j are the cell numbers in the x and y directions, respectively. In this example the E_{error} at 3.5GHz is $\approx 4\%$. We speculate that the wooden block is a heterogeneous object and the permittivity varies within the block. Therefore, the reconstructed permittivity map is probably closer to the real values.

5.3.2 Experimental data from Institut Frsenel's MWT system

In order to test the *blind* inversion capabilities of the proposed algorithm for solving the inverse scattering problem, we present inversion results from 2D experimental scattering data collected by the Institut Frsenel. In 2005, the Centre Commun de Ressources Micro-Ondes (CCRM) at the Institute Fresnel in Marseilles, France provided an invaluable public database of experimental multi-frequency electromagnetic field data from multiple scatterers. This database has been used by many researchers around the world for evaluating their MWT algorithms. For more details about the measurement data including system dimensions, transmitting and receiving antennas, frequencies, polarizations, and targets, see reference [239]. This data set was collected for TE and TM polarizations in free-space. For this measurement, a double ridged horn antenna was used in an anechoic chamber setup with a frequency of 1-18GHz. Antenna was 1.67 meters away from the center of the imaging region. The two antennas mechanically rotated around the OI and collected the data at 241 positions per transmitter. The measured data was then calibrated such that the transmitted field by antennas can be approximated by a plane-wave and the effects of antennas are removed. To calibrate this data, the offset calibration method was used [240]. In this type of calibration, a single correction factor is used for all transmitter/receiver pairs. Such a calibration has provided good results in far-field measurement systems.

Fig. 5.11 (a) shows the cross-section of a foam cylinder (SAITEC SBF 300) with $80mm$ diameter and dielectric constant of 1.45 ± 0.15. A plastic cylinder (berylon)

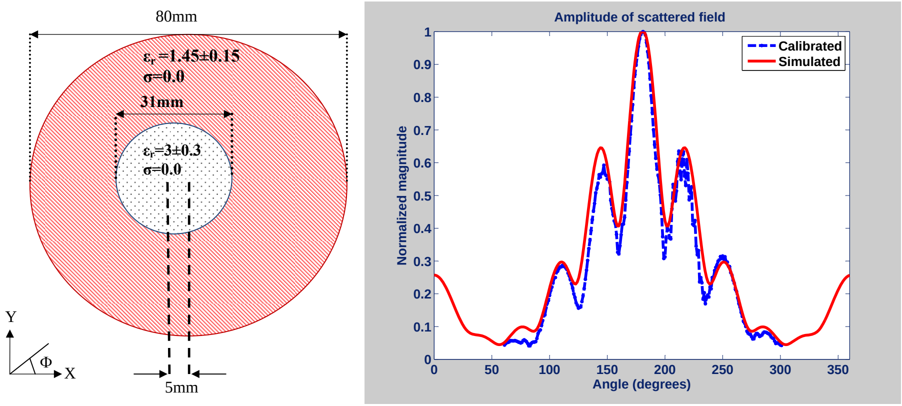

(a) (b)

Fig. 5.11: Geometry for Frsenel Data Set FoamDielint, (a) schematic of the scattering cylinders, b) comparing the calibrated and simulated scattered field at 8GHz where the transmitter antenna is positioned at 180^o.

with diameter of $31mm$ and dielectric constant of 3 ± 0.3 is placed inside the foam cylinder, $5mm$ away from the center. The data for this setup was collected for 8 transmitters and 241 receivers per transmitter at 9 frequencies from 2-10GHz in 1GHz steps. Fig. 5.11 (b) and Fig. 5.12 (a),(b) compare the scattered field given by simulation and measurement, after calibration at 8GHz, when the transmitter antennas are positioned at $\Phi = 90^o$, 180^o, and 270^o. The inversion of this data set using the $(\text{FD})^2$TD/RGA method is shown on the grid of 8×8 in Fig. 5.13. We considered that the location, size, and material of the foam cylinder is known. We also constrained the inversion process for loss-less material and the relative permittivity of the scatterers to be in the range of 1-10 ($1 < \epsilon_r \leq 10$). We utilized multiple-frequencies in our techniques for the frequency band between 2-8GHz, in 2GHz steps. While the $(\text{FD})^2$TD method has been used in the forward solver, the data for all frequencies are

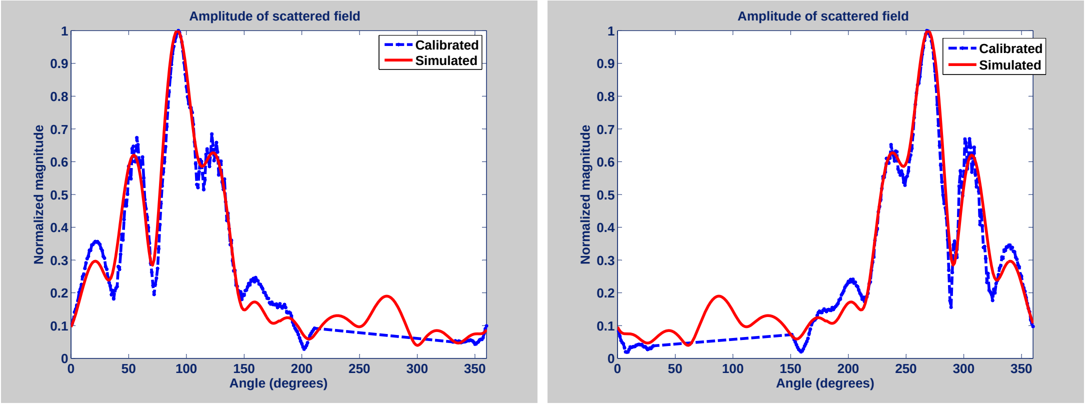

(a) (b)

Fig. 5.12: Comparing the calibrated and simulated data at 8GHz where the transmitter antenna is positioned at (a) 90^o, and (b) 270^o.

utilized simultaneously. As a proof of concept, we considered only one transmitter at $\Phi = 0^o$ and 241 receiver antennas within $60^o \leq \Phi \leq 300^o$. However, it is expected that using multi-view techniques will provide significantly better results. The search space area was divided into 64 square cells, with $1cm$ side. As it can be seen in Fig. 5.13, the algorithm accurately reconstructs the location of the target. In terms of dielectric properties of the object, the reconstructed image is close enough to the actual one, but there are still differences in some parts of the image. In this example the E_{error} at 2GHz is $\approx 7.6\%$. For the shape of the scatterer, there is a discrepancy between the actual image and the reconstructed image. This inaccuracy in the result of shape and dielectric properties can be decreased if the cell size is decreased at the price of increasing the runtime.

In both examples, the multi-frequency reconstructions were used. There were

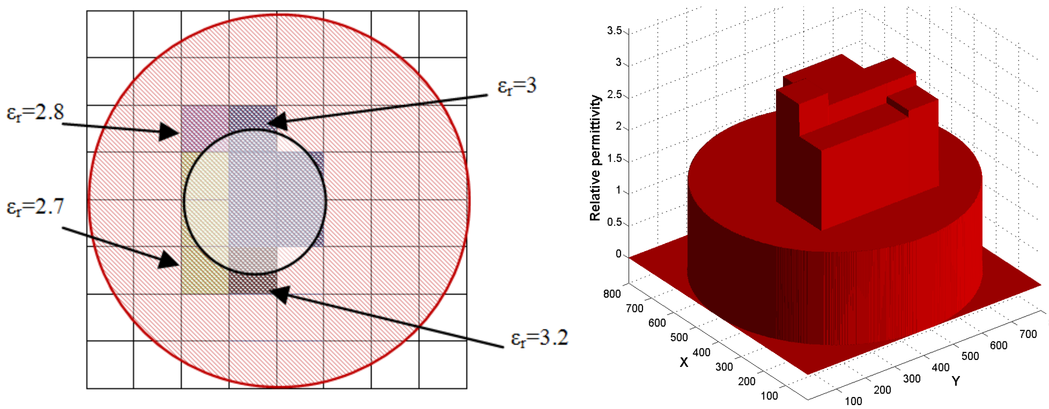

(a) (b)

Fig. 5.13: Reconstruction of Fresnel Data Set FoamDielint (map of permittivity), (a) 2D view, and (b) 3D view.

some cases where the data collected by dipole antennas yielded results that did not converge by using only a single-frequency. We have determined that the proposed MWT algorithm is very sensitive to the data collection and calibrations, and any error in the model will lead to significant error in results. In other words, the simulated data needs to be as close as possible to the calibrated data. In particular, the 3D modelling effects are extremely important, and we need to build a system to be as close as possible to 2D approximations. Therefore, the image quality is essentially compromised by the various approximations associated with operating in 2D. From a practical point of view, the measurement chamber is considered to be an infinitely long cylinder in order to model the 2D structure, but complications arise with 3D diffraction and scattering of electromagnetic waves at microwave frequencies that produce transverse electric field components into the measurement results. This mismatch between the physical situation and model assumptions has the possibility of leading to errors in the reconstruction. In order to mitigate this problem, we should use antennas with a narrow beamwidth in the horizontal direction and attempt to create a 2D slice of the 3D object under investigation. As we saw in these examples, the mutual coupling between antennas is a source of error and can't be removed by calibration. The mutual coupling problem can be reduced using an array with low mutual coupling. In the forward solver, we considered the observation point at the far-field zone, but in practice this may not be the case. When a lossy dielectric matching medium (such as oil or water) is used, or the object to be imaged is small enough, then the far-field assumption is acceptable. However, the matching medium and boundary of the imaging chamber have effects on the antenna's behavior that can not be ignored. Reflections from the Plexiglas which is holding the antennas also might be a source of error. By using the lossy dielectric matching medium, the interactions between the antennas, the surrounding system, and the object can be ignored. On the other hand, using the lossy dielectric matching material provides low energy, or sometimes no energy, at the receiver points due to the high conductivity, and this creates a poor SNR for collecting data compared with using low-loss matching material or free space. Therefore, there is a trade-off between using the lossy dielectric background for better 2D approximation and the sensitivity of the system. In addition, in the simulation we considered plane-wave as an incident field which has only z polarized component, but in a 3D structure it may not be a true incident field model.

Therefore, it is absolutely necessary to adjust the 3D scattered field data into the 2D model. Antenna design for UWB-signal radiation is also one of the main challenges, because antennas with low-cross-polarization, high gain, and efficient structures are required.

While the proposed MWT method has made successful inversion in heterogeneous and dispersive environments for hypothetical measured data, for experimental data in some cases due to the sensitivity of the system to the calibration, the results did not converge to the right solutions. We hope that this sensitivity will be advantageous once the calibration issues have been solved.

6. CONCLUSIONS AND FUTURE WORK

> *If we knew what it was we were doing, it would not be called research, would it?*
> Albert Einstein

The objective of this thesis is to introduce a novel method based on stochastic approaches without any simplification in the non-linear wave equation, in order to circumvent the inverse problem. This approach is effectively capable of retrieving the unknown electrical parameters from the inside of the target and creates a 2D quantifying image in a reliable way from a known host object. The proposed technique deals with an object that has a complex distribution of dielectric properties and provides an image of permittivity and conductivity, as well as a quantitatively reconstructed frequency-dependent profile of these properties. This method is based on the time domain iterative approach to solve an inverse scattering problem that is efficient and accurate for dispersive and heterogeneous media.

The proposed method in this thesis is based on a time-domain forward solver (i.e. Frequency Dependent Finite Difference Time Domain ($(FD)^2TD$)), and global optimization method (Genetic Algorithm (GA)). This combination is novel and unique in its kind. Similar to other inverse scattering problems, MWT poses an ill-posed optimization problem. This means the cost-function to be minimized has multiple local minima. Therefore, we choose GA to reduce the risk of ending up with non-true solution (local minima). Within this framework, we briefly study different classes of GA optimization methods such as real-coded GA, binary-coded GA, and hybrid GA (combination of real-coded and binary-coded GA). The implications and possible advantages of each type of GA optimization were discussed throughout this thesis. Synthetic and measurement inversion results were presented. For all cases, the images were successfully reconstructed. The hybrid GA improved the accuracy of the inversion method. The proposed technique is capable of using multi-frequency and multi-incident/multi-view techniques which provide additional information for the reconstruction of the dielectric properties profile and improve image quality. One of the main advantages of the proposed technique is its flexibility of accommodating *a-priori* information into the algorithm. The key distinction between the proposed method and similar methods based on GA that have been previously proposed is the utilization of $(FD)^2TD$ to accurately evaluate the field and fitness values. Inclusion of *a-priori* information for regularization is also novel.

In the last decade, there has been significant attention and subsequently great advances in the application of MWT in biomedical imaging (BMI). We considered the breast cancer imaging as a primary application for the proposed technique. We analyzed the scattered field and penetration depth for different tissue compositions of breast phantom and optimized the matching material in order to increase the penetration depth. The dispersive characteristic, heterogeneity, and water content dependency were all considered in the development of the MWT system. The proposed MWT technique has been tested using MRI of a patient. The results show an encouraging ability to differentiate between different breast tissue types and to detect small tumours with a few millimeters size. The presence of noise on synthetic data was also considered and the dependence of the reconstruction accuracy on the signal-to-noise ratio was investigated. It is important to note that matching the measurement and simulation results is the fundamental factor for determining the MWT image quality. After comparing the results of simulation and measurement of the direct problem, we found that the noise is not simply receiver thermal noise and that the "modelling errors" contribute more to the errors present in the data. Therefore, the model calibration is absolutely necessary to adjust the 3D scattered field data so that they can be effectively employed by the approximate 2D model upon which the inversion algorithm is based. It was demonstrated that for any MWT experimental system the field and model calibrations need to be performed prior to inversion. We discussed the "field calibration" and "model calibration" in detail and their application into the University of Manitoba's MWT system.

In the proposed technique for image reconstruction, depending on the number of unknowns and the size of the reconstruction problem, the computation time needed for the convergence of the solution varies from a few hours to several days. Therefore, the parallel version of the proposed algorithm was implemented in order to overcome the computational runtime and improve the convergence rate.

We presented preliminary image reconstruction results for experiments performed by the University of Manitoba's and the Institut Frsenel's MWT systems. Although further analysis should be performed for a complete assessment of the methodology, the obtained results are indicative of the potential of MWT as an effective diagnostic technique deserving further investigations.

6.1 Future work

MWT techniques are potentially very appealing, but they have some intrinsic drawbacks related to the nature of the inverse scattering problems and to the complexity of the hardware setup required to collect the necessary field measurements. In order to overcome these drawbacks, more research is needed.

- Theoretically speaking, the microwave tomographic system improves the image quality, if the number of the transmitter and receiver antennas as well as the number of sampling frequencies are increased. Therefore, choosing optimal parameters such as number of frequencies, number of antennas, and antenna configuration can have significant effects on the image quality.
- In the FDTD technique, in order to model the complex shape composed of curved surfaces, the staircasing method has been used. In this method, the

curved surface is represented by approximating its trajectory with a series of steps in the grid. However, the electric field scattered from sharp edges can cause singularities in the numerical analysis. Implementation of non-uniform mesh or the sub-gridding technique is suggested to model the shape of the curve more closely.

- Due to its straightforward formulation, the proposed algorithm can be extended into a 3D imaging technique by using the 3D FDTD/GA method or by creating different images of different cross-sections. However, the simulation runtime increases and needs to be addressed by using parallel computing techniques.

- The parallel approach has been used in this thesis to reduce the computation time. However, the rapid advances in computer technology will even further reduce the computation time and memory requirement. In addition, the parallel GA has been used in terms of a parallel computer system; however, the GA can be parallel by using a parallel search from multiple points in the investigation domain as well. In addition to the GA, in this thesis, for parallel FDTD the computational domain is divided along the x-axis. The parallelization can be extended to x and y directions.

- MWT is on the edge of becoming a useful clinical tool for the detection and subsequent treatment of breast cancer. If MWT is to become competitive with the current gold-standard of mammography, the minimum detectable lesion size must be reduced (to $3mm$), which implies that the resolution must increase. Enhancing the resolution (the smallest detectable size) of MWT needs more research.

- In this thesis, we have shown that vector-field measurements improved the sensitivity. In addition, there is some early evidence that vector-field measurements improve the resolution [87]. Further development of both experimental system capable of collecting vector-field measurements as well as 3D full-vectorial inversions would allow for significant improvement in MWT.

- Once the resolution is improved, the specificity of the new imaging technique needs to be investigated. In order to measure the specificity of the MWT for breast cancer imaging, some information about the dielectric properties of the abnormalities and cancerous tissues need to be available. Thus, more investigation needs to be performed to find the amount of contrast between benign and malignant tissues in terms of dielectric properties.

- One of the main advantages of MWT for breast cancer imaging is the dependency of the tissue dielectric properties on its physiological condition. This has been briefly discussed in Chapter 4 of this thesis. Some investigation into the correlation between tissue dielectric properties and the physiological condition is needed. This investigation can open up many opportunities to MWT technology and improve the imaging techniques explicitly and implicitly.

- Due to the dependency of dielectric properties of biological tissues on physiological conditions, MWT has the potential to be a high specificity imaging technique and to become a complementary method for magnetic resonance imaging. Of course, this is just the speculation and is not conclusive in any sense, and more research is needed to provide further evidence. In general, each of the breast cancer modalities offers its own advantages and disadvantages. Ultimately, it is expected that the right combination of multiple imaging modalities can provide a solution to early detection of breast cancer.

Appendices

Appendix A

INSTABILITY OF THE INVERSE SCATTERING PROBLEM

A.1 Several local minima for the inverse scattering problem

As was indicated in Chapter 3, the inverse scattering problem is unstable because a small arbitrary change in the incident field may result in an arbitrarily large change in the material parameters. From an optimization point of view, non-uniqueness means that there are multiple global minima, and instability means that convergence depends on the initial point. In order to show the non-uniqueness and instability we ran a forward simulation of 2D $12cm$ diameter dielectric cylinder at 6GHz while the permittivity and conductivity was changed from 0 to 80 and from 0 to 8, respectively. Fig. A.1 shows the scattered field at two different observation points ($\Phi = 90^o$ and $\Phi = 270^o$). This figure demonstrated that different global minima appear when the input parameters (permittivity and conductivity) change in respect to output which is scattered field.

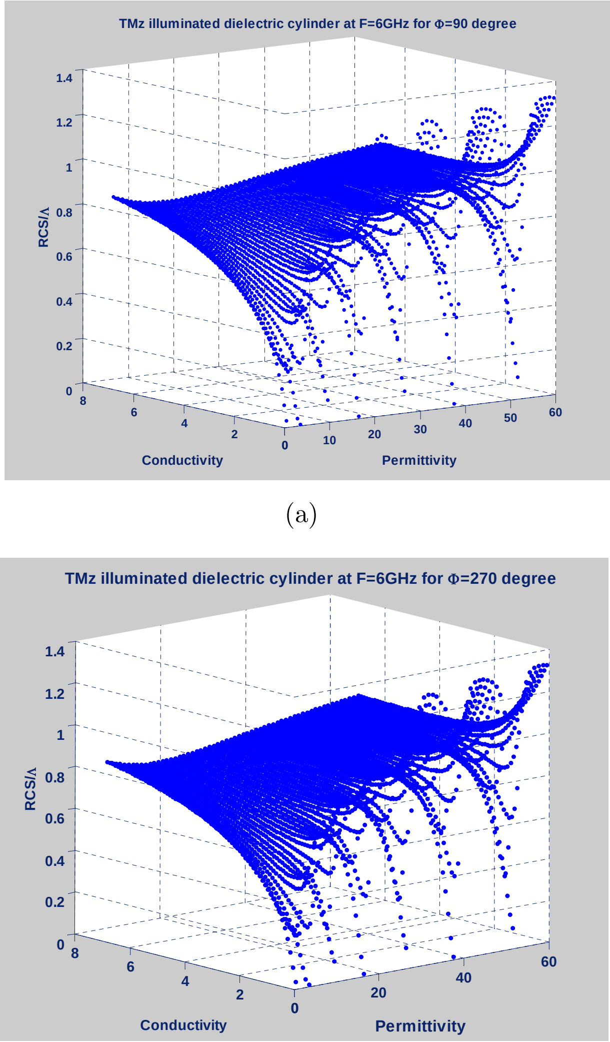

(a)

(b)

Fig. A.1: Normalized scattered field of dielectric circular cylinder while observation point is at (a) $\Phi = 90^o$, (b) $\Phi = 270^o$.

Appendix B

GENETIC ALGORITHM OPERATORS

B.1 Selection, crossover, and mutation

This procedure is to stochastically select from one generation to create the basis of the next generation. There are many different algorithms in literatures for selecting individuals such as the Roulette Wheel Selection (RWS), Tournament Selection (TS), Elitist Selection (ES), Rank Selection (RS), and so on [147]. In this thesis, the TS has been used for the selection procedure. Crossover and mutations are procedures used to create the new chromosome from selected parents. The crossover operation takes a pair of chromosomes called the parents and gives a pair of offspring chromosomes. Crossover enables each generation to inherit the best properties of the previous generation while mutation is performed to ensure that the solution is not stuck in a local minimum. Suitable operators possibly enhance the convergence speed and prevent the solution from being trapped in a local minimum. An effective design greatly increases the convergence rate of the maximization process. There are many types of possible crossover operations such as single point crossover, two point crossover, uniform crossover, and arithmetic crossover. In BGA optimization, in this thesis, the simple one-point crossover was used. In this operation, we chose a number between *1* and *n-1* (n is the total number of bit in each chromosome) and considered this number as a crossover point. In RGA, the arithmetic crossover is applied in this thesis. Based on the probability of crossover, two individuals $C_i^k, k = 1, 2$ and i, a random number between *1* and n, are randomly selected from the population and two offspring h_i^k are generated, where

$$h_i^1 = \varsigma C_i^1 + (1 - \varsigma) C_i^2 \tag{B.1}$$

$$h_i^2 = (1 - \varsigma) C_i^1 + \varsigma C_i^2 \tag{B.2}$$

where ς is a random number uniformly distributed in [0, 1].

Mutation is the last operator in each iteration of the GA, which is applied to the output of the crossover operation and randomly changes each symbol of the chromosome with a given probability Q_m. In BGA, the changes correspond to complementing the corresponding bits; that is, we replace each bit with probability Q_m from 0 to 1 or vice versa. Typically, Q_m is very small. In RGA, we used boundary mutation where one gene C_i in the range [a b] is randomly selected and set equal to either its lower or upper bound.

$$C_i = \begin{cases} a & Q_m \geq 0.5 \\ b & Q_m < 0.5 \end{cases} \tag{B.3}$$

B.2 Elitism

To prevent the best individual from being lost during the crossover and mutation processes, “elitism” [179, 241], which passes this individual to the new generation, is used. In this way, the best solution is directly propagated into the next iteration and by that we keep track of the best chromosome which has the lowest cost-function value.

B.3 Population and generation sizes and rates

In GA, we have to define some parameters such as the number of generation and population and the probability of crossover, mutation, and elitism. In order to obtain a good balance between the rate of convergence and prevent the trial solution from being trapped in a local minimum, it is necessary to take great care of the choice of these parameters. Unfortunately, there is not a criterion for the optimal values for this parameter. Typically, the mutation rate and the population size for a GA are the major contributors to the convergence speed of a GA. These parameters have been studied by different researchers [242–244]. For example, reference [242] reports that a small population size improved performance in early generation, while a large population size improved performance in late generations. It claims that the type of crossover rate is not a factor and the best crossover rate is approximately 1. Reference [243] shows that for optimizing 20 parameters, the population size was 30, the crossover rate was 0.95, and the mutation rate was 0.01. In 1998, Gao showed that the larger the probability of mutation and the smaller the population size, the faster the GA should converge for short-term performance [244]. However, we should note that even though this choice presents some arbitrariness, in general selecting the value for these parameters is strongly dependent on the number of unknowns and the non-linearity order of the fitness-function. In particular, the inverse scattering problems depend on the scatterer under test, the assumed imaging configuration (size of the object and number of measurement points), and also on the available *a-priori* information.

Appendix C

FDTD FORMULATIONS

C.1 Fundamentals of FDTD method (Yee algorithm)

In this thesis the interactions between the pulse and the multilayer dispersive objects have been modeled by FDTD method in a manner described in [170]. Being compared with the IE formulation or other numerical methods used as forward solver, the FDTD approach is very efficient for modelling inhomogeneous objects and complex geometries. The Yee-cell (Fig. C.1) technique is implemented in the FDTD code for modelling the shape of the cylindrical object more closely. This method uses a staggered grid approximation for solving the Maxwell's equations [245]. The Yee-cell allows the properties of the medium including the permittivity, permeability, and conductance to be presented as a discrete grid. In this way the domain can be divided into areas with different properties by defining the cell parameters in each area. This allows the FDTD solver to incorporate the heterogeneity by defining the dielectric properties cell by cell. The differential operators required for calculating the explicit update equations have their simplest form in rectangular coordinates and when working with

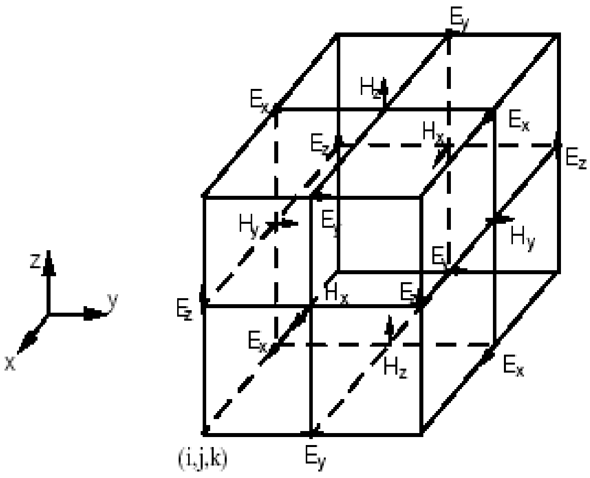

Fig. C.1: Yee-cell schematic.

plane-waves this coordinate system is the obvious choice for expressing such waves. Therefore, rectangular coordinates as well as plane-waves as the incident field have been chosen in this thesis. In order to model the complex shape composed of varying curve surfaces, the staircasing method has been used [170]. In this method the curved surface is represented by approximating its trajectory with a series of steps in the grid. This approximation does not work very well for a small radius of curvature. One way to make it better is to introduce a smaller cell size which leads to high computational requirements. The following cell size was used for all simulations: $\Delta x = \Delta y = \lambda_{min}/20$.

$$\lambda_{min} = \frac{C_{background}}{f_{max}} \tag{C.1}$$

where $C_{background}$ is the velocity of propagation, f_{max} is the maximum value of the frequency components of the excitation signal, (e.g. a modulated or differentiated Gaussian pulse) and Δx and Δy is the cell size in x and y direction [170]. In fact, for designing the mesh size we must take into account the required bandwidth and the available computational power. In addition, the cell size also relates to runtime. The time step is calculated given the cell sizes and the speed of the propagation of the wave in the free space. The time increment Δt is equal to 0.98 of the Courant stability limit. The Courant stability limit is

$$\Delta t \leq \frac{1}{C_{background}\sqrt{(\frac{1}{\Delta x})^2 + (\frac{1}{\Delta y})^2}} \tag{C.2}$$

Thus, smaller the cell sizes, smaller the associated time steps leading to the longer runtime. The proposed MWT technique requires wideband pulse for high resolution imaging. The incident wave used in this thesis is a Gaussian pulse given by:

$$G(t) = exp\left[-(t-t_0)^2/2\tau_p^2\right] \tag{C.3}$$

where τ_p is the pulse width. The frequency spectrum of Gaussian pulse is given by:

$$G(\omega) = \sqrt{2\pi\tau_p} exp\left[-(\omega\tau_p)^2/2\right] \tag{C.4}$$

Fig. C.2 shows the Gaussian pulse spectrum and Tab. C.1 indicates the pulse duration

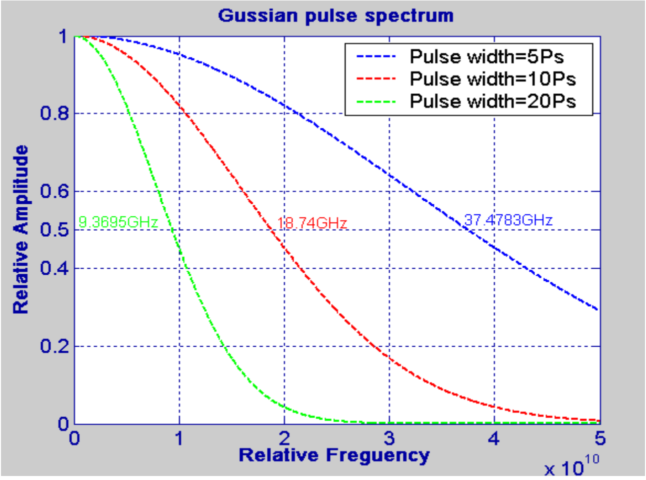

Fig. C.2: Gaussian pulse spectrum.

Tab. C.1: Pulse duration versus bandwidth frequency.

Pulse duration (ps)	Gaussian bandwidth (GHz)
1	186.8
2	93.42
5	37.37
10	18.68
20	9.34

for different bandwidth. Depending on the bandwidth that we are interested in, the corresponding pulse duration needs to be used.

Different parts of the 2D model are shown in Fig. C.3. In the central region, both incident and scattered fields exist ($E_{total} = E_{scat} + E_{inc}$) and this is called the Total Field (TF) region. Any structure under the test should be in this region. The next region contains only the scattered field which is called Scattered Field (SF) region. The TF and SF regions are separated by a non-physical virtual surface that serves to connect the fields in each region, and thereby generates the incident wave. The

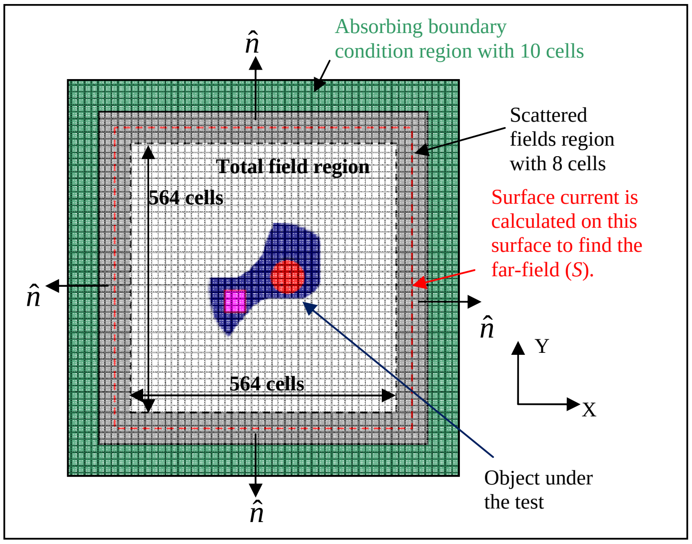

Fig. C.3: Different regions of solution space.

transmitting antennas are posed at the boundary separating TF region and SF region. We used the TF/SF formulation, which makes the values of scattered field directly obtainable from the FDTD code [170]. Typically, the scattered field is calculated by subtracting the total field from incident field ($E_{scat} = E_{total} - E_{inc}$). However, by using the TF/SF formulation the scattered field can be calculated directly without extra processing [170]. The magnitude of the fields at the TF region, when the background is free space ($\sigma = 0.0S/m$, $\epsilon_r = 1.0$) is:

$$E_{zx,total}|_{i,j}^{n+1} = E_{zx,total}|_{i,j}^{n} + \frac{\Delta t}{\epsilon_0 \Delta x}[H_{y,total}|_{i,j}^{n+\frac{1}{2}} - H_{y,total}|_{i-1,j}^{n+\frac{1}{2}}] \tag{C.5}$$

$$E_{zy,total}|_{i,j}^{n+1} = E_{zy,total}|_{i,j}^{n} - \frac{\Delta t}{\epsilon_0 \Delta y}[H_{x,total}|_{i,j}^{n+\frac{1}{2}} - H_{x,total}|_{i,j-1}^{n+\frac{1}{2}}] \tag{C.6}$$

$$\begin{aligned} H_{x,total}|_{i,j}^{n+\frac{1}{2}} = H_{x,total}|_{i,j}^{n-\frac{1}{2}} - \frac{\Delta t}{\mu_0 \Delta y}[&E_{zx,total}|_{i,j+1}^{n} + E_{zy,total}|_{i,j+1}^{n} \\ &-E_{zx,total}|_{i,j}^{n} - E_{zy,total}|_{i,j}^{n}] \end{aligned} \tag{C.7}$$

$$\begin{aligned} H_{y,total}|_{i,j}^{n+\frac{1}{2}} = H_{y,total}|_{i,j}^{n-\frac{1}{2}} + \frac{\Delta t}{\mu_0 \Delta x}[&E_{zx,total}|_{i+1,j}^{n} + E_{zy,total}|_{i+1,j}^{n} \\ &-E_{zx,total}|_{i,j}^{n} - E_{zy,total}|_{i,j}^{n}] \end{aligned} \tag{C.8}$$

The magnitude of the field at the SF region with free space background ($\sigma = 0.0S/m$, $\epsilon_r = 1.0$) is:

$$E_{zx,scat}|_{i,j}^{n+1} = E_{zx,scat}|_{i,j}^{n} + \frac{\Delta t}{\epsilon_0 \Delta x}[H_{y,scat}|_{i,j}^{n+\frac{1}{2}} - H_{y,scat}|_{i-1,j}^{n+\frac{1}{2}}] \tag{C.9}$$

$$E_{zy,scat}|_{i,j}^{n+1} = E_{zy,scat}|_{i,j}^{n} - \frac{\Delta t}{\epsilon_0 \Delta y}[H_{x,scat}|_{i,j}^{n+\frac{1}{2}} - H_{x,scat}|_{i,j-1}^{n+\frac{1}{2}}] \tag{C.10}$$

$$\begin{aligned} H_{x,scat}|_{i,j}^{n+\frac{1}{2}} = H_{x,scat}|_{i,j}^{n-\frac{1}{2}} - \frac{\Delta t}{\mu_0 \Delta y}[&E_{zx,scat}|_{i,j+1}^{n} + E_{zy,scat}|_{i,j+1}^{n} \\ &-E_{zx,scat}|_{i,j}^{n} - E_{zy,scat}|_{i,j}^{n}] \end{aligned} \tag{C.11}$$

$$\begin{aligned} H_{y,scat}|_{i,j}^{n+\frac{1}{2}} = H_{y,scat}|_{i,j}^{n-\frac{1}{2}} + \frac{\Delta t}{\mu_0 \Delta x}[&E_{zx,scat}|_{i+1,j}^{n} + E_{zy,scat}|_{i+1,j}^{n} \\ &-E_{zx,scat}|_{i,j}^{n} - E_{zy,scat}|_{i,j}^{n}] \end{aligned} \tag{C.12}$$

and also at the TF region the relationship between the total field and scattered field is:

$$E_{total} = E_{scat} + E_{inc} \tag{C.13}$$

$$H_{total} = H_{scat} + H_{inc} \tag{C.14}$$

$$\tag{C.15}$$

Based on the consistency condition, the magnitude of fields at the boundary between TF region and SF region should be as follows:

At front face of TF region ($j = j_0$; $i = i_0, ..., i_1$):

From the continuity of tangential magnetic field at the boundary:

$$H_{x,total}\big|_{i,j_0+\frac{1}{2}}^{n+\frac{1}{2}} = H_{x,scat}\big|_{i,j_0-\frac{1}{2}}^{n+\frac{1}{2}} \tag{C.16}$$

$$E_{zy}\big|_{i,j_0}^{n+1} = \left\{E_{zy}\big|_{i,j_0}^{n+1}\right\} + \frac{\Delta t}{\epsilon_0 \Delta y}\left[H_{x,inc}\big|_{i,j_0-\frac{1}{2}}^{n+\frac{1}{2}}\right] \tag{C.17}$$

At back face of TF region ($j = j_1$; $i = i_0, ..., i_1$)

From the continuity of tangential magnetic field at the boundary:

$$H_{x,scat}\big|_{i,j_1+\frac{1}{2}}^{n+\frac{1}{2}} = H_{x,total}\big|_{i,j_1-\frac{1}{2}}^{n+\frac{1}{2}} \tag{C.18}$$

$$E_{zy}\big|_{i,j_1}^{n+1} = \left\{E_{zy}\big|_{i,j_1}^{n+1}\right\} - \frac{\Delta t}{\epsilon_0 \Delta y}\left[H_{x,inc}\big|_{i,j_1+\frac{1}{2}}^{n+\frac{1}{2}}\right] \tag{C.19}$$

At left face of TF region ($i = i_0$; $j = j_0, ..., j_1$)

From the continuity of tangential magnetic field at the boundary:

$$H_{y,total}\big|_{i_0+\frac{1}{2},j}^{n+\frac{1}{2}} = H_{y,scat}\big|_{i_0-\frac{1}{2},j}^{n+\frac{1}{2}} \tag{C.20}$$

$$E_{zx}\big|_{i_0,j}^{n+1} = \left\{E_{zx}\big|_{i_0,j}^{n+1}\right\} - \frac{\Delta t}{\epsilon_0 \Delta x}[H_{y,inc}\big|_{i_0-\frac{1}{2},j}^{n+\frac{1}{2}}] \tag{C.21}$$

At right face of TF region $(i = i_1;\ j = j_0, ..., j_1)$

From the continuity of tangential magnetic field at the boundary:

$$H_{y,scat}\big|_{i_1+\frac{1}{2},j}^{n+\frac{1}{2}} = H_{y,total}\big|_{i_1-\frac{1}{2},j}^{n+\frac{1}{2}} \tag{C.22}$$

$$E_{zx}\big|_{i_1,j}^{n+1} = \left\{E_{zx}\big|_{i_1,j}^{n+1}\right\} + \frac{\Delta t}{\epsilon_0 \Delta x}[H_{y,inc}\big|_{i_1+\frac{1}{2},j}^{n+\frac{1}{2}}] \tag{C.23}$$

At outside front face of TF region $(j = j_0 - 1/2;\ i = i_0, ..., i_1)$

From the continuity of tangential electric field at the boundary:

$$E_{z,total}\big|_{i,j_0+1}^{n} = E_{z,scat}\big|_{i,j_0}^{n} \tag{C.24}$$

$$H_x\big|_{i,j_0-\frac{1}{2}}^{n+\frac{1}{2}} = \left\{H_x\big|_{i,j_0-\frac{1}{2}}^{n+\frac{1}{2}}\right\} + \frac{\Delta t}{\mu_0 \Delta y}[E_{z,inc}\big|_{i,j_0}^{n}] \tag{C.25}$$

At outside back face of TF region $(j = j_0 + 1/2;\ i = i_0, ..., i_1)$

From the continuity of tangential electric field at the boundary:

$$E_{z,scat}\big|_{i,j_1}^{n} = E_{z,total}\big|_{i,j_1-1}^{n} \tag{C.26}$$

$$H_x\big|_{i,j_1+\frac{1}{2}}^{n+\frac{1}{2}} = \left\{H_x\big|_{i,j_1+\frac{1}{2}}^{n+\frac{1}{2}}\right\} - \frac{\Delta t}{\mu_0 \Delta y}[E_{z,inc}\big|_{i,j_1}^{n}] \tag{C.27}$$

At outside left face of TF region $(i = i_0 - 1/2;\ j = j_0, ..., j_1)$

From the continuity of tangential electric field at the boundary:

$$E_{z,total}\big|^{n}_{i_0+1,j} = E_{z,scat}\big|^{n}_{i_0,j} \tag{C.28}$$

$$H_x\big|^{n+\frac{1}{2}}_{i_0-\frac{1}{2},j} = \left\{ H_x\big|^{n+\frac{1}{2}}_{i_0-\frac{1}{2},j} \right\} - \frac{\Delta t}{\mu_0 \Delta x}\left[E_{z,inc}\big|^{n}_{i_0,j}\right] \tag{C.29}$$

At outside right face of total field region $(i = i_1 + 1/2;\ j = j_0, ..., j_1)$

From the continuity of tangential electric field at the boundary:

$$E_{z,scat}\big|^{n}_{i_1,j} = E_{z,total}\big|^{n}_{i_1,j} \tag{C.30}$$

$$H_y\big|^{n+\frac{1}{2}}_{i,j_1+\frac{1}{2}} = \left\{ H_y\big|^{n+\frac{1}{2}}_{i,j_1+\frac{1}{2}} \right\} + \frac{\Delta t}{\mu_0 \Delta x}\left[E_{z,inc}\big|^{n}_{i_1,j}\right] \tag{C.31}$$

In order to show the accuracy of the FDTD method used to determine the scattered field, two examples with two different methods are provided. In the first example we compare the scattered field calculated with FDTD and the scattered field computed with the Richmond procedure [229]. In this example the dielectric shell cylinder has a permittivity of 4 and no conductivity with inner diameter equal to 0.5λ and 0.6λ outer diameter (Fig. C.4 (a)). Eighty one observation points are assigned around the shell-cylinder to calculate the scattered field in the far-field zone. The 2D near field to far field transformation is developed based on reference [170]. The same as other examples in this thesis, 10 layers UPML ABC are used for these two simulations.

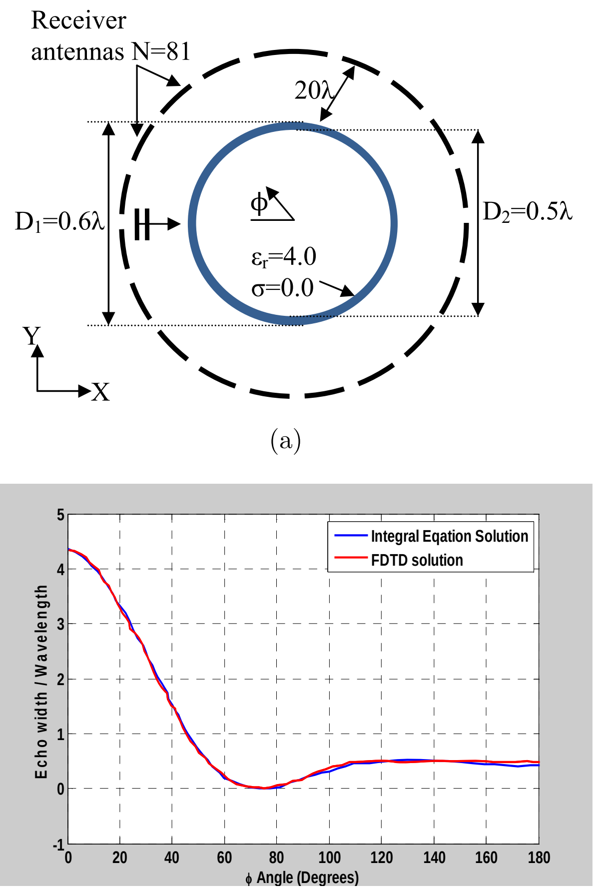

(a)

(b)

Fig. C.4: (a) Dielectric shell cylinder with 81 observation points, (b) distant scattering pattern of circular dielectric cylinder with plane-wave incident.

Fig. C.4 (b) shows the scattered field at 2.5GHz using the FDTD compared with IE solution.

Fig. C.5 (a) shows another example for a lossy dielectric cylinder with permittivity (1) and conductivity ($1.57 S/m$) with radius 0.53λ and 100 receiver probes in the far-field zone. Fig. C.5 (b) shows the scattered field at 2.5GHz using the FDTD and MoM method [246], respectively.

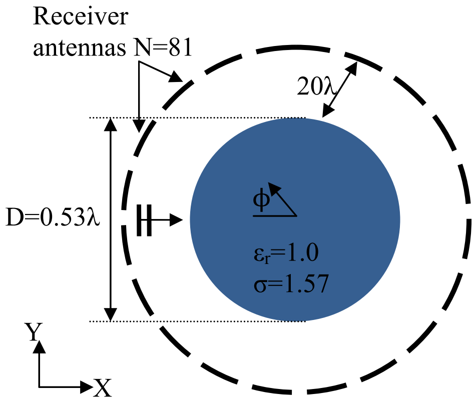

(a)

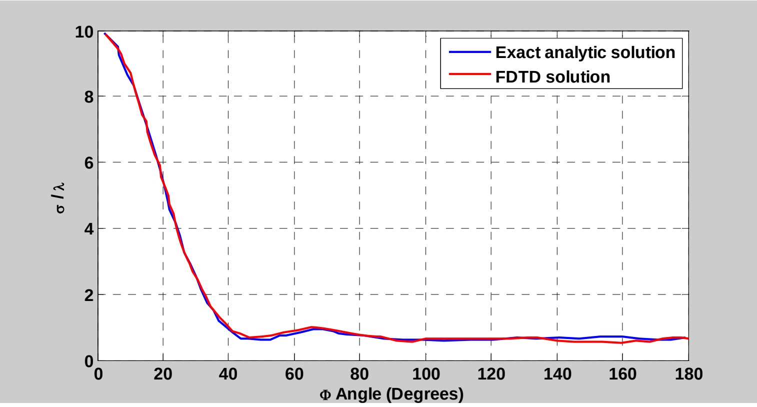

(b)

Fig. C.5: (a) Lossy circular cylinder, (b) TM plot of $2\pi|E_{scat}|^2/\lambda$ against Φ for case of lossy circular cylinder at 2.5GHz frequency.

Appendix D

PARALLEL FDTD

FDTD numerical method is data-parallel in nature and exhibits apparent nearest-neighbour communication pattern. Distributed memory machines, using MPI, are therefore a suitable parallel architecture for this application. FDTD code can run on a cluster which has a number of single or multiple processor nodes. MPI consists of the usual master-slave communication, where the first master process is started with identifying slave processors in which all slave nodes share a common memory. Data is distributed among the slave processes and the master collects the results. The master-slave architecture is capable of running the same code for all slave processors. This situation will give the maximum possible speed-up if all the available processors can be assigned processes for the total duration of the computation. Moreover, there is minimal interaction between slave processes (embarrassingly parallel). In the Single-Program Multiple-Data (SPMD) parallel programs global data is partitioned with a portion of the data assigned to each processing node.

In 2006 Yu *et al.* introduced three communication schemes for parallel FDTD [247].

The division of the computational domain is on the $\vec{E}$ along the Cartesian axis, but the three schemes differ in the way that components of $\vec{E}$ and $\vec{H}$ should be exchanged, and also in the way how the processor updates the $\vec{E}$ components at the interface layer.

In our approach, the computational domain is divided along the x-axis (Fig. D.1 (a)) of $\vec{E}$. Given the computation domain is divided into $N \times N$ cells and p processors, then each processor receives a matrix of $m \times N$ cells where $m = N/p$. Each processor q (q is not equal to 1 and p, the first or last processors) shares the first and m^{th} row of its computational domain with processor $q-1$ and $q+1$, respectively. Therefore, $\vec{E}$ at the interface of adjacent processors are calculated on both processors (Fig. D.1 (b)). The purpose of this scheme is to eliminate the communication of $\vec{E}$ and only exchange values of $\vec{H}$ to improve the computation/communication efficiency. Tab. D.1 shows few examples of different FDTD codes reported in the literature. As it can be seen in this table, the maximum speed-up has been increased with others parallel FDTD codes with the same parameters. Note that this table only provides a summary of previous work and due to the differences in the speed and type of processors it is not possible to make a fair comparison.

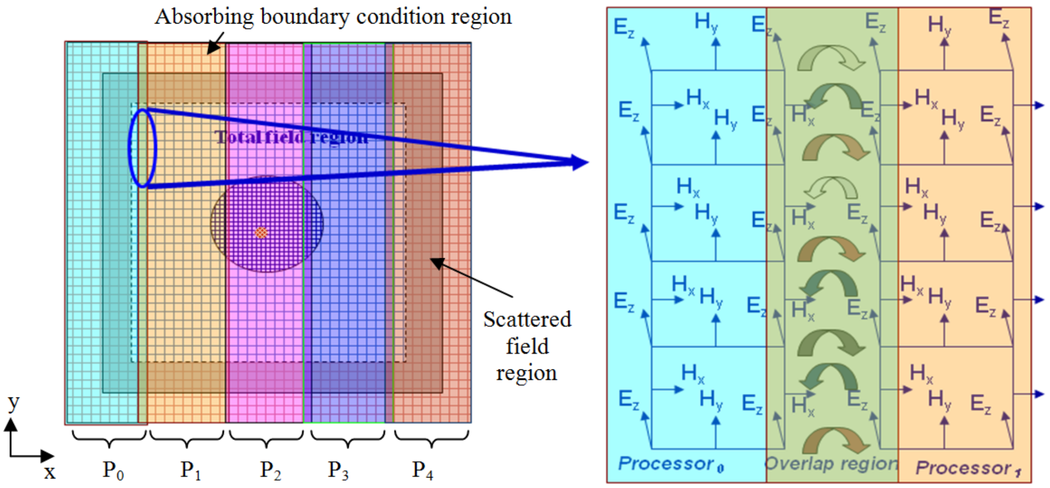

(a) (b)

Fig. D.1: (a) Spatial decomposition, and (b) the data communication between two processors at the boundaries.

Tab. D.1: Example of different PFDTD codes with different parameters.

Authors	Processor per node	Number of nodes	Maximum Speed-up	System
Varadarajan-Mittra [248]	1	8	7.06	HP-735
Liu *et al.* [249]	4	32	100	Sparc II
Tinniswood *et al.* [250]	1	128	32	IBM PS/2
Sypniewski *et al.* [251]	4	1	2.1	Intel PII
Schiavone *et al.* [252]	2	14	12	Dual PII
Guiffaut-Mahjoubi [253]	1	16	14	Cray T3E
Sabouni [254] *et al.*	2	8	6.25	AMD Athlon

Appendix E

DIELECTRIC PROPERTIES MEASUREMENT OF BREAST TISSUE

E.1 Ex-vivo measurement at the hospital

In order to characterize the dielectric properties of the *ex-vivo* breast tissues based on the time of excision and temperature, different dielectric properties measurements from woman undergoing breast surgery were performed at the Altru Hospital, Grand Forks, ND, USA. An Agilent E5071C ENA network analyzer and Agilent 85070E dielectric probe kit with high performance probe were used for these measurements. Prior to each measurement all probes were calibrated using short and open circuit loads, and 25^oC distiled water as described in [255]. In order to minimize calibration errors associated with the bending of the signal transmission cable attached to the network analyzer during the measurement procedure, all cables were fixed. Fig. E.1 shows pictures of dielectric properties measurement setup. Women scheduled for surgical resection were referred to our clinical coordinator for possible inclusion in this study. The protocol was approved by Institutional Review Board and all women

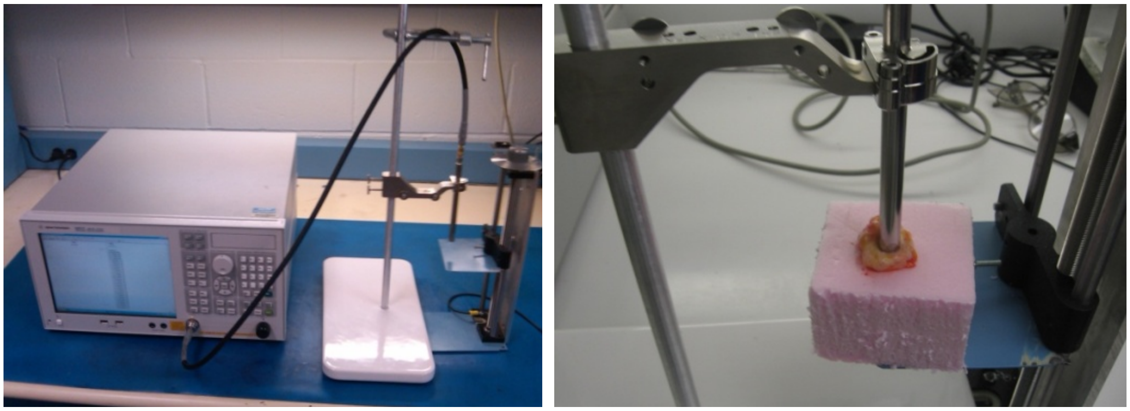

(a) (b)

Fig. E.1: Measurement setup for breast tissues dielectric properties measurement (a) ENA network analyzer and Agilent 85070E dielectric probe kit, and (b) tissue under the performance probe measurement.

enrolled in this study signed consent forms. Immediately after surgery, the biopsy specimen was taken to the site where the dielectric properties measurements took place. After measurements were completed, the tissue was transferred to the pathology department where it was sectioned and processed for histological evaluation. Fig. E.2 shows photos of different tissue samples from mastectomy.

E.1.1 Dielectric properties vs. temperature

For this study, a sample tissue was measured about half an hour after the surgery to determine the effect of temperature on the dielectric properties of the tissue. Fig. E.3 shows the effect of decreasing temperature on (a) permittivity, and (b) conductivity, and increasing the temperature after freezing the tissue, on (c) permittivity and (d) conductivity. A conclusion from these graphs is that the temperature of the breast

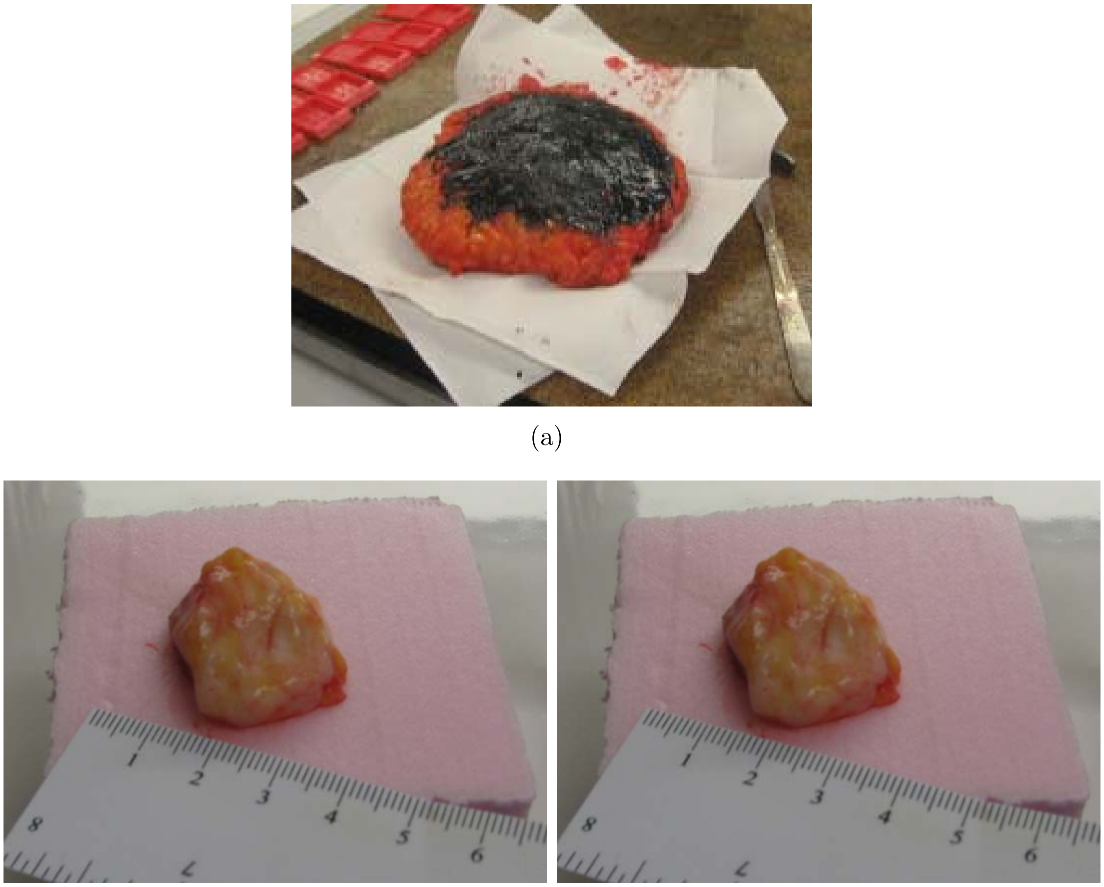

(a)

(b) (c)

Fig. E.2: Breast tissue samples from mastectomy surgery (a) the entire breast sample, (b) benign tissue sample, and (c) malignant tissue.

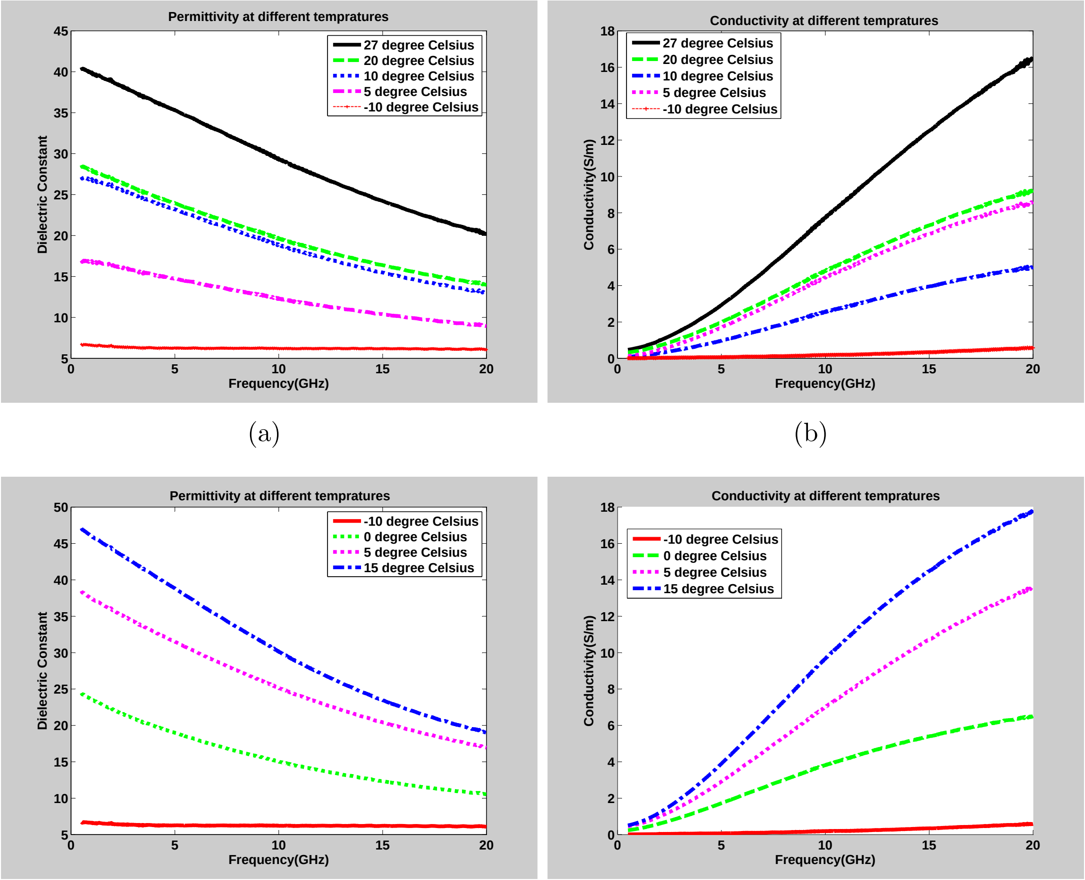

(a) (b)

(c) (d)

Fig. E.3: Dielectric properties of breast tissue vs. frequency at different temperatures (a) permittivity when temperatures decreased from room temperature to freezing, (b) conductivity when temperatures decreased from room temperature to freezing, (c) permittivity when temperature increased from freezing to room temperature, and (d) conductivity when temperature increased from freezing to room temperature.

tissue significantly changes the dielectric properties. Therefore, for accurate dielectric properties measurement the temperature of the tissue needs to be as close as possible to the body temperature.

E.1.2 Dielectric properties vs. time of excision

For this study a specimen from a full mastectomy surgery was selected from a 47 year old Women with fibrocystic changes. The entire breast was transferred to the pathology department within 5 minutes of removal. The mastectomy surgery has been selected for this part, because a fresh tissue was required. Since the entire breast is removed in mastectomy surgery, if a sample is cut from inside breast at the pathology laboratory, this can be considered as a fresh sample. A sample from central breast was measured at different times, with the sample fixed under the probe. After the measurement, a selected sample was processed for histopathology and identified as fibrocystic breast tissue. Fig. E.4 shows the results of permittivity and conductivity at different frequencies for different times after excision. Both parameters decreased with increasing time. This decrease may be due to changes in the physiological condition of the tissue, such as water content, blood content, and blood oxygenation.

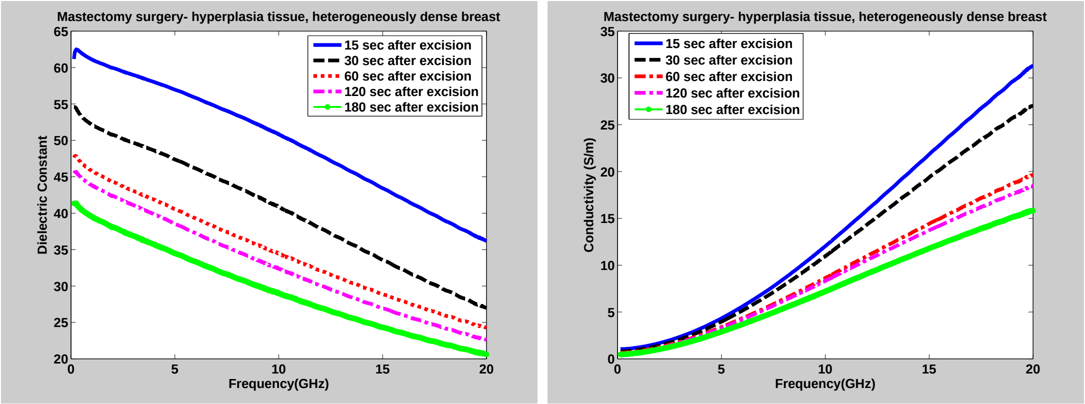

(a) (b)

Fig. E.4: Dielectric properties for fibro-glandular tissue from mastectomy surgery at different times after excision (a) permittivity, and (b) conductivity.

REFERENCES

[1] M. Pastorino, “Modern microwave: inverse-scattering techniques for image reconstruction,” *Instrumentation Measurement Magazine, IEEE*, vol. 1, no. 4, pp. 20–25, 1998.

[2] J. C. Bolomey and N. Joachimowicz, “Dielectric metrology via microwave tomography: Present and future,” *Mat. Res. Soc. Symp. Proc*, vol. 347, pp. 259–265, 1997.

[3] K. Belkebir, C. Pichot, J. C. Bolomey, P. Berthaud, G. Gottard, X. Derobert, and G. Fauchoux, “Microwave tomography system for reinforced concrete structures,” in *Proc. 24th European Microwave Conf, Cannes, France*, 1994.

[4] D. D. Ferris and N. Currie, “A survey of current technologies for through-the-wall-surveillance,” *Proc. SPIE*, vol. 3577, pp. 62–68, 1998.

[5] D. Daniels, *Ground Penetrating Radar*. London, U.K. IEE Press, 2004.

[6] L. P. Song, C. Yu, and Q. H. Liu, “Through-wall imaging (twi) by radar: 2-d tomographic results and analyses,” *Geoscience and Remote Sensing, IEEE Transactions on*, vol. 43, no. 12, pp. 2793–2798, 2005.

[7] C. Huber, H. Abiri, S. Ganchev, and R. Zoughi, “Modeling of surface hairline-crack detection in metals under coatings using an open-ended rectangular waveguide,” *Microwave Theory and Techniques, IEEE Transactions on*, vol. 45, no. 11, pp. 2049–2057, 1997.

[8] A. Abubakar, T. Habashy, V. Druskin, L. Knizhnerman, and D. Alumbaugh, “2.5d forward and inverse modeling for interpreting low-frequency electromagnetic measurements,” *Geophysics*, vol. 73, no. 2, pp. F165–F177, 2008.

[9] A. Abubakar and P. M. van den Berg, “Non-linear three-dimensional inversion of cross-well electrical measurements,” *Geophysical Prospecting*, vol. 48, p. 109134, 2000.

[10] J. L. Davis, A. P. Annan, and C. Vaughan, “Placer exploration using radar and seismic methods,” in *54th Annual meeting, Soc. Expl. Geophysicist*, 1984.

[11] S. J. Lockwood and H. Lee, “Pulse-echo microwave imaging for nde of civil structures: Image reconstruction, enhancement, and object recognition,” *International Journal of Imaging Systems and Technology*, vol. 8, pp. 407–412, 1997.

[12] S. Semenov, “Microwave tomography: review of the progress towards clinical applications,” *Phil. Trans. R. Soc. A*, vol. 367, p. 30213042, 2009.

[13] S. Caorsi, A. Massa, and M. Pastorino, “Numerical assessment concerning a focused microwave diagnostic method for medical applications,” *Microwave Theory and Techniques, IEEE Transactions on*, vol. 48, no. 11, pp. 1815–1830, 2000.

[14] S. Semenov, A. Bulyshev, A. Abubakar, V. Posukh, Y. Sizov, A. Souvorov, P. van den Berg, and T. Williams, “Microwave-tomographic imaging of the high dielectric-contrast objects using different image-reconstruction approaches,” *Microwave Theory and Techniques, IEEE Transactions on*, vol. 53, no. 7, pp. 2284–2294, 2005.

[15] S. Semenov, R. Svenson, K. Dezern, M. Quinn, M. Thompson, and G. Tatsis, “Myocardial ischemia and infarction can be detected by microwave spectroscopy. i. experimental evidence,” in *Proceedings of the Engineering in Medicine and Biology Society International Conference of the IEEE*, vol. 4, 1996.

[16] S. Semenov, R. Svenson, A. Boulyshev, A. Souvorov, V. Borisov, Y. Sizov, A. Starostin, K. Dezern, G. Tatsis, and V. Baranov, “Microwave tomography: two-dimensional system for biological imaging,” *Biomedical Engineering, IEEE Transactions on*, vol. 43, no. 9, pp. 869–877, 1996.

[17] S. Semenov, R. Svenson, A. Bulyshev, A. Souvorov, A. Nazarov, Y. Sizov, V. Posukh, A. Pavlovsky, P. Repin, and G. Tatsis, “Spatial resolution of microwave tomography for detection of myocardial ischemia and infarction-experimental study on two-dimensional models,” *Microwave Theory and Techniques, IEEE Transactions on*, vol. 48, no. 4, pp. 538–544, 2000.

[18] P. M. Meaney, M. W. Fanning, T. Raynolds, C. J. Fox., Q. Fang, C. A. Kogel, S. P. Poplack, and K. D. Paulsen, “Initial clinical experience with microwave breast imaging in women with normal mammography,” *Acad Radiol.*, vol. 14, no. 2, pp. 207–218, 2007.

[19] S. Poplack, T. Tosteson, W. Wells, B. Pogue, P. Meaney, A. Hartov, C. Kogel, S. Soho, J. Gibson, and P. K., “Electromagnetic breast imaging: Results of a pilot study in women with abnormal mammograms,” *Radiology*, vol. 243, no. 2, pp. 350–359, 2007.

[20] T. Rubk, P. Meaney, P. Meincke, and K. Paulsen, "Nonlinear microwave imaging for breast-cancer screening using gauss-newton's method and the cgls inversion algorithm," *Antennas and Propagation, IEEE Transactions on*, vol. 55, no. 8, pp. 2320–2331, 2007.

[21] E. Fear, X. Li, S. Hagness, and M. Stuchly, "Confocal microwave imaging for breast cancer detection: localization of tumors in three dimensions," *Biomedical Engineering, IEEE Transactions on*, vol. 49, no. 8, pp. 812–822, 2002.

[22] P. Meaney, M. Fanning, D. Li, S. Poplack, and K. Paulsen, "A clinical prototype for active microwave imaging of the breast," *Microwave Theory and Techniques, IEEE Transactions on*, vol. 48, no. 11, pp. 1841–1853, 2000.

[23] D. Li, P. Meaney, and K. Paulsen, "Conformal microwave imaging for breast cancer detection," *Microwave Theory and Techniques, IEEE Transactions on*, vol. 51, no. 4, pp. 1179–1186, 2003.

[24] Q. Fang, P. Meaney, S. Geimer, A. Streltsov, and K. Paulsen, "Microwave image reconstruction from 3-d fields coupled to 2-d parameter estimation," *Medical Imaging, IEEE Transactions on*, vol. 23, no. 4, pp. 475–484, 2004.

[25] P. M. Meaney, Q. Fang, E. Demidenko, and K. D. Paulsen, "Error analysis in microwave breast imaging: Variance stabilizing transformations," in *Proc. of ICONIC*, 2005.

[26] X. Li, S. Hagness, B. Van Veen, and D. van der Weide, "Experimental investigation of microwave imaging via space-time beamforming for breast cancer detection," in *Microwave Symposium Digest, IEEE MTT-S International*, 2003.

[27] G. Bindu, S. J. Abraham, A. Lonappan, V. Thomas, C. K. Aanandan, and M. K. T., "Active microwave imaging for breast cancer detection," *PIER Progress In Electromagnetic Research*, vol. 58, pp. 149–169, 2006.

[28] E. Bond, X. Li, S. Hagness, and B. Van Veen, "Microwave imaging via space-time beamforming for early detection of breast cancer," *Antennas and Propagation, IEEE Transactions on*, vol. 51, no. 8, pp. 1690–1705, 2003.

[29] M. Miyakawa, T. Ishida, and M. Watanabe, "Imaging capability of an early stage breast tumor by cp-mct," in *Engineering in Medicine and Biology Society, 26th Annual International Conference of the IEEE*, vol. 1, 2004.

[30] A. Fhager, P. Hashemzadeh, and M. Persson, "Reconstruction quality and spectral content of an electromagnetic time-domain inversion algorithm," *Biomedical Engineering, IEEE Transactions on*, vol. 53, no. 8, pp. 1594–1604, 2006.

[31] S. Y. Semenov and D. R. Corfield, "Microwave tomography for brain imaging: Feasibility assessment for stroke detection," *International Journal of Antennas and Propagation*, vol. 2008, no. 2008, pp. 1–8, 2008.

[32] P. Meaney, T. Zhou, M. Fanning, S. A. Geimer, and P. K. D., "Microwave imaging for bone fracture risk assessment," in *Applied Computational Electromagnetics Symp*, 2008.

[33] S. Semenov, R. Svenson, V. Posukh, A. Nazarov, Y. Sizov, A. Bulyshev, A. Souvorov, W. Chen, J. Kasell, and G. Tatsis, "Dielectrical spectroscopy of canine myocardium during acute ischemia and hypoxia at frequency spectrum from 100 khz to 6 ghz," *Medical Imaging, IEEE Transactions on*, vol. 21, no. 6, pp. 703–707, 2002.

[34] L. E. Larsen and J. H. Jacobi, *Medical Applications of Microwave Imaging.* Piscataway, NJ: IEEE Press, 1986.

[35] J. Jacobi, L. Larsen, and C. Hast, "Water-immersed microwave antennas and their application to microwave interrogation of biological targets," *Microwave Theory and Techniques, IEEE Transactions on*, vol. 27, no. 1, pp. 70–78, 1979.

[36] A. Abubakar and P. M. Van den Berg, "Iterative forward and inverse algorithms based on domain integral equations for three-dimensional electric and magnetic objects," *J. Comput. Phys.*, vol. 195, pp. 236–262, 2004.

[37] I. Rekanos and A. Raisanen, "Microwave imaging in the time domain of buried multiple scatterers by using an fdtd-based optimization technique," *Magnetics, IEEE Transactions on*, vol. 39, no. 3, pp. 1381–1384, 2003.

[38] J. R. Reitz and F. J. Milford, *Funcations of electromagnetic theory.* Addison Wesley Publishing Company, 1967.

[39] J. A. Kong, *Electromagnetic Wave Theory.* Wiley-Interscience, New York, 1990.

[40] S. Hagness, A. Taflove, and J. Bridges, "Two-dimensional fdtd analysis of a pulsed microwave confocal system for breast cancer detection: fixed-focus and antenna-array sensors," *Biomedical Engineering, IEEE Transactions on*, vol. 45, no. 12, pp. 1470–1479, 1998.

[41] X. Li and S. Hagness, "A confocal microwave imaging algorithm for breast cancer detection," *Microwave and Wireless Components Letters, IEEE*, vol. 11, no. 3, pp. 130–132, 2001.

[42] R. Nilavalan, A. Gbedemah, I. Craddock, X. Li, and S. Hagness, "Numerical investigation of breast tumour detection using," *Electronics Letters*, vol. 39, no. 25, pp. 1787–1789, 2003.

[43] H. B. Lim, N. T. T. Nhung, E.-P. Li, and N. D. Thang, "Confocal microwave imaging for breast cancer detection: Delay-multiply-and-sum image reconstruction algorithm," *Biomedical Engineering, IEEE Transactions on*, vol. 55, no. 6, pp. 1697–1704, 2008.

[44] M. Klemm, I. J. Craddock, J. A. Leendertz, A. Preece, and R. Benjamin, "Improved delay-and-sum beamforming algorithm for breast cancer detection," *International Journal of Antennas and Propagation*, vol. 2008, no. 9, 2008.

[45] B. Guo, Y. Wang, J. Li, P. Stoica, and R. Wu, "Microwave imaging via adaptive beamforming methods for breast cancer detection," *Journal of Electromagnetic Waves and Applications,*, vol. 20, no. 1, pp. 53–63, 2006.

[46] Y. Xie, B. Guo, L. Xu, J. Li, and P. Stoica, "Multistatic adaptive microwave imaging for early breast cancer detection," *Biomedical Engineering, IEEE Transactions on*, vol. 53, no. 8, pp. 1647–1657, 2006.

[47] J. Sill and E. Fear, "Tissue sensing adaptive radar for breast cancer detection - experimental investigation of simple tumor models," *Microwave Theory and Techniques, IEEE Transactions on*, vol. 53, no. 11, pp. 3312–3319, 2005.

[48] M. Klemm, I. Craddock, J. Leendertz, A. Preece, and R. Benjamin, "Experimental and clinical results of breast cancer detection using uwb microwave radar," in *Antennas and Propagation Society International Symposium, IEEE*, 2008.

[49] C. Gilmore and J. LoVetri, "On fourier imaging techniques for biomedical imaging," in *Antennas and Propagation Society International Symposium 2006, IEEE*, 2006.

[50] M. Cheney and B. Borden, "Problems in synthetic-aperture radar imaging," *Inverse Problems*, vol. 25, no. 12, pp. 1–18, 2009.

[51] W. C. Chew, *Waves and Fields in Inhomogeneous Media.* IEEE Press, 1994.

[52] M. Oristaglio and H. Blok, *Wavefield imaging and inversion in electromagnetics and acoustics.* Course Notes TU Delft, 1995.

[53] T. M. Habashy, R. Groom, and B. Spies, "Beyond the born and rytov approximations: a nonlinear approach to electromagnetic scattering," *J. Geophys. Res.*, vol. 98, pp. 1759–1775, 1993.

[54] P. C. Hansen, *Rank-deficient and discrete ill-posed problems: Numerical aspects of linear inversion.* Philadelphia, PA: SIAM, 1998.

[55] M. Slaney, A. Kak, and L. Larsen, "Limitations of imaging with first-order diffraction tomography," *Microwave Theory and Techniques, IEEE Transactions on*, vol. 32, no. 8, pp. 860–874, 1984.

[56] S. Barkeshli and R. G. Lautzenheiser, "An iterative method for inverse scattering problems based on an exact gradient search," *Radio Science*, vol. 29, pp. 1119–1130, 1994.

[57] R. E. Kleinman and P. M. Van den Berg, "A modified gradient method for two-dimensional problems in tomography," *J. Comput. Appl. Math.*, vol. 42, no. 1, pp. 17–35, 1992.

[58] P. Van den Berg, "Nonlinear scalar inverse scattering: Algorithms and applications," *Scattering and Inverse Scattering in Pure and Applied Sciences, Editors: E. R. Pike and P. C. Sabatier (London: Academic)*, vol. 1, pp. 121–141, 2001.

[59] P. M. van den Berg and R. E. Kleinman, "A contrast source inversion method," *Inverse Problems*, vol. 13, no. 6, pp. 1607–1620, 1997.

[60] A. Abubakar, P. van den Berg, and J. Mallorqui, "Imaging of biomedical data using a multiplicative regularized contrast source inversion method," *Microwave Theory and Techniques, IEEE Transactions on*, vol. 50, no. 7, pp. 1761–1771, 2002.

[61] P. M. van den Berg, A. L. van Broekhoven, and A. Abubakar, "Extended contrast source inversion," *Inverse Problems*, vol. 15, no. 5, pp. 1325–1344, 1999.

[62] C. Gilmore and J. LoVetri, "Enhancement of microwave tomography through the use of electrically conducting enclosures," *Inverse Problems*, vol. 24, no. 3, pp. 1–21, 2008.

[63] A. Abubakar, P. M. van den Berg, and T. M. Habashy, "Application of the multiplicative regularized contrast source inversion method on tm- and te-polarized experimental fresnel data," *Inverse Problems*, vol. 21, no. 6, pp. S5–S13, 2005.

[64] A. Abubakar and P. van den Berg, "Two and three-dimensional algorithms for microwave imaging and inverse scattering," *Journal of Electromag. Waves and Applicat.*, vol. 17, pp. 209–231, 2003.

[65] A. Abubakar, W. Hu, P. M. van den Berg, and T. M. Habashy, "A finite-difference contrast source inversion method," *Inverse Problems*, vol. 24, no. 6, pp. 1–17, 2008.

[66] C. Gilmore, A. Abubakar, W. Hu, T. Habashy, and P. van den Berg, "Microwave biomedical data inversion using the finite-difference contrast source inversion method," *Antennas and Propagation, IEEE Transactions on*, vol. 57, no. 5, pp. 1528–1538, 2009.

[67] J. Chung, J. G. Nagy, and D. P. Oleary, "A weighted-gcv method for lanczoshybrid regularization," *Electronic Transactions on Numerical Analysis*, vol. 28, pp. 149–167, 2008.

[68] M. E. Kilmer and D. P. Oleary, "Choosing regularization parameters in iterative methods for ill-posed problems," *SIAM J. Matrix Anal. Appl.*, vol. 22, pp. 1204–1221, 2001.

[69] M. L. Oristaglio, "Accuracy of the born and rytov approximations for reflection and refraction at a plane interface," *J. Opt. Soc. Am. A*, vol. 2, pp. 1987–1993, 1985.

[70] J. Bolomey, A. Izadnegahdar, L. Jofre, C. Pichot, G. Peronnet, and M. Solaimani, "Microwave diffraction tomography for biomedical applications," *Microwave Theory and Techniques, IEEE Transactions on*, vol. 30, no. 11, pp. 1998–2000, 1982.

[71] C. Pichot, L. Jofre, G. Peronnet, and J. Bolomey, "Active microwave imaging of inhomogeneous bodies," *Antennas and Propagation, IEEE Transactions on*, vol. 33, no. 4, pp. 416–425, 1985.

[72] S. Pan and A. Kak, "A computational study of reconstruction algorithms for diffraction tomography: Interpolation versus filtered-backpropagation," *Acoustics, Speech and Signal Processing, IEEE Transactions on*, vol. 31, no. 5, pp. 1262–1275, 1983.

[73] Y. Wang and W. Chew, "An iterative solution of the two-dimension electrom,agnetic inverse scattering problem," *Int. J. Sys. Technology*, vol. 1, pp. 100–108, 1989.

[74] W. Chew and Y. Wang, "Reconstruction of two-dimensional permittivity distribution using the distorted born iterative method," *Medical Imaging, IEEE Transactions on*, vol. 9, no. 2, pp. 218–225, 1990.

[75] W. Chew and G. Otto, "Microwave imaging of multiple metallic cylinders using shape functions," in *Antennas and Propagation Society International Symposium, Digest. Held in Conjuction with: URSI Radio Science Meeting and Nuclear EMP Meeting., IEEE*, 1992.

[76] G. Otto and W. C. Chew, "Microwave inverse scattering - local shape function imaging for improved resolution of strong scatterers," *Microwave Theory and Techniques, IEEE Transactions on*, vol. 42, no. 1, pp. 137–141, 1994.

[77] K. Paulsen, P. Meaney, M. Moskowitz, and J. Sullivan, J.M., "A dual mesh scheme for finite element based reconstruction algorithms," *Medical Imaging, IEEE Transactions on*, vol. 14, no. 3, pp. 504–514, 1995.

[78] W. Chew and J. Lin, "A frequency-hopping approach for microwave imaging of large inhomogeneous bodies," *Microwave and Guided Wave Letters, IEEE*, vol. 5, no. 12, pp. 439–441, 1995.

[79] S. Caorsi, M. Donelli, D. Franceschini, and A. Massa, "A new methodology based on an iterative multiscaling for microwave imaging," *Microwave Theory and Techniques, IEEE Transactions on*, vol. 51, no. 4, pp. 1162–1173, 2003.

[80] S. Caorsi, M. Donelli, and A. Massa, "Detection, location, and imaging of multiple scatterers by means of the iterative multiscaling method," *Microwave Theory and Techniques, IEEE Transactions on*, vol. 52, no. 4, pp. 1217–1228, 2004.

[81] G. Franceschini, M. Donelli, R. Azaro, and A. Massa, "Inversion of phaseless total field data using a two-step strategy based on the iterative multiscaling approach," *Geoscience and Remote Sensing, IEEE Transactions on*, vol. 44, no. 12, pp. 3527–3539, 2006.

[82] T. M. Habashy and A. Abubakar, "A general framework for constraint minimization for the inversion of electromagnetic measurements," *Progress in Electromagnetics Research*, vol. 46, pp. 265–312, 2004.

[83] J. De Zaeytijd, A. Franchois, C. Eyraud, and J.-M. Geffrin, "Full-wave three-dimensional microwave imaging with a regularized gauss-newton method; theory and experiment," *Antennas and Propagation, IEEE Transactions on*, vol. 55, no. 11, pp. 3279–3292, 2007.

[84] P. Mojabi and J. LoVetri, "Microwave biomedical imaging using the multiplicative regularized gauss–newton inversion," *Antennas and Wireless Propagation Letters, IEEE*, vol. 8, pp. 645–648, 2009.

[85] ——, "Enhancement of the krylov subspace regularization for microwave biomedical imaging," *Medical Imaging, IEEE Transactions on*, vol. 28, no. 12, pp. 2015–2019, 2009.

[86] ——, "Overview and classification of some regularization techniques for the gauss-newton inversion method applied to inverse scattering problems," *Antennas and Propagation, IEEE Transactions on*, vol. 57, no. 9, pp. 2658–2665, 2009.

[87] ——, “Comparison of te and tm inversions in the framework of the gauss-newton method,” *Antennas and Propagation, IEEE Transactions on*, vol. 58, no. 4, pp. 1336–1348, 2010.

[88] G. Bozza, C. Estatico, M. Pastorino, and A. Randazzo, “An inexact newton method for microwave reconstruction of strong scatterers,” *Antennas and Wireless Propagation Letters, IEEE*, vol. 5, no. 1, pp. 61–64, 2006.

[89] G. Bozza and M. Pastorino, “An inexact newton-based approach to microwave imaging within the contrast source formulation,” *Antennas and Propagation, IEEE Transactions on*, vol. 57, no. 4, pp. 1122–1132, 2009.

[90] A. Franchois and A. G. Tijhuis, “A quasi-newton reconstruction algorithm for a complex microwave imaging scanner environment,” *Radio Sci.*, vol. 38, no. 2, pp. 1–13, 2003.

[91] N. Joachimowicz, J. Mallorqui, J.-C. Bolomey, and A. Broquets, “Convergence and stability assessment of newton-kantorovich reconstruction algorithms for microwave tomography,” *Medical Imaging, IEEE Transactions on*, vol. 17, no. 4, pp. 562–570, 1998.

[92] A. Franchois and C. Pichot, “Microwave imaging-complex permittivity reconstruction with a levenberg-marquardt method,” *Antennas and Propagation, IEEE Transactions on*, vol. 45, no. 2, pp. 203–215, 1997.

[93] R. F. Remis and P. M. van den Berg, “On the equivalence of the newton-kantorovich and distorted born methods,” *Inverse Problems*, vol. 16, no. 1, pp. L1–L4, 2000.

[94] A. N. Tikhonov, “Regularization of incorrectly posed problems,” *Soviet Math. Dokl*, vol. 4, pp. 1624–1627, 1963.

[95] A. N. Tikhonov, V. Y. Aresnin, and F. John, *Solutions of Ill-posed Problems*. New York: John Wiley and Sons, 1977.

[96] N. Joachimowicz, C. Pichot, and J. Hugonin, “Inverse scattering: an iterative numerical method for electromagnetic imaging,” *Antennas and Propagation, IEEE Transactions on*, vol. 39, no. 12, pp. 1742–1753, 1991.

[97] P. Mojabi and J. LoVetri, “Preliminary investigation of the ncp parameter choice method for inverse scattering problems using bim: 2-d tm case,” *Applied Computational Electromagnetics Society Journal*, vol. 23, no. 3, pp. 207–214, 2008.

[98] C. Gilmore, P. Mojabi, and J. LoVetri, "Comparison of an enhanced distorted born iterative method and the multiplicative-regularized contrast source inversion method," *Antennas and Propagation, IEEE Transactions on*, vol. 57, no. 8, pp. 2341–2351, 2009.

[99] M. Hanke, *Conjugate Gradient Type Methods for Ill-Posed Problems.* Longman Scientific and Technical, 1995.

[100] W. Yu, Z. Peng, and L. Jen, "The time-domain born iterative method for two-dimensional inhomogeneous lossy dielectric," *Journal of Microwaves*, vol. 11, no. 12, 1995.

[101] P. Chaturvedi and R. Plumb, "Electromagnetic imaging of underground targets using constrained optimization," *Geoscience and Remote Sensing, IEEE Transactions on*, vol. 33, no. 3, pp. 551–561, 1995.

[102] M. Moghaddam and W. Chew, "Study of some practical issues in inversion with the born iterative method using time-domain data," *Antennas and Propagation, IEEE Transactions on*, vol. 41, no. 2, pp. 177–184, 1993.

[103] W. H. Weedon and W. C. Chew, "Time-domain inverse scattering using the local shape function (lsf) method," *Inverse Problems*, vol. 9, no. 5, pp. 551–564, 1993.

[104] J. Ma, W. C. Chew, C.-C. Lu, and J. Song, "Image reconstruction from te scattering data using equation of strong permittivity fluctuation," *Antennas and Propagation, IEEE Transactions on*, vol. 48, no. 6, pp. 860–867, 2000.

[105] T. Takenaka, Z. Q. Meng, T. Tanaka, and W. C. Chew, "Local shape function combinedwith genetic algorithm appliedto inverse scattering for strips," *Microwave and Optical Technology Letters*, vol. 16, pp. 337–341, 1997.

[106] A. Yapar, H. Sahinturk, I. Akduman, and R. Kress, "One-dimensional profile inversion of a cylindrical layer with inhomogeneous impedance boundary: a newton-type iterative solution," *Geoscience and Remote Sensing, IEEE Transactions on*, vol. 43, no. 10, pp. 2192–2199, 2005.

[107] S. Caorsi, G. Gragnani, S. Medicina, M. Pastorino, and G. Zunino, "Microwave imaging method using a simulated annealing approach," *Microwave and Guided Wave Letters, IEEE*, vol. 1, no. 11, pp. 331–333, 1991.

[108] L. Garnero, A. Franchois, J.-P. Hugonin, C. Pichot, and N. Joachimowicz, "Microwave imaging-complex permittivity reconstruction-by simulated annealing," *Microwave Theory and Techniques, IEEE Transactions on*, vol. 39, no. 11, pp. 1801–1807, 1991.

[109] M. Pastorino, “Stochastic optimization methods applied to microwave imaging: A review,” *Antennas and Propagation, IEEE Transactions on*, vol. 55, no. 3, pp. 538–548, 2007.

[110] E. Bermani, S. Caorsi, and M. Raffetto, “A microwave object recognition approach based on neural networks,” in *Instrumentation and Measurement Technology Conference, IMTC, Proceedings of the 16th IEEE*, vol. 3, 1999.

[111] M. Pastorino, A. Massa, and S. Caorsi, “A microwave inverse scattering technique for image reconstruction based on a genetic algorithm,” *Instrumentation and Measurement, IEEE Transactions on*, vol. 49, no. 3, pp. 573–578, 2000.

[112] S. Caorsi and M. Pastorino, “Two-dimensional microwave imaging approach based on a genetic algorithm,” *Antennas and Propagation, IEEE Transactions on*, vol. 48, no. 3, pp. 370–373, 2000.

[113] S. Caorsi, A. Massa, and M. Pastorino, “A computational technique based on a real-coded genetic algorithm for microwave imaging purposes,” *Geoscience and Remote Sensing, IEEE Transactions on*, vol. 38, no. 4, pp. 1697–1708, 2000.

[114] ——, “A crack identification microwave procedure based on a genetic algorithm for nondestructive testing,” *Antennas and Propagation, IEEE Transactions on*, vol. 49, no. 12, pp. 1812–1820, 2001.

[115] S. Caorsi, A. Massa, M. Pastorino, and M. Donelli, “Improved microwave imaging procedure for nondestructive evaluations of two-dimensional structures,” *Antennas and Propagation, IEEE Transactions on*, vol. 52, no. 6, pp. 1386–1397, 2004.

[116] M. Benedetti, M. Donelli, and A. Massa, “Multicrack detection in two-dimensional structures by means of ga-based strategies,” *Antennas and Propagation, IEEE Transactions on*, vol. 55, no. 1, pp. 205–215, 2007.

[117] X. Chen, D. Liang, and K. Huang, “Microwave imaging 3-d buried objects using parallel genetic algorithm combined with fdtd technique,” *J. Electromagnetic Waves and Applications*, vol. 20, no. 13, pp. 1761–1774, 2006.

[118] M. Benedetti, M. Donelli, A. Martini, M. Pastorino, A. Rosani, and A. Massa, “An innovative microwave-imaging technique for nondestructive evaluation: Applications to civil structures monitoring and biological bodies inspection,” *Instrumentation and Measurement, IEEE Transactions on*, vol. 55, no. 6, pp. 1878–1884, 2006.

[119] A. Qing, “Electromagnetic inverse scattering of multiple two-dimensional perfectly conducting objects by the differential evolution strategy,” *Antennas and Propagation, IEEE Transactions on*, vol. 51, no. 6, pp. 1251–1262, 2003.

[120] K. V. Price, *An introduction to differential evolution*, M. D. D. Corne and F. Glover, Eds. McGraw-Hill, New York, 1999.

[121] K. A. Michalski, "Electromagnetic imaging of circular-cylindrical conductors and tunnel using a differential evolution algorithm," *Microw. Opt. Technol. Lett.*, vol. 27, no. 5, pp. 330–334, 2000.

[122] ——, "Electromagnetic imaging of elliptical-cylindrical conductors and tunnel using a differential evolution algorithm," *Microw. Opt. Technol. Lett.*, vol. 28, no. 3, pp. 164–169, 2001.

[123] M. Donelli and A. Massa, "Computational approach based on a particle swarm optimizer for microwave imaging of two-dimensional dielectric scatterers," *Microwave Theory and Techniques, IEEE Transactions on*, vol. 53, no. 5, pp. 1761–1776, 2005.

[124] M. Donelli, G. Franceschini, A. Martini, and A. Massa, "An integrated multiscaling strategy based on a particle swarm algorithm for inverse scattering problems," *Geoscience and Remote Sensing, IEEE Transactions on*, vol. 44, no. 2, pp. 298–312, 2006.

[125] M. Donelli, D. Franceschini, P. Rocca, and A. Massa, "Three-dimensional microwave imaging problems solved through an efficient multiscaling particle swarm optimization," *Geoscience and Remote Sensing, IEEE Transactions on*, vol. 47, no. 5, pp. 1467–1481, 2009.

[126] T. Huang and A. S. Mohan, "A hybrid boundary condition for robust particle swarm optimization," *Antennas Wireless Propag. Lett.*, vol. 4, pp. 112–117, 2005.

[127] P. Rocca, M. Benedetti, M. Donelli, D. Franceschini, and A. Massa, "Evolutionary optimization as applied to inverse scattering problems," *Inverse Problems*, vol. 25, no. 12, pp. 1–41, 2009.

[128] S. Caorsi, A. Massa, and M. Pastorino, "A numerical solution to full-vector electromagnetic scattering by three-dimensional nonlinear bounded dielectrics," *Microwave Theory and Techniques, IEEE Transactions on*, vol. 43, no. 2, pp. 428–436, 1995.

[129] P. Meaney, Q. Fang, S. Geimer, A. Streltsov, and K. Paulsen, "3d scalar microwave image reconstruction algorithm," in *Microwave Symposium Digest, 2002 IEEE MTT-S International*, vol. 3, 2002.

[130] A. E. Bulyshev, A. E. Souvorov, S. Y. Semenov, V. G. Posukh, and Y. E. Sizov, "Three-dimensional vector microwave tomography: theory and computational experiments," *Inverse Problems*, vol. 20, no. 4, pp. 1239–1259, 2004.

[131] C.-S. Park and B.-S. Jeong, "Reconstruction of a high contrast and large object by using the hybrid algorithm combining a levenberg-marquardt algorithm and a genetic algorithm," *Magnetics, IEEE Transactions on*, vol. 35, no. 3, pp. 1582–1585, 1999.

[132] A. Sabouni, D. Flores-Tapia, S. Noghanian, G. Thomas, and S. Pistorius, "Hybrid microwave tomography technique for breast cancer imaging," in *Engineering in Medicine and Biology Society, EMBS, 28th Annual International Conference of the IEEE*, 2006.

[133] A. Ashtari, S. Noghanian, A. Sabouni, J. Aronsson, G. Thomas, and S. Pistorius, "Using a priori information for regularization in breast microwave image reconstruction," *Biomedical Engineering, IEEE Transactions on*, vol. 57, no. 9, pp. 2197–2208, 2010.

[134] I. Catapano, L. Crocco, M. D'Urso, and T. Isernia, "On the effect of support estimation and of a new model in 2-d inverse scattering problems," *Antennas and Propagation, IEEE Transactions on*, vol. 55, no. 6, pp. 1895–1899, 2007.

[135] M. Brignone, G. Bozza, A. Randazzo, R. Aramini, M. Piana, and M. Pastorino, "Hybrid approach to the inverse scattering problem by using ant colony optimization and no-sampling linear sampling," in *Antennas and Propagation Society International Symposium, IEEE*, 2008.

[136] M. Brignone, G. Bozza, A. Randazzo, M. Piana, and M. Pastorino, "A hybrid approach to 3d microwave imaging by using linear sampling and aco," *Antennas and Propagation, IEEE Transactions on*, vol. 56, no. 10, pp. 3224–3232, 2008.

[137] P. Merz and B. Freisleben, "Fitness landscape analysis and memetic algorithms for the quadratic assignment problem," *Evolutionary Computation, IEEE Transactions on*, vol. 4, no. 4, pp. 337–352, 2000.

[138] P. Moscato, L. Plata, L. Plata, and M. G. Norman, "A memetic approach for the traveling salesman problem implementation of a computational ecology for combinatorial optimization on message-passing systems," in *Proceedings of the International Conference on Parallel Computing and Transputer Applications.* IOS Press, 1992.

[139] S. Caorsi, A. Massa, M. Pastorino, M. Raffetto, and A. Randazzo, "Detection of buried inhomogeneous elliptic cylinders by a memetic algorithm," *Antennas and Propagation, IEEE Transactions on*, vol. 51, no. 10, pp. 2878–2884, 2003.

[140] T. C. Williams, J. M. Sill, J. Bourqui, and E. C. Fear, "Tissue sensing adaptive radar for breast cancer detection: Practical improvements," in *IEEE International Symposium on Antennas and Propagation*, 2010.

[141] M. Bertero and P. Boccacci, *Inverse Problems in Imaging.* Bristol, CT: IOP, 1998.

[142] R. Harrington, *Time-Harmonic Electromagnetic Fields.* New York: IEEE Press, 2001.

[143] F. Ahmad, M. Amin, and S. Kassam, "Synthetic aperture beamformer for imaging through a dielectric wall," *Aerospace and Electronic Systems, IEEE Transactions on*, vol. 41, no. 1, pp. 271–283, 2005.

[144] Hadamard, *Lectures on Cauchys Problem in Linear Partial Differential Equations.* New Haven, CT: Yale University Press, 1923.

[145] J. H. Holland, *Adaptation in Natural and Artificial Systems.* Ann Arbor, MI: Univ. Michigan Press, 1975.

[146] R. Haupt, "An introduction to genetic algorithms for electromagnetics," *Antennas and Propagation Magazine, IEEE*, vol. 37, no. 2, pp. 7–15, 1995.

[147] J. Johnson and Y. Rahmat-Samii, "Genetic algorithms in engineering electromagnetics," *Antennas and Propagation Magazine, IEEE*, vol. 39, no. 4, pp. 7–21, 1997.

[148] M. Converse, E. Bond, B. Veen, and C. Hagness, "A computational study of ultra-wideband versus narrowband microwave hyperthermia for breast cancer treatment," *Microwave Theory and Techniques, IEEE Transactions on*, vol. 54, no. 5, pp. 2169–2180, 2006.

[149] C. S. Park, S. K. Park, and J. W. Ra, "Microwave imaging in angular spectral domain based on the improved newton's procedure," *Microwave and Optical Technology Letters*, vol. 7, no. 1, pp. 28–31, 1994.

[150] A. Sabouni, S. Noghanian, and S. Pistorius, "Effects of tissue composition on the accuracy of microwave breast tumour imaging," in *World Congress on Medical Physics and Biomedical Engineering*, 2006.

[151] M. Pastorino, S. Caorsi, and A. Massa, "A global optimization technique for microwave nondestructive evaluation," *Instrumentation and Measurement, IEEE Transactions on*, vol. 51, no. 4, pp. 666–673, 2002.

[152] E. Bort, G. Franceschini, A. Massa, and P. Rocca, "Improving the effectiveness of ga-based approaches to microwave imaging through an innovative parabolic crossover," *Antennas and Wireless Propagation Letters, IEEE*, vol. 4, pp. 138–142, 2005.

[153] S. Caorsi and M. Pastorino, "Microwave imaging using a genetic algorithm," *Electromagnetic Nondestructive Evaluation (II)*, vol. 14, pp. 233–242, R. Albanese et al., Eds. Amsterdam, The Netherlands: IOS, 1998.

[154] ——, "Microwave nondestructive testing: A stochastic optimization approach," *Electromagnetic Nondestructive Evaluation (III)*, vol. 15, pp. 145–156, D. Lesselier and A. Razek, Eds. Amsterdam, The Netherlands: IOS, 1999.

[155] S. Caorsi, G. Gragnani, S. Medicina, M. Pastorino, and G. Zunino, "Microwave imaging based on a markov random field model," *Antennas and Propagation, IEEE Transactions on*, vol. 42, no. 3, pp. 293 –303, mar 1994.

[156] C. C. Chiu and W. T. Chen, "Electromagnetic imaging for an imperfectly conducting cylinder by the genetic algorithm [medical application]," *Microwave Theory and Techniques, IEEE Transactions on*, vol. 48, no. 11, pp. 1901–1905, 2000.

[157] S. Caorsi, A. Costa, and M. Pastorino, "Microwave imaging within the second-order born approximation: stochastic optimization by a genetic algorithm," *Antennas and Propagation, IEEE Transactions on*, vol. 49, no. 1, pp. 22–31, 2001.

[158] S. Caorsi, G. Gragnani, and M. Pastorino, "Two-dimensional microwave imaging by a numerical inverse scattering solution," *Microwave Theory and Techniques, IEEE Transactions on*, vol. 38, no. 8, pp. 981–990, 1990.

[159] P. Meaney, K. Paulsen, and T. Ryan, "Two-dimensional hybrid element image reconstruction for tm illumination," *Antennas and Propagation, IEEE Transactions on*, vol. 43, no. 3, pp. 239–247, 1995.

[160] I. T. Rekanos and T. D. Tsiboukis, "An iterative numerical method for inverse scattering problems," *Radio Sci.*, vol. 34, no. 6, pp. 1401–1412, 1999.

[161] W. Chien and C. C. Chiu, "Using nu-ssga to reduce the searching time in inverse problem of a buried metallic object," *Antennas and Propagation, IEEE Transactions on*, vol. 53, no. 10, pp. 3128–3134, 2005.

[162] A. Qing, "An experimental study on electromagnetic inverse scattering of a perfectly conducting cylinder by using the real-coded genetic algorithm," *Microwave and Optical Technology Letters*, vol. 30, pp. 315–320, 2001.

[163] V. Thomas, C. Gopakumar, J. Yohannan, A. Lonappan, G. Bindu, A. V. P. Kumar, V. Hamsakutty, and K. T. Mathew, "A novel technique for localizing the scatterer in inverse profiling of two dimensional circularly symmetric dielectric scatterers using degree of symmetry and neural networks," *Journal of Electromagnetic Waves and Applications*, vol. 19, no. 15, pp. 2113–2121, 2005.

[164] D. Colton and R. Kress, *Inverse Acoustic and Electromagnetic Scattering Theory.* Springer-Verlag, New York, 1992.

[165] I. T. Rekanos, "Time-domain inverse scattering using lagrange multipliers: An iterative fdtd-based optimization technique," *Journal of Electromagnetic Waves and Applications*, vol. 17, no. 2, pp. 271–289, 2003.

[166] N. W. Kang, Y. S. Chung, C. Cheon, and H. K. Jung, "A new 2-d image reconstruction algorithm based on fdtd and design sensitivity analysis," *Microwave Theory and Techniques, IEEE Transactions on*, vol. 50, no. 12, pp. 2734–2740, 2002.

[167] T. Takenaka, H. Jia, and T. Tanaka, "Microwave imaging of electrical property distributions by a forward-backward time stepping method," *Journal of Electromagnetic Waves Application*, vol. 14, pp. 1609–1625, 2000.

[168] S. He, P. Fuks, and G. Larson, "An optimization approach to time-domain electromagnetic inverse problem for a stratified dispersive and dissipative slab," *Antennas and Propagation, IEEE Transactions on*, vol. 44, no. 9, pp. 1277–1282, 1996.

[169] I. Rekanos and T. Tsiboukis, "A finite element-based technique for microwave imaging of two-dimensional objects," *Instrumentation and Measurement, IEEE Transactions on*, vol. 49, no. 2, pp. 234–239, 2000.

[170] A. Taflove and S. C. Hagness, *Computational Electrodynamics: The Finite-difference Time-domain Method.* 3rd ed. Artech House, Norwood, 2005.

[171] J. Berenger, "A perfectly matched layer for the absorption of electromagnetic waves," *Journal of Computational Physics*, vol. 114, no. 2, pp. 185–200, 1994.

[172] P. Kosmas, C. Rappaport, and E. Bishop, "Modeling with the fdtd method for microwave breast cancer detection," *Microwave Theory and Techniques, IEEE Transactions on*, vol. 52, no. 8, pp. 1890–1897, 2004.

[173] M. Bui, S. Stuchly, and G. Costache, "Propagation of transients in dispersive dielectric media," *Microwave Theory and Techniques, IEEE Transactions on*, vol. 39, no. 7, pp. 1165–1172, 1991.

[174] J. Kaipio and E. Somersalo, *Statistical and Computational Inverse Problems.* Springer Science and Business Media, 2004.

[175] A. Ashtari, "Signal processing methods for high resolution microwave image reconstruction," Ph.D. dissertation, University of Manitoba, Winnipeg, Manitoba, Canada, 2009.

[176] D. Flores-Tapia, "Wavefront reconstruction of subsurface radar imagery acquired along cylindrical scan trajectories," Ph.D. dissertation, University of Manitoba, Winnipeg, Manitoba, Canada, 2008.

[177] D. Flores-Tapia and G. Thomas, "Breast microwave imaging and focusing based on range migration techniques," in *16th Int. Zurich Symposium on Electromagnetic Compatibility, Topical Meeting on Biomedical EMC*, vol. 1, 2005.

[178] M. Snir, S. Otto, S. H. Leaderman, D. Walker, and J. Dongarra, *MPI The Complete Reference.* Cambridge: MIT Press, 1998.

[179] R. Haupt and S. E. Haupt, *Practical Genetic Algorithms.* John Wiley and Sons, New York, 1998.

[180] C. A. Balanis, *Antenna theory: Analysis and design.* John wiley & Son Inc. Hoston New Jeresy, 2005.

[181] J. Rockway and J. Logan, MININEC Software, 1980.

[182] W. Yu, "Gems a high performance em simulation tool," in *Electrical Design of Advanced Packaging Systems Symposium, EDAPS, IEEE*, 2009.

[183] "Breast cancer facts and figures," Amreican Cancer Society, Atlanta, Tech. Rep., 2010.

[184] E. Fear, S. Hagness, P. Meaney, M. Okoniewski, and M. Stuchly, "Enhancing breast tumor detection with near-field imaging," *Microwave Magazine, IEEE*, vol. 3, no. 1, pp. 48–56, 2002.

[185] K. Carr, "Microwave radiometry: its importance to the detection of cancer," *Microwave Theory and Techniques, IEEE Transactions on*, vol. 37, no. 12, pp. 1862–1869, 1989.

[186] A. Rosen, M. Stuchly, and A. Vander Vorst, "Applications of rf/microwaves in medicine," *Microwave Theory and Techniques, IEEE Transactions on*, vol. 50, no. 3, pp. 963–974, 2002.

[187] E. Zastrow, S. K. Davis, and S. C. Hagness, "Safety assessment of breast cancer detection via ultrawideband microwave radar operating in pulsed-radiation mode," *Microwave and Optical Technology Letters*, vol. 49, no. 1, pp. 221–225, 2007.

[188] S. Salvador and G. Vecchi, "Experimental tests of microwave breast cancer detection on phantoms," *Antennas and Propagation, IEEE Transactions on*, vol. 57, no. 6, pp. 1705–1712, 2009.

[189] M. O'Halloran, E. Jones, and M. Glavin, "Quasi-multistatic mist beamforming for the early detection of breast cancer," *Biomedical Engineering, IEEE Transactions on*, vol. 57, no. 4, pp. 830–840, 2010.

[190] M. Klemm, I. Craddock, J. Leendertz, A. Preece, and R. Benjamin, "Radar-based breast cancer detection using a hemispherical antenna array-experimental results," *Antennas and Propagation, IEEE Transactions on*, vol. 57, no. 6, pp. 1692–1704, 2009.

[191] S. K. Davis, E. J. Bond, X. Li, S. C. Hagness, and B. D. Van-Veen, "Microwave imaging via space-time beamforming for the early detection of breast cancer: Beamformer design in the frequency domain," *Journal of Electromagnetic Waves and Applications*, vol. 17, no. 2, pp. 357–381, 2003.

[192] E. Fear and M. Stuchly, "Microwave detection of breast cancer," *Microwave Theory and Techniques, IEEE Transactions on*, vol. 48, no. 11, pp. 1854–1863, 2000.

[193] E. Fear and M. Okoniewski, "Confocal microwave imaging for breast tumor detection: application to a hemispherical breast model," in *Microwave Symposium Digest, 2002 IEEE MTT-S International*, vol. 3, 2002.

[194] Y. Xie, B. Guo, J. Li, and P. Stoica, "Novel multistatic adaptive microwave imaging methods for early breast cancer detection," *EURASIP J. Appl. Si. P.*, vol. 2006, 2006.

[195] M. Klemm, I. J. Craddock, J. Leendertz, A. W. Preece, and R. Benjamin, "Breast cancer detection using symmetrical antenna array," in *Proceedings of the 2nd European Conference on Antennas and Propagation*, 2007.

[196] I. J. Craddock, M. Klemm, J. Leendertz, A. W. Preece, and R. Benjamin, "Development and application of a uwb radar system for breast imaging," in *Antennas and Propagation Conference, LAPC*, 2008.

[197] R. C. Conceicao, M. O'Halloran, M. Glavin, and E. Jones, "Comparison of planar and circular antenna configurations for breast cancer detection using microwave imaging," *Progress In Electromagnetics Research*, vol. 99, pp. 1–20, 2009.

[198] X. Li, E. Bond, B. Van Veen, and S. Hagness, "An overview of ultra-wideband microwave imaging via space-time beamforming for early-stage breast-cancer detection," *Antennas and Propagation Magazine, IEEE*, vol. 47, no. 1, pp. 19–34, 2005.

[199] E. Fear, J. Sill, and M. Stuchly, "Experimental feasibility study of confocal microwave imaging for breast tumor detection," *Microwave Theory and Techniques, IEEE Transactions on*, vol. 51, no. 3, pp. 887–892, 2003.

[200] R. Nilavalan, I. Craddock, A. Preece, J. Leendertz, and R. Benjamin, "Wideband microstrip patch antenna design for breast cancer tumour detection," *Microwaves, Antennas Propagation, IET*, vol. 1, no. 2, pp. 277–281, 2007.

[201] S. Davis, H. Tandradinata, S. Hagness, and B. Van Veen, "Ultrawideband microwave breast cancer detection: a detection-theoretic approach using the generalized likelihood ratio test," *Biomedical Engineering, IEEE Transactions on*, vol. 52, no. 7, pp. 1237–1250, 2005.

[202] *University of Bristol, Reseach Review*, issue 19, Winter 2008.

[203] P. Meaney, K. Paulsen, B. Pogue, and M. Miga, "Microwave image reconstruction utilizing log-magnitude and unwrapped phase to improve high-contrast object recovery," *Medical Imaging, IEEE Transactions on*, vol. 20, no. 2, pp. 104–116, 2001.

[204] P. Meaney, K. Paulsen, A. Hartov, and R. Crane, "An active microwave imaging system for reconstruction of 2-d electrical property distributions," *Biomedical Engineering, IEEE Transactions on*, vol. 42, no. 10, pp. 1017 –1026, 1995.

[205] P. M. Meaney, S. A. Pendergrass, M. W. Fanning, D. Li, and K. D. Paulsen, "Importance of using reduced contrast coupling medium in 2d microwave breast imaging," *Journal of Electromagnetic Waves and Application*, vol. 17, pp. 333–355, 2003.

[206] T. Rubaek, O. Kim, and P. Meincke, "Computational validation of a 3-d microwave imaging system for breast-cancer screening," *Antennas and Propagation, IEEE Transactions on*, vol. 57, no. 7, pp. 2105–2115, 2009.

[207] P. Kosmas and C. Rappaport, "Time reversal with the fdtd method for microwave breast cancer detection," *Microwave Theory and Techniques, IEEE Transactions on*, vol. 53, no. 7, pp. 2317–2323, 2005.

[208] ——, "Fdtd-based time reversal for microwave breast cancer detection-localization in three dimensions," *Microwave Theory and Techniques, IEEE Transactions on*, vol. 54, no. 4, pp. 1921–1927, 2006.

[209] G. Ku, B. D. Fornage, X. Jin, M. H. Xu, K. K. Hunt, and L. V. Wang, "Thermoacoustic and photoacoustic tomography of thick biological tissues toward breast imaging," *Tech. Cancer Res. Treatment*, vol. 4, pp. 559–565, 2005.

[210] R. A. Kruger, K. D. Miller, H. E. Reynolds, W. L. Kiser, D. R. Reinecke, and G. A. Kruger, "Breast cancer in vivo: Contrast enhancement with thermoacoustic ct at 434 mhzfeasibility study," *Radiology*, no. 216, pp. 279–283, 2000.

[211] M. Zhao, J. Shea, S. Hagness, D. van der Weide, B. Van Veen, and T. Varghese, "Numerical study of microwave scattering in breast tissue via coupled dielectric and elastic contrasts," *Antennas and Wireless Propagation Letters, IEEE*, vol. 7, pp. 247–250, 2008.

[212] M. S. Hawley, A. Broquetas, L. Jofre, J. C. Bolomey, and G. Gahoriaud, "Microwave imaging of tissue blood content changes," *J. Biomed. Eny*, vol. 13, pp. 197–202, 1991.

[213] E. C. Burdctte, F. L. Cain, and J. Seals, "In situ tissue permittivity at microwave frequencies: perspective, techniques, results," *Medical Applicarioris of Microwave Imaging*, pp. 13–40, 1986.

[214] S. S. Chaudhary, R. K. Mishra, A. Swarup, and J. M. Thomas, "Dielectric properties of normal and malignant human breast tissues at radiowave and microwave frequencies," *Indian Journal of Biochemistry and Biophysics*, vol. 21, pp. 76–79, 1984.

[215] C. Gabriel, S. Gabriel, and E. Corthout, "The dielectric properties of biological tissues: I. literature survey," *Physics in Medicine and Biology*, vol. 21, pp. 2231–2249, 1996.

[216] S. Gabriel, R. W. Lau, and C. Gabriel, "The dielectric properties of biological tissues: Ii. measurements in the frequency range 10 hz to 20 ghz," *Physics in Medicine and Biology*, vol. 41, pp. 2251–2269, 1996.

[217] ——, "The dielectric properties of biological tissues: Iii. parametric models for the dielectric spectrum of tissues," *Physics in Medicine and Biology*, vol. 41, pp. 2271–2293, 1996.

[218] G. C. Gabriel and S. Gabriel, "Compilation of the dielectric properties of body tissues at rf and microwave frequencies," King's Coll London(United Kingdom), Dept of Physics, Tech. Rep., 1996.

[219] W. T. Joines, Y. Zhang, C. Li, and R. L. Jirtle., "The measured electrical properties of normal and malignant human tissues from 50 to 900 mhz," *Medical Physics*, vol. 21, pp. 547–550, 1994.

[220] M. Lazebnik, L. McCartney, D. Popovic, B. Watkins, M. J. Lindstrom, J. Harter, S. Sewall, A. Magliocco, J. H. Booske, M. Okoniewski, and S. C. Hagness, "large-scale study of the ultrawideband microwave dielectric properties of normal breast

tissue obtained from reduction surgeries," *Physics in Medicine and Biology*, vol. 52, pp. 2637–2656, 2007.

[221] M. Lazebnik, D. Popovic, L. McCartney, C. Watkins, M. Lindstrom, J. Harter, S. Sewall, T. Ogilvie, A. Magliocco, T. M. Breslin, D. Temple, W. abd Mew, J. H. Booske, M. Okoniewski, and S. C. Hagness, "A large-scale study of the ultrawideband microwave dielectric properties of normal, benign, and malignant breast tissues obtained from cancer surgeries," *Physics in Medicine and Biology*, vol. 52, pp. 6093–6115, 2007.

[222] H. Fricke and S. Morse, "The electrical capacity of tumors of the breast," *J. Cancer Res.*, vol. 10, pp. 340–376, 1926.

[223] H. P. Schwan, *Electrical properties measured with alternating currents; body tissues.* Handbook of Biological Data. Philadelphia: W. B, Saunders Co, 1956.

[224] A. Surowiec, S. Stuchly, J. Barr, and A. Swarup, "Dielectric properties of breast carcinoma and the surrounding tissues," *Biomedical Engineering, IEEE Transactions on*, vol. 35, no. 4, pp. 257–263, 1988.

[225] E. Zastrow, S. K. Davis, M. Lazebnik, F. Kelcz, B. D. Van Veen, and S. C. Hagness, "Database of 3d grid-based numerical breast phantoms for use in computational electromagnetics simulations," *Instruction manual*, 2007.

[226] R. J. Halter, T. Zhou, P. M. Meaney, A. Hartov, R. J. B. Jr, K. M. Rosenkranz, W. A. Wells, C. A. Kogel, A. Borsic, E. J. Rizzo, and K. D. Paulsen, "The correlation of in vivo and ex vivo tissue dielectric properties to validate electromagnetic breast imaging: initial clinical experience," *Physiological Measurement*, vol. 30, no. 6, pp. S121–S136, 2009.

[227] E. Zastrow, S. Davis, M. Lazebnik, F. Kelcz, B. Van Veen, and S. Hagness, "Development of anatomically realistic numerical breast phantoms with accurate dielectric properties for modeling microwave interactions with the human breast," *Biomedical Engineering, IEEE Transactions on*, vol. 55, no. 12, pp. 2792–2800, 2008.

[228] *UWCEM Numerical Breast Phantoms Repository*, University of Wisconsin - Madison.

[229] J. Richmond, "Scattering by a dielectric cylinder of arbitrary cross section shape," *Antennas and Propagation, IEEE Transactions on*, vol. 13, no. 3, pp. 334–341, 1965.

[230] S. Poplack, T. D. Tosteson, W. A. Wells, B. W. Pogue, P. M. Meaney, A. Hartov, C. A. Kogel, S. K. Soho, J. J. Gibson, and K. D. Paulsen, "Electromagnetic

breast imaging: Results of a pilot study in women with abnormal mammograms,," *Radiology*, vol. 243, no. 2, pp. 350–359, 2007.

[231] B. Kolundzija, J. Ognjanovic, M. Tasic, D. Olcan, M. Paramentic, D. Sumic, M. Kostic, and M. Paviovic, "Wipl-d pro v7.1: 3d electromagnetic solver," Europe: WIPL-D Ltd, Tech. Rep., 2009.

[232] T. Gunnarsson, "Microwave imaging of biological tissues: the current status in the research area," Mlardalen University, Department of Computer Science and Electronics, Tech. Rep., 2006.

[233] A. Joisel, J. Mallorqui, A. Broquetas, J. M. Geffrin, N. Joachimowicz, M. Iossera, L. Jofre, and J. C. Bolomey, "Microwave imaging techniques for biomedical applications," in *Instrumentation and Measurement Technology*, 1999.

[234] C. Eyraud, J. M. Geffrin, A. Litman, P. Sabouroux, and H. Giovannini, "Drift correction for scattering measurements," *Applied Physics Letters*, vol. 89, pp. 2 441 041–43, 2006.

[235] C. Gilmore, P. Mojabi, A. Zakaria, M. Ostadrahimi, C. Kaye, S. Noghanian, L. Shafai, S. Pistorius, and J. LoVetri, "A wideband microwave tomography system with a novel frequency selection procedure," *Biomedical Engineering, IEEE Transactions on*, vol. 57, no. 4, pp. 894–904, 2010.

[236] J. Geffrin and A. Joisel, "Comparison of measured and simulated incident and scattered fields in a 434 mhz scanner," in *Proceedings of the 22th URSI General Assembly*, 2002.

[237] T. Gunnarsson, "Quantitative microwave breast phantom imaging using 2.45ghz system," in *International Union of Radio Science General Assembly*, 2008.

[238] M. Ostadrahimi, S. Noghanian, L. Shafai, A. Zakaria, C. Kaye, and J. LoVetri, "Investigating a double layer vivaldi antenna design for fixed array field measurement," *International Journal of Ultra Wideband Communications and Systems*, vol. 1, pp. 282–290, 2010.

[239] J.-M. Geffrin, P. Sabouroux, and C. Eyraud, "Free space experimental scattering database continuation: experimental set-up and measurement precision," *Inverse Probl.*, vol. 21, pp. S117–S130, 2005.

[240] A. Franchois, A. Joisel, C. Pichot, and J. C. Bolomey, "Quantitative microwave imaging with a 2.45-ghz planar microwave camera," *Medical Imaging, IEEE Transactions on*, vol. 17, no. 4, pp. 550–561, 1998.

[241] Y. Rahmat-Samii and E. Michielssen, *Electromagnetic Optimization by Genetic Algorithms.* John Wiley & Sons, New York, 1999.

[242] K. De Jong, "Analysis of the behaviour of a class of genetic adaptive system," Ph.D. dissertation, Univ Micghighan, Ann Arbor, MI, 1975.

[243] J. Grefenstette, "Optimization of control parameters for genetic algorithms," *Systems, Man and Cybernetics, IEEE Transactions on*, vol. 16, no. 1, pp. 122–128, 1986.

[244] Y. Gao, "An upper bound on the convergence rates of canonical genetic algorithms," *Complexity International*, vol. 5, 1998.

[245] K. Yee, "Numerical solution of initial boundary value problems involving maxwell's equations in isotropic media," *Antennas and Propagation, IEEE Transactions on*, vol. 14, no. 3, pp. 302–307, 1966.

[246] M. Ouda and A. Sebak, "Scattering from lossy dielectric cylinders using a multifilament current model with impedance boundary conditions," *Microwaves, Antennas and Propagation, IEE Proceedings H*, vol. 139, no. 5, pp. 429–434, 1992.

[247] W. Yu, R. Mittra, Y. Su, T. Liu, and X. Yang, *Parallel Finite-Difference Time-Domain Method*. Artech House, 2006.

[248] V. Varadarajan and R. Mittra, "Finite-difference time-domain (fdtd) analysis using distributed computing," *Microwave and Guided Wave Letters, IEEE*, vol. 4, no. 5, pp. 144 –145, 1994.

[249] Z. Liu, A. Mohan, T. Aubrey, and W. Belcher, "Techniques for implementation of the fdtd method on a cm-5 parallel computer," *Antennas and Propagation Magazine, IEEE*, vol. 37, no. 5, pp. 64 –71, Oct. 1995.

[250] A. Tinniswood, P. Excell, M. Hargreaves, S. Whittle, and D. Spicer, "Parallel computation of large-scale fdtd problems," in *Computation in Electromagnetics, Third International Conference*, 1996.

[251] M. Sypniewski, J. Rudnicki, and M. Celuch-Marcysiak, "Investigation of multithread fdtd schemes for faster analysis on multiprocessor pcs," in *Antennas and Propagation Society International Symposium, IEEE*, 2000.

[252] G. Schiavone, I. Codreanu, R. Palaniappan, and P. Wahid, "Fdtd speedups obtained in distributed computing on a linux workstation cluster," in *Antennas and Propagation Society International Symposium, IEEE*, 2000.

[253] C. Guiffaut and K. Mahdjoubi, "A parallel fdtd algorithm using the mpi library," *Antennas and Propagation Magazine, IEEE*, vol. 43, no. 2, pp. 94 –103, 2001.

[254] A. Sabouni, M. Xu, S. Noghanian, P. Thulasiraman, and S. Pistorius, "Efficient microwave breast imaging technique using parallel finite difference time domain and parallel genetic algorithms," in *Antennas and Propagation Society International Symposium, IEEE*, 2007.

[255] Agilent technology manual, Agilent 85070E Dielectric Probe Kit 200 MHz to 50 GHz, 2008.